Antenna Devices and Measurement of Radio Emission from Cosmic Ray induced Air Showers at the Pierre Auger Observatory

Diplom-Physiker

Stefan Fliescher

aus Mönchengladbach

Contents

1. Introduction

One century after the discovery of cosmic radiation by Victor Hess in 1912 [1] many questions regarding the nature, the origin and the creation of cosmic rays at the highest energies are still remaining. Ultra-high energy cosmic rays (UHECRs) are one of the most extreme phenomena known to mankind. Macroscopic energies of up to several 10^{20} eV are carried by single particles.

The Pierre Auger Observatory [2] is a hybrid detector for the observation of UHE-CRs. The atmosphere of the earth is used as a calorimeter measuring the particle shower that evolves after the collision of a primary cosmic ray with a particle of the air. These air showers are observed with an array of 1660 ground based particle detectors covering an area of 3600 km^2. The array is overlooked by 27 optical telescopes which are sensitive to the fluorescence light emitted by air molecules which have been excited by the passing particle shower [3]. The combination of both detection techniques allows for a precise determination of the energy and arrival direction of cosmic rays and gives information on the chemical composition of the cosmic ray flux.

The vast dimensions of the Pierre Auger Observatory are due to the rareness of cosmic rays at the highest energies. In the first six years of operation ~ 5000 air showers exceeding 10^{19} eV were observed [4].

For future instrumentations even larger detector arrays are desired. The challenge for alternative novel detection techniques to air showers is to allow for a cost-effective instrumentation of the observational areas as well as the enhancement of accessible shower properties in comparison to the established detection techniques.

The emission of electromagnetic radiation from air showers in the MHz frequency regime was first observed by Jelley and co-workers in 1965 [5]. It was found that air showers emit an electromagnetic pulse in the direction of propagation. The observation of the wavefront with an array of individual antennas at different positions with respect to the shower axis allows for a reconstruction of the properties of the air shower and the corresponding cosmic ray. In the following years progress was made with experiments reporting air-shower observations in a frequency range from 2 to 550 MHz [6, 7]. The realization of a comprehensive radio detector, however, was not feasible until the appearance of fast digital scopes in the last decade. Since 2005 the experiments CODALEMA [8] and LOPES [9] succeed in detecting air showers up to energies of 10^{18} eV.

The Auger Engineering Radio Array (AERA) [10] is a radio detector at the Pierre Auger Observatory. AERA will realize a sensitive area of 20 km^2 instrumented with 160 detector stations and is the first detector which allows for a substantial

measurement of radio signals of air showers beyond 10^{18} eV. AERA is co-located with fluorescence telescopes and the surface detector of Auger. Hence the Pierre Auger Observatory offers the unique possibility to study the radio emission in a calibrated environment even at large distances from the shower axis. The first stage of AERA consists of 21 autonomous detector stations and operates since Sep. 2010.

The data recorded by the detector stations of AERA is a convolution of the radio signal and the response of the read out electronics. To recover as precisely as possible the properties of the electromagnetic wave good knowledge of all components of the detector is required. Here, the antenna deserves special attention as its response is highly frequency dependent and changes with the incoming direction of the signal.

Within the scope of this thesis we develop the fundamental antenna description required to create a calibrated measurement of the transient radio emission from air showers. Having identified the relevant antenna characteristics we present our research and development including the calibration of the antenna which is used in the current setup of AERA.

With a precise detector description at hand we analyze radio detector data that were recorded at the Pierre Auger Observatory. Here we focus on the lateral distribution function (LDF) of the radio signal with respect to the air shower axis and study the data that is recorded during the start up phase of AERA.

Finally, we evaluate candidate antennas for the next setup phase of AERA regarding their response characteristics to transient signals. Using comparative measurements of the variation of the galactic noise level performed at the Nançay Radio Observatory we discriminate the candidate antennas with respect to galactic radio signals.

2. Physics of Ultra-High Energy Cosmic Rays

The atmosphere of the Earth is constantly exposed to a flux of energetic ionizing radiation referred to as cosmic rays. The first experimental observation that consequences partially from the presence of cosmic rays goes back to T. A. Coulomb. In 1785 he discovered the conductivity of the air which was thought to be a perfect isolator.

At the end of the 19th century C.T.R. Wilson realized that the air conductivity is a consequences of the ionization of its molecules. Radio activity was discovered by Becquerel in 1895. Radio active isotopes located in the Earth's crust seemed as conclusive source of the air ionization. A probe to the hypothesis lied in the observation of an decreasing air ionization with increasing height above ground. Experimental results obtained from measurements performed at relatively small heights initially supported this theory.

In 1912 Victor Hess measured in one of his famous balloon flights that the amount of air ionization increases with growing heights above 1000 m rather than decreases [1]. This was the first proof that at least a part of the ionizing radiation is coming from an extraterrestrial origin. For his discovery of cosmic rays Hess was awarded the Nobel Price in 1936.

In the late 1930s Pierre Auger [11] and Werner Kohlhörster [12] operated particle detectors that were spatially separated up to 300 m. They observed that the detectors are often triggered in coincidence despite their distance. This indicated that the observed particles are secondaries produced by a common source and marks the discovery of cosmic ray induced air showers. In his article, P. Auger already concluded that the energies of the primary particles extend above 10^{15} eV at a time when the highest known energies came from radioactive sources up to a few MeV.

2.1 Energy Spectrum

The work stated by Auger led to a series of experiments investigating the energies of cosmic rays. In Fig. 2.1 the energy distribution obtained from various experimental setups is displayed. The energy distribution is commonly expressed as differential flux spectrum:

$$J(E) = \frac{d^4 N}{dE \, dA \, d\Omega \, dt} \quad , \tag{2.1}$$

which counts the number of cosmic rays N that incident per unit area A, time t, solid angle Ω and energy E.
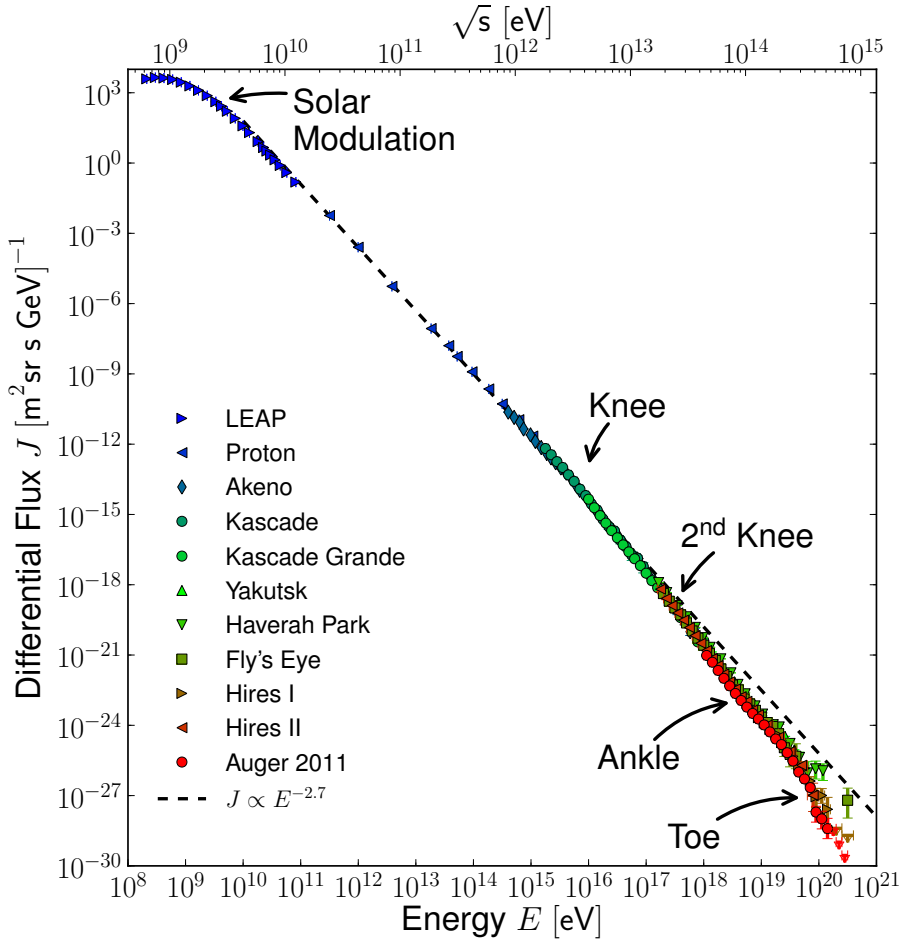
Figure 2.1: The Spectrum of Ultra-High Energy Cosmic Rays as measured by several experiments. For comparison the center-of-mass energy for the collision with a proton in rest is given. The references to the experiments in the order of appearance: [13],[14], [15],[16](QGS),[17],[18],[19],[20],[21](Hires I&II),[4]

Today we are able to observe a flux of comic rays that ranges over 12 orders of magnitude in energy from a few GeV up to the largest energies observed in single particles of several 10^{20} eV. Besides small variations, the cosmic ray spectrum can be described by a power law over the full energy range:

$$J \propto E^{-\gamma} \quad , \tag{2.2}$$

with a spectral index of $\gamma = 2.7$.

At the lowest energies displayed in Fig. 2.1 the flux of cosmic rays is modulated by interplanetary magnetic fields. Here the shape of the spectrum changes depending on the activity of the sun. The term 'cosmic ray' refers to particles that come from sources outside our solar system.

At GeV energies several thousand cosmic rays per square meter and second reach the Earth. The flux of cosmic rays is reduced by a factor ~ 1000 per decade energy. Technically this imposes a bisection of the energy range. Up to ~ 100 TeV cosmic

rays can be observed with relatively small detectors. These are usually realized as balloon born experiments such as 'LEAP' or as satellite experiments such as 'Proton' both treated in Fig. 2.1. Direct observation techniques allow for precise determination of the individual properties of the cosmic ray particles and are a vivid field of research (i.e. Ref. [22]).

To study cosmic rays at higher energies the suppression of the comsic ray flux requires large instrumented areas and long periods of observation. At energies above 100 TeV today's detection techniques rely on detectors placed on the ground. These perform an observation of cosmic rays with help of the associated air showers. The energy of 10^{18} eV marks the point above which cosmic rays are referred to as ultra-high energy cosmic rays (UHECRs). Beyond 10^{20} eV only one cosmic ray is observed per km^2 and century. Besides the need for very large aperture areas the experimental challenge at the highest energies is to infer the nature of cosmic rays from the remnants of its interaction in the atmoshpere.

As visible in Fig. 2.1 the spectral slope changes from $\gamma = 2.7$ to $\gamma = 3.1$ at energies around several 10^{15} eV constituting the so-called 'knee' of the spectrum. An additional slight steepening of the spectrum is observed at the 'second knee'. At the 'ankle' the enhanced surpression of cosmic rays is stopped with the spectral index changing back to $\gamma = 2.7$. Finally, the latest spectrum measurements at the highest energies show an strong reduction of the flux above 10^{19} eV which is referred to as 'toe' of the spectrum.

2.2 Composition

In the energy range that allows for a direct measurement of cosmic rays the abundance of elements is well known. It follows roughly the distribution of elements as observed in our solar system [24] with a domination by 79 % protons and 15 % helium nuclei [25]. Variations exists and are interpreted to be induced by spalation processes during the propagation of the cosmic rays through interstellar matter. Particles that are produced during the propagation are referred to as secondary cosmic rays to which also a small fraction of leptonic particles belongs. Towards higher energies magnetic fields suppress the amount of charged leptons due to synchrotron radiation which are subject to the field of radio astronomy (i.e. Ref. [26]).

The precision of composition measurements changes at cosmic ray energies that are only accessible with indirect detection techniques. Here, an identification of the primary particle is not possible on an event-by-event basis. Due to the statistical fluctuations in the development of the air showers usually only the average mass of the primary particles composing the cosmic ray flux is accessed.

Measurements of the composition from the KASCADE experiment in the intermediate energy range between the knee and the second knee are shown in Fig. 2.2. The KASCADE experiment profits from a separate detection of different particle types that are produced during the air shower development. This is used to identify different mass number ranges in the incoming flux of cosmic rays. Although there are differences in the detailed interpretation of the data using Monte Carlo techniques,
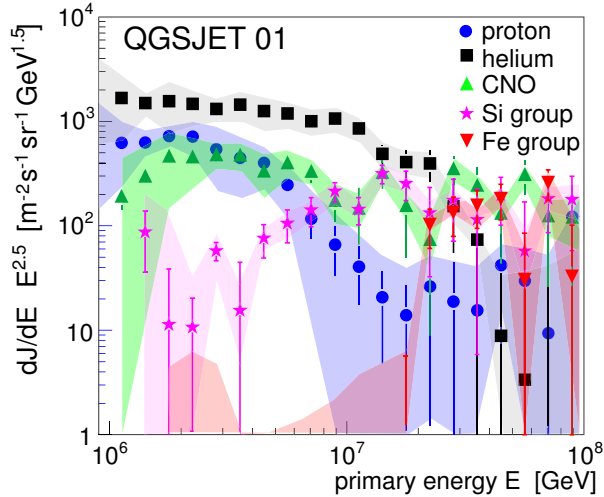
Figure 2.2: The Composition of cosmic rays around from the Knee to the second Knee measured with the KASCADE-Grande experiment. In comparison to the spectrum in Fig. 2.1 the flux is scaled with the energy using $E^{2.5}$ to accentuate changes in the steeply falling spectrum. Note that J here denotes the flux instead of the differential flux. The total cosmic ray flux is decomposed into contributions from elements and element groups of increasing mass number. At $\sim 2 \cdot 10^{15}$ eV the spectral index changes considering the spectrum summed over all element groups which know as 'Knee'. The displayed spectrum ranges up to energies of the second knee and is decomposed into different elements or element groups. For the discrimination the measurements need to be interpreted in terms of Monte Carlo simulations of the air-shower development. Model uncertainties exist on subtleties of the composition but agree on a change of the composition from light elements towards a domination of heavier element groups. From Ref. [23].

models agree that the measurements show a transition towards a dominant heavy element contribution in this energy range. The knee feature hence originates from a decreasing flux of the light primary cosmic ray particles [27].

In Fig. 2.3 a study of the composition of the cosmic ray flux above 10^{18} eV using data from the Pierre Auger Observatory is displayed. The average mass of the cosmic ray primaries is here investigated observing the average penetration depths $\langle X_{\max} \rangle$ of air showers into the atmoshpere as a function of energy. The fluctuations of this observable $RMS(X_{\max})$ are studied as well.

The qualitative dependencies of these quantities on the mass numbers of the primary cosmic rays can be calculated analytically [29]. However, for an interpretation of the measurements comparisons to air shower simulations are needed. The comparisons suggest a change from light to heavy elements towards the highest energies. However, differences exist to similar measurements of the HiRes experiment which indicate light composition also at the highest energies [30].

The energy range between 10^{17} and 10^{18} eV is an active subject to current detector installations. The low energy enhancements of the Pierre Auger Observatory [31], of the Telescope Array [32] as well as the Auger Engineering Radio Array address this energy range. Previous studies of the HiRes experiment indicate a change
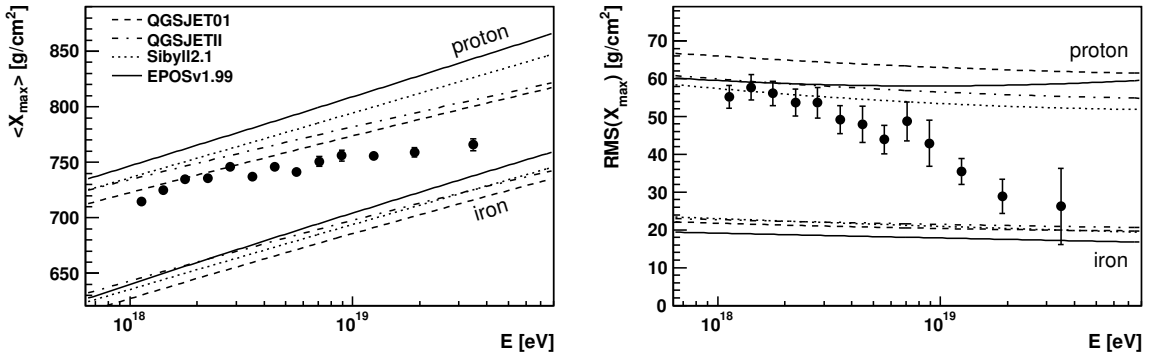
Figure 2.3: The average depth of the shower maximum $\langle X_{\max} \rangle$(left) and its fluctuation $RMS(X_{\max})$ (right) as a function of energy as estimator of the composition of ultra-high energy cosmic rays by comparison to simulations. From Ref. [28].

from a heavy to light composition [33] which is in agreement with the observations in adjacent energy ranges. Features in the spectral slope and indications for the composition of the flux are used to infer properties of the sources and the propagation of cosmic rays.

2.3 Propagation

Prior to the detection at the Earth cosmic rays propagate through magnetic fields which induce a deflection of the propagation direction. The deflections scale with the Larmor radius r_L both for a single directed magnetic field as well for trajectories through a series of fields with random orientations [34][1]:

$$r_L = 1.08 \, \mathrm{pc} \, \frac{E/10^{15} \, \mathrm{eV}}{Z \cdot B/\mu \mathrm{G}} \quad . \tag{2.3}$$

Here, Z is the atomic number of the cosmic ray primary and B the magnetic field strength. Typical magnetic field strengths within our galaxy are in the order of few μG [35]. Energetic cosmic rays will therefore leave the galactic plane which has a thickness of a few kpc. With increasing energy a magnetic confinement of the particles to the Galaxy becomes increasingly unlikely. Since the Larmor radius scales with the charge of the cosmic ray $r_L \propto 1/Z$ a leakage from the Galaxy occurs first for light elements sub-sequentially followed by the heavier elements. Taking proper diffusion and propagation models into account this 'leaky box' model can be used to explain the steepening of the cosmic ray spectrum above the ankle and the associated shift towards heavier primary particles [36].

Upper limits on the magnetic field strengths between galaxies exists constraining them to a few nG [37]. Regarding distance between galaxies at the Mpc scale, deflection during the intergalactic propagation of cosmic rays hence range in the same order as the deflection induced within our Galaxy. UHECRs thus potentially point back to their source when being detected. Simulations predict that this is

---

[1]Additional factors enter in latter case.
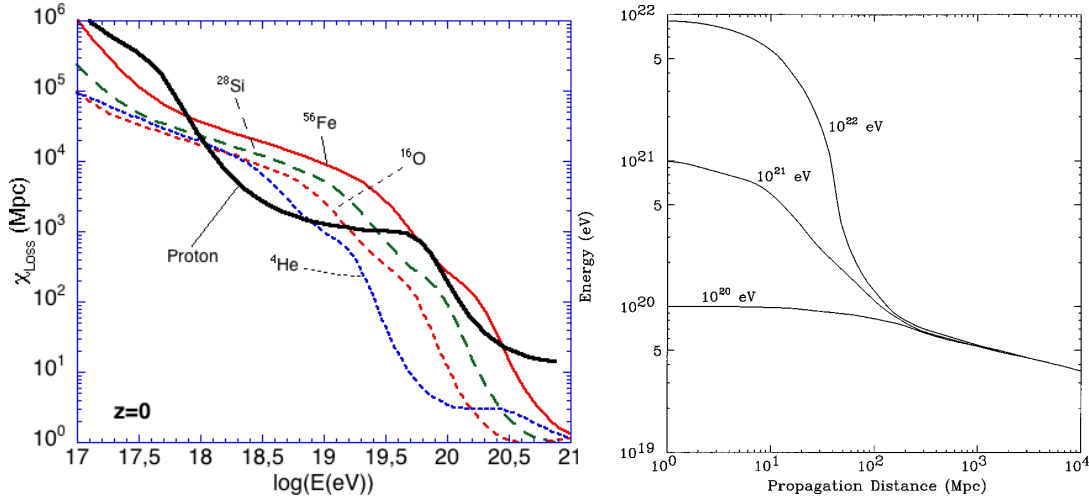
Figure 2.4: Left: Attenuation length as a function of the energy of the cosmic ray primary for various particle types. The two strong decreases of the attenuation length in the case of the proton correspond to launching productions of electron pairs and pions. Taken from Ref. [42]. Right: The development of the proton energy as a function of propagation distance for three different initial energies. From Ref. [43].

the case for protons exceeding $4 \cdot 10^{19}$ eV [38]. The ankle of the spectrum and the associated change from heavier to lighter primary cosmic ray elements is commonly interpreted as change from a flux of cosmic rays produced within our Galaxy towards the observation of a flux dominated by extra-galactic sources.

Besides deflections from magnetic fields, cosmic ray protons are predicted to be attenuated during propagation due to interactions with the cosmic microwave background [39]. Here, energy losses are induced by the production of secondaries particles. Above 10^{18} eV losses due to electron-positron pair production yield major contributions. Beyond $6 \cdot 10^{19}$ eV the production of pions is dominant:

$$
\begin{aligned}
p + \gamma_{\mathrm{CMB}} &\longrightarrow n + \pi^+ \\
&\longrightarrow p + \pi^0 \quad .
\end{aligned}
\tag{2.4}
$$

The latter process and its implications for the flux of UHECRs was proposed by Greizen, Zatsepin and Kuzmin [40, 41] and is known as GZK-cutoff. In Fig. 2.4 (left) this 'particle production energy loss' is summarized in terms of attenuation lengths. Distinct features of the spectrum above 10^{18} eV such as the ankle and the toe are here the result particle production channels that enter successively with increasing energy. Modifications of this model exist and incorporate the admixture of heavier primary cosmic rays [44] as suggest by experimental data.

The predicted strong surpression of the cosmic ray flux beyond 10^{20} eV has direct implications to the sources of cosmic rays. Cosmic rays above 10^{20} eV are rare but present in the flux that is measured at Earth [45]. In Fig. 2.4 (right) the average energy for primary protons is studied as a function of traveled distance. Different initial energies are inspected. After a distance of $\sim$100 Mpc all protons have been attenuated due to the GZK effect to the same average energy below 10^{20} eV. The

observation of cosmic rays with energies beyond the GZK cutoff hence implies that the sources to UHECRs are located relatively close to the Earth. The scale of 100 Mpc should here be compared to distances that can be observed with optical telescopes of up to 3.5 Gpc [46].

2.4 Sources of Cosmic Rays

Feasible acceleration mechanisms provide constraints to possible astrophysical sources of cosmic rays [2]. The most favorite acceleration mechanism is based on a model by Enrico Fermi. Fermi proposed that charged particles gain their energy by a statistical acceleration due to multiple scattering in turbulent magnetic fields [48]. Such fields occur for instance when a plasma shock wave propagates into the interstellar medium as observed at the remnants of supernova explosions. Traversing through the shock front back and forth, the particle gains an amount of energy $\Delta E \propto \beta_s^\alpha E$ per cycle. Here $\beta_s = v/c$ is the velocity of the shock and α a model dependent parameter.

The mechanism can only provide energy as long as the particle is trapped within the extend of the source region L. At each cycle exists a probability that the particle is lost. An upper limit of the maximum energy $E_{\max}$ that a source can provide is imposed by the Larmor radius (cf. Eqn. 2.3) of the particle track. When the radius exceeds the size of the source region the acceleration is stopped. This was summarized by A. M. Hillas in the following constraint [49]:

$$E_{\max}/10^{15}\,\text{eV} < \frac{1}{2}\,B/\mu\text{G}\,\cdot\,L/\text{pc}\,\cdot\,\beta_s\,\cdot\,Z\quad.\tag{2.5}$$

Using typical values for supernovas remnants with $B = 100\mu\text{G}$, $L = 1\text{pc}$ (cf. Fig. 2.5) and $\beta_s \approx \frac{1}{40}$ for Tycho's supernova [50] yields $E_{\max} \approx Z \cdot 10^{15}$ eV. The dependence of the maximum energy on the charge number Z leads to consecutive cutoffs of the spectra of individual elements starting with the light elements. The resulting decreasing efficiency for the acceleration of lighter elements is a popular model to explain the experimental observations between the knee and the ankle with Galactic supernovas as sources.

With respect to the highest energies above the ankle, Fig. 2.5 illustrates possible sources to UHECRs with respect to their size and magnetic field strength. Objects that lie below the diagonals do not fulfill the constraint of Eqn. 2.5 and cannot produce protons above 10^{20} eV. Four feasible astrophysical source to UHECRs remain: Neutron stars, active galactic nuclei (AGNs), radio galaxy lobes and clouds of intergalactic matter.

On large distance scales the Universe is filled isotropically with source candidates for UHECRs. However, within the particle horizon imposed by the GZK cut-off the distribution of source candidates is not isotropic. In combination with the rigidity of trajectories at the highest energies, the arrival directions of cosmic ray should

---

[2]So-called 'top-down' models explaining UHECRs as decay products of heavy particles are disfavored by recent observations. For a discussion see Ref. [47].
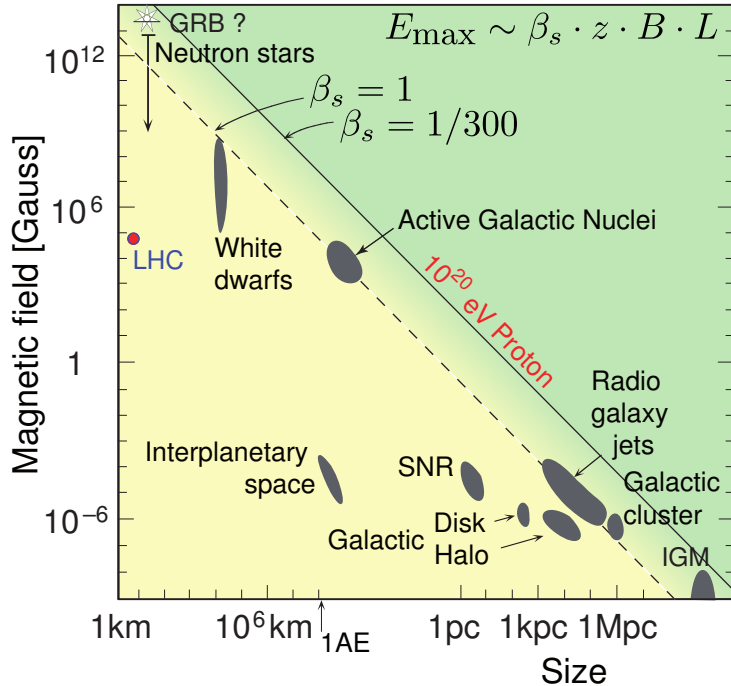
Figure 2.5: The Hillas Plot regarding potential sources of cosmic with respect to their extend and their magnetic field strength. Possible accelerators for proton energies up to 10^{20} eV have to touch the diagonals or lie above. Adapted from Ref. [24], originally published in Ref. [49].

yield a map of their sources. The consequent anisotropy in the arrival direction of the highest energy cosmic rays is being observed with the Pierre Auger Observatory [51].

Anisotropy is here studied by measuring the correlation between the arrival directions of cosmic rays and the location of active galactic nuclei in the neighborhood of our galaxy. As measure for the correlation, the number of cosmic rays that can be traced back to an AGN is compared with the total number of cosmic rays that should possibly point back to their sources.

This correlation has to be compared with the expectation arising from an isotropic distribution of arrival directions. If a comparable correlation cannot be received just by chance from an isotropic distribution, an anisotropy of the cosmic rays is evident. Three parameters influence this comparison of correlations:

- The distance D_{max} up to which AGNs are taken into consideration. When this distance is too large, the sources will distribute more and more isotropically over the sky and every arrival direction of a cosmic ray will correlate with an AGN. The GZK cutoff implies, that such a maximum distance exists.

- The angular distance ψ needs to be defined up to which cosmic rays are counted to be correlated with an AGN. Also the highest energy cosmic rays will be deflected by magnetic fields and the resolution of the detector is limited.
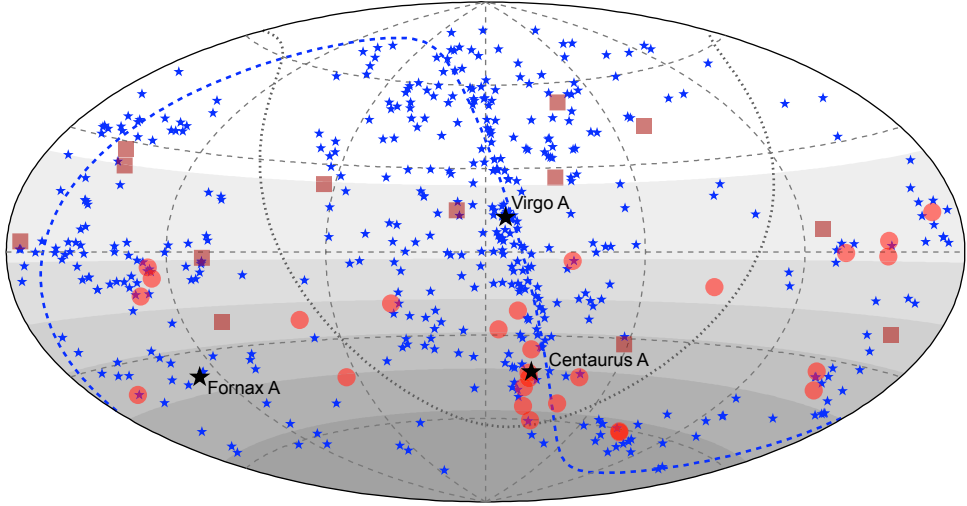
Figure 2.6: The arrival direction of cosmic rays at the highest energies as measured with the Pierre Auger Observatory [52] (circles) and the HiRes detector [53] (squares). The stars symbols show the location of AGN closer than 75 Mpc from the Veron-Cetty and Veron catalog [54]. The shaded area indicates the exposure of the Auger data set. The dashed line marks the super galactic plane and demonstrates that the AGNs follow the mass distribution of the local Universe. Taken from Ref. [24].

- The lowest energy E_{th} down to which a cosmic ray might point back to its source.

In an update on the correlation signal with an increased data set [52] the Auger Collaboration finds the following parameters to minimize the chance probability to accidentally identify an isotropic flux as an anisotropy:

$$D_{max} = 75 \, \text{Mpc}, \qquad \psi = 3.1°, \qquad E_{th} = 5.5 \cdot 10^{19} eV \quad . \tag{2.6}$$

Auger reports 69 cosmic rays exceeding the threshold energy E_{th}. 318 AGNs closer than D_{max} lie within the field of view of the experiment. 14 events are excluded from the analysis as they were used in an exploratory scan to approach the parameters listed in Eqn. 2.6. From the remaining events a fraction of $(38^{+7}_{-6})\%$ is correlating to AGNs where only a fraction of 21 % is expected from an isotropic distribution of arrival directions.

The HiRes collaboration has analyzed their set of measured UHECRs making use of the same set and values of parameters as proposed by Auger [53]. From a total of 13 UHECRs, two associations with AGNs were found. This is conform with the expectation from an isotropic distribution of arrival directions. Whether this result is contradictory or not is currently under debate. In Fig. 2.6 the arrival direction of the considered cosmic ray from Auger as well as from HiRes are displayed. It should be noted that the HiRes and Auger are observing almost opposite directions of the celestial sphere.

3. Cosmic Ray Induced Air Showers

The observation of UHECRs is closely related to the detection of extensive air showers. In the first part of this chapter we describe the phenomenology of air showers and discuss the most important methods of observation. In the second part we will focus on the theoretical description of air showers. The detection and generation of the radio signal from air showers will be emphasized in the discussion.

When a cosmic ray enters the atmosphere of the Earth it collides with an air nucleus. The collision produces secondary particles which themselves participate in further collisions. In the resulting particle cascade hadronic and electromagnetic interactions as well as particle decays take place. The resulting disc of particles is called air shower.
Air showers have a lateral radius of up to several kilometers. Moving through the atmosphere with almost the speed of light, the longitudinal extend of the air shower disc is a few meters only. In Fig. 3.1 a schematic view of an air shower is illustrated.
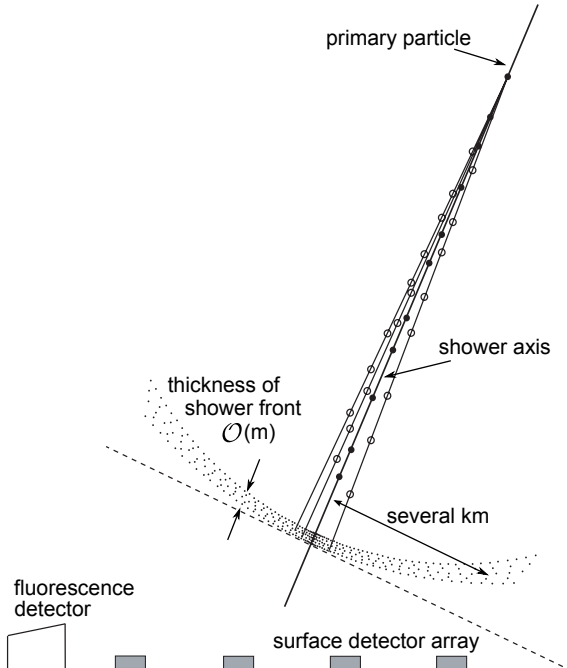
Figure 3.1: Sketch of an air shower with the primary particle, the air shower axis and the resulting curved shower disc. Different techniques for the detection of air showers are indicated. Adapted from Ref. [55] and [56].

3.1   Experimental Methods of Observation

Todays measurement techniques to UHECRs rely on ground based observations of air showers. Here, two measurement technique are well establish: The observation of the lateral particle content of the shower on the ground, and the measurement of the longitudinal shower development in the atmosphere. The measurement of the radio emission of the air shower is currently a vivid field of research.

3.1.1   The Longitudinal Shower Profile Observed in the Atmosphere

The charged particles of the air shower excite the molecules of the air while traversing the atmosphere. Fluorescence light is emitted isotropically when the molecules de-excite. The path of the shower can be tracked when the fluorescence light is observed with a telescope that allows for a segmented observation of the atmosphere.

A segmented observation is usually realized with a camera assembled from photo multipliers. The resulting measurement resembles a movie of the air shower in the field of view of the telescope. The air shower axis is reconstructed and the amount of fluorescence light is corrected for geometry effects, scattering and absorption in the atmosphere during the propagation to the telescope. The conversion factor between the number of radiated fluorescence light photons N_γ and energy deposit dE/dX is called fluorescence yield. The fluorescence yield is measured in dedicated experiments [57].

The observation results in a measurement of the shower's longitudinal energy deposit profile $dE(X)/dX$. The slant depth X [g/cm^2] is the amount of traversed matter and is counted from the top of the atmosphere. The energy deposit is essentially proportional to the number of ionizing particles present in the shower development $N_e(X)$ which is governed by low energy electrons and positrons. A measured air shower profile is shown in Fig. 3.2.

The displayed profile shows the start of the shower development high up in the atmosphere at a slant depth of 200 g/cm^2. The shower quickly develops and reaches its maximum size at the slant depth $X_{\max}$. For the incoming cosmic ray the atmosphere is calorimeter with a thickness of at least ~ 11 nuclear interaction lengths when measured vertically down to the sea level[1]. In the case of the displayed air shower almost the full primary particle energy is deposited in atmosphere.
Measured shower profiles are usually parameterized with the Gaisser-Hillas function [58, 59]:

$$f_{GH}(X) = dE/dX_{\max} \left(\frac{X - X_0}{X_{\max} - X_0} \right)^{\frac{X_{\max} - X_0}{\lambda}} \cdot e^{\frac{X_{\max} - X}{\lambda}} \quad . \qquad (3.1)$$

Here, X_0 and λ are referred to as shape parameters of the function. Historically they were identified as the depth where the first interaction occurs and absorption

---

[1]The sea level is located at an atmospheric depths of ~ 1034 g/cm^2. The nuclear interaction length for protons in air is $\lambda_I^p \approx 90$ g/cm^2.
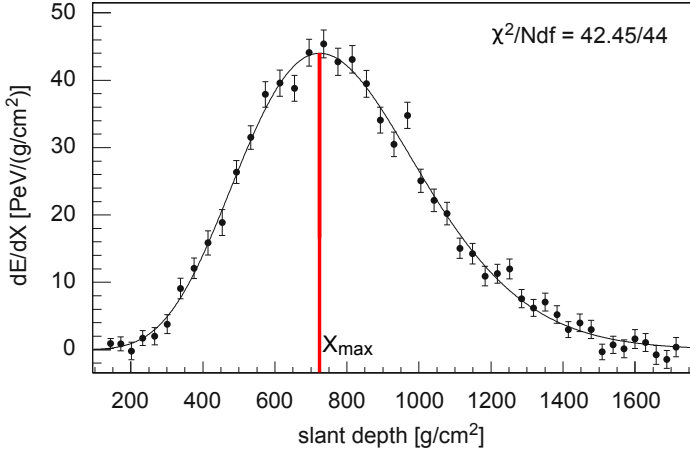
Figure 3.2: Shower profile in the atmosphere observed with the fluorescence detector of the Pierre Auger Observatory. Displayed is the energy deposit as a function of slant depth. The observation of the maximum of the shower development is important for a reliable fit of the Gaisser-Hillas function to the shower development (solid line). The energy of the cosmic ray was reconstructed to $(3.0 \pm 0.2) \cdot 10^{19} eV$. Adapted from Ref. [3].

length respectively. By integration the total deposited energy E_{cal} of the shower is obtained:

$$E_{\mathrm{cal}} = \int f_{GH}(X) \, dX \quad , \tag{3.2}$$

which corresponds to the energy of the primary particle besides a fraction of ~ 10 % carried by more penetrating particle in the shower development which are muons and neutrinos.

3.1.2 The Lateral Shower Profile Observed on the Ground

An array of particle detectors is placed on the ground to measure the density of the shower particles at different distances form the shower axis. To outweigh the low flux of cosmic rays a large instrumented area is preferred. The distance between the detector stations need to be chosen in such way that still enough information of the air shower signal is recorded. As the size of the shower disc depends on the energy of the primary particle, the distance between the detector stations determines a lower energy threshold for efficient observation of cosmic rays with the detector. To measured UHECRs typical spacings of ~ 1 km are realized.

The arrival direction of the air shower is measured by the arrival time of the shower particles in the different detector stations. Each detector station measures the density n of charged shower particles in terms of a detector response S. The total number of particles N_{total} at the ground can in principle be obtained from an integral over the particle density:

$$N_{\mathrm{total}} = \int n(r) \, dr \quad \propto \quad \int S(r) \, dr \quad . \tag{3.3}$$
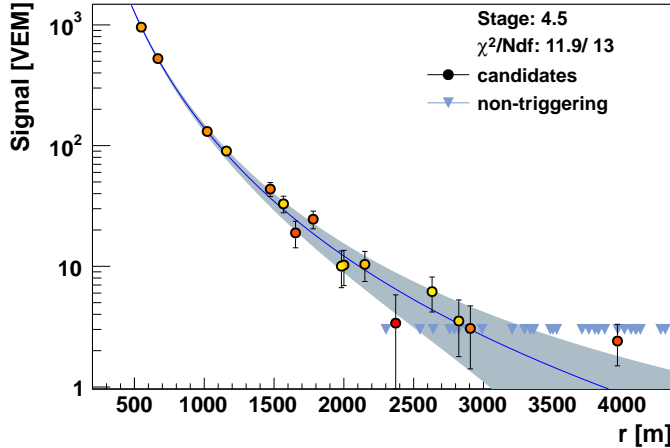
Figure 3.3: Measurement of an air shower with the Surface Detector of the Pierre Auger Observatory. The signal of the detector stations is observed as a function of distance from the shower axis. The arrival time of the shower at the individual stations is indicated by the colors of the circles from yellow (early) to red (late). The line represents the fit of an LDF to the data. The energy of the cosmic ray was reconstructed to $\sim 2.9 \cdot 10^{19} eV$.

As the air shower measurement is only performed at discrete distance r from the shower axis, a lateral distribution function (LDF) is used to estimate a continuous particle distribution. Most experiments use a generalized form of the Nishimura-Kamata-Greisen formula [60] to perform the adjustment:

$$S(r) = k \left(\frac{r}{r_0} \right)^{-\alpha} \left(1 + \frac{r}{r_0} \right)^{-(\eta - \alpha)} \quad . \tag{3.4}$$

The Molière radius r_0 is a typical quantity for particle showers and confines 95% of the shower energy in a cylinder with $2 \cdot r_0$ diameter around the axis. The functions α and η arise empirically from the data. The factor k scales the LDF proportional to the number N_{total} of particles present in the shower front.

Modifications of Eqn. 3.4 exist depending on the experiment and the used particle detector type (see Ref. [61] and references there within). Using Eqn. 3.4 a rough estimate of the energy of the primary particle E_p can be obtained as:

$$N_{\text{total}} \propto E_p \quad . \tag{3.5}$$

The surface detector measurement samples a snapshot of the shower development usually detecting the tail of the processes that have evolved in the atmosphere. For a more precise determination of the kinetic properties of the primary particle, surface detector measurements need to be corrected for a multitude of effects which impose additional uncertainties. An example is the so-called age of the air shower which comprises a correction for the moment in the air shower development when the particle density is sampled.

In Fig. 3.3 we see the lateral signal falloff with increasing distance from the shower core in the case of an air shower detected with the Pierre Auger Observatory.
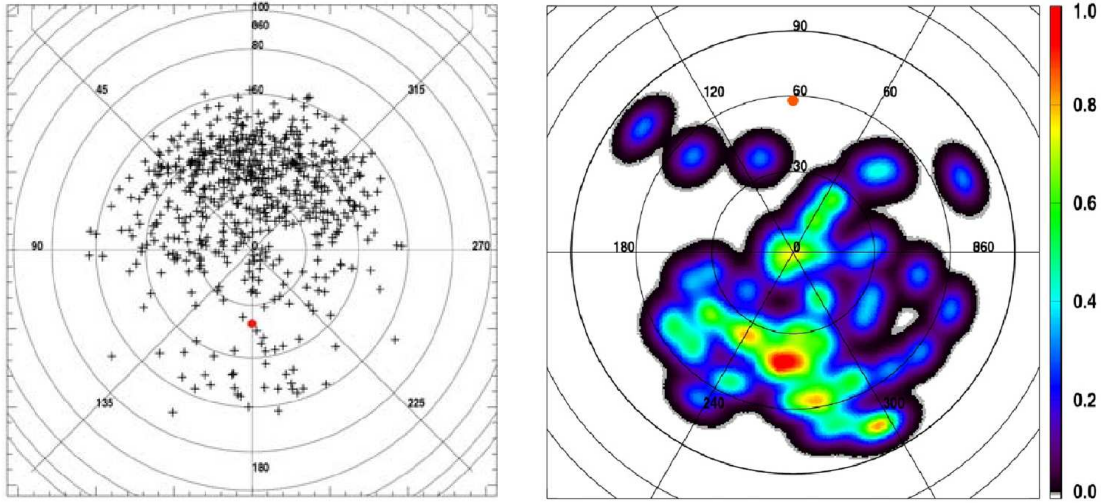
Figure 3.4: Geomagnetic Origin of Radio Signal. Displayed are polar diagrams of zenith and azimuth directions of air showers. The zenith is in the center, North at the top, South at the bottom. In the sky views the direction of the magnetic field of the Earth is indicated as red circle. Left: Air showers detected with CODALEMA radio antenna array in coincidence with particle detectors. Incoming direction that are perpendicular to the magnetic field of the Earth are triggered most efficiently. From Ref. [62]. Right: Same as the left panel but measured at a radio detector setup at Pierre Auger Observatory. As Auger is located in the southern hemisphere the direction of the magnetic field points north. This leads to a flip in the distribution of detected arrival directions which have here been smeared with a point spread function. From Ref. [63].

3.1.3 The Radio Pulse Originating from Air Showers

When antennas are placed along with an array of surface detectors, an electromagnetic pulse with frequencies in the radio regime $\mathcal{O}(1\text{-}100 \text{ MHz})$ is observed in coincidence with the particle detectors. The received field strength per unit bandwidth ranges up to several $\mu\text{Vm}^{-1}\text{MHz}^{-1}$. The pulse front follows the shape of the particle disc and allows for reconstruction of the shower axis with help of the signal timing as in the case of the surface detectors measurements.

Observing the dependencies of the radio signal on different parameters, Allan found the following parametrization of the pulse amplitude already in the late 1960s [64]:

$$\mathcal{E}_\nu = 25 \cdot E_p/10^{17}\text{eV} \cdot \sin\alpha \cdot \cos\theta \cdot exp\left(-\frac{R}{R_0(\nu, \theta)}\right) \quad \left[\frac{\mu\text{V}}{\text{m MHz}}\right] \quad . \quad (3.6)$$

In this parametrization $\mathcal{E}_\nu$ is the electric field strength of the pulse at center frequency ν of the receiver system. Eqn. 3.6 is derived from separate measurements at 32, 44 and 55 MHz. The receivers used at that time had a limited bandwidth of a few MHz. To have a quantity comparable to other experiments, $\mathcal{E}_\nu$ denotes the measured electric field strength divided by the bandwidth of the receiver.

Allan introduces a factor $(\sin\alpha \propto \vec{v} \times \vec{B})$ as consequence of his own observations [66] and in accordance with theoretical ideas about the radiation mechanism for the
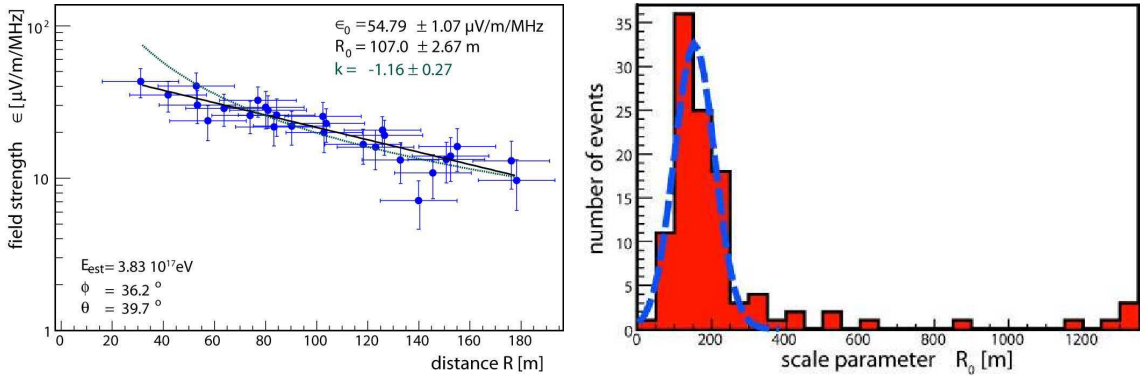
Figure 3.5: The LDF measured with LOPES. Left: An air shower observed with multiple antennas at different distances from the shower axis. The fit of an exponential function yields the scaling parameter R_0. Also a power law is tested but found to fit the data worse. Right: The distribution of scaling parameters from a set of air showers. The fit of a Gaussian to the inner part of the distribution gives an average scaling parameter of $R_0 \approx 150$ m from a wide distribution with a tail towards larger values. From Ref. [65].

radio pulse [67]. Here, $\vec{v}$ is the direction of the air shower axis and $\vec{B}$ the magnetic field of the Earth. In Fig. 3.4 (left) the distribution of arrival directions of air showers that were recorded in the CODALEMA radio detector array in coincidence with a particle detector are displayed.

At the site of the CODALEMA detector the magnetic field of the Earth points from South. The $(\vec{v} \times \vec{B})$-factor enhances the radio emission from air showers coming from North. These showers are consequently detected more efficiently in the radio detector. In the right panel of Fig. 3.4 we see a corresponding measurement from a radio detector installation at the site of the Pierre Auger Observatory. Auger is located in the southern hemisphere. Here $\vec{B}$ is pointing northwards which reverses the detected distribution of arrival direction. The comparison underlines the importance of the Earth's magnetic field in the generation process of the radio pulse.

Going back to Eqn. 3.6 the factor $\cos\theta$ is introduced to account for a reduction of radio signal towards larger zenith angles due to an increasing distance towards the shower development. In the parametrization the amplitude decreases with an exponential function with increasing distance R between the antenna and the shower axis. Allan reported scaling parameters R_0 ranging between 100 and 170 m depending on the chosen frequency band. In analogy to the measurements from particle surface detectors the function governing the lateral signal falloff is called LDF. In Fig. 3.5 (left) the LDF of a single air shower observed with a multitude of antennas of the LOPES experiment is displayed [65]. The fit of an exponential function yields an LDF parameter $R_0 \approx 100$ m. Evaluating the distribution of the scaling parameters (right panel of Fig. 3.5) from many detected air showers, LOPES finds an average scaling parameter of $\overline{R_0} \approx 157$ m. The distribution shows a tail towards much larger scaling parameters which is currently not well understood.
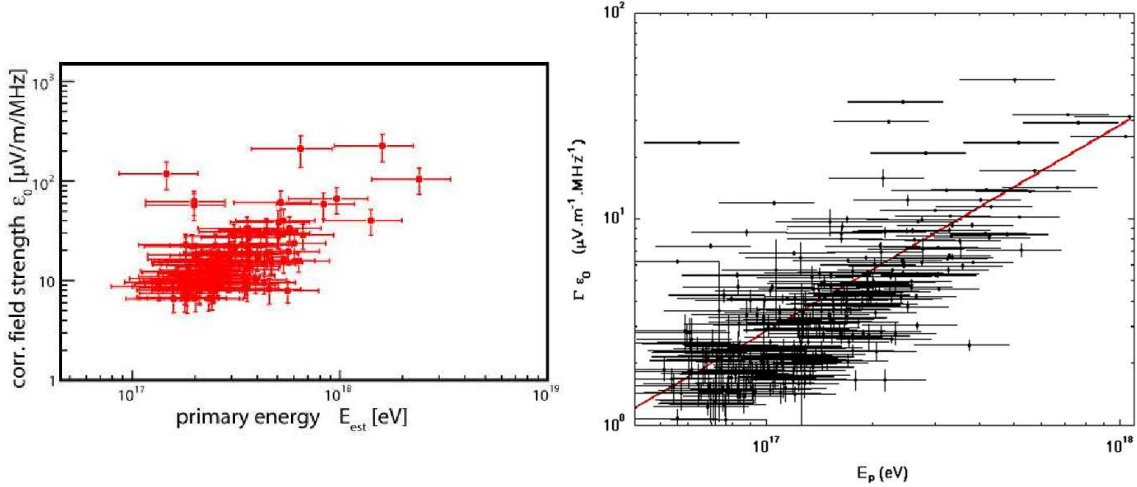
Figure 3.6: Energy estimate based on radio measurements of the LOPES (left) and the CODALEMA (right) experiments. The electric field strengths on the y-axes are corrected for the LDF and angular dependencies and compared to the corresponding energy reconstruction of the associated particle detectors. Both experiments observe a linear correlation between the two observables. From Refs. [65] and [68].

Finally, the observed amplitude scales linearly with the energy E_p of the primary particle.[2] In Fig. 3.6 the energy estimators derived from radio measurements of LOPES and CODALEMA are compared to the corresponding energies coming from surface detector reconstructions. In both cases the electric field strength corrected for geometric dependencies $\mathcal{E}_0$ is used as the energy estimator. The experiments see a clear correlation with the energy of the primary particle following $\mathcal{E}_0 \propto E_p{}^k$ with an index $k \approx 1$. However, the scatter in the distributions may suggest that additional effects contribute to the radio pulse which are beyond the scope of the current phenomenological descriptions.

Due to the importance of the Earth's magnetic field for the observation of the radio pulse the radio emission is often referred to as geo-magnetic radiation. Current studies of the polarization of the radio signal suggest at least one additional contribution to the signal that does not scale with $\sin \alpha$ [69]. Here is interesting to note a modified version of the pulse height parametrization based on LOPES data [70]. The modification suggests that the magnetic field direction impacts with a factor $\mathcal{E} \propto (b - \cos \alpha)$ with $b = 1.16 \pm 0.03$. This allows in principle for contributions to the radio signal at level of 10 % that do not scale with $\vec{v} \times \vec{B}$.

3.2 Theory and Simulations of Air Showers

When a cosmic ray has hit an air nucleus, the developing particle cascade can be considered with respect to an electromagnetic, a muonic and a hadronic component.

The hadronic component is directly initiated by the incident primary particle. Its collision will produce approximately 90% pions and 10% kaons. The kaons and

---

[2]As the intensity of the radiation goes with the square of the amplitude this implies a quadratic scaling of the radio signal power with energy of the primary.
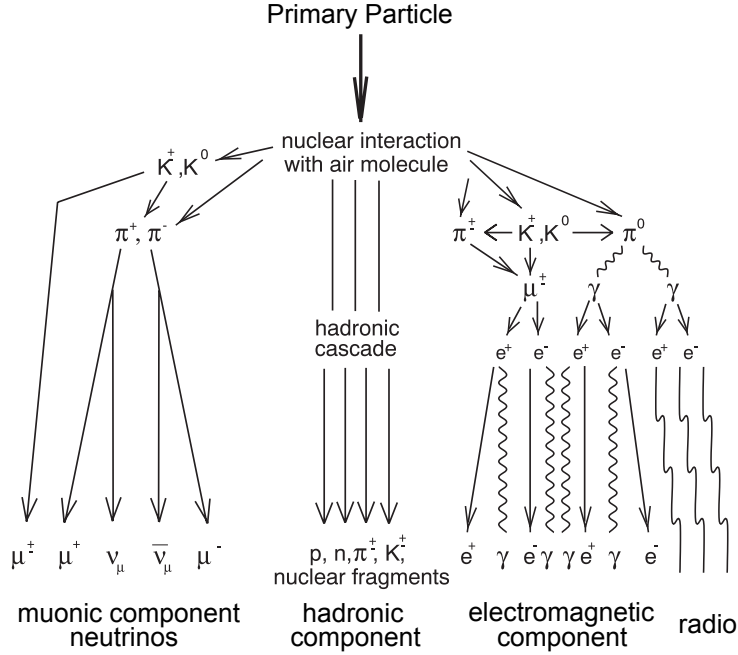
Figure 3.7: Overview of the shower development with different components. Adapted from Ref. [56]

the charged pions will collide with air molecules and contribute to the hadronic component of the shower. Besides participating in hadronic interactions, the kaons and the charged pions decay into muons and muon neutrinos constituting the muonic component of the air shower.

Charged and neutral pions ($\pi^{\pm}$, π^0) are produced with the same rate in the hadronic interactions. While the charged pions are rather long lived, the neutral pions decay via electromagnetic interaction after only $\sim 8 \cdot 10^{-17}$ s into two photons. In this way $\sim 1/3$ of the energy of the hadronic component is transfered into photons after each hadronic radiation length. The photons initiate electron-photon cascades by pair production of electrons and positrons and subsequent bremsstrahlung processes. An overview over the shower development with its different components is given in Fig. 3.7.

The basic properties of the air shower development can be understood using a model proposed by Heitler [71] which has been extended by Mathews [29]. To take into account the fluctuation of the underlying statistical processes finally Monte Carlo simulations of the full shower development are used.

3.2.1   Heitler Model of Shower Development

Following the discussion in Ref. [29] we first focus on the electromagnetic component of the air shower. An approximation of the electromagnetic cascade is visible in Fig. 3.8 (left). The energy E_0 of an initial photon is split in a first interaction via pair production on an electron and a positron equally. The radiation length λ_{em} denotes the characteristic amount of matter that electrons and photons pass to be attenuated to $1/e$ of their initial energy. If we consider cascades where an equal division of the
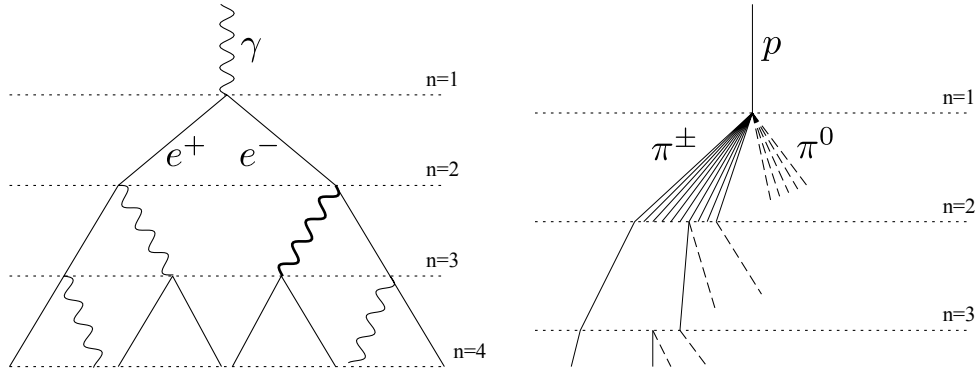
Figure 3.8: Electromagnetic (left) and hadronic (right) cascades in the air shower development. From Ref. [29]

energy occurs, a typical width between the interactions is given by the splitting length d:

$$d = \ln 2 \cdot \lambda_{em} \approx \ln 2 \cdot 36.7 \text{ g/cm}^2 \text{ (air)} \approx 25.4 \text{ g/cm}^2 \quad . \tag{3.7}$$

The splitting length is indicated in Fig. 3.8 (left) as horizontal lines. After each splitting length the number of particles doubles over which the initial energy is distributed. After n splittings there are $N = 2^n$ participants in the cascade where the individual energies E_e have decreased exponentially with the traversed column density X:

$$E_e = E_0 \cdot e^{-X/\lambda_{em}} \quad . \tag{3.8}$$

When the energy E_e is too low for pair production or bremsstrahlung the further progression of the cascade is stopped. This energy is usually identified with the critical energy $E_c = 85$ MeV where ionization becomes the dominant process for energy loss in air. The maximum number of electrons that will be reached is:

$$N_e^{\max} = \frac{E_0}{g \cdot E_c} \quad . \tag{3.9}$$

In the simple model depicted here is $g = 1$. Comparisons to accelerator experiments show that the maximum number of particle is overestimated in the model by one order of magnitude underlining the need for Monte Carlo techniques for a quantitative understanding of particle cascades. Using a factor $g \approx 13$ as proposed in Ref. [72] leads to $\sim 10^6$ particles in the maximum of the cascade per 10^{15} eV initial energy.

In the right part of Fig. 3.8 the cascade model is extended to hadronic constituents. In comparison to the left part of the figure the increased width between the interaction layers indicates that the hadronic interaction length λ_I yields the typical scale for the cascade progression. In the collisions predominantly pions are produced which yields a splitting distance of:

$$d = \ln 2 \cdot \lambda_I^\pi \approx \ln 2 \cdot 120 \text{ g/cm}^2 \approx 83 \text{ g/cm}^2 \quad . \tag{3.10}$$

One third of the produced pions are neutral and decay into two photons almost immediately initiating electromagnetic cascades. Comparing the splitting distances

of the hadronic and the electromagnetic cascades indicates that the hadronic component governs the elongation of the air shower into the atmosphere.

As 1/3 of the energy is transferred to the electromagnetic component at each step the total energy E_π^{tot} residing in the hadronic cascade decreases with an increasing amount n of interactions:

$$E_\pi^{\text{tot}} = (\frac{2}{3})^n \cdot E_0 \quad . \tag{3.11}$$

The average energy per pion E_π is obtained diving E_π^{tot} by the total number of pions N_π. The number of pions is given by the multiplicity of charged hadrons N_{ch} created in each interaction:

$$N_\pi = N_{ch}{}^n \tag{3.12}$$

which leads to:

$$E_\pi = \frac{E_\pi^{\text{tot}}}{N_\pi} = \frac{E_0}{(\frac{3}{2} N_{ch})^n} \quad . \tag{3.13}$$

The cascade will progress until E_π drops below a critical energy. For pions a critical energy is given with $E_\pi^c = 20$ GeV where the probability for the electroweak decay into a muon and neutrino equals to the probability for a further hadronic interaction.

Muons are consequently created with an energy of several GeV. A typical energy loss of a GeV muon is 2 MeV g^{-1}cm^{-2}. In combination with an atmospheric depths of $X_{\text{atm}} \approx 1000$ g cm^{-2} and a relativistic dilatation of the lifetime with γ-factors of 10, muons are save candidates to be detected on the ground.

Solving Eqn. 3.13 for n gives the number of steps in the cascade until the development is stopped:

$$n_c = \frac{\ln(E_0/E_\pi^c)}{\ln(3/2\, N_{ch})} \quad . \tag{3.14}$$

This is useful as all pions present at this stage of the cascade can be assumed to decay into muons. The total number of muons is:

$$N_\mu \quad = \quad N_{ch}{}^{n_c} \tag{3.15}$$

$$\Leftrightarrow \quad \ln N_\mu \quad = \quad n_c \ln N_{ch} \tag{3.16}$$

$$= \quad \ln(\frac{E_0}{E_\pi^c}) \underbrace{\frac{\ln N_{ch}}{\ln(3/2\, N_{ch})}}_{\equiv \beta} \tag{3.17}$$

$$\Leftrightarrow \quad N_\mu \quad = \quad (\frac{E_0}{E_\pi^c})^\beta \quad . \tag{3.18}$$

As obviously $\beta < 1$ the number of muons scales differently with the energy of the primary particle than in the case of the linear scaling of electromagnetic cascade discussed in Eqn. 3.9.[3] The non-linear scaling implies an interesting feature concerning the number of muon when treating primary particles with different mass numbers A. As the nuclear binding energies are small in comparison to the energy in the center

---

[3]If the number of electrons is derived from a hadron initiated shower, a power law is found with an power law index of $\beta_{em} \approx 1.046$. [72]

of mass system of the first collision, an iron induced air shower can for instance be seen as the superposition of 56 single proton induced showers — each with the 56th part of the total energy. For Eqn. 3.18 this consequences in:

$$N_\mu \;=\; A \cdot \left(\frac{E_0/A}{E_\pi^c}\right)^\beta = \left(\frac{E_0}{E_\pi^c}\right)^\beta \cdot A^{1-\beta} \quad . \tag{3.19}$$

The separate measurement of muonic and electromagnetic component of an air shower hence provides sensitivity to the composition of the primary cosmic ray flux as demonstrated by the KASCADE experiment discussed in Fig. 2.2. Moreover, the superposition averages fluctuations of the individual sub-showers. In Fig. 2.3 (right) this effect was used to measure the composition of the cosmic rays in terms of variation of the air shower maximum $RMS(X_{\max})$.

The number of muons indicates how much energy was transfered into the electromagnetic component of the air shower. Using energy conservation results in:

$$\frac{E_{em}}{E_0} \;=\; \frac{E_0 - N_\mu E_\pi^c}{E_0} \;=\; 1 - \left(\frac{E_0}{A\,E_\pi^c}\right)^{\beta-1} \quad . \tag{3.20}$$

Using a typical value $N_{ch} = 10$ renders $\beta \approx 0.85$ in Eqn. 3.17. With respect to a proton initiated shower of $E_0 = 10^{18}$ eV more than 80 % of the shower energy end in the electromagnetic component and are deposited in the atmosphere. To measure this large fraction of the air shower development is subject to radio detection technique.

Complications in the interpretation of measured data arise from simplifications in the model. For example the number of charged particle N_{ch} produced in the hadronic interaction changes as a function energy. Using a typical value $N_{ch} = 10$ can only give a first estimator for β. To handle the impact of the statistical processes in the air shower development Monte Carlo models are used to derive quantitative dependencies between experimental observables and cosmic ray properties.

3.2.2 Simulation of the Particle Content of the Air Shower

A Monte-Carlo simulation of an air shower will track every shower particle and apply possible interactions and decays according to their individual probability. In this way the impact of the individual particles on the air shower as a whole is taken into account.

The abundance for the creation of different particle types in proton collisions is measured in collider experiments. The energy in the center of mass system of a $10^{20}eV$ cosmic ray exceeds the energy of current experiments by a factor ~ 1000. Monte-Carlo simulations of air showers hence extrapolate measurements into the desired energy regime to receive the needed cross sections.

CORSIKA is a state-of-the-art Monte-Carlo simulation program of extensive air showers [73]. It allows to observe energy, position and direction of movements of every shower particle during the complete development of the shower in the atmosphere. The properties of the primary particle can be fixed to the desired values
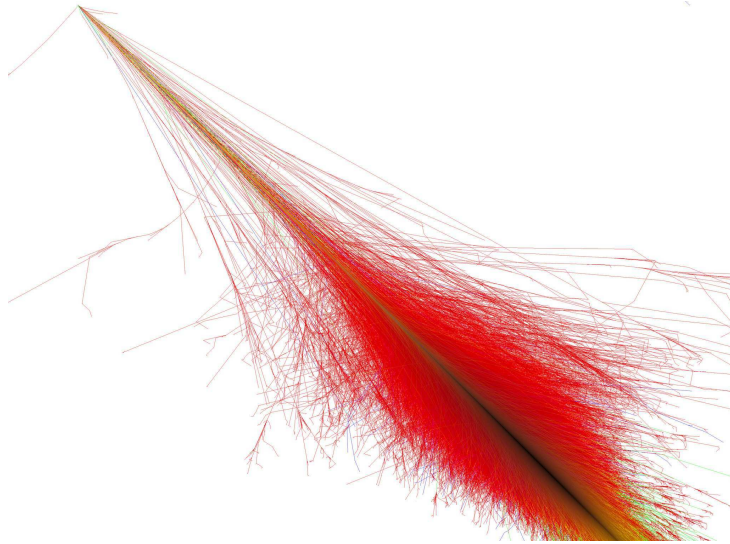
Figure 3.9: Side view of a proton induced Air shower of 10^{15} eV simulated with COR-SIKA. Electrons, positron and photon tracks are red, muon tracks green and hadron tracks are blue. The z- and x-axis range at ~ 72 km. From Ref. [74].

of energy, species and arrival direction. Furthermore the environmental conditions of the detector site can be modeled in the simulation which includes the strength and the direction of the magnetic field of the Earth. An example of an extensive air shower simulated with CORSIKA is shown in Fig. 3.9.

3.2.3   Generation of the Radio Pulse from Air Showers

The idea of a radio pulse evolving along with the shower was first introduced by Askaryan in 1962 [75]. In his model two effects are considered that generate the radio signal. Cherenkov radiation is emitted by the shower particles as their velocities exceed the speed of light in air. However, a charge excess is needed so that the radiation emitted from negative and positive charges does not cancel.
A charge access is realized by scattering of ambient electrons into the shower front and by an increased absorption cross section of positrons due to annihilations with electrons of the surrounding material.
The variation of the net charge excess in the shower front itself is an additional source of radiation that contributes even if the index of refraction is n=1.
The radiation is produced coherently when the longitudinal extend of the shower front is smaller than the emitted wavelength. With respect to the thickness of an air shower disc of several meters this is the case for wavelengths in the radio regime. Askaryan emission was observed in particle showers at accelerator experiments [76]. However, the model does not explain the dependence of the pulse amplitude on the inclination of the air shower axis with the geo-magnetic field.

Keeping the idea of coherent emission, Kahn and Lerche presented a geo-magnetic origin of the underlying emission process [67]. The electrons and positrons in the shower front are separated by the Lorentz force due to the movement in the magnetic field of the Earth. The induced transverse current emits dipole radiation that is

oriented in the direction of the air shower propagation due to the relativistic velocity of the dipole.

In recent macroscopic models for the generation of the radio pulse the transverse current and the charge excess are the two dominant contributions to the signal [77]. However, the interest in the radio detection technique in the last decade was re-initiated by a model of Falcke and Gorham in 2002 [78]. In this model the radio pulse is interpreted as synchrotron radiation from the electrons and positrons gyrating in the geo-magnetic field. The geo-synchrotron model draws an intuitive picture of the importance of the geo-magnetic field and the coherent emission. The radiated power due to synchrotron radiation from a single particle with charge q and mass m_q is [79] (Gaussian-cgs units):

$$P_{\text{single}} = \frac{2}{3} \frac{q^2 c}{r^2} \beta_\perp^4 \gamma^4 \quad , \tag{3.21}$$

where r is the turning radius, $\beta_\perp$ the charged particle's velocity perpendicular to the axis of rotation in units of speed of light and γ the Lorentz factor. The axis of rotation is defined by the magnetic field $\vec{B}$ of the Earth. The curvature r of the track of the charge is caused by the Lorentz force:

$$r = \frac{c\, p_\perp}{q\, |\vec{B}|} = \frac{\gamma\, m_q\, c^2\, \beta_\perp}{q\, |\vec{B}|} \quad . \tag{3.22}$$

Hence, Eqn. 3.21 can be written as:

$$P_{\text{single}} = \frac{2\, \gamma^2}{3\, c^3} \cdot \frac{q^4}{m^2} \cdot \beta_\perp^2\, |\vec{B}|^2 \tag{3.23}$$

or to emphasize the geometric effect:

$$P_{\text{single}} = \frac{2\, \gamma^2}{3\, c^3} \cdot \frac{q^4}{m^2} \cdot |\vec{\beta} \times \vec{B}|^2 \quad . \tag{3.24}$$

The coherence of the emission is now stressed by treating the shower as a single particle with the charge $q = Ne$ and mass $m = Nm_e$:

$$P_{\text{shower}} = \frac{2\, \gamma^2}{3\, c^3} \cdot \frac{(N\, q)^4}{(N\, m_e)^2} \cdot |\vec{\beta} \times \vec{B}|^2 = N^2\, P_{\text{single}} \quad . \tag{3.25}$$

The power emitted in the coherent regime will be enhanced by a factor N^2 over the single particle emission. Since the maximum number of electrons increases essentially linearly with the energy of the cosmic ray (cf. Eqn. 3.9) a quadratic scaling also applies to the air shower signal. Considering the radio signal amplitude $A \propto \sqrt{P}$ a linear scaling is predicted which matches the result of the measurements in Fig. 3.6. The geo-synchrotron model includes as well the more efficient triggering of incoming directions perpendicular to the magnetic field direction seen in Fig. 3.4.

Also the absolute strength of the magnetic field $|\vec{B}|$ scales the radio signal. In Fig. 3.10 a map of the current magnetic field strength of the Earth is visible. Depending

TOTAL INTENSITY (NT)
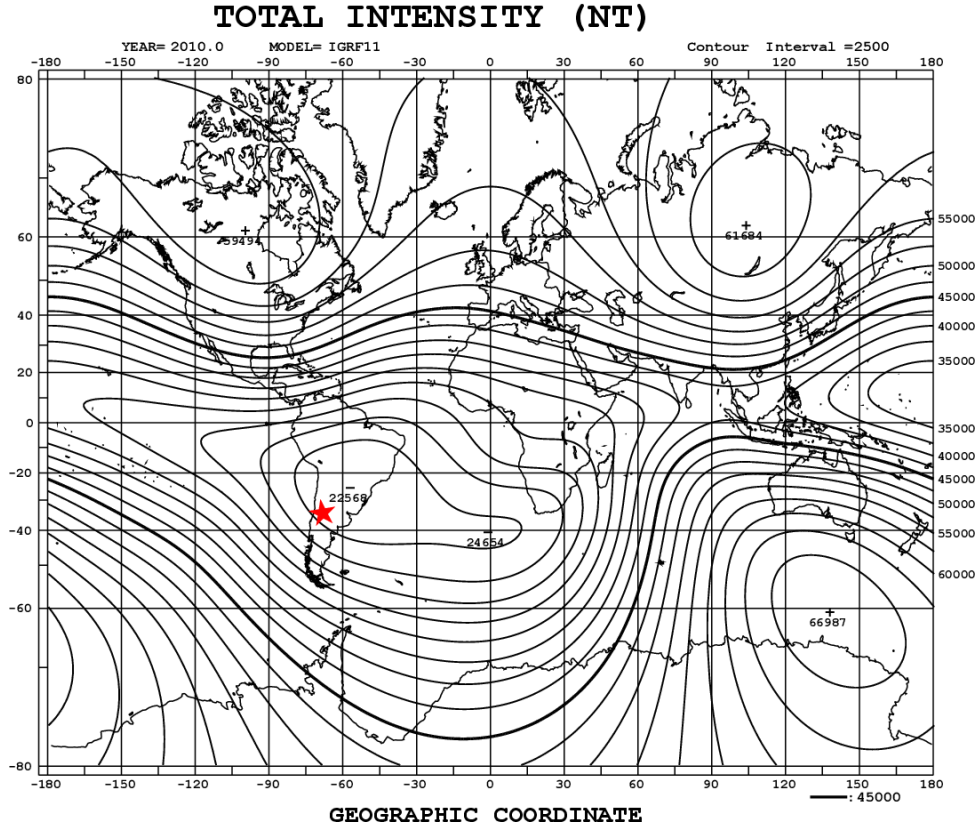
Figure 3.10: Strength of the magnetic field of the Earth. The location of the Pierre Auger Observatory is indicated with the red star. With an absolute field strength of ~24000 nT Auger is located in the South Atlantic Anomaly. Typical field strength in Europe range above 45000 nT. Adapted from Ref. [81] on basis of Ref. [82]

on the location chosen for observation, the magnetic field strength varies up to a factor of three. The location of the Pierre Auger Observatory is indicated with a star in the map. Auger is located close the absolute minimum of the geo-magnetic field strength. However, radio detector installations at the Auger site profit from a low continuous background noise level [80] and from the presence of the other detection techniques to cosmic ray induced air showers.

3.2.3.1   Macroscopic Radio Emission Model

Macroscopic models for the radio emission summarize the movements and placements of charges in the air shower development and derive the emission from the combined quantities. MGMR — the Macroscopic GeoMagnetic Radiation model [83, 84] — is a recent macroscopic model for the radio pulse generation. Within the model analytic expressions for different macroscopic contributions are derived. In Fig. 3.11 the different components treated in the model are summarized.

A major contribution to the radio pulse is given by a transverse current in the shower front. The current reflects the separation of electrons and positrons induced by the magnetic field of the Earth. In a simplified relation that ignores the longitu-
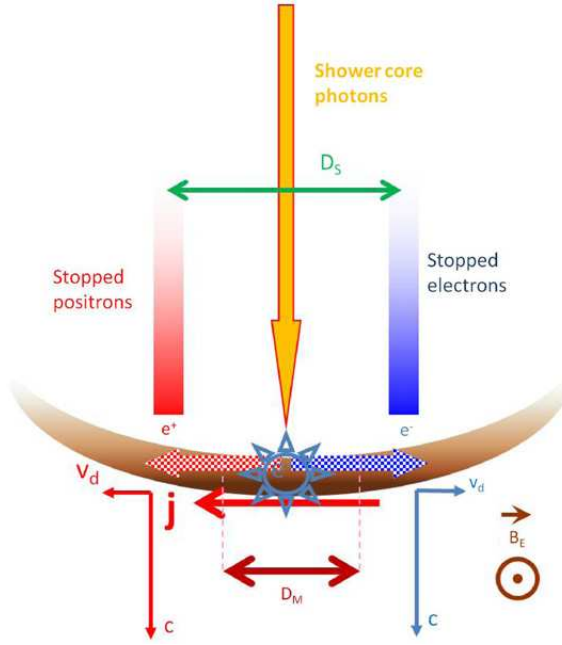
Figure 3.11: Macroscopic components to model of the radio emission from air showers in MGMR. Major contributions are given by the transverse current density j induced by the geo-magnetic field and by the charge excess in the shower front which is here depicted as sun symbol. Further electrics fields due to charge separations to distances D_s and D_m are considered. From Ref. [85].

dinal thickness of the shower front the consequent time dependent electric field in a polarization direction perpendicular to the magnetic field is calculated as [84]:

$$E_x(t,d) \approx -\frac{1}{4\pi\epsilon_0} \frac{d}{dt} \Big[\frac{\langle q\,v_d \rangle\, e\, N_e\, f_t(t_r)}{c\,\mathcal{D}(t)} \Big] \quad . \tag{3.26}$$

The expression $N_e\, f_t$ is the longitudinal development of the number of electrons and positrons in the shower front. It can for instance be parameterized by the Gaisser-Hillas function which we have discussed in terms of the energy deposit in Eqn. 3.1. The drift velocity $\langle q\,v_d \rangle$ is induced by the magnetic field. As a first approximation it can assumed to be constant throughout the shower development [85].

The combination of the number of charges and the drift velocity yields the current in the shower front. The opposite charge signs of electrons and positrons are taken into account with the factor $q = \pm 1$. Implication arise due to the time derivative of the retarded distance $\mathcal{D}(t)$. However, in a limiting case where the velocity of the shower front is c and the index of refraction is set to unity $n = 1$ a more simple relation is derived [85]:

$$E_x(t,d) \approx J \frac{4\,c^2\,t_r^2}{d^4} \frac{d}{dt_r} [t_r \cdot f_t(t_r)] \quad . \tag{3.27}$$

The constant J summarizes the constant parameters of the model and depends on the shower energy. In Eqns. 3.26 and 3.27 $t_r \approx -d^2/(2c^2t)$ is the retarded time. It counts the age of the shower backwards in time such that large negative values of
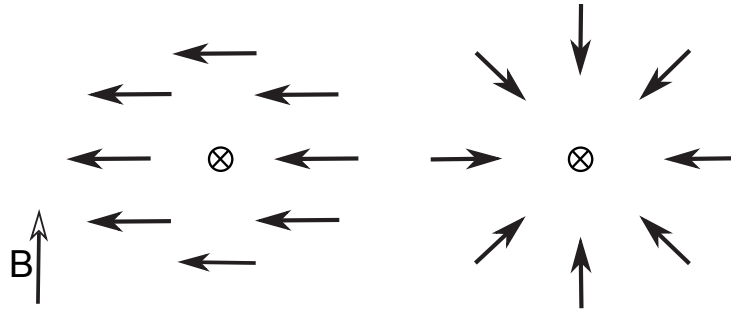
Figure 3.12: Polarizations patterns of different contributions to the radio emission from air showers. The shower is indicated by the $\otimes$-symbol and propagating into the paper plane. Geo-magnetic emission processes induce uni-polar polarization patterns (left). The variation of the charge access is the shower front yields a radial pattern (right). Adapted from Ref. [86]

t_r indicate early stages in the shower development. With respect to a longitudinal shower profile f_t such as given in Fig. 3.2 the derivative of $t_r \cdot f_t(t_r)$ implies that the largest radio emission is created before the maximum of the shower development is reached. The radio detection technique should hence be sensitivity to early stages of the shower development.

Eqn. 3.27 also indicates that the amplitude of the electric field scales with a power law depending on the distance d between the observer position and the shower axis. However, in the given calculation the lateral extend of the air shower front is ignored such that a power law index of 4 might only apply to distances far away from the shower axis.

The geo-magnetic contributions shown in Fig. 3.11 have a preferred direction perpendicular to the air shower axis and to the Earth's magnetic field. In Fig. 3.12 (left) the resulting polarization direction projected to a plane perpendicular to the shower axis is depicted. In the given projection an uni-directional pattern evolves. The variation of the negative charge excess corresponds to a longitudinal separation of charges along the air shower axis. It results in the radial polarization pattern visible in the right part of Fig. 3.12.

3.2.3.2 Microscopic Radio Emission Model

Microscopic models of the air shower signal calculate the emission of the individual particles during the shower development. The final radio signal is the superposition of the individual emission contributions. This approach is especially applicable in combination with a simulation of the particle content of the air shower as realized in CORSIKA (cf. Sec. 3.2.2). REAS3 [86] is a recent program that implements this scheme. To derive the emission of the individual particles an 'endpoint'-formalism is used [87]. A sketch of the procedure is visible in Fig. 3.13.

The track of a particle is approximated by a series of straight segments and instantaneous acceleration processes. The acceleration processes may include the instantaneous de-acceleration of the particle at the end of a track segment as well as a corresponding acceleration at the beginning of the next segment.
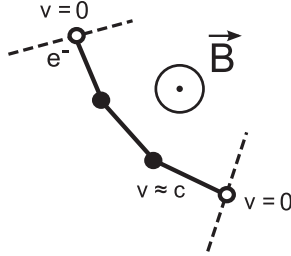
Figure 3.13: Microscopic generation of radio emission from a single particle including the endpoint formalism. The endpoints are indicated as hollow circles. In REAS3 also contribution from track 'kinks' are calculated which are given here a solid circles. The change in particle momentum is induced by the presence of the magnetic field. From Ref. [86].
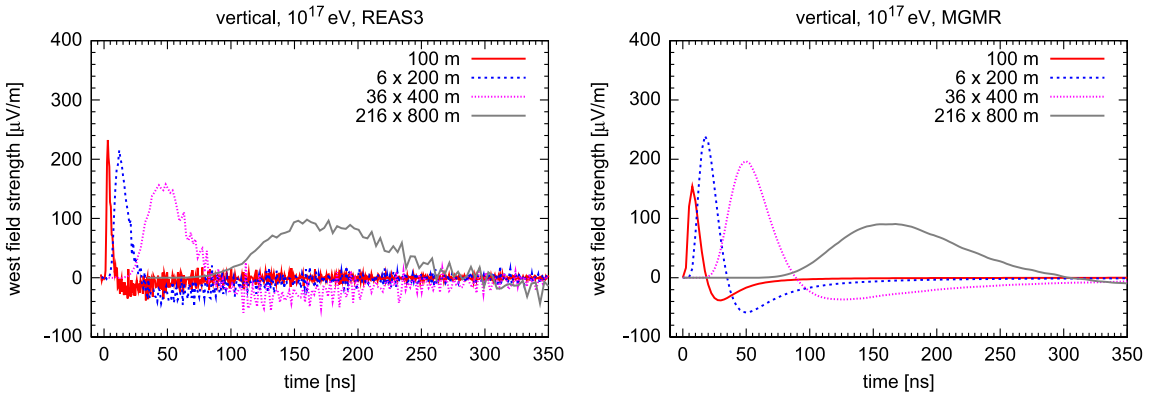
Figure 3.14: Simulated radio signal amplitude as a function of time from an air shower with an energy of 10^{17} eV at different distance from the shower axis. The simulations are performed with REAS3 (left) and MGMR (right). For a common display the amplitudes have been scaled. From Ref. [88].

The instantaneous processes result in hard radiation. However, the polarization directions resulting from an acceleration and a de-acceleration process are flipped. The radiation emitted at the endpoint of a track hence cancels when superposed with the emission from the next starting point. Only a soft fraction of the radiation remains when the particle momentum has changed before and after the endpoint.

As pointed out in Ref. [87] this scheme results in a complete treatment of radiation processes arising from particle acceleration with a single formalism. Due to is discreteness the 'endpoint'-formalism is especially suited for numerical simulations. With respect to the radio emission from an air shower the combination of CORSIKA and REAS3 is used to generate the signals visible in Fig. 3.14 (left).

In Fig. 3.14 the emission of an air shower is inspected at different distances from the shower axis. The shape and the amplitude of the signal changes with increasing distance. Note that the amplitudes have been scaled for a common display. In the right panel of Fig. 3.15 the corresponding simulation based on the MGMR model is displayed. In the given example both models yield a similar result. In the case of the REAS3 simulations numeric noise is present at high frequency components [88].
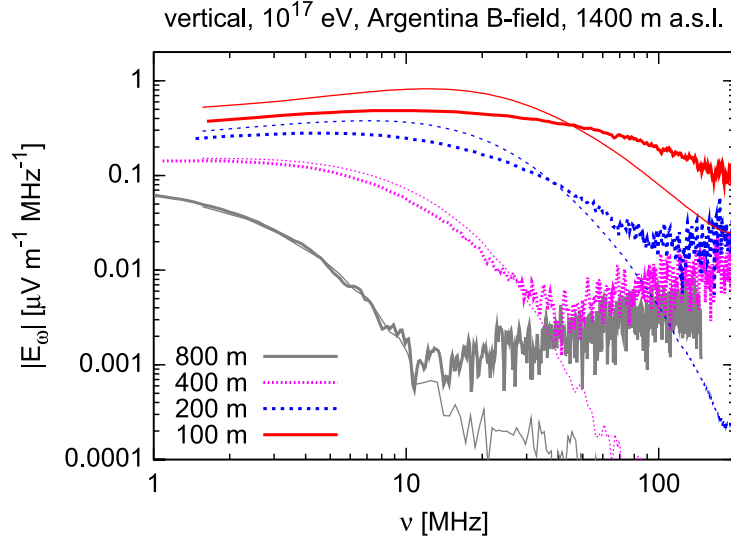
Figure 3.15: Spectral content of radio pulses of Fig. 3.14 simulated with REAS3 (solid) and MGMR (dashed). Note that at larger distances the frequency content becomes dominated by the lower frequencies. From Ref. [88].

For the realization of a radio detector experiment the changing shape of the pulse has direct implications. In Fig. 3.15 the frequency spectra of the pulses are displayed. The simulations predict that the air shower signal is dominated by the lower frequency components when observed at larger distance from the shower axis. To observe distant air showers the sensitive range of the detector should hence be optimized towards lower frequencies.

3.2.3.3   Direction of Poynting Vector of Radio Emission

In Sec. 6 we will study the response of the antenna used as sensor to the incoming radio signal. For a proper reconstruction of the air shower signal the incoming direction of the signal has to be known.

In a plane wave approximation the incoming direction of the signal $\vec{n}_s$ is given by the direction of the Poynting vector $\vec{S} = \vec{E}_{xyz} \times \vec{B}_{xyz}$. In current simulations of radio signals only the 3-dimensional electric field vector $\vec{E}_{xyz}(t)$ but not the magnetic field $\vec{B}_{xyz}(t)$ is calculated. Hence, the incoming direction of the signal at an observer position is only determined to a plane perpendicular to the electric field vector.

In Fig. 3.16 (top) the electric field $\vec{E}_{xyz}(t)$ of a radio pulse simulated with REAS2 [89] is displayed.[4]. As first ansatz the incoming direction $\vec{n}_s$ of the pulse is approximated to be aligned with the axis of the air shower $\vec{v}$. In the middle panel of Fig. 3.16 we have rotated the electric field into a new coordinated system $\vec{E}_{\theta,\phi,r}$. The direction of the third axis $\vec{e}_r$ of this coordinate system is chosen to point into the direction of the air shower axis $\vec{e}_r \parallel \vec{v}$. If the propagation direction of the signal is fully aligned with

---

[4]In this example we use a pulse generated with REAS2 as these simulations are not affected by numerical noise which simplifies the treatment. The shower simulation was prepared by Tim Huege with REAS V2.59 for a comparison to measured air shower signals at the Pierre Auger Observatory.
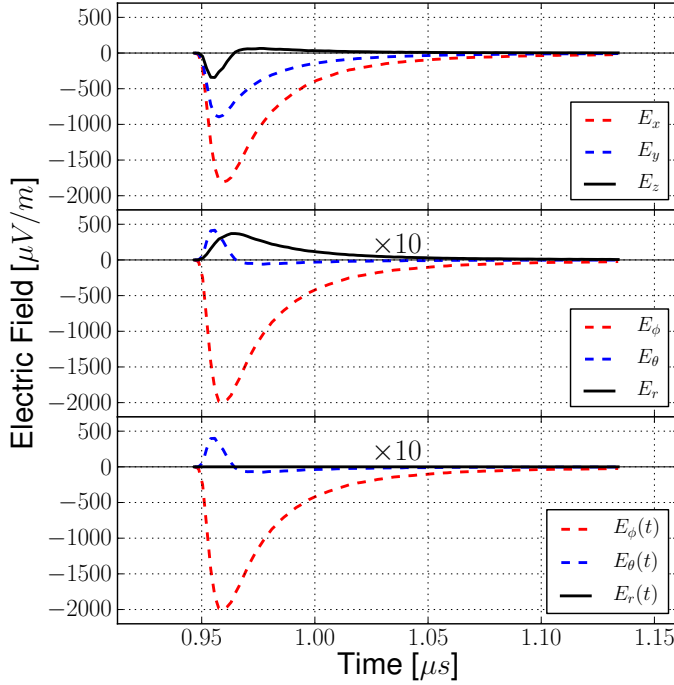
Figure 3.16: Radio air shower signal in different coordinate systems. Top: A local coordinate system where xyz are usually identified with the East-West, North-South and vertical direction. Middle: The same signal but rotated into a fix coordinate system with the third direction (r) parallel to the air shower axis. The E_r component is emphasized with a factor of 10 and is not vanishing. Bottom: For each point of the time series an individual coordinate system is chosen such that E_r is zero.

the air shower axis $\vec{n}_s \parallel \vec{v}$, the electric field component E_r should vanish completely in this coordinate system. We notice that a fraction of electric field remains in the $\vec{e}_r$-polarization direction. In the display we have emphasized this component by a factor 10.

As consequence, the incoming direction of the radio signal is not completely given by the direction of the air shower axis. This corresponds to the picture of a curved or cylindrical front of the radio signal which is discussed in terms of signal timing in Ref. [90].

We investigate the pointing direction of the pulse as a function of time. To do so, we assume that the Poynting vector $\vec{S}(t)$ of the air shower signal is contained at all times in the shower detector plane.[5] The shower detector plane is defined by the air shower axis and the position where the air shower signal is observed. Going through the simulated time series we identify at each point in time a direction in the shower detector plane such that the third component of the electric field pulse vanishes. The lower panel of Fig. 3.16 shows the result of this transformation.

---

[5]Shower detector plane in analogy to fluorescence detector measurements.
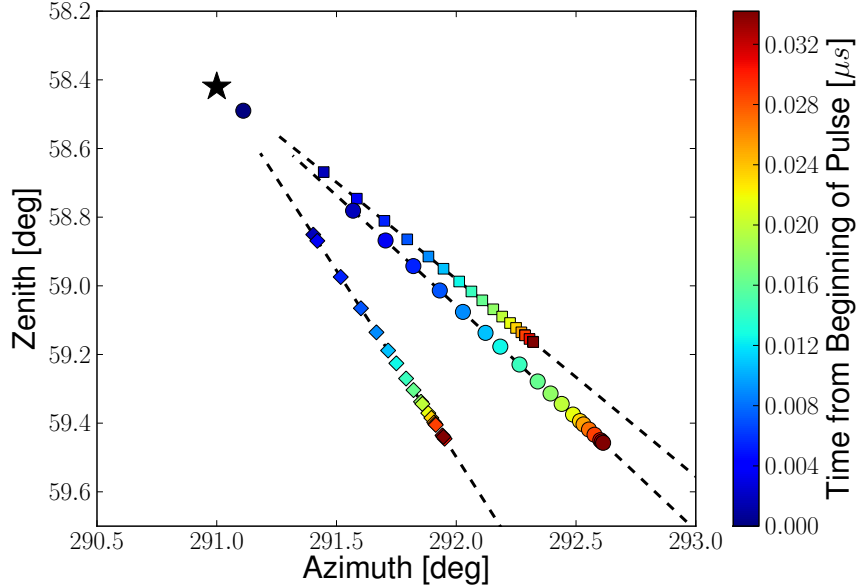
Figure 3.17: Track of an air shower reconstructed from point-wise rotation of the electric field vector. Displayed are three different observer position. The dashed lines indicate the individual shower detector planes. The star denotes the incoming direction of the cosmic ray in the underlying air shower simulation. Of each pulse the first $\sim 0.03\,\mu s$ are displayed as here the variation of the signal direction is most distinct. The time is given by the color scale. The electric field displayed in Fig. 3.16 here corresponds to the circle markers.

From the transformation we receive a series of directions $(\theta(t), \phi(t))$ which we interpret as the instantaneous directions of the Poynting vector $\vec{S}(t)$ of the signal. In Fig. 3.17 the time progression of these directions is displayed. To stress the effect, the transformation is done for three different observer position of the same simulated air shower. The air shower direction is indicated as star, the dashed lines indicate the respective shower detector planes.

The early parts of the considered pulses point towards directions early in the shower development. The subsequent tilt towards larger zenith angles in Fig. 3.17 indicates directions deeper in the atmosphere. The intersection of each direction with the axis of the air shower corresponds to a certain height above ground. Using the same atmospheric model as used to set up the air shower simulation we calculate the slant depth X that belongs to each of the intersection points. In Fig. 3.18 the absolute field strength of the pulse is shown as a function slant depth calculated from the pointing directions.

We find that the information available from the simulation of a radio signal at a single antenna position are sufficient to create a fluorescence detector like measurement of the shower development. Within the pulse maximum the atmospheric depth varies rapidly. In this example we find the maximum of the radio emission prior to the maximum of the shower development. This corresponds to the expectation arising from our discussion of the macroscopic radio emission model. Late signal
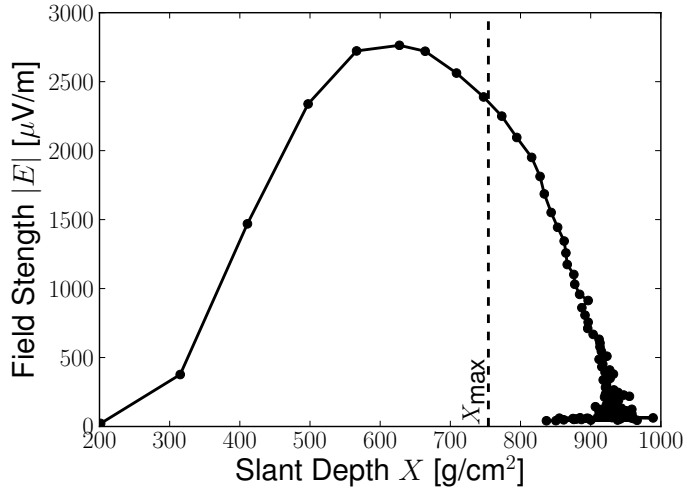
Figure 3.18: Slant depth of radio emission from electric field information at a single antenna generated with REAS2. The same electric field as in Fig. 3.16 is displayed. Each of the point markers correspond to an electric field sample. The position of the shower maximum as known from the simulation setup is given by the vertical line. Taking into account the zenith angle of displayed air shower of $\theta \approx 58°$ the electric field was simulated at a slant depth of ~ 1650 g/cm^2

portions from the fade out of the pulse in Fig. 3.16 accumulate at similar depths in the atmosphere. Our result corresponds qualitatively to the findings obtained in Ref. [91] where the radio emission from different atmospheric depths was accessed explicitly in the simulation.

As pointed out in Ref. [83] the exact arrival times of signal portions from different stages of the shower development is affected by the refractive index n. Realistic indices of refraction are a current matter of research to be implemented in REAS3 [92]. For now, we take Fig. 3.18 to underline the detailed information available on the shower development that are present already at a level of single radio detector stations.

For the discussion in the next sections we notice that the incoming direction of the radio signal can offset by few degrees from the air shower axis and slightly changes throughout the pulse development.

3.2.3.4 Additional Radio Emission Processes

The idea to detect extensive air showers via emitted radiation in the GHz frequency regime referred to as molecular bremsstrahlung was first discussed by Gorham et al. [93]. In contrast to the pulse in the MHz regime that is strongly beamed in the propagation direction of the shower, molecular bremsstrahlung is expected to be emitted isotropically. This potentially allows for an observation of the air shower development along the axis with access to calorimetric information and realizes a measurement similar to the known fluorescence-detector technique — however, without being constraint to dark observation conditions. Moreover, the laboratory experiments described in Ref. [93] indicate that the GHz emission can be at least partially

coherent which would enhance the scaling of the shower signal with the energy of the primary particle.

In a novel study using an accelerator setup a linear scaling of the GHz signal power with the beam intensity has been reported [94]. This would be consistent with incoherent radiation. However, further accelerator experiments are planned to measured the GHz yield and several air shower detector installations are on their way to explore the GHz emission [95, 96].

4. Detection of Air Shower at the Pierre Auger Observatory

The Pierre Auger Observatory (PAO) is the world's largest detector dedicated to the study of UHECRs. To observe the full sky the observatory has been planned to consist of two sites. The planning for the setup of a detector in the northern hemisphere has reached an advanced phase of R&D [97]. The construction of the Southern site was finished in 2008. In Fig. 4.1 a map of the detector is given.

The Southern site of the PAO is located in the Argentinian Pampa in the province of Mendoza near the town Malargüe. The site is located on flat plateau at a height of 1400 m a.s.l. that is sparsely populated. To the West the area is bordered by the Andes reaching to heights above 4000 m. The combination of remoteness, elevation of the site and steady weather conditions in the downwind of the Andes constitutes perfect conditions for the hybrid detector approach of the PAO.
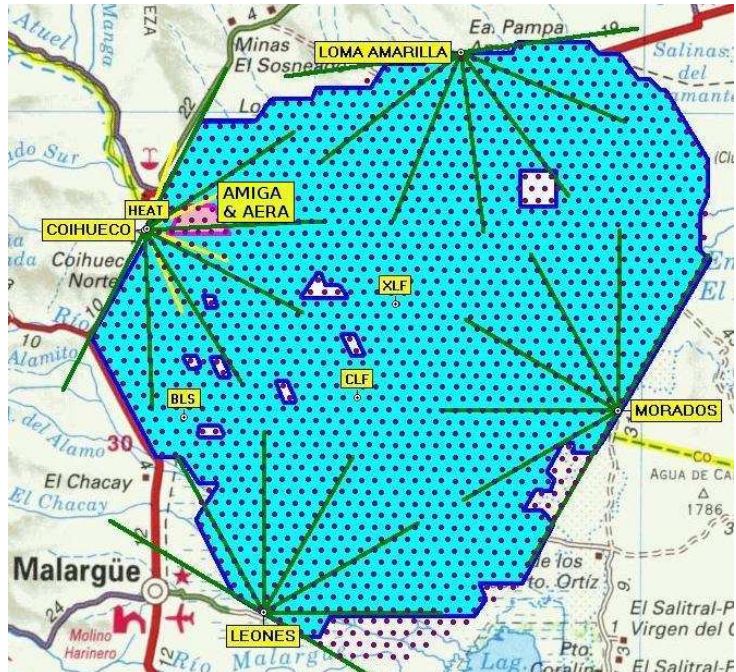
Figure 4.1: The Southern Site of the Pierre Auger Observatory near Malargüe in Argentina. The red dots mark the position of the 1660 water tanks positioned in a hexagonal grid of 1.6 km spacing. The green lines mark the viewing angles of the 24 fluorescence telescopes situated at the four sites. The detector covers an area of roughly 50×70 km^2. Adapted from Ref. [2].
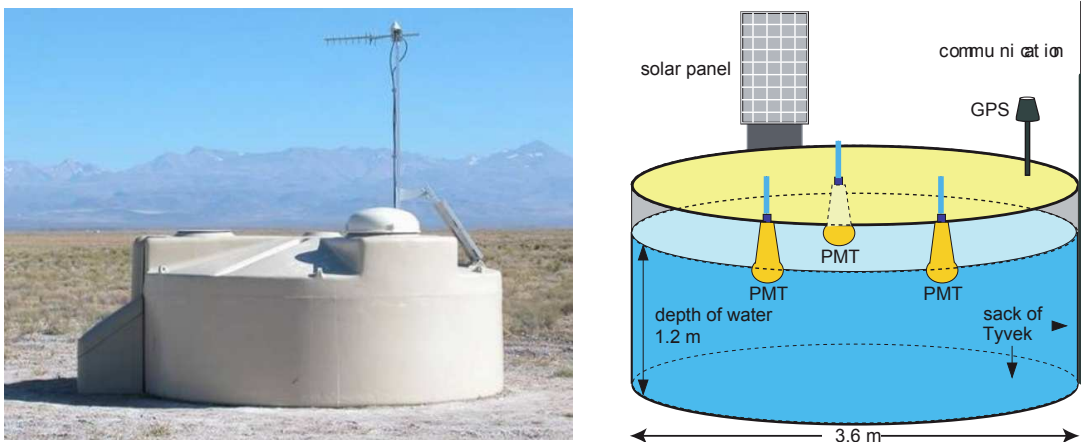
Figure 4.2: Left: Water Cherenkov Detector of the Pierre Auger Observatory [2], Right: Schematic view of a detector station [98]. Three photomultipliers observe 12 m^2 of ultra-pure water. The detector is operated as autonomous station with solar power and wireless communication.

The PAO employs two complementary detection techniques for the observation of extensive air showers induced by UHECRs. An array of 1660 particle detectors is overlooked by 24 fluorescence telescopes located at four positions around the particle detector array. The surface detector measures a snapshot of the lateral particle distribution of the air shower evolving through the atmosphere at the moment when it reaches the ground. The fluorescence detector is sensitive to the longitudinal development of the air shower observing the excitation of the air molecules when the air shower traverses. The combination of both detection techniques is referred to as hybrid detection. The hybrid approach allows for an inter-calibration of the two detectors, independent verification of the results and precise measurement of air showers that are observed with both detectors simultaneously.

Since the start of the data taking in 2004 until the end of 2010 more than 60000 cosmic rays above $10^{18.5}$ eV of high quality were recorded with the PAO. About 3600 air showers were detected with the fluorescence detector with at least one coincident station of the surface detector above 10^{18} eV [4].

4.1 The Surface Detector

The surface detector (SD) contributes the majority of detected air showers of the PAO. Its 1660 water Cherenkov detectors are distributed over an area ∼3000 km^2. The detector stations are arranged in an hexagonal grid with a spacing of 1500 m. Each station consists of a tank filled with 12 m^3 ultra-pure water. Charged particles of an air shower traversing the water emit Cherenkov radiation as the particles' velocities exceed the speed of light in water. The Cherenkov light is detected by three photomultiplier tubes (PMTs) located at the ceiling of the tank. A photo and a schematic view of a surface detector station are visible in Fig. 4.2.

The PMTs are readout with 40 MHz flash analog-to-digital converters which imposes a time binning to the recorded traces of 25 ns. The absolute timing to the series of
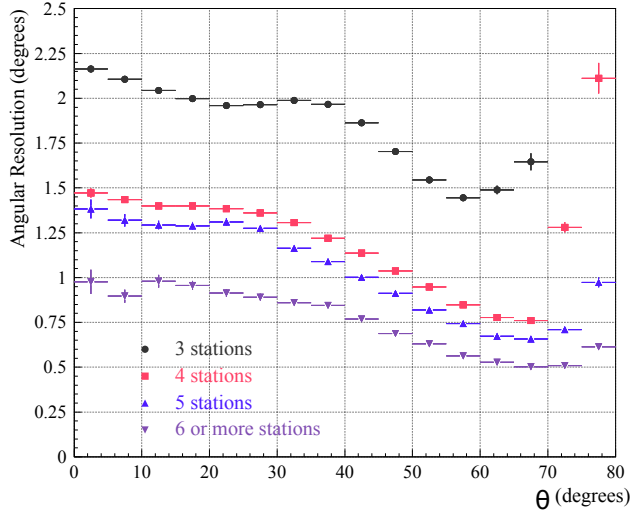
Figure 4.3: The angular resolution of the surface detector as a function of the zenith angle and the multiplicity of the detector stations that contribute to the reconstruction of an air shower. From Ref. [99].

recorded samples is delivered by a GPS clock with an accuracy of about 10 ns. With this hardware setup the arrival time of the air shower at the position of the tank is measured to reach a precision of ~ 14 ns [99].

The electronics of the individual surface detector stations discriminate potential air shower signal from background processes using a time-over-threshold trigger. At least two of the three PMTs are required to record a increased signal over 13 trace samples in comparison to a noise threshold.
Background noise is induced by single atmospheric muons at a rate of 2.5 kHz. Single muons originate from low energetic cosmic rays and induce on average the same signal in each station of the detector array. The single muon flux hence constitutes a convenient source of calibration for the individual detector station by expressing their signals in units of vertical equivalent muons (VEM) [100].
In addition to the time-over-threshold trigger, a more simple signal-over-threshold trigger is operated which requires a coincidence of all three PMTs in single trace samples. This trigger aims at the detection of short signals as originating from distant air showers.
The combination of the two triggers is set up to yield single station trigger rates of about 20 Hz. Station triggers are forwarded to a central data acquisition using wireless communication. As soon as at least three neighboring detector stations report a signal within an adequate time window (3ToT) the FADC traces are read out and analyzed. 90% of the events selected with this trigger scheme correspond to reconstructible air showers. In combination with the spacing of the stations of 1500 m the surface detector array reaches full efficiency for the detection of cosmic rays above an energy of $10^{18.5}$ eV [101].

In Fig. 4.3 the angular resolution of the air shower direction of the surface detector is displayed. The angular resolution is measured exchanging co-located surface detector stations in the reconstruction of single air shower events. The precision of the
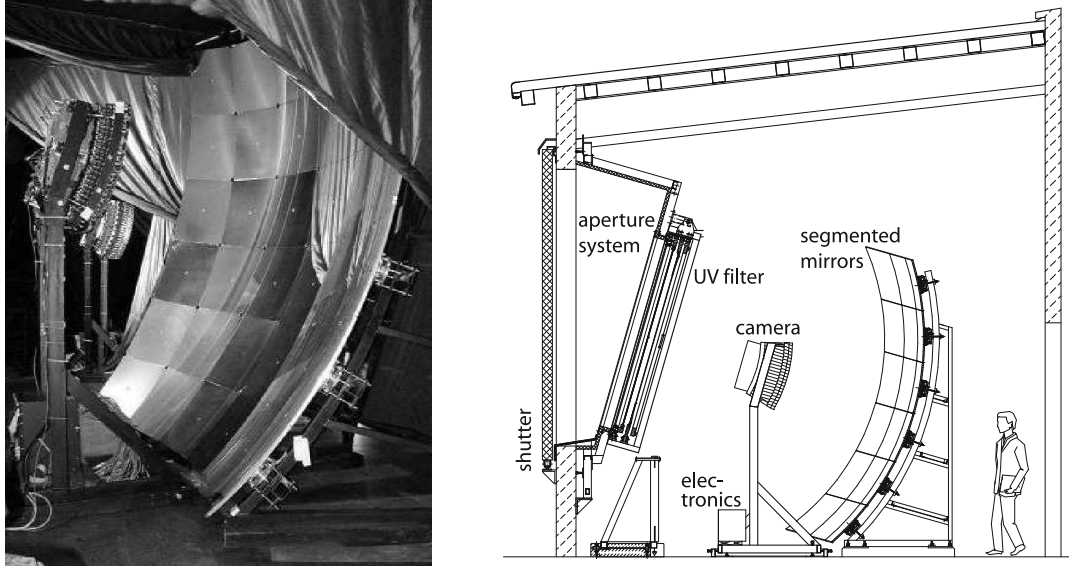
Figure 4.4: Left: Picture of an Auger fluorescence telescope with the spherical mirror and the pixel camera. Right: Schematic view of an fluorescence telescopes inside its housing. Also indicated is the aperture system consisting of a Schmidt optics corrector ring and shutter system to shade the room during daytime. Taken from Ref. [3].

reconstruction depends on the zenith direction and ranges from $2°$ for air showers measured in three detector stations to values well below $1°$ for higher multiplicities. An air shower caused by a cosmic ray of 10^{19} eV will typically be detected in 10 detector stations.

As discussed in Sec. 3.1.2 the energy of the primary particle is correlated with the signal at a fixed distance from the core of the air shower. For the regular surface detector the signal at 1000 m from the axis $S(1000)$ is used as the energy estimator. The distance of 1000 m is chosen as here model uncertainties to the precise shape of the LDF are minimal. It is difficult to infer from pure surface detector measurements the absolute energy scale of the air showers that have been observed. The surface detector takes here great advantage of the fluorescence detector. With their calorimetric measurements the fluorescence telescopes provide a calibration of the energy estimator of the surface detector.

4.2 The Fluorescence Detector and Hybrid Detection of Air Showers

The fluorescence detector (FD) is composed of 24 single telescopes placed at four detector sites. The six telescopes at each detector site constitute an 'eye' of fluorescence detector. As can be seen in Fig. 4.1 the placement of the eyes at the perimeter of Auger maximizes the survey of atmosphere above the surface detector.

In Fig. 4.4 one of the fluorescence telescopes is displayed. Incoming light is focused by a 3.5×3.5 m^2 spherical mirror onto a camera consisting of 440 photomultipliers. In combination with a corrector optic the field of view of a single telescope is $30°$
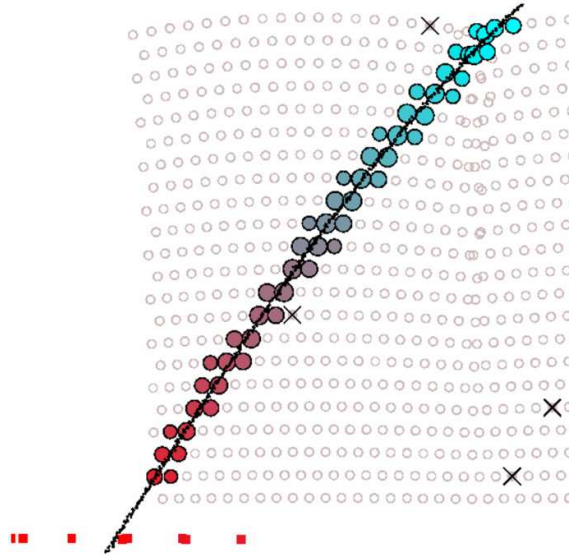
Figure 4.5: Light track of an air shower detected with the fluorescence detector. The colors indicate the time progression of the air shower signal in the field of view of the camera. The black line yields a step in the reconstruction of the air shower parameters. Black crosses mark accidentally triggered pixels of the camera. In the lower left red squares indicate surface detector stations that recorded the same air shower. Taken from Ref. [3]

both in zenith and azimuth direction. The photomultiplier signals are digitized with a sampling rate of 10 MHz. A hierarchical structure of trigger decisions is applied to choose signal patterns that match air showers. High quality events that are finally used for physics analysis are recorded at a rate of one event per two hours with the full detector [3].

In Fig. 4.5 an air shower reconstructed with the fluorescence detector is displayed. The shower axis is derived from the timing information and the pointing directions of the triggered PMT pixels. In addition, the timing information and position of the surface detector station with the highest signal is taken into account. This usually adds a strong constraint to the reconstruction of the air shower axis as the surface detector provides a precise timing information at a well defined direction in the field of view of the telescope. With this reconstruction scheme an angular resolution below 1° is realized [99].

After the reconstruction of the air shower geometry the longitudinal profile of the air shower as a function of traversed matter in the atmosphere is determined. Here, corrections for the detected amount of fluorescence light due to Cherenkov light, light scattering and attenuation are applied. From the estimated fluorescence light the profile of the energy deposit is obtained using the absolute fluorescence yield. With a relative uncertainty of 14% the fluorescence yield is the dominant source of systematic uncertainty to the reconstructed air shower energy. It is followed by the reconstruction method itself (10 %) and the calibration of the telescopes (9%). The systematic uncertainties add up to 22 % on top of a relatively small statistical uncertainty of 10% [3].
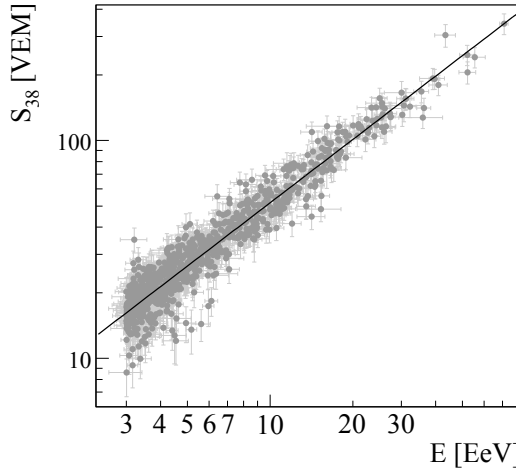
Figure 4.6: Correlation between $S38$ and E_{FD} for 839 'golden' hybrid events. The observable $S38$ is closely related to the aforementioned $S(1000)$ but corrected for subtle zenith angle dependencies. The curve represents the fit of a power law to the distribution and yields the calibration curve for the SD energy estimator. Taken from Ref. [102].

The operation of the FD is constraint to darkish and cloudless observation conditions which amounts to a duty cycle of 13%. The energy scale of the FD is transfered to the SD which is operational continuously. This calibration is performed using a subset of air shower events that are reconstructed in the surface detector alone but also accessed in the hybrid reconstruction. For these 'golden' hybrid events the energy estimator of the surface detector is investigated as function of the energy given by the corresponding FD reconstruction. As shown in Fig. 4.6 the fit of a power law with two parameters $E_{\mathrm{FD}} = A \cdot S_{38}{}^B$ yields the desired calibration of the SD. The statistical energy uncertainty of the SD ranges from $\sim 16\%$ for energies around $10^{18.5}$ eV and improves to $\sim 12\%$ above 10^{19} eV. The systematic uncertainty of the FD of 22% also charges for the surface detector reconstruction.

4.3 The Low Energy Enhancements

The surface detector and the fluorescence detector are designed to provide a fully efficient detection of cosmic rays starting at an energy of $10^{18.5}$ eV. However, also the energy range down to 10^{17} eV is of great interest as here the change from galactic to extra-galactic sources of the cosmic rays is expected (cf. Sec. 2.3). Moreover, an enhancement of the PAO towards lower energies provides an overlap to other current cosmic ray experiments which allow for profound measurements up to 10^{18} eV as the KASCADE-Grande detector [17].

To both standard detectors of the PAO, enhancements towards lower energies have been deployed: the Auger muon and infill for the ground array (AMIGA) and the high-elevation Auger telescopes (HEAT). Both enhancements are concentrated in the north-western part of the Auger detector to maximize the number of events detected in coincidence in both detectors (cf. Fig. 4.1). An overview of the layout of the low energy enhancements is depicted in Fig. 4.7.
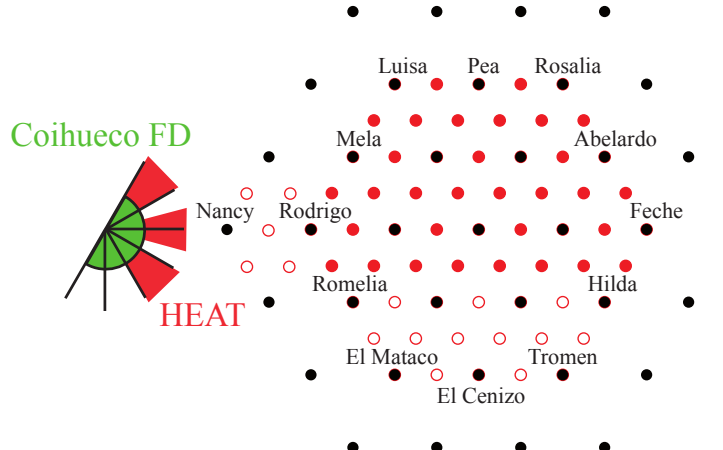
Figure 4.7: Layout of the low energy enhancements of the Pierre Auger Observatory. The HEAT telescopes are co-located with the standard FD detector 'Coihueco' and partially overlook the same field of view in azimuth. In front of the fluorescence telescopes the AMIGA detector stations (red circles) reduce the spacing of the usual SD grid (black circles) to 750 m. Hollow circles mark detector stations that are yet to be deployed. Adapted from Ref. [103]
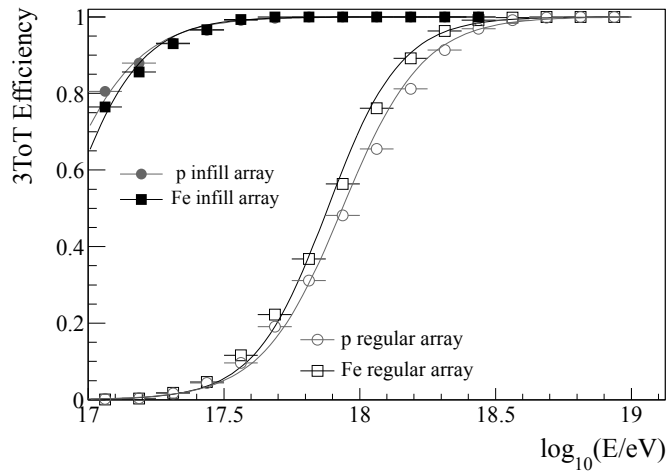
Figure 4.8: The trigger efficiency of the regular surface detector in comparison to the infill array [104]

Air showers of lower energy reach the maximum of their shower development earlier in the atmosphere and emit less fluorescence light. The HEAT detector compensates for this using three standard Auger fluorescence telescopes tilted upwards by 29°. This provides an observation of higher altitudes in the atmosphere at closer distances from the telescope. HEAT is operating since Sep. 2009 and first data is presented in Ref. [103].

The AMIGA detector provides an infill to the SD with a reduced lattice constant of 750 m. Currently 53 of 61 foreseen additional surface detector stations are deployed. The smaller distance between the detector stations compensates for the reduced

lateral spread of the particle disc of the air shower at lower energies. In Fig. 4.8 the trigger efficiency for the detection of air showers in at least three detector stations (3ToT) is displayed.

The infill array provides a fully efficient detection of air showers starting at $10^{17.5}$ eV. This enhances the accessible energy range by one decade in comparison to the standard SD array. Currently the infill array is detecting air showers with 3ToT rate of $\sim$770 events per day [105].

In addition to the infill detector stations AMIGA employs buried muon counters close to selected SD stations. The soil shields the electromagnetic component of the air shower and enables a separated measurement of the muonic component which is more penetrating. A discrimination between the electromagnetic and the muonic components is expected to provide detailed information of the air shower development and the properties of the underlying cosmic ray as suggested by the results of the KASCADE experiment (cf. Fig. 2.2).

5. The Radio Detectors of the Pierre Auger Observatory

The increasing interest in the radio detection technique to cosmic ray induced air showers in the last decade has lead to the installation of two pioneering setups at the site of the Pierre Auger Observatory. These two setups succeed in detecting the radio pulse emitted by air shower in the MHz regime in coincidence with the surrounding surface detector.

The successful realization of a self-triggered radio detector that is sensitive to the radio emission of cosmic ray without additional detector components marked a milestone towards the installation of a large scale radio detector at the site of the PAO. The two efforts converged in the current setup of the Auger Engineering Radio Array (AERA).

Moreover, several setups are on their way to investigate the GHz emission of air showers.

5.1   GHz Radio Detectors

The results of the accelerator experiments discussed in Sec. 3.2.3.4 indicate that air showers can be detected by their emission of microwaves in the GHz regime. As this radiation is emitted isotropically from the air shower the detection of GHz emission potentially creates a calorimetric measurement of the air shower development but without the constrain to darkish observation conditions as the fluorescence technique. These prospects triggered the setup of first prototype detectors by members of the Pierre Auger Collaboration.

MIDAS & AMBER
The AMBER 'Air-shower Microwave Bremsstrahlung Experimental Radiometer' as installed at 'Coihueco' fluorescence detector site is visible in Fig. 5.1 (a). AMBER is an updated version of the detector already used along with the first accelerator measurements of the GHz emission in Ref. [93]. AMBER uses individual antennas as pixels forming a camera for GHz frequencies. Incoming radio signals are concentrated onto the camera by a reflector dish. A similar setup is realized by MIDAS the 'MIcrowave Detection of Air Showers' detector which is visible in Fig. 5.1 (b).

A major difference between AMBER and MIDAS is the trigger concept to select air-shower information from the continuous background sources.
MIDAS aims for realizing a self-triggered setup. The trigger logic is set up to look for signatures in the pixel camera that fit down-going air showers. Stable data taking was achieved with this method during test runs at the home university. The

(a)

(b)

(c)
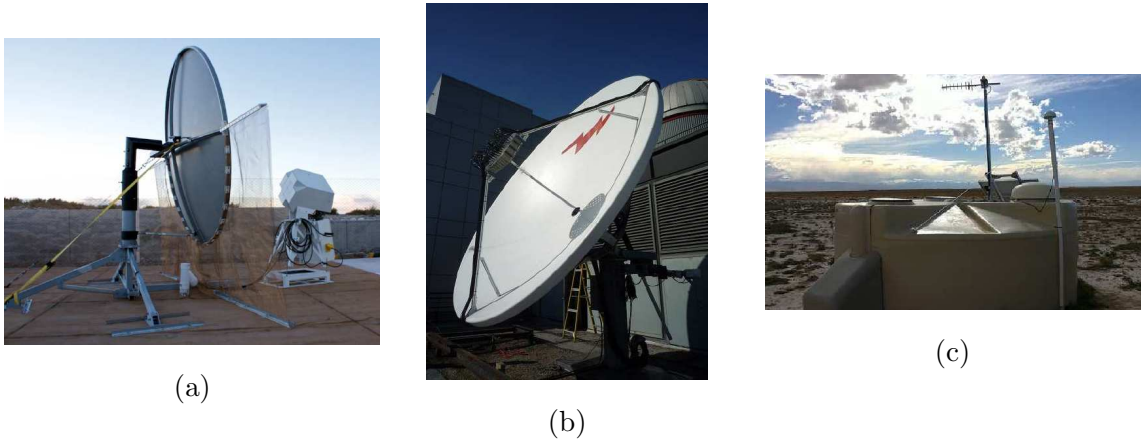
Figure 5.1: GHZ Radio Detector at the Pierre Auger Observatory. (a) The AMBER dish antenna installed at the Coihueco Fluorescence Detector. (b) The MIDAS detector during test measurement at the home institute. (c) A SD tank equipped with a GHz antenna of EASIER which is placed on the right pole. From Ref. [96]

detector is foreseen to be installed at the 'Los Leones' FD site [96].

The AMBER detector, however, is triggered by the SD. The latency of SD information is a several seconds to be available for other detectors. AMBER employs large ring buffers to store a continuous data stream from all pixels for several seconds. Using a fast reconstruction of the SD information time windows in the buffered data are identified which contain air shower signals.

FDWave

A recent idea towards the realization of GHz detection of air showers using existing Auger technology is FDWave. FDWave plans to equip unused slots for PMT pixels at the cameras of a standard Auger FD site 'Los Leones'. Due to the compact size of the FD camera small antennas for frequencies above 9 GHz are foreseen. The aluminum mirrors of the FD telescope serve as reflector dish. The usual firmware of the fluorescence telescope is adjusted to accept the data delivered by the antennas. In this way data can be acquired along with the usual FD data taking and in the same data format. [96]

EASIER

A different ansatz towards the detection of GHz emission is aimed for by the EASIER 'Extensive Air Shower Identification using Electron Radiometer' setup. Instead of detecting the lateral emission from the air shower, EASIER equips hexagons of usual SD tanks with GHz antennas for a detection of the emission in the forward direction. A GHz antenna mounted on a SD tank is visible in Fig. 5.1 (c). The data acquisition is realized with an unused FADC channel of the surface detector tank. This includes the digitization of the signal and the data transport with the usual SD communication. In recent measurement for the first time experimental evidence was given for the GHz emission of air showers [106]. Besides GHz antennas also fat dipole antennas from the CODALEMA II setup [68] are deployed as sensor to MHz frequencies following the same data acquisition scheme. Here as well, air showers are being observed [107].

Detector	Frequency band	Sampling Rate	Trigger	N Sensors
MIDAS	3.4 - 4.2 GHz	20 MHz	self-triggered	53 (pixel)
AMBER	3.4 - 4.2 & 10.95 - 14.5 GHz	100 MHz	external (SD)	16 (pixel)
FDWave	> 9 GHz		external (FD)	up to 264 (pixel)
EASIER	3.4 - 4.2 GHz	40 MHz	external (SD)	7 (stations)

Table 5.1: Overview of GHz detectors at the Pierre Auger Observatory.

The GHz detectors do not sample the full waveform of the incoming signal. Usually a signal envelope is created that is recoded with a sampling rate in the MHz range. In Tab. 5.1 characteristics of the GHz detectors are summarized.

5.2 Recent MHz Radio Detectors

The radio detection technique promises to access kinematic and atomic properties of the primary cosmic ray particle with a duty cycle of 100 %. The success of the CODALEMA [8] and LOPES [9] experiments detecting air showers at frequencies in the 40 to 80 MHz band encouraged the installation of two pioneering radio detector at the site of the Pierre Auger Observatory to study the radio emission of air showers in a calibrated environment.

Both setups used existing infrastructure of the Auger detector for their installations. The RAuger setup is located in the center of the SD array using the central laser facility as base point for the detector installation (see Fig. 4.1). The second setup is located at the balloon launching station (BLS) which is used as shelter for a central data acquisition.

At both radio detector setups an additional surface detector station is installed to lower the energy threshold of the SD to cosmic rays locally to below 10^{17} eV [108].

5.2.1 Setups at the Balloon Launching Station

Scintillator Triggered Setup

The installation of a radio detector at the BLS started in 2006. The core experiment consisted of three detector stations forming an isosceles triangle with a base length of 100 m. At two position logarithmic-periodic dipole antennas were installed that allow for a separate detection of signals polarized in East-West and North-South direction. At the other observing position an inverted v-shaped dipole of the LOFAR experiment [109] and a first version of a LPDA made from thin Copper wires were employed [110].

The antennas were read out by a central DAQ system placed in the BLS over coaxial cables. In Fig. 5.2 a sketch of the DAQ including the trigger scheme is given. Next to the BLS a HiSPARC particle detector [111] was placed. Its two scintillator plates provided the trigger to the read out of the radio antennas sampling the signals with 400 MHz 12 bit ADCs.
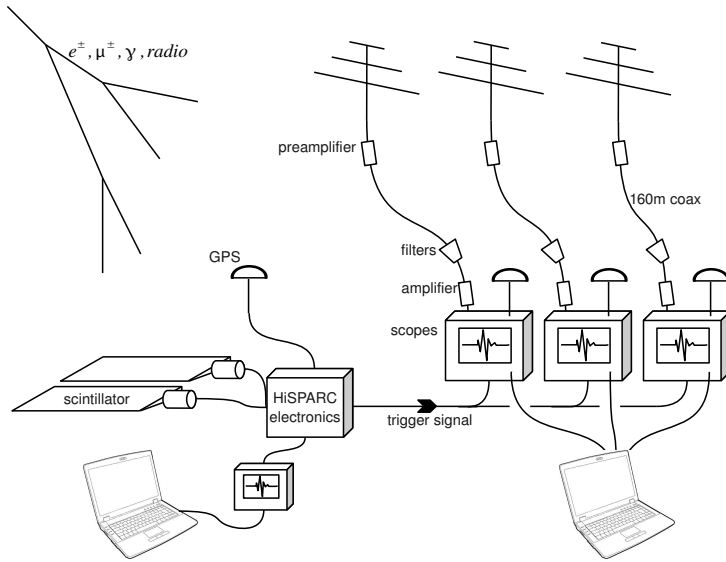
Figure 5.2: Sketch of the electronics used for data acquisition in the externally triggered BLS setup. The setup includes 160 m coaxial cables, a set of analog filters and several stages of amplification. Timing is provided by a GPS system. The setup was triggered with scintillator particle detector from the HiSPARC project [111]. For convenience, only one antenna polarization is drawn. Adapted from Refs. [112, 110]

With the BLS setup the first radio signal from an air shower in coincidence with the Auger surface detector was measured [110]. Within one year of operation from April 2007 until to May 2008, overall 494 coincidences were recorded. We will use this data to study the lateral signal fall-off of the radio emission from air showers in Sec. 9.

MAXIMA

The 'Multi Antenna eXperiment in Malargüe Argentina' employs four radio detector stations installed near the BLS in 2008 [113]. The stations are operated autonomously with solar panels and a wireless communication system. A picture of a MAXIMA station is visible in Fig. 5.3 (a). The stations are equipped with 'Black Spider' wire LPDAs. The Black Spider is the predecessor model of the antennas which are used in the first stage of the AERA setup which we will discuss in the next section.

The MAXIMA setup was initiated as self-triggered enhancement to the scintillator triggered setup already located at the BLS. The challenge to a self-triggered setup is to discriminate the air shower emission from background sources of pulsed signals. The site near the BLS here turned out to be non-optimal due to the close proximity of a high voltage power line. The trigger strategy was changed for the MAXIMA setup equipping each detector station with an individual scintillator particle detector to provide a trigger to the read out. Moreover, the detector is currently operated with a high speed optical network and serves as a testbed for electronics which are to be installed in the AERA setup.

(a)

(b)
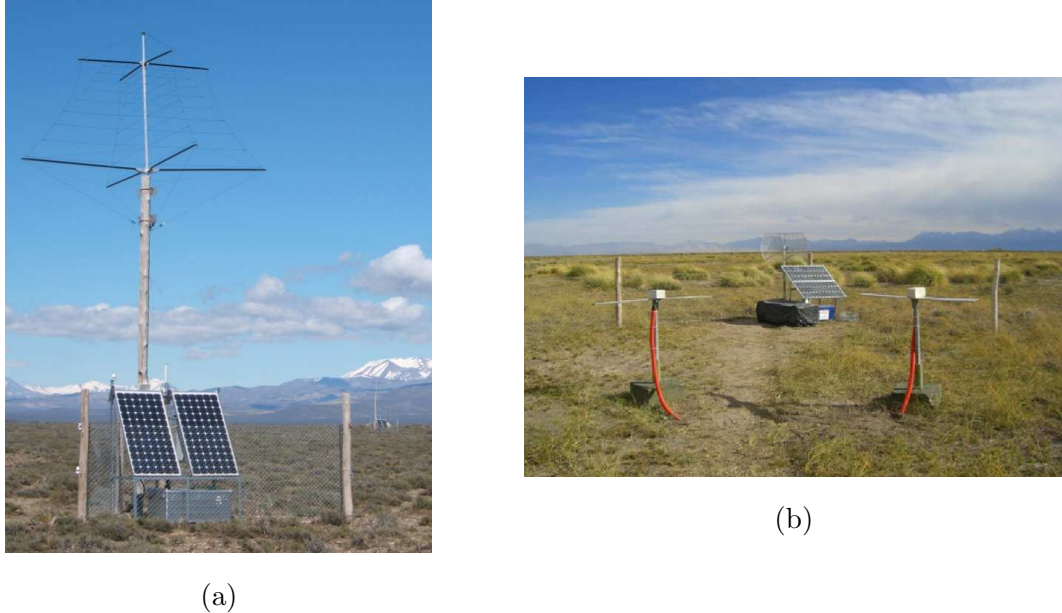
Figure 5.3: (a) A radio detector station from the MAXIMA setup at the BLS equipped with a Black Spider LPDA. (b) A radio detector station with fat dipole antennas at the RAuger setup close to the central laser facility. From Ref. [63].

Up to August 2011 MAXIMA recorded 321 air shower signals in coincidence with the SD [114]. Detailed studies investigating the polarization of the radio signal are currently being performed using this data set [115].

5.2.2 RAuger

The setup of the RAuger detector at the CRS started as well in 2006. The RAuger detector stations were directly realized as autonomous radio detector stations with solar power and wireless communication system. The three RAuger stations form a triangle with a base length of 140 m surrounding the additional SD station at the site. A RAuger station equipped with fat dipole antennas of the CODALEMA experiment [68] can be seen in Fig. 5.3 (b). The fat dipole antennas have been replaced in the meantime with a bowtie antenna which we will treat in a comparison of radio antennas in Sec. 11.1.

The RAuger setup is operated as self-triggered radio detector with a simple threshold trigger to pulsed signals. Using a trigger band from 50 to 70 MHz, RAuger succeeded for the first time to detect a radio signal from an air shower in coincidence with an surface detector array without the help of additional particle detectors components [116]. The waveform of this radio event in the full recorded bandwidth from 100 kHz to 100 MHz is shown in Fig. 5.4.

Up to March 2011 the RAuger setup recorded more than 100 self-triggered events in coincidence with the SD [63, 108]. We have discussed a subsample of these events in Fig. 3.4 (right) highlighting the importance of the magnetic field to the radio emission process.
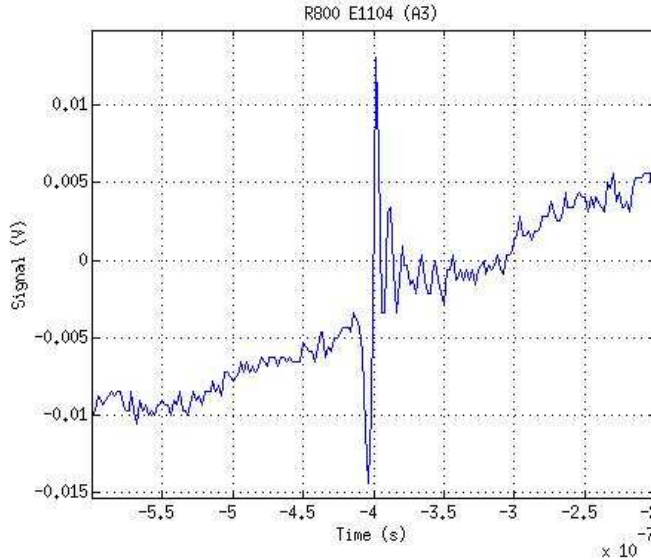
Figure 5.4: Radio signal from the first air shower that was identified in a self-triggered radio detector setup. The signal is recorded in an East-West oriented antenna with a sampling rate of 500 MHz using the full bandwidth of the detector from 100 kHz to 100 MHz. The shift in the baseline is due the presence of an AM band transmitter at 800 kHz. Major signal contributions occur within a few 10 ns of the trace constituting two major oscillations. The y-axis yields an internal voltage measure of the detector system. Taken from Ref. [116]

With experience gained in the pioneering radio detection setups the MHz efforts converged in the current installation of the Auger Engineering Radio Array.

5.3 The Auger Engineering Radio Array

The Auger Engineering Radio Array (AERA) is a diversified approach towards realizing the radio detection technique with respect to a large scale cosmic ray detector. AERA will include the realization of a 20 km^2 detector array with 161 autonomously operating radio detector stations.

AERA addresses four major science goals:

1. Examine the details of the radio-emission process.

2. Explore the potential of the radio-detection technique.

3. Realize the combined detection of individual air showers with all three detector components of the Pierre Auger Observatory, surface -, fluorescence- and radio detector.

4. Probe the nature of cosmic rays for energies up to 10^{19} eV with a novel and independent detector technique.
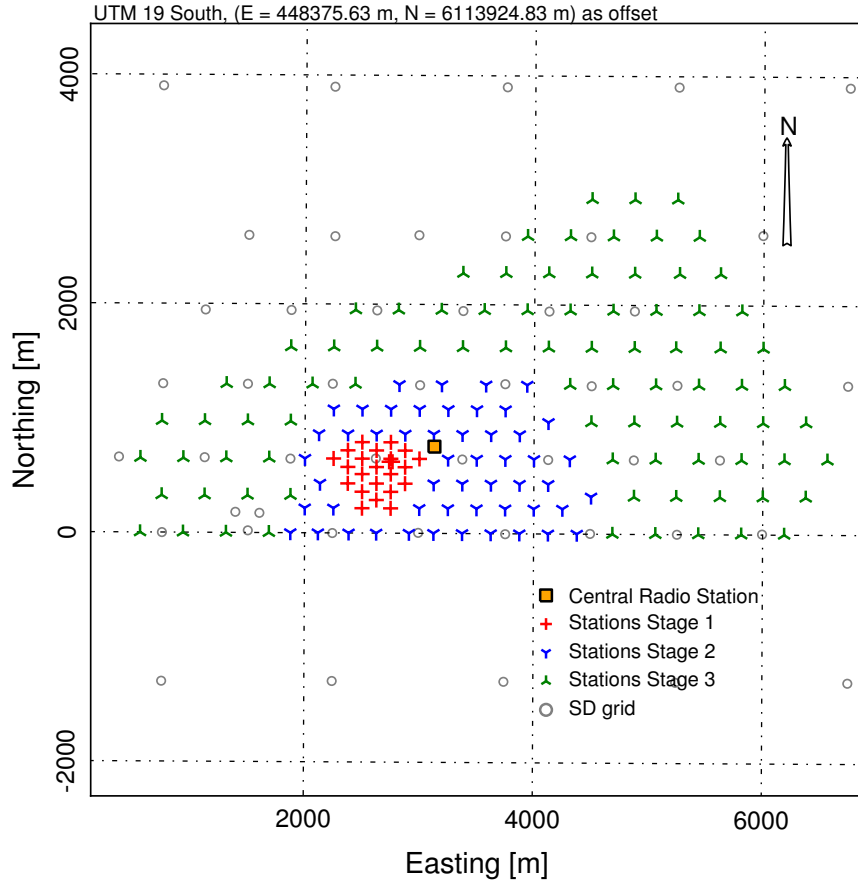
Figure 5.5: Overview of the layout of the Auger Engineering Radio Array. The extension of the fully equipped array is ∼ 6 km in East-West and ∼ 3 km in North-South. See text for details.

AERA is placed within the north-western part of the SD (see Fig. 4.1). The array is co-located with Auger low energy enhancements AMIGA and Heat described in Sec. 4.3. The core of AERA is located 5.6 km east in the line of sight of the fluorescence-detector site Coihueco. The location of AERA is chosen to allow for a maximum number of events to be detected in coincidence with the other detectors.

The layout of AERA is depicted in Fig. 5.5. Its grid of 161 radio detector stations (RDSs) features three different spacings. A dense core is formed by 22 stations in a distance of 150 m. At one of the positions of the dense core two additional RDSs are deployed forming a triangle with a base line of 30 m. This triplet station allows to study fluctuations of the radio signal on small scales. The dense core is surrounded by 52 stations with a pitch of 250 m. Beyond this medium density, AERA will reach its final extent with 85 RDSs with a spacing of 375 m. The graded layout of AERA is chosen to maximize the number of recorded events over a wide energy range from roughly 10^{17} to 10^{19} eV.

Figure 5.6: A radio-detector station installed at the AERA site. Visible is the 'Small Black Spider' LPDA, the GPS antenna and the solar panels above the electronics box.

The three different spacings of the RDSs reflect three stages of installation of AERA. The dense core is the first step towards the installation of the complete array. 21 of its 22 detector stations are operating since Sep. 2010 and we will analyze its data in Sec. 10.

The extent of AERA as well as the amount of individual detector stations do not allow for the RDSs to have a cabled connection to a central data acquisition in the final setup. The data recorded by the stations need to be transferred with a wireless network connection. The amount of data that can be transfered from the RDSs to the central data acquisition is hence significantly limited in comparison to an analog transfer of data with coaxial cables as it is realized in LOPES and CODALEMA (cf. Sec. 3.1.3). The remote radio observation imposes tight constraints on the used hard- and software setup. In first stage of AERA the 24 RDSs are connected with a high-speed optical fiber network to the central data acquisition as an intermediate step towards the realization of a fully wireless setup.

5.3.1 The Radio Detector Station

The continuous radio signal is digitized directly at each RDS and the data that is transferred is constrained to probable air shower signals. As the need of a non-cabled setup also applies to the power supply, the RDSs are operated as autonomous detector stations using solar panels which limits the power consumption of the used hardware. In Fig. 5.6 a picture of a RDS installed at the AERA site is visible.

The initial timing of the recorded radio signal is provided by a GPS system and an internal clock with a precision of ~ 5 ns. A high timing resolution of the data

recorded by individual RDSs is mandatory for a precise reconstruction of air-shower parameters. To further improve the resolution a beacon timing system [117] is deployed at the AERA site as well. For the combination of the two methods a timing resolution of 1 ns is envisaged. In Sec .10.2 we will perform an initial timing calibration of the RDSs with a data driven method.

The position of the RDSs were measured with a relative precision of a few centimeters in a dedicated differential GPS survey [118].

The electronics of the RDSs are placed in a shielded box placed in the shadow of the solar panels. As the readout electronics of the RDSs are operated close to the radio antennas special care has to be taken to ensure the electromagnetic compatibility of the setup. For first stage of AERA a double shielded electronics box is used that was developed dedicatedly for the radio detection of air shower in the course of the CODALEMA experiment. Also the individual hardware components are sealed. Measurements have been performed in an EMC chamber with a running RDS supplied by its photovoltaic power system [119]. The electronics of the stations show negligible contributions to the radio spectrum in the sensitive frequency range.

The RDSs in the first stage of AERA are equipped with logarithmic periodic dipole antennas (LPDAs). The current version called 'Small Black Spider' realizes the LPDA principle as wire antenna. It integrates two independent antenna planes in the same mechanical structure which allows to detect two perpendicular polarization directions of radio signals at the same position. The antenna is designed to be sensitive from 30 - 80 MHz. A detailed description of the antenna including its alignment at the RDSs and calibration measurements is given in Sec. 7.

5.3.2 The Central Radio Station

The central radio station (CRS) houses the central data acquisition of AERA. As visible in Fig. 5.7, a 12 m long sea container has been adapted to the needs of AERA. The CRS operates autonomously using a photovoltaic system with 39 m^2 of solar panels that is designed to supply a power of 460 W for the data acquisition and media converters continuously. The CRS shelters a workshop which allows for flexible setup and maintenance of AERA.

5.3.3 Data Processing

The efficient processing and communication of the data observed at the individual RDSs is crucial for the realization of a large-scale radio-detector array. AERA addresses this challenge with a multi-level approach including dedicated hardware and software solutions [120].

The RDSs of the first stage of AERA read out the two polarization directions of the attached radio antenna using 12 bit ADCs with a sampling rate of 200 MHz. Prior to the digitizer the analog signal is amplified with a low-noise and a main amplifier. For each polarization direction the digitizer extracts a raw data stream and a trigger data stream. The trigger data stream is analyzed by means of an FPGA to derive trigger decisions on air shower candidates. The FPGA processing includes Fourier

Figure 5.7: The central radio station installed at the AERA site. The CRS serves as central data acquisition to the RDSs. Furthermore, electronics placed in the CRS form the high level trigger of the radio detector. 39 m^2 of solar panels allow an autonomous operation of the station.

transforms of the continuous data stream to allow for an application of digital filters prior to the trigger decision. Sensors to the trigger logic are the number of threshold crossings of a signal and the occurrence of multiple pulses within short periods of time. Trigger decision can derived requiring a pulse in a single polarization direction or requiring an 'and'-condition. In either case 2048 samples of data from each channel are recorded.

In the case of a positive trigger decision the data is saved in a buffer that contains the last 10000 triggered signals. The RDSs broadcast only the time stamps of their individual trigger decisions to the central data acquisition. The DAQ combines these trigger information from different RDSs and their locations in the detector array. It searches for signal patterns that match radio signals which have been recorded by multiple detector stations. Only if this second-level trigger is formed the central data acquisition demands the transfer of the full waveform data yet residing in the buffer of the participating RDSs. In the current setup RDS trigger rates of up to 500 MHz are observed depending on the occurrence of artificial noise sources. The data for the RDSs needs hence to be requested by the DAQ within 20 seconds.

With a view to the second setup phase of AERA, an advanced version of the digitizer is currently being integrated into the AERA setup. The new digitizer includes additional sensors to the shape of the waveform of the incoming signal and hence promises a further increase in purity and efficiency in the detection of air showers. The digitizer includes a large ring buffer to store the digitized radio data stream for several seconds continuously. In this way also data from RDSs can be readout that did not contribute with an own trigger decision to an air shower event.

Whereas in stage 1 the 24 RDSs are connected with a high-speed optical fiber cable to the central data acquisition a dedicated deterministic wireless system is being developed for AERA to guarantee a high data throughput in combination with high reliability of the response time in the future setup. The latest commercial versions of wireless networks are being discussed.
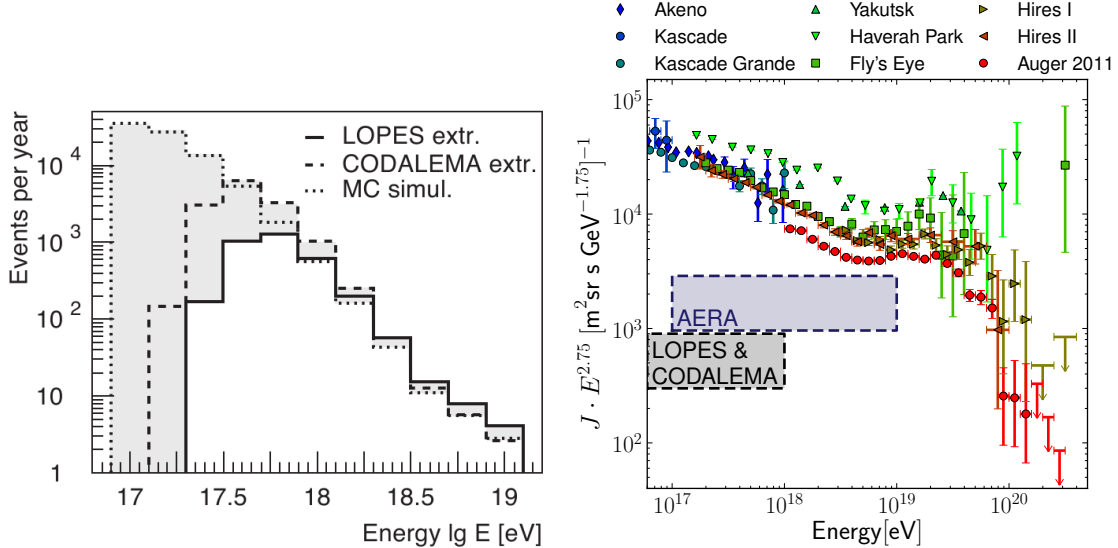
Figure 5.8: Left: Expected number of event recorded per year with the fully equipped AERA detector. Taken from Ref. [123]. Right: The cosmic ray flux spectrum at the highest energies multiplied with $E^{2.75}$ to stress features of the spectral index. AERA will enhance the energy accessible to radio techniques by about one order of magnitude in comparison to the highest energies reached by other recent radio experiments [9, 124]. For reference to the data see Fig. 2.1.

5.3.4 Calibration and Monitoring

The effective operation of AERA with a multitude of RDSs over several years with high data quality and minimized need for maintenance demands a precise knowledge of the status of each part of the used equipment. This includes i.e. the status of the different photovoltaic systems but also parameters of the data processing such as trigger rates and performance of the electronics. The AERA electronics thus include sensors for these parameters.

As local weather conditions might affect the reception and generation of radio signals, a weather monitoring system is installed at the CRS. Of special interest is here the monitoring of the static electric field of the atmosphere which serves to identify thunderstorms that occur close to the AERA site. In the self-triggered setups described in section 5.2 transient signals from thunderstorms have been observed to trigger the radio-detection setups. Furthermore, the additional electric fields during thunderstorms can affect the generation of the radio pulse and thus influence the signal observed by the setup [121, 122].

5.3.5 Prospects for AERA

To estimate the performance of the fully equipped AERA as visible in Fig. 5.5, calculations have been performed with parameterizations of the radio signal based on observations with LOPES [70] and CODALEMA [125] as well as on basis of radio pulses and detector responses simulated with the REAS2 [91] and RDAS [126] softwares. These studies result in an energy-dependent effective area of AERA which

is then multiplied with the flux of cosmic rays as measured with the Pierre Auger Observatory. For energies lower than $10^{18.45}$ eV the measured cosmic-ray flux is extrapolated assuming a spectral index of $\gamma = -3.3$. In Fig. 5.8 (left) the resulting spectra integrated for one year of operation of AERA and zenith angles $\theta < 60°$ are displayed [123].

The estimates agree that AERA will record several thousand cosmic rays per year between 10^{17} and 10^{19} eV. The main difference between the predictions is the lower energy threshold where AERA starts detecting cosmic rays efficiently. Using an energy range from 10^{17} to 10^{19} eV the cosmic-ray flux accessible for AERA is depicted in Fig. 5.8 (right) in comparison to measurements of other experiments observing cosmic rays with established techniques. AERA will observe cosmic rays at energies around the 'ankle' where the sources of cosmic rays are expected to change from galactic to extra galactic (cf. Sec. 2.4).

6. Antenna Theory

To perform a calibrated measurement of the radio emission from cosmic ray induced air showers the impact of the detector and especially of the antenna needs be unfolded from the recorded signals.

The goal of this section is to introduce theoretical aspects of ultra-wideband antennas needed to describe the interrelation between the measured voltage $V(t)$ as response to an incident electric field $\vec{E}(t)$. Here, we aim to unify the calculations for a broad spectrum of antennas including the antenna types which we will describe in Sec. 11.1. Having identified the relevant quantities, a closer evaluation of these antenna models will take place in the later chapters of this thesis.

6.1   Vector Effective Length

For antenna calculations it is convenient to choose a spherical coordinate system with the antenna in its center as depicted in Fig. 6.1. In this coordinate system the electric field of a plane wave that arrives from a given direction (θ, ϕ) at the antenna will be contained in the plane spanned by the unity vectors $\vec{e}_\theta$ and $\vec{e}_\phi$ only. The electric field can be written as a two-component vector and is called instantaneous electric field. Its two components denote two independent polarization directions which vary as a function of time:

$$\vec{E}(t) = \vec{e}_\theta\, E_\theta(t) + \vec{e}_\phi\, E_\phi(t) \quad . \tag{6.1}$$

The mapping between the voltage response $V(t)$ and the electric field $\vec{E}(t)$ is represented by the vector effective length (VEL) $\vec{H}(t)$ of the antenna [127]. As displayed in Fig. 6.1 the VEL is a two-component vector in the antenna-based coordinate system as well:

$$\vec{H}(t) = \vec{e}_\theta\, H_\theta(t) + \vec{e}_\phi\, H_\phi(t) \quad . \tag{6.2}$$

Here, $H_\theta(t)$ encodes the response characteristics of the antenna to the component of the incident field in $\vec{e}_\theta$ direction and $H_\phi(t)$ accordingly. The VEL contains the full information on the response of an arbitrary antenna structure to an arbitrary plane wave signal.

The antenna response is realized as superposition of the response voltages to the two independent polarizations of the field [128]:

$$V(t) = V_\theta(t) + V_\phi(t) \quad , \tag{6.3}$$
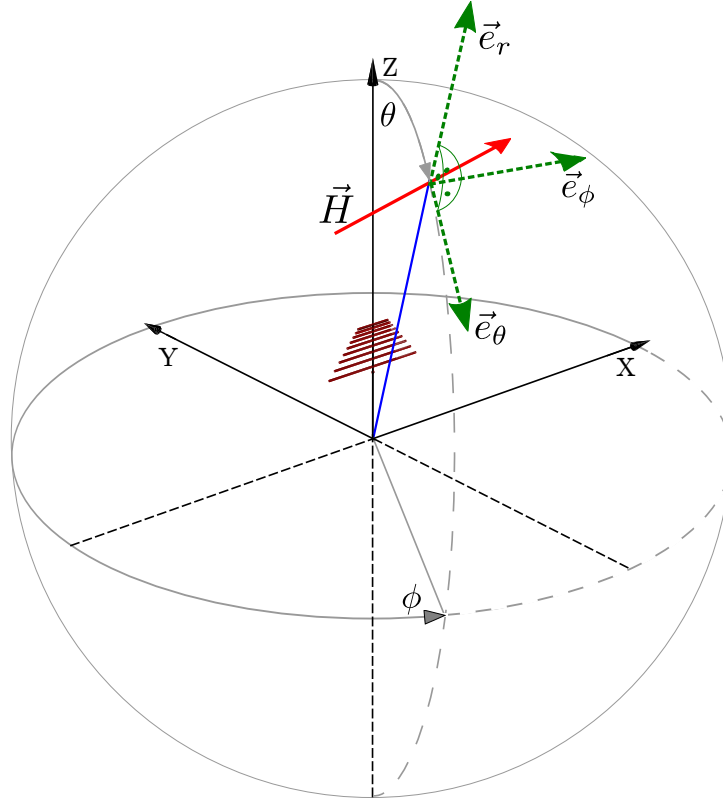
Figure 6.1: The spherical coordinate system with the antenna structure in the center. Depicted is a logarithmic periodic antenna structure. The zenith angle θ is counted from the top, the azimuth angle ϕ counterclockwise from the x-axis of the coordinate system. A specific direction (θ, ϕ) is considered as incoming direction of a signal. The vector of the effective antenna length $\vec{H}$ for the specified direction is given. $\vec{H}$ as well as the vector of the electric field (not depicted) are contained in the plane spanned by the unity vectors $\vec{e}_\theta$ and $\vec{e}_\phi$.

where the individual induced voltages are the convolution of the respective field polarization and the corresponding component of the VEL:

$$V(t) = H_\theta(t) * E_\theta(t) + H_\phi(t) * E_\phi(t) \quad , \tag{6.4}$$

where the symbol '$*$' marks the convolution transform:

$$(H_k * E_k)(t) = \int\limits_{-\infty}^{\infty} H_k(\tau)\, E_k(t - \tau)\, d\tau \quad , k = \theta, \phi\,. \tag{6.5}$$

Using the eqns. 6.1 and 6.2 we write conveniently:

$$V(t) = \vec{H}(t) * \vec{E}(t) \quad . \tag{6.6}$$

Up to now we have treated the antenna response calculation in the time domain. However, the antenna characteristics contained in $\vec{H}(t)$ are usually accessed in the

frequency rather than the time domain. We define the Fourier transforms of the quantities by:

$$\mathcal{V}(\omega) \equiv \mathcal{F}(V(t)) \tag{6.7}$$

$$\vec{\mathcal{H}}(\omega) \equiv \vec{e}_\theta\,\mathcal{F}(H_\theta(t)) + \vec{e}_\phi\,\mathcal{F}(H_\phi(t)) \tag{6.8}$$

$$\vec{\mathcal{E}}(\omega) \equiv \vec{e}_\theta\,\mathcal{F}(E_\theta(t)) + \vec{e}_\phi\,\mathcal{F}(E_\phi(t)) \quad, \tag{6.9}$$

where $\omega = 2\,\pi\,\nu$ is the angular frequency corresponding to the frequency ν.

The Fourier transform of the response voltage can be rewritten with the convolution stated in Eqn. 6.4 and using the linearity of the Fourier transform:

$$\mathcal{V}(\omega) = \mathcal{F}(V(t)) \tag{6.10}$$

$$= \mathcal{F}(H_\theta(t) * E_\theta(t) + H_\phi(t) * E_\phi(t)) \tag{6.11}$$

$$= \mathcal{F}(H_\theta(t) * E_\theta(t)) + \mathcal{F}(H_\phi(t) * E_\phi(t)) \tag{6.12}$$

The convolution theorem allows to perform the convolution of functions as point wise multiplication of their Fourier transforms:

$$\mathcal{V}(\omega) = \mathcal{F}(H_\theta(t))\,\mathcal{F}(E_\theta(t))$$
$$+ \mathcal{F}(H_\phi(t))\,\mathcal{F}(E_\phi(t)) \tag{6.13}$$

$$= \underbrace{\mathcal{H}_\theta(\omega)\,\mathcal{E}_\theta(\omega)}_{\mathcal{V}_\theta} + \underbrace{\mathcal{H}_\phi(\omega)\,\mathcal{E}_\phi(\omega)}_{\mathcal{V}_\phi} \tag{6.14}$$

$$= \vec{\mathcal{H}}(\omega) \cdot \vec{\mathcal{E}}(\omega) \quad. \tag{6.15}$$

The voltage response in the time domain follows from the inverse Fourier transform $V(t) = \mathcal{F}^{-1}(\mathcal{V}(\omega))$. It should be noted that Eqn. 6.15 represents a condensed way to calculate the antenna response to arbitrary waveforms.

6.2 Polarization

In Fig. 6.1 the antenna-based spherical coordinate system along with an exemplary antenna structure is shown. The pictured vector $\vec{H}$ can either be understood as the VEL at a certain point in time $\vec{H}(t = t_i)$, or at a given frequency $\vec{\mathcal{H}}(\omega = \omega_j)$. In the latter case the components of $\vec{\mathcal{H}}$ are complex functions:

$$\vec{\mathcal{H}} = \vec{e}_\theta\,\mathcal{H}_\theta + \vec{e}_\phi\,\mathcal{H}_\phi \tag{6.16}$$

$$= \vec{e}_\theta\,|\mathcal{H}_\theta|\,e^{i\varphi_{\mathcal{H}_\theta}} + \vec{e}_\phi\,|\mathcal{H}_\phi|\,e^{i\varphi_{\mathcal{H}_\phi}} \quad. \tag{6.17}$$

At a specific frequency the VEL in Eqn. 6.16 resembles a Jones vector [129] which is commonly used to describe the polarization of light. Of special interest is the phase difference between the two components:

$$\Delta\varphi_{\mathcal{H}} = \varphi_{\mathcal{H}_\phi} - \varphi_{\mathcal{H}_\theta}. \tag{6.18}$$

Using this phase difference we separate Eqn. 6.17 into a global and a relative phase:

$$\vec{\mathcal{H}} = e^{i\varphi_{\mathcal{H}_\theta}}\,(\vec{e}_\theta\,|\mathcal{H}_\theta| + \vec{e}_\phi\,|\mathcal{H}_\phi|\,e^{i\Delta\varphi_{\mathcal{H}}}) \quad. \tag{6.19}$$
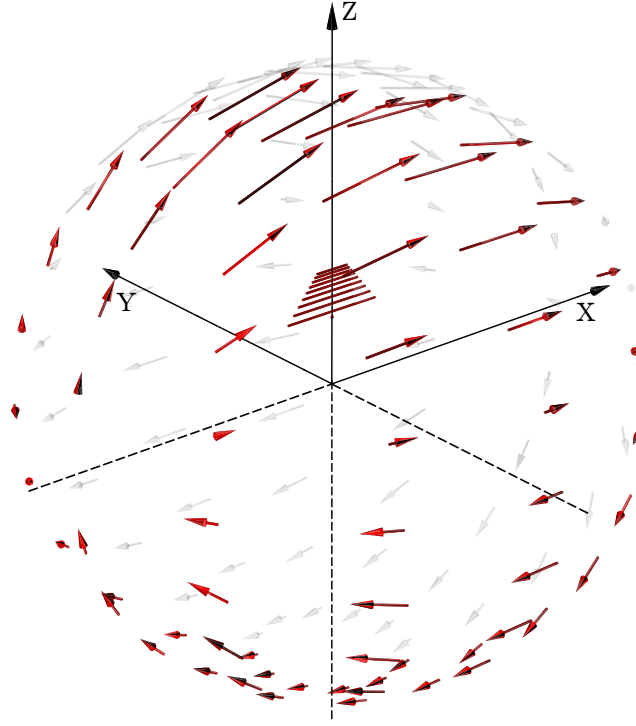
Figure 6.2: The VEL in the case of the depicted logarithmic periodic dipole structure from simulations at 75 MHz. For a single frequency the VEL can be expressed as a vector field in the spherical coordinate system of the antenna.

If the phase difference $\Delta\varphi_{\mathcal{H}}$ at a given frequency ω is a multiple of π

$$\Delta\varphi_{\mathcal{H}} = n\pi, \quad n = \dots, -1, 0, 1, \dots \tag{6.20}$$

the maximum sensitivity of the antenna is reached at reception of a linear polarized signal. In this case an intuitive picture of the antenna can be drawn. Following the Jones calculus we rewrite Eqn. 6.19 omitting the global phase:

$$\vec{\mathcal{H}}' = |\vec{\mathcal{H}}| \, (\vec{e}_\theta \, \cos\alpha + \vec{e}_\phi \, \sin\alpha) \quad , \tag{6.21}$$

where

$$\alpha = (-1)^n \arctan(\frac{|\mathcal{H}_\phi|}{|\mathcal{H}_\theta|}) \tag{6.22}$$

denotes the angle of the VEL axis in the $\vec{e}_\theta$-$\vec{e}_\phi$-plane counted counterclockwise from $\vec{e}_\theta$. The VEL $\vec{\mathcal{H}}'$ is pictured in Fig. 6.1 for a single direction on the unit sphere. In Fig. 6.2 $\vec{\mathcal{H}}'$ is displayed for a set of incoming directions.

The displayed characteristics were accessed via simulations for the displayed logarithmic-periodic antenna structure. The length of the vector changes as a function of zenith angle which denotes the directionality of the antenna. The LPDA is most sensitive to the vertical (zenith) direction.

When approaching the x-axis in Fig. 6.2 the VEL vanishes. For the given antenna structure the electric field of a wave incoming along the x-axis will have no components parallel to the dipoles of the antenna and cannot be detected.

For a simple antenna structure as in Fig. 6.2 the VEL is aligned with the projection of the antenna dipole on the unit sphere for a given direction. For every incoming direction the configuration of the electric field and the effective antenna length a configuration exists with no signal detection. This is referred to as polarization mismatch.

For single frequencies the VEL is thus a vector field of 2-dimensional complex vectors in the antenna-based spherical coordinate system. For a given antenna structure the VEL thus has three major dependencies:

$$\vec{\mathcal{H}}(\omega) = \vec{\mathcal{H}}(\omega, \theta, \phi) \quad . \tag{6.23}$$

In the general case of an elliptic polarization the VEL can be presented as ellipse on the unit sphere. However, in the case of the displayed antenna the VEL is a vector. The omission of a global phase in Eqn. 6.21 enables the inspection of the polarization of an antenna at single frequencies. The wideband characteristics of antennas are contained in the development of $\vec{\mathcal{H}}$ as a function of frequency.

6.3 Moving Source of Radiation

In Fig. 3.17 we have demonstrated that the direction of the Poynting vector of an air shower signal changes by few degrees throughout the development of the pulse at the position of the observer. In Fig. 6.2 we have seen that the VEL is a function of the incoming direction of the signal. The VEL hence changes slightly during the transition of the pulse through the antenna. To extend our discussion on this effect we inspect the electric field in the time domain and make use of the identity:

$$\vec{E}(t) = \int_{-\infty}^{\infty} \vec{E}(\tau)\, \delta(\tau - t)\, d\tau \quad , \tag{6.24}$$

where $\delta(t)$ is the Dirac delta function. In Fig. 3.17 at each point in time t an incoming direction (θ, ϕ) of the signal is associated to the incoming direction of the integrand of Eqn. 6.24:

$$(\theta, \phi) = (\theta(t),\, \phi(t)) \quad . \tag{6.25}$$

In Eqn. 6.6 we have calculated the response voltage as convolution of the electric field with the VEL of the antenna:

$$V(t) = \vec{H}(t) * \vec{E}(t) \quad . \tag{6.26}$$

In the appendix A.1 we show that this equation can be rewritten in analogy to Eqn. 6.24 as follows:

$$V(t) = \int_{-\infty}^{\infty} \vec{H}(t,\, \theta(t),\, \phi(t)) * \vec{E}(\tau)\, \delta(\tau - t)\, d\tau \quad , \tag{6.27}$$
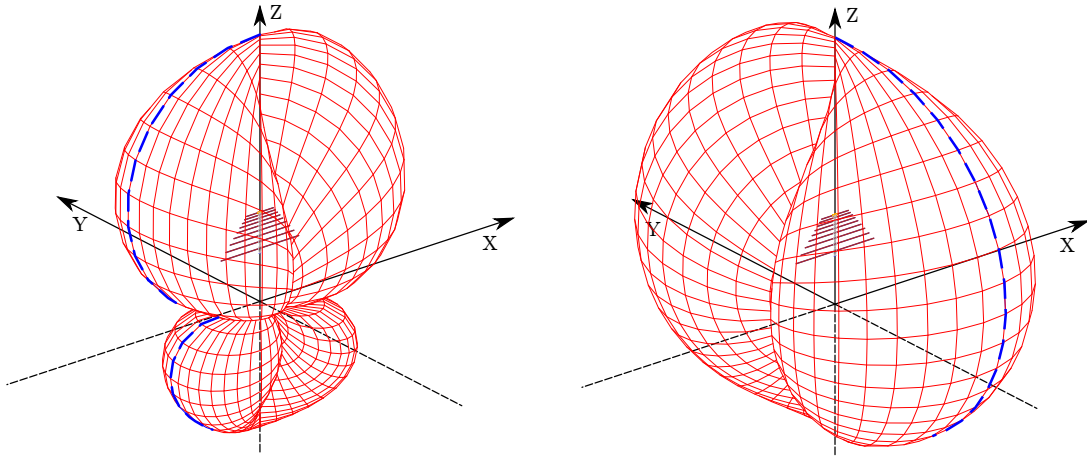
Figure 6.3: Representation of the vector field of the VEL depicted in Fig. 6.2 as the antenna gain. For each incoming direction of a signal the gain is given as the distance between the surface and the center of the coordinate system on a logarithmic scale. Left: The components of $\vec{\mathcal{H}}$ in $\vec{e}_\theta$-direction yield the partial gain G_θ which is sometimes called vertical gain. The dashed blue curve presents a cut in the gain sphere which is referred to as E-field plane gain. Right: The components of $\vec{H}$ in $\vec{e}_\phi$-direction yield the partial gain G_ϕ also referred to as horizontal gain. Here, the blue dashed curve is called H-field plane gain.

which allows to incorporate a moving source of radiation in the calculation. In the appendix A.1 also an exemplary response based on Eqn. 6.27 is calculated. The small angular variation in the pulse development induces only minor changes in the response voltage in comparison to a fixed incoming direction. Currently, Eqn. 6.27 is not used in the reconstruction and simulation of radio signals.

6.4   Vector Effective Length and Gain

In Eqn. 6.15 the VEL allows antenna calculations to be performed on the basis of complex amplitudes. The VEL is related to more commonly used quantities to describe antennas such as the antenna directivity. Directivity is usually based on the discussion of induced signal power. In this section we will summarize the interrelation between the power- and the amplitude-based calculations.

The average intensity of a wave in a single polarization direction S_k with $k = \theta, \phi$ at a specific frequency is given by:

$$S_k = \frac{1}{2}\frac{|\mathcal{E}_k|^2}{Z_0} \quad \text{with} \quad Z_0 \approx 120\,\pi\,\Omega \quad . \tag{6.28}$$

The power that is available to the readout (load) of the antenna is then accessible via the maximum effective aperture $A_{\mathrm{em},k}$ of the antenna:

$$P_{L,k} = A_{\mathrm{em},k}\,S_k \quad . \tag{6.29}$$

In antenna theory [130] the effective aperture is related to the directivity D of the antenna. The directivity for a specific polarization D_k is called partial directivity:

$$A_{\mathrm{em},k} = \frac{\lambda^2}{4\pi} D_k \quad . \tag{6.30}$$

Hence the power that is delivered by the antenna structure is:

$$P_{L,k} = \frac{\lambda^2}{8\pi} D_k \frac{|\mathcal{E}_k|^2}{Z_0} \quad . \tag{6.31}$$

Using Eqn. 6.14 we can introduce the VEL into the power calculation:

$$P_{L,k} = \frac{\lambda^2}{8\pi} D_k \frac{|\mathcal{V}_k|^2/|\mathcal{H}_k|^2}{Z_0} \quad . \tag{6.32}$$

The directivity describes the relative antenna properties to different incoming directions of the signal only. It does not take into account losses inside the antenna structure nor possible mismatches between the antenna and the readout system. The impact of such mismatches will be discussed in Sec. 6.6.1.

The power given in Eqn. 6.32 will only be realized with the condition of conjugate matching. Conjugate matching is discussed in detail in antenna literature as it simplifies the relevant equations and describes an optimal condition for the reception of signals [130]. In this case the power available at the read out is related to the open circuit voltage $\mathcal{V}_{\mathrm{oc}}$ that is induced by the signal over the footpoint impedance Z_A of the antenna:

$$P_{L,k} = \frac{|\mathcal{V}_{\mathrm{oc},k}|^2}{8 Re(Z_A)} \quad . \tag{6.33}$$

The standards in [131] define the VEL to map the electric field to the open circuit voltage. Hence we identify $\mathcal{V}_{\mathrm{oc},k}$ with the partial voltages given in Eqn. 6.14. The combination of Eqn. 6.32 and Eqn. 6.33 then yields the relationship between VEL and the directivity:

$$D_k = \frac{Z_0}{Re(Z_A)} \frac{\pi}{\lambda^2} |\mathcal{H}_k|^2 \quad . \tag{6.34}$$

When accessing the VEL in simulations and measurements usually losses inside the antenna structure e.g. due to ohmic resistance are included. In terms of power these losses are accounted for by multiplying the directivity with a dimensionless efficiency factor ϵ. If losses inside the antenna structure are included in the VEL, Eqn. 6.34 relates to the antenna gain G:

$$G_k = \epsilon\, D_k = \frac{Z_0}{Re(Z_A)} \frac{\pi}{\lambda^2} |\mathcal{H}_k|^2 \quad . \tag{6.35}$$

The treatment of losses inside the antenna structure is important as the loaded loop antenna Salla discussed in Sec. 11.1 explicitly introduces an ohmic resistor into its structure to give a specific shape to its gain.

Although not explicitly stated in the calculations in this section, the gain depends on the incoming direction and the frequency as the VEL:

$$G_k = G_k(\omega, \theta, \phi) \quad . \tag{6.36}$$

It should be noted that here the gain is a real number for each of the two polarization directions. Hence the gain is not sufficient to describe subtle effects such as the polarization dependence of the recorded signal as discussed in Sec. 6.2 or dispersion effects within the antenna structure which invoke a complex phase. To save the concept of a power based calculation, a phase can be introduced in addition to the gain. Polarization mismatch factors can be added to power based antenna calculations as for instance done in the appendix A.8.

In Fig. 6.3 the partial gains corresponding to the $\mathcal{H}_\theta$ (left) and the $\mathcal{H}_\phi$ (right) component of the VEL at a single frequency are displayed. Consequently, the two plots present a subset of the information given in Fig. 6.2. For a specific direction (θ, ϕ) the magnitude of the gain is displayed as the distance from the center of the coordinate system. The gain spheres given in Fig. 6.3 and subsequent cuts through the patterns are more common representation of antenna characteristics. They are helpful when discussing the directional properties of antennas.

6.5 Reconstruction of the Electric Field in Dually Polarized Measurements

In current radio detection experiments at each observing position at least two antennas are installed. In this section we will discuss a major benefit of such dual measurements which is the reconstruction the 3-dimensional electric field vector of the incoming signal.

In the case of the Small Black Spider LPDA uses in AERA (cf. Fig. 5.6) two rotated antennas are realized in the same hardware structure. In typical setups one antenna is rotated by 90° with respect to the other. In principle such setup allows for two independent measurements of the same electric field $\vec{\mathcal{E}}$ with two different VELs $\vec{\mathcal{H}}_1$ and $\vec{\mathcal{H}}_2$. The corresponding vector field of the combined measurement is depicted in Fig. 6.4. It results in two recorded signals that relate as follows:

$$
\begin{aligned}
\mathcal{V}_1(\omega) &= \vec{\mathcal{H}}_1(\omega, \theta, \phi) \cdot \vec{\mathcal{E}}(\omega) \\
&= \mathcal{H}_{1,\theta}(\omega, \theta, \phi)\, \mathcal{E}_\theta(\omega) \\
&\qquad + \mathcal{H}_{1,\phi}(\omega, \theta, \phi)\, \mathcal{E}_\phi(\omega) \\
\mathcal{V}_2(\omega) &= \vec{\mathcal{H}}_2(\omega, \theta, \phi) \cdot \vec{\mathcal{E}}(\omega) \\
&= \mathcal{H}_{2,\theta}(\omega, \theta, \phi)\, \mathcal{E}_\theta(\omega) \\
&\qquad + \mathcal{H}_{2,\phi}(\omega, \theta, \phi)\, \mathcal{E}_\phi(\omega) \quad .
\end{aligned}
$$

$$\tag{6.37}$$
$$\tag{6.38}$$

The system of eqns. 6.37-6.38 can be solved for the two components of the electric field vector. To do so, the antenna characteristics need to be evaluated at the incoming direction of the signal (θ, ϕ) which can for instance be identified by a timing
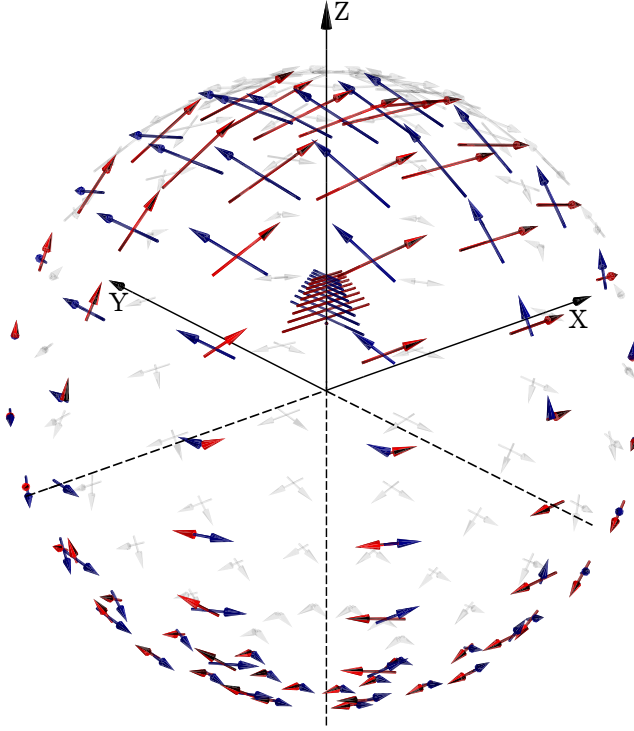
Figure 6.4: Double polarized antenna setup. Due to two independent measurements of the same incident electric field the full vectorial signal information can be reconstructed when the incoming direction of the signal is known.

measurement of the wave front in multiple detector stations. Then the system of eqns. 6.37-6.38 can be solved yielding the full electric field vector:

$$
\mathcal{E}_\theta(\omega) = \frac{\mathcal{V}_1(\omega)\,\mathcal{H}_{2,\phi}(\omega) - \mathcal{V}_2(\omega)\,\mathcal{H}_{1,\phi}(\omega)}{\mathcal{H}_{1,\theta}(\omega)\,\mathcal{H}_{2,\phi}(\omega) - \mathcal{H}_{1,\phi}(\omega)\,\mathcal{H}_{2,\theta}(\omega)} \tag{6.39}
$$

$$
\mathcal{E}_\phi(\omega) = \frac{\mathcal{V}_2(\omega) - \mathcal{H}_{2,\theta}(\omega)\,\mathcal{E}_\theta(\omega)}{\mathcal{H}_{2,\phi}(\omega)} \quad . \tag{6.40}
$$

An implementation of this reconstruction scheme is implemented in the 'Offline' software framework of the Pierre Auger Observatory [132].

At this point the response of the dually polarized measurement setup can be expressed in terms of a matrix calculus when the two measured voltage functions in Eqn. 6.37 are interpreted in terms of a response vector:

$$
\vec{\mathcal{V}}(\omega) = \begin{pmatrix} \mathcal{H}_{1,\theta} & \mathcal{H}_{1,\phi} \\ \mathcal{H}_{2,\theta} & \mathcal{H}_{2,\phi} \end{pmatrix} \cdot \vec{\mathcal{E}}(\omega) \quad . \tag{6.41}
$$

For single frequencies the matrix containing the components of the VEL is referred to as Jones antenna matrix or voltage beam matrix in radio polarimetry [133].
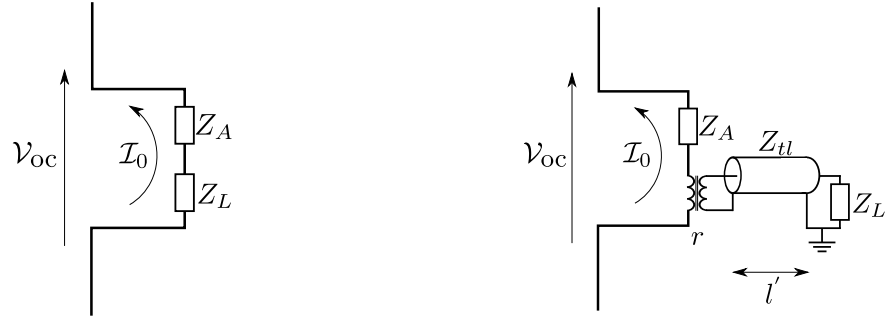
**Figure 6.5:** Left: Thevenin equivalent of an active antenna used for reception. Right: Thevenin equivalent of an antenna used for reception with intermediate transmission line and transmission line transformer.

6.6 Realized Vector Effective Height in a Measurement Setup

In Sec. 6.4 we have used the VEL to relate the incident electric field to the open circuit voltage $\mathcal{V}_{\text{oc}}$ at the antenna terminals. In an actual measurement setup the antenna will be read out at a load impedance. In this section we will focus on the impact of the read out system on the measured signal.

6.6.1 Thevenin Equivalent Antenna Description

In Fig. 6.5 (left) Thevenin equivalent circuit diagram for a simple measurement situation is displayed. The antenna is read out introducing a load resistance Z_L in addition to the antenna impedance Z_A. The voltage measured over the load impedance follows from the voltage divider relation:

$$\mathcal{V}_L = \frac{Z_L}{Z_A + Z_L}\mathcal{V}_{\text{oc}} \equiv \rho\,\mathcal{V}_{\text{oc}}\quad. \tag{6.42}$$

The impedances Z_A and Z_L are complex functions of the frequency ω. The situation of conjugate matching referred to in Sec. 6.4 is realized when the readout impedance is the complex conjugate of the antenna impedance $Z_L = Z_A^*$. This is the optimum situation in terms of signal information transferred to the load.

If the complex matching function ρ in Eqn. 6.42 is included in the formulation of the measurement equation 6.15, the VEL is referred to as realized or normalized VEL $\vec{\mathcal{H}}_r$ [134]:

$$\mathcal{V}_L = \rho\,\vec{\mathcal{H}} \cdot \vec{\mathcal{E}} = \vec{\mathcal{H}}_r \cdot \vec{\mathcal{E}}\quad. \tag{6.43}$$

The matching factor ρ as given in Eqn. 6.42 is sufficient to calculate the response voltage in the case of active antennas where the reception elements are directly connected to the input of an amplifier. The Butterfly antenna which will be discussed in Sec. 11.1 realizes this setup. For the other antennas more elaborate diagrams are required.

6.6.2 Transformers for Impedance Matching

The matching function ρ may include more complex setups than the one displayed in Fig. 6.5 (left). In the case of the antennas discussed in Sec. 11.1 the small aperiodic loop antenna Salla includes a transformer to realize a better matching between the antenna impedance Z_A and the impedance of read out amplifier Z_L.

We denote the impedance transformation ratio of the transformer by r. In the circuit diagram Fig. 6.5 (left) the load impedance due to the combination of read out impedance and transformer is then $r \cdot Z_L$. Along with impedance transformation the transformer changes the voltage that is delivered to the readout impedance. Here an additional factor $1/\sqrt{r}$ needs to added [135]. Hence, if a transformer is used to optimize matching, the matching factor ρ becomes:

$$\rho = \frac{1}{\sqrt{r}} \frac{r\, Z_L}{Z_A + r Z_L} \quad . \tag{6.44}$$

6.6.3 Intermediate Transmission Lines

The calculations performed in Sec. 6.6.1 and 6.6.2 implicitly assumed that electric distances between the position of the impedances are short in comparison to the wavelength processed. However, the Small Black Spider LPDA uses a transformer to feed the antenna signals into a coaxial cable to the first amplifier. With increasing length of the coaxial cable the direct current approximation becomes invalid and propagation effects have to be taken into account. A circuit diagram for this setup is displayed in Fig. 6.5 (right).

Here the open circuit voltage induces an initial forward traveling voltage $\mathcal{V}_+$ into the transmission line of impedance Z_{tl}. Using the result from Eqn. 6.44 this voltage is:

$$\mathcal{V}_+ = \frac{\sqrt{r}\, Z_{tl}}{Z_A + r\, Z_{tl}} \mathcal{V}_{\mathrm{oc}} \quad . \tag{6.45}$$

Looking at Fig. 6.6 we derive a model for the desired voltage amplitude over the read out impedance $\mathcal{V}_L$. The complex voltage amplitude at the end of the transmission is the initial voltage $\mathcal{V}_+$ multiplied with a propagation factor:

$$\mathcal{V}_+ \left(\text{at } l' \right) = \mathcal{V}_+ \cdot e^{-(i\frac{\omega}{c}+\alpha)l'} \equiv \mathcal{V}_+ \cdot e^{-\gamma l'} \quad , \tag{6.46}$$

where γ is the complex propagation constant and α the attenuation loss per unit electrical length l' of the transmission line. According to the Fresnel coefficients the voltage over the load impedance follows as:

$$\mathcal{V}_{0,L} = \mathcal{V}_+ \cdot e^{-\gamma l'} (1 + \Gamma_L) \quad . \tag{6.47}$$

Here Γ_L is the voltage reflection coefficient:

$$\Gamma_L = \frac{Z_L - Z_{tl}}{Z_L + Z_{tl}} \quad . \tag{6.48}$$
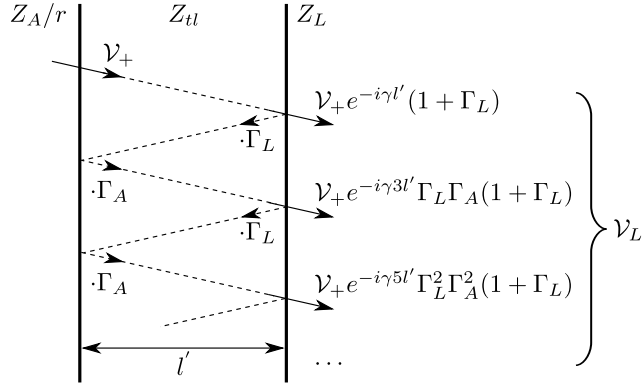
Figure 6.6: Model for multiple reflection between mismatched source and load impedance with intermediate transmission line.

Following Fig. 6.6, part of the amplitude is reflected back towards the antenna. There a further reflection Γ_A occurs at the antenna impedance including the transformer operating with the inverted transformation ratio:

$$\Gamma_A = \frac{Z_A/r - Z_{tl}}{Z_A/r + Z_{tl}} \quad . \tag{6.49}$$

If the scheme in Fig. 6.6 is continued it yields the total voltage over the load impedance $\mathcal{V}_L$ as sum over all amplitudes transferred from the antenna to the load at the end of the transmission line:

$$\mathcal{V}_L = \sum_{n=0}^{\infty} \mathcal{V}_{i,L} \tag{6.50}$$

$$= \mathcal{V}_+ \left(1 + \Gamma_L\right) e^{-\gamma l'} \sum_{n=0}^{\infty} \left(\Gamma_A \, \Gamma_L \, e^{-\gamma 2l'}\right)^n \tag{6.51}$$

$$= \mathcal{V}_+ \left(1 + \Gamma_L\right) e^{-\gamma l'} \frac{e^{\gamma 2l'}}{e^{\gamma 2l'} - \Gamma_A \, \Gamma_L} \tag{6.52}$$

$$= \mathcal{V}_+ \left(1 + \Gamma_L\right) \frac{e^{\gamma l'}}{e^{\gamma 2l'} - \Gamma_A \, \Gamma_L} \quad . \tag{6.53}$$

Eqn. 6.53 enables calculations of multiple signal reflections between read out impedance and antenna as a single step in the frequency domain. The results for the less complex setups are included in Eqn. 6.53 e.g. when the transmission line is short: $l' \to 0$ or the transformer ratio is $r = 1$. An example for the convergence of the model is given in Fig.6.7. Eqn. 6.53 unifies the calculation for all antennas that will be discussed in Sec. 11.1.

In Fig. 6.8 the result for the response $V_L(t) = \mathcal{F}^{-1}(\mathcal{V}_L(\omega))$ to an exemplary open circuit voltage V_{oc} in the time domain is displayed. In this example a setup of
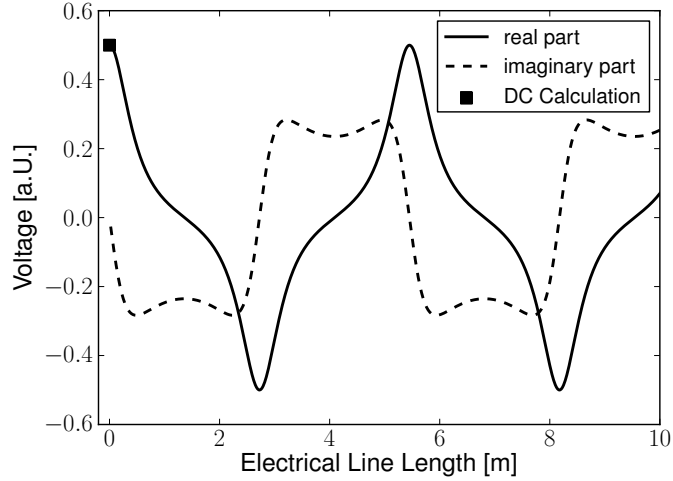
Figure 6.7: The voltage amplitude calculated with Eqn. 6.53 for 55 MHz as a function of the electrical length of the transmission line. For short line length the Bounce model calculation converges to the result of the simplified calculation in Eqn. 6.43.

$Z_A = Z_L = 200\,\Omega$, $Z_{tl} = 50\,\Omega$ and an electrical line length of $l' = 9\,\mathrm{m}$ is chosen. These parameters lead to a reappearance of the pulse at the load due to multiple reflections. As a cross check the result for the corresponding setup realized with the circuit simulator program QUCS [136] is displayed showing excellent agreement.

In the case of the Small Black Spider LPDA the electrical line length is $l' \approx 4.4\,\mathrm{m}$. With respect to the discussion in this section special care was taken during the design of the amplifier impedance to match the $50\,\Omega$ transmission line. Hence Eqn. 6.53 introduces only slight changes to the signal shape in the case of the Small Black Spider LPDA and a time delay due to the length of the transmission line.

In summary we obtain the VEL that will be realized in a measurement setup with the considered antennas by:

$$\vec{\mathcal{H}}_r(\omega, \theta, \phi) = \frac{\sqrt{r}\, Z_{tl}}{Z_A + r\, Z_{tl}} \cdot \frac{(1 + \Gamma_L)\, e^{\gamma l'}}{e^{\gamma 2l'} - \Gamma_A\, \Gamma_L} \cdot \vec{\mathcal{H}}(\omega, \theta, \phi)\,. \tag{6.54}$$

6.7 Signal Amplification

With eqns. 6.15 and 6.54 the incident electrical field is related to the voltage $\mathcal{V}_L$ over the read out impedance of the antenna. For the considered antennas this read out impedance is the input impedance of a low noise amplifier. Amplifiers are characterized by the complex scattering or S-parameters [137]. The S-parameter $S21$ is the ratio of the amplified to the incoming voltage amplitude. It should be noted that the amplification characteristics expressed by $S21$ implicitly assume that the amplifier is operated within a system with the same impedance as during the S-parameter measurement. Looking e.g. at Fig. 6.5 (left) this assumption is not fulfilled: the antenna impedance Z_A replaces the generator impedance used during the S-parameter measurement and may itself be frequency dependent. In the
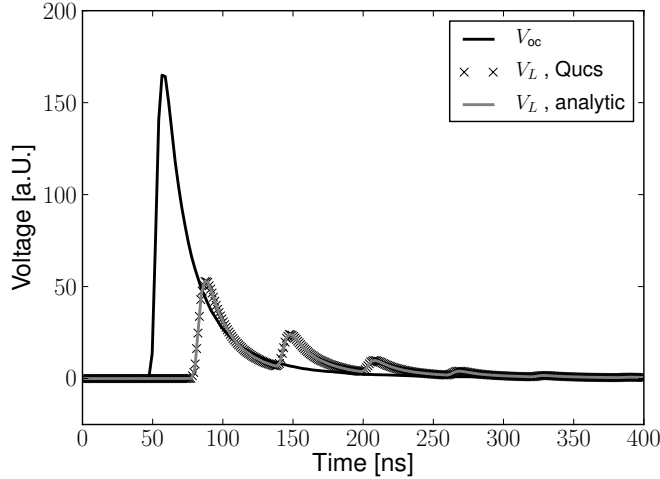
Figure 6.8: Analytic calculation of the voltage V_L over the load impedance as response to an initial voltage pulse V_{OC} for the circuit diagram depicted in Fig. 6.5(right). The calculation is performed with the ansatz presented in Fig. 6.6. The result is compared to the response simulated with the circuit simulator QUCS. Both models agree perfectly on the appearance of multiple reflections.

appendix A.6 we show that in this case a corrected amplification factor $S21'$, the voltage gain, can be used which is normalized to the voltage over the amplifier input impedance $\mathcal{V}_L$ during the S-parameter measurement:

$$S21' = \frac{S21}{1 + S11} \quad . \tag{6.55}$$

Usually $S21'$ relates the voltage at the amplifier to the voltage amplitude fed into a well defined $50\,\Omega$ system:

$$\mathcal{V}_a = S21' \cdot \mathcal{V}_L \quad . \tag{6.56}$$

This amplified voltage is used for further signal processing. $\mathcal{V}_a$ is of special interest as signal to noise ratios are essentially fixed in a read out chain after the first amplification. The realization of an optimum noise performance is not discussed here but will be determined experimentally in Sec. 11.3 for the discussed antennas.

Especially for antennas where the LNA is directly integrated into the antenna structure, e.g. for the Butterfly (cf. 11.1.3), it is useful to define a VEL that includes the amplification of the signal:

$$\vec{\mathcal{H}}_a \equiv S21' \cdot \vec{\mathcal{H}}_r \quad . \tag{6.57}$$

$\vec{\mathcal{H}}_a$ provides convenient access for antenna calibration measurements.

6.8   Simulation of Antennas with NEC-2

The characteristics of an antenna depend on a multitude of parameters. Most prominent is the considered frequency of reception and the geometry of the antenna. Moreover, the proximity of the surrounding has impact, especially the presence of

the ground. Because of this complexity only a limited number of antennas have been evaluated analytically. For an actual antenna design it is preferable to access the antenna characteristics experimentally as we will do in Sec. 7.7.

However, especially the measurement of the directional characteristics of an antenna is an immense experimental effort. For an initial investigation of antenna properties numeric antenna simulations are a useful tool.

An advanced software for the simulations of antennas is the NEC program (Numerical Electromagnetics Code) [138]. Several versions of the NEC program exist, however, the most widely used and distributed version is NEC-2 as it is released as open source code. The NEC-2 version used for our studies is obtained from Linux Debian package management system and is close to the originally published Fortran code [139]. Two examples of recent experiments investigating antenna characteristics on bases of NEC-2 are given with Ref. [140] and Ref. [141].

6.8.1 Electric Field Integral Equation and Method of Moments

The task which we request from NEC-2 is calculation of the response of a metal structure to an incident electric field. This is done by a numeric solution of the electric field integral equation (EFIE):

$$
\vec{\mathcal{E}}(\vec{r}) \;=\; -i\,\omega\,\mu \iiint\limits_{V} \frac{e^{-i\,k\,|\vec{r}-\vec{r}\,'|}}{4\,\pi\,|\vec{r}-\vec{r}\,'|}\,[\vec{J}(\vec{r}\,') + \frac{1}{k^2}\nabla'\nabla'\,\vec{J}(\vec{r}\,')]\,d\vec{r}\,' \tag{6.58}
$$

$$
\;=\; -i\,\omega\,\mu \iiint\limits_{V} \vec{G}(\vec{r},\vec{r}\,')\;\vec{J}(\vec{r}\,')\;d\vec{r}\,' \quad . \tag{6.59}
$$

The EFIE connects the electric field $\vec{\mathcal{E}}(\vec{r})$ to the current density $\vec{J}(\vec{r}\,')$ which will in our case be located in the volume defined by the wires of the antenna structure. Here, $\mu = \mu_0\mu_r$ is the permeability and the terms summarized in $\vec{G}(\vec{r},\vec{r}\,')$ are the dyadic Green's function. For a derivation of the EFIE please refer to the detailed treatment in Ref. [142].

Eqn. 6.59 resembles a generalized problem in the form of:

$$
E = F(I) \tag{6.60}
$$

where E is a known excitation function, F is a linear operator and I is the response function. One technique to solve Eqn. 6.60 for the desired response function is the method of moments (MOM). The MOM requires to approximate the response function as expansion into a sum of N weighted basis functions:

$$
I \approx \sum_{n=0}^{N} a_n\,I_n \quad . \tag{6.61}
$$
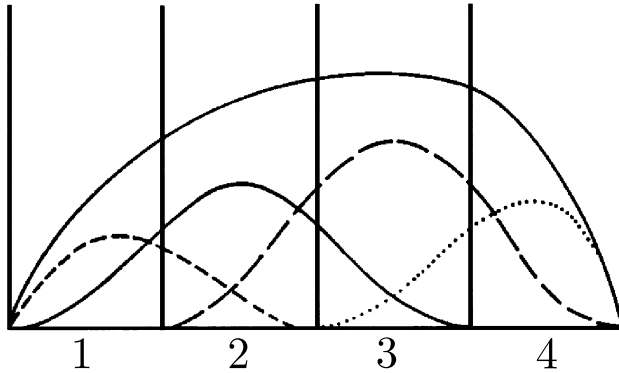
Figure 6.9: Current expansion in NEC-2: The antenna wire is here split into four segments. At each segment we see a current basis function. The overall current results from the superposition of the basis functions originating from the single segments. Taken from Ref. [138].

Each weight a_n is an unknown constant and I_n is a function chosen such that $F(I_n)$ can be calculated conveniently. The linearity of F then allows to write:

$$E \approx \sum_{n=0}^{N} a_n \, F(I_n) \quad . \tag{6.62}$$

In the case of NEC-2 the antenna structure is subdivided into N segments. Each segment serves the MOM to allocate a current with a basis function in the form of:

$$a_n \, I_n = A_n + B_n \sin k(s - s_n) + C_n \cos k(s - s_n) \quad \text{with} \quad |s - s_n| < l_n/2 \tag{6.63}$$

where s is a position along the segment, s_n is the center and l_n the length of the segment.

With respect to Eqn. 6.62 this leads to a function with $3N$ unknown constants. The task for NEC-2 is to calculate the constants which is finally achieved by solving a system of equations that arises from boundary conditions between the segments and to the ends of the wires. The transition between current density and current is done by NEC-2 depending on the geometry of the used structure elements.

In Fig. 6.9 a current expansion on a wire separated into four segments is displayed. A guideline for the segmentation of the structure is that the lengths of the individual segments should not exceed $1/10$ of the considered wavelength. For the upper bandwidth limit of AERA of 80 MHz this results in a maximum segment length of ~ 37 cm.

6.8.2 Access to the Vector Effective Length from NEC-2 simulations

We identify two options how to access the VEL directly using the antenna simulation program NEC-2:

- The first option of NEC-2 is to excite the tested antenna with a plane wave. Here the simulation computes the resulting currents in the receiving antenna and the impedances of the segments which enables the calculation of the response voltage. For each incoming direction the two components of the VEL are accessed as ratio of the response voltage and electric field amplitude by choosing the polarization of the plane wave accordingly (cf. Eqn. 6.14).

- The second option to access the VEL uses the tested antenna as transmitter. With the NEC-2 program it is possible to directly access the far field generated by an antenna at a certain distance R. In antenna theory (e.g. Ref. [130]) it is shown that the vectorial electric field emitted by an antenna is related to the VEL as:

$$\vec{\mathcal{E}}(R) = -i \, Z_0 \, \frac{1}{2 \, \lambda \, R} \, \mathcal{I}_0^t \, \vec{\mathcal{H}} \, e^{-i \, \omega \, R/c} \tag{6.64}$$

where $\mathcal{I}_0^t$ is the current used to operate the antenna. The reciprocity theorem states the equivalence of antenna characteristics obtained from receiving and transmitting measurements. Solving Eqn. 6.64 for the VEL hence yields the desired sensitivity of the antenna to incoming signals. Here should be noted that the electric field $\vec{\mathcal{E}}'$ given by the NEC-2 simulation is normalized to a unit distance of $R = 1$ m:

$$\vec{\mathcal{E}}' = \vec{\mathcal{E}}(R) \, R \, e^{i \, \omega \, R/c} \quad . \tag{6.65}$$

We find that both options yield equivalent results. The illustrations in the figures 6.2, 6.3 and 6.4 are based on simulations of the Small Black Spider antenna with NEC-2.

6.8.3 Signal Reflections on Ground Plane

In most air shower radio detector setups the antenna is installed at a certain height above the ground. This has direct impact on the measured response as the incoming signal is seen twice: First the direct wave induces a response in the antenna structure, then the wave reflected from the ground causes a second signal. The final response is the superposition of these two.

We see two major dependencies that impact the superposition: the path difference of the directed and the reflected wave at the position of the antenna and the duration of the response answer of the antenna to the wave.

If we consider a fast transient signal, the distance between the antenna and the ground induces a delay to the reflected signal. The delay can exceed the duration of the response to the direct wave in the antenna. In this case the reflected wave will be measured separately. A minimal response duration Δt is imposed by the bandwidth of the setup — in the case of AERA:

$$\Delta t \approx \frac{1}{(80 - 30) \, \text{MHz}} = 20 \, \text{ns} \quad . \tag{6.66}$$

For an antenna height below 3 m the field at the position of the antenna will hence always be a superposition of the direct and the reflected wave.
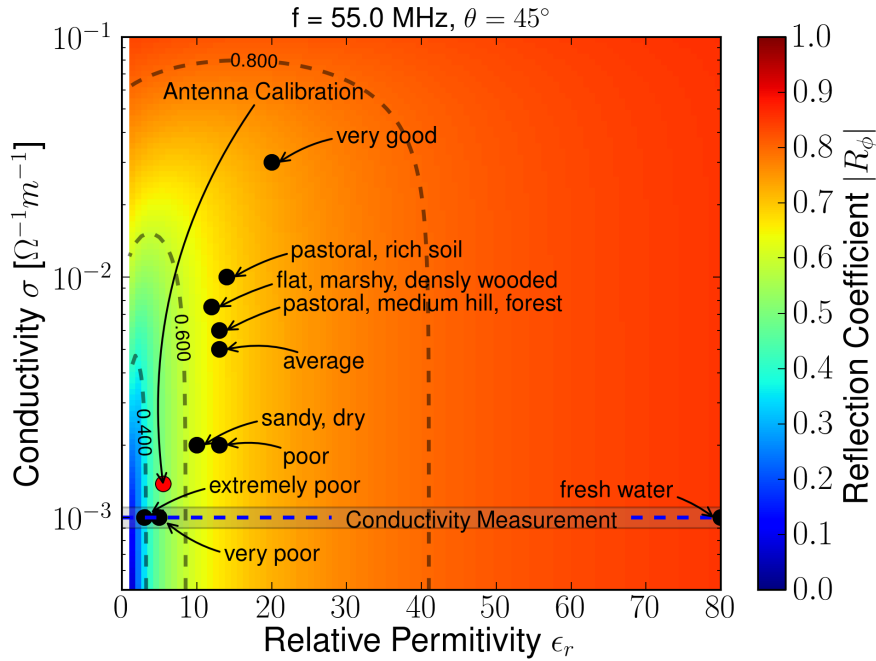
Figure 6.10: The absolute value of the reflection coefficient R_ϕ in the range of typical ground types determined by their conductivity and relative permittivity. The characterization of the points is taken from Ref. [143] and has been cross-checked with recommendations in Ref. [144]. A first measurement of the soil at the AERA site from Ref. [145] is indicated.

To model the impact of a ground plane in the simulation we use the option of the NEC-2 program to calculate the signal reflections on basis of the Fresnel reflection coefficients. In the antenna based coordinate system of Fig. 6.1 we have considered the two field polarizations $\mathcal{E}_\theta$ and $\mathcal{E}_\phi$. The corresponding reflection coefficients are denoted with R_θ and R_ϕ respectively. We constrain our discussion on the R_ϕ coefficient which governs the reflection to all electric field components that are parallel to the ground plane. R_ϕ is given by [138]:

$$R_\phi = \frac{Z_R \cos\theta - \sqrt{1 - Z_R^2 \sin^2\theta}}{Z_R \cos\theta + \sqrt{1 - Z_R^2 \sin^2\theta}} \quad . \tag{6.67}$$

The information about the properties of the ground are contained in the function Z_R which is:

$$Z_R = (\epsilon_r - \frac{i\,\sigma}{\omega\,\epsilon_0})^{-\frac{1}{2}} \quad . \tag{6.68}$$

The reflection coefficient hence depends on the relative permittivity ϵ_r and the conductivity σ of the soil. Further dependencies are the zenith angle θ and the considered frequency $\omega = 2\,\pi\,f$. The reflected electric field is calculated with:

$$\mathcal{E}_\phi^R = R_\phi \cdot \mathcal{E}_\phi \quad . \tag{6.69}$$

In Fig. 6.10 we show the absolute value of R_ϕ as a function of conductivity and relative permittivity. For the display, the center frequency of the AERA of 55 MHz
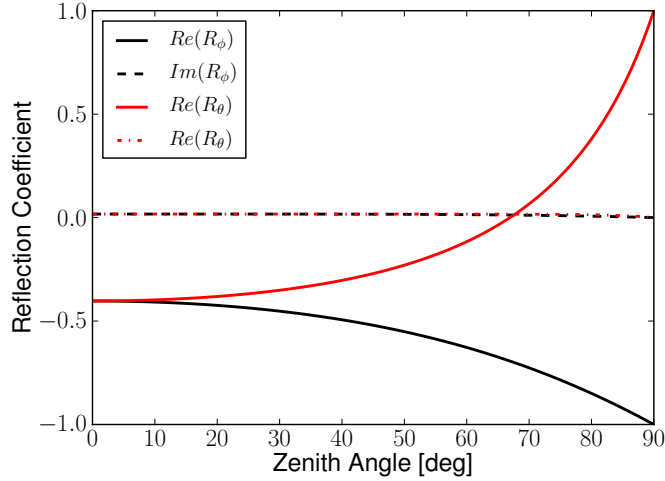
Figure 6.11: Reflection coefficients as a function of zenith angle for 55 MHz. As ground parameters the 'Antenna Calibration' point in Fig. 6.10 is used. Notably, the reflection coefficient for the electric field polarized in $\vec{e}_\phi$-direction approaches -1 for $\theta \to 90°$. The superposition of direct and reflected wave hence cancels for this polarization direction for propagation paths along the horizon. As consequence usually vertically polarized waves (and antennas) are used for communication. The imaginary parts are small but non-vanishing.

and a zenith direction of $\theta = 45°$ has been evaluated. In the vicinity of typical grounds scenarios the reflection amounts to about 60 % of the incoming wave. The conductivity σ spans a wide range of values. With respect to Eqn. 6.68, a change of the frequency within the AERA band from 30 to 80 MHz has only minor influence on the reflection. The behavior for the R_θ coefficient is similar. Depending on the antenna type the reflected wave gives a significant contribution to the detected signal.[1]

Between different types of ground the reflection can change up to several 10 %. Calibration measurement are hence preferably to be performed directly at the detector site.

For a proper simulation setup reasonable values for the conductivity and the relative permittivity need to be chosen as well. A first measurement of the conductivity at the AERA site from Ref. [145] is indicated in Fig. 6.10. Our current choice of ground parameters for antenna simulations is indicated as 'Antenna Calibration'. It is already close to the conductivity indicated by the measurement. A comparison between measured and simulated antenna characteristics will be discussed in Sec. 7.7.4.

The zenith angle dependency of the reflection coefficient is discussed in Fig. 6.11 for both reflection coefficients R_θ and R_ϕ. For incoming directions towards the horizon ($\theta \to 90°$) field components parallel to the ground will be reflected with

---

[1]In Sec. 11.1 different antenna types will be discussed: The 'Butterfly' is explicitly set up to profit from the signal reflection. The 'Salla' antenna avoids the reflected wave by reducing the reception from the bottom direction.
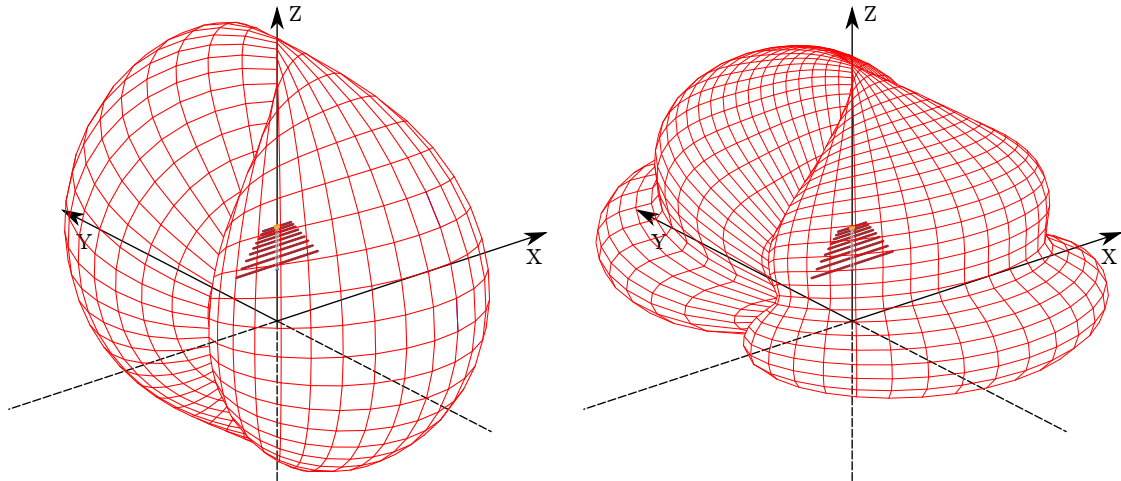
Figure 6.12: Antenna Simulation without ground (left) and including a ground plane (right). For each incoming direction of a signal the directional characteristics are indicated as gain which is represented as the distance between the surface and the center of the coordinate system in a logarithmic scale. Only the partial gain corresponding to the $\mathcal{H}_\phi$ component of the VEL is displayed. The left diagram was already presented in Fig. 6.3. In the right diagram only a ground plane is added in the simulation. The ground plane is defined by the xy-plane of the depicted coordinate system. A frequency of 75 MHz is used for the simulation. The ground causes a vanishing sensitivity for directions towards the xy-plane (horizon) and a side lobe structure that evolves with the zenith angle.

$100\,\%$ including a sign flip of the signal amplitude imposed by the negative reflection coefficient. The path difference between direct and reflected wave vanishes for signal propagation along the horizon when the distance between the source of the radiation and the receiver is large. The negative reflection coefficient therefore leads to a cancellation of the direct and reflected wave — in far field simulations the antenna seems to be insensitive towards the horizon. An exemplary simulation including a ground plane is given in Fig. 6.12.

7. The Small Black Spider LPDA

For the first stage of AERA logarithmic periodic dipole antennas (LPDAs) are used. LPDAs have first been adapted to the needs of radio detection for the LOPES$^{\text{STAR}}$ experiment [146]. The Small Black Spider (SBS) realizes the LPDA principle as wire antenna and is depicted in Fig. 5.6 as installed at AERA.

7.1 The Small Black Spider as Logarithmic Periodic Dipole Antenna

The application of the logarithmic periodic concept to an array of dipoles was proposed in 1960 by D.E. Isbell [147]. Fig. 7.1 shows the principal configuration of a LPDA which is also valid for the SBS.

LPDAs assemble a series of n half wave dipoles of increasing length l_i to keep the radiation resistance of the antenna constant over a wide frequency range. The dipoles are fed into a central wave guide to provide a common readout to the structure. Due to the different lengths l_i each dipole resonates at a different frequency and couples a corresponding wavelength λ_i into the waveguide. To find a single point on the central wave guide that provides stable readout to the full frequency range it is favorable to
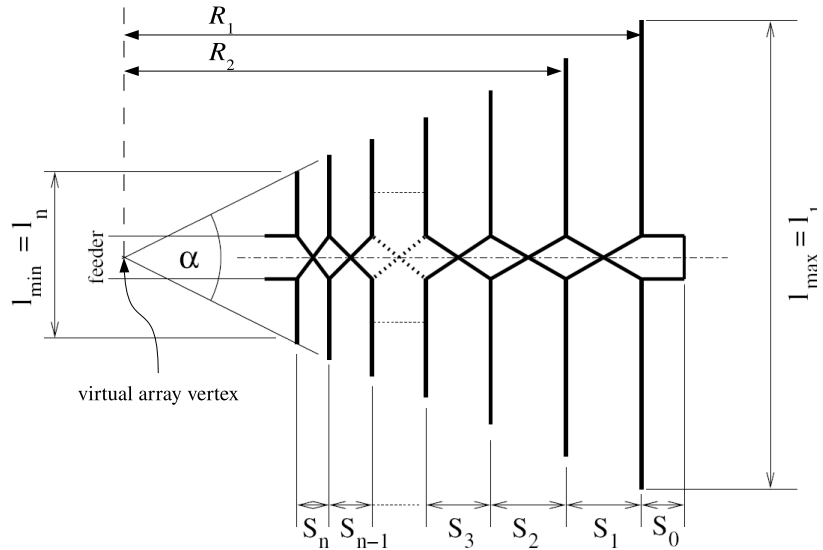

Figure 7.1: Principal configuration of a LPDA. (adapted from [148], based on [149])

choose the dipole positions R_i along the wave guide such that they form a constant ratio with the dipoles' characteristic wavelengths:

$$\frac{\lambda_i}{R_i} = \text{const.}, \qquad i = 1 \dots n \quad . \tag{7.1}$$

Here the distances R_i are measured from the virtual array vertex which is indicated in Fig. 7.1. With respect to the reception of a wideband signal Eqn. 7.1 leads to a constructive interference of the different wavelengths coupled into the waveguide at the virtual array vertex.

For the design of the antenna the demand of Eqn. 7.1 imposes a relationship between consecutive dipoles with:

$$\frac{\lambda_i}{R_i} = \frac{\lambda_{i-1}}{R_{i-1}} \qquad \Rightarrow \qquad \frac{\lambda_i}{\lambda_{i-1}} = \frac{R_i}{R_{i-1}} \equiv \tau \quad . \tag{7.2}$$

Here τ is know as the LPDA's scaling constant. As the wavelength λ_i is proportional to the dipole length l_i, the choice of a scaling constant τ, two initial dimensions R_1 and l_1 and the number of dipoles n fixes the dimensions and locations of all other dipoles:

$$l_i = \tau^{i-1} \, l_1 , \qquad R_i = \tau^{i-1} \, R_1 \qquad \text{for} \quad i = 1 \dots n \quad . \tag{7.3}$$

The antenna is hence periodic in the logarithm of its characteristic dimensions. For the SBS these design parameters are:

$$l_1 \ = \ l_\text{max} \ = \ 4250 \, \text{mm}, \qquad R_1 \ = \ 2584 \, \text{mm}, \qquad \tau = 0.875 \quad . \tag{7.4}$$

The SBS is assembled with $n = 9$ dipoles. This leads to the dimension of the shortest dipole:

$$l_9 \ = \ l_\text{min} \ = \ 1470 \, \text{mm} \quad . \tag{7.5}$$

The lengths of the shortest and longest dipoles indicate the accessible frequency range of the LPDA. A typical estimator for LPDAs applied to the dimension of the SBS yields:

$$f_\text{min} \ \approx \ \frac{c}{2 \cdot l_\text{max}} \ \approx \ 35 \, \text{MHz} \quad \text{and} \quad f_\text{max} \ \approx \ \frac{c}{3 \cdot l_\text{min}} \ \approx \ 68 \, \text{MHz} \quad . \tag{7.6}$$

As we will see in the next sections the actual setup of the Small Black Spider allow to access the full AERA frequency band from 30 to 80 MHz.

7.2   Electrical Setup

From the discussion in Sec. 7.1 the optimum choice for the position of the footpoint where the antenna is read out is the virtual array vertex. In the case of LPDAs that are used for the transmission of signals this location of the footpoint is often realized by extending the series of dipoles towards shorter lengths until the array vertex is reached. The SBS is explicitly set up to limit the accessible frequency range to ~ 80 MHz to suppress the reception of FM band transmitters at higher frequencies. In
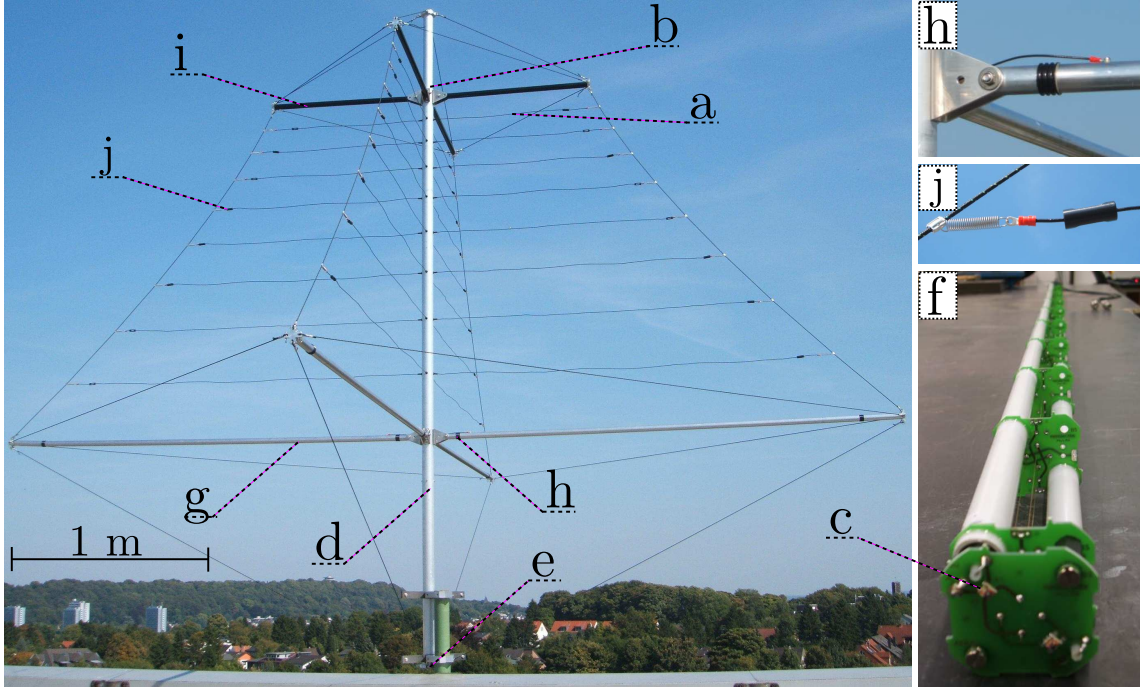
Figure 7.2: Overview of the Small Black Spider LPDA. Please see the text for details.

Fig. 7.2 a detailed overview over the structure of the SBS is given. The log-periodic series of dipoles is stopped after the 9th dipole (a) which provides access to highest desired frequency. Due to practical reasons the footpoint is realized short above the shortest dipole at position (b).

The footpoint of the antenna is the optimum position for a low noise amplifier (LNA). However, the footpoint of the Small Black Spider located in a height of 4.5 m when the antenna is installed in the field. Such a placement of the LNA is not feasible with respect to maintenance. Instead, a matched feed of the footpoint into a 50 Ω coaxial cable is realized with a 4:1 transmission line transformer (TLT) (c). This is possible because of the rather constant antenna impedance Z_a within the frequency range which is displayed in Fig. 7.3 (left).

In the right panel of Fig. 7.3 the antenna impedance is translated into the power reflection coefficient R with respect to the 50 Ω coaxial cable:

$$R = |\frac{Z_a - 50\,\Omega}{Z_a + 50\,\Omega}|^2 \quad .$$

(7.7)

The power reflection coefficient indicates the fraction of received signal power that cannot be transfered to the coaxial cable due to impedance mismatch. Within the bandwidth the SBS couples more than 80 % of the available power into the coaxial cable which guides the signal through the boom of the antenna (d) to the LNA at the bottom of the structure (e).

For the SBS a dedicated LNA has been developed [150]. As visible in Fig. 7.4 (left), also the input impedance of the LNA is set up to match 50 Ω. In this way signal
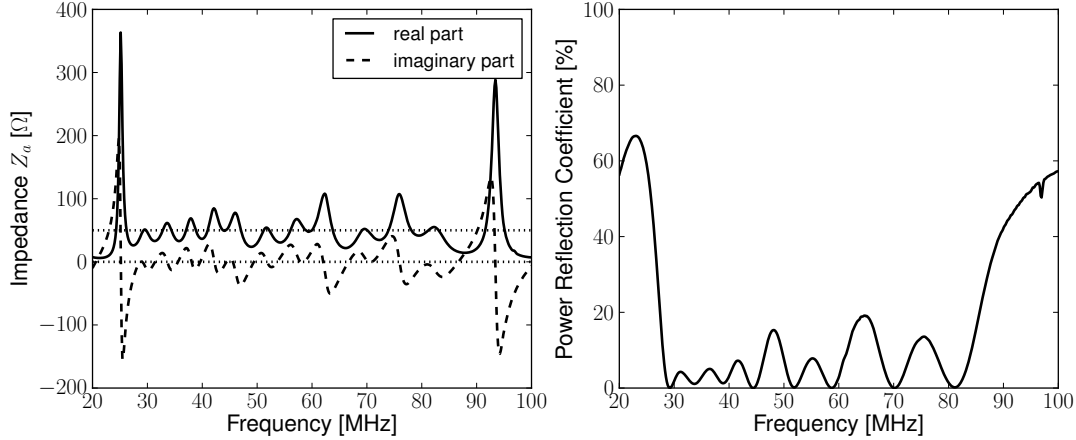
Figure 7.3: Left: The impedance Z_a of the SBS displayed as a function of frequency. Within a bandwidth from ~ 30 to 85 MHz the impedance of the SBS is dominated by a real impedance oscillating around 50 Ω. The bandwidth limitation of the antenna is visible in the large impedance variation outside the bandwidth. Right: The reflection coefficient of the SBS corresponding to its impedance. Small reflection coefficients indicate that the antenna is matched to the read out system.

reflections back into the antenna structure are avoided which have been discussed in Sec. 6.6.3. In Fig. 7.4 (right) the amplification factor of the LNA to the incoming signal power is displayed in a decibel scale[1]. The LNA includes filter elements at its input to further enhance the frequency selectivity of the antenna to the AERA band. Further details of the development of the LNA are presented in Ref. [151].

7.3   Mechanical Setup

The SBS integrates two independent antenna planes in the same mechanical structure which has a dimension of $4.5 \times 4.5 \times 3.5$ m^3 and a weight of 18 kg. The antenna planes feed their signals into two Lecher wave guides. These wave guides are fixed by a common support structure (panel (f) of Fig. 7.2) which is located inside the boom of the antenna. The support structure consists of a series of printed circuit boards and two PVC tubes. Each tube contains one of the coaxial cables which guide from the footpoints at the top to the bottom of the antenna. The printed circuit boards provide the connection of the individual dipoles to the Lecher wave guides. Due to a symmetric arrangement of the two wave guides the crosstalk between the antenna planes is measured to be less than 0.06 % of the received signal power within the bandwidth [152].

---

[1]The decibel scale is commonly used to display amplification and attenuation factors f in electrical engineering. It translates at follows:

$$f_{\mathrm{dB}} = 10 \cdot \log_{10} f_{\mathrm{lin}} \quad . \tag{7.8}$$

Examples:

$$f_{\mathrm{lin}} = 2 \quad \widehat{=} \quad f_{\mathrm{dB}} \approx 3 \quad , \qquad f_{\mathrm{lin}} = 100 \quad \widehat{=} \quad f_{\mathrm{dB}} = 20 \quad . \tag{7.9}$$
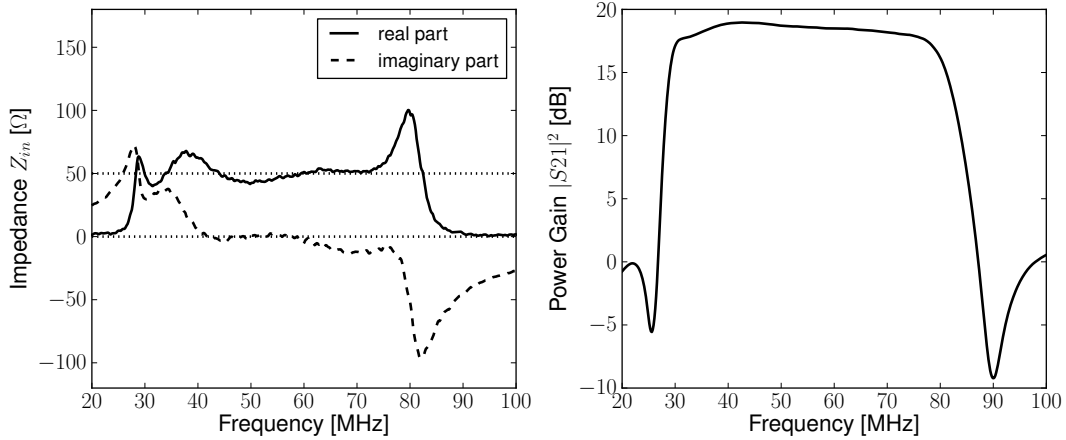
Figure 7.4: Input impedance (left) and power gain (right) of the LNA of the SBS. The input impedance of the LNA closely matches an impedance of 50 Ω in the bandwidth. The LNA features a gain of $\sim$ 18 dB sharply reducing the amplification at the edges of the AERA band from 30 to 80 MHz.

The lowest antenna dipole (g) is realized as a rigid aluminum tube and is used to support the structure of the antenna. As visible in panel (h) this dipole is isolated from the antenna boom and fed into the wave guide using short wires. The rigid dipole has a diameter of 3 cm and enhances the accessible bandwidth towards lower frequencies.

At the top of the antenna the structure is spanned using glass fiber reinforced plastic tubes (i). Dyneema® ropes are used as guy to the structure. The individual dipoles are anchored towards the ropes using isolators and springs (j). The tension of the springs is sufficient to tighten the structure and avoids the need for additional clamping fixtures.

Prior to the installation of the antenna in the field stress tests were performed on subcomponents of the antenna. The tests included temperature tests of the support structure to the Lecher guides to ensure that thermal expansions are within the flexible range of the used materials. The wire dipoles connected to the printed circuit boards of the inner structure were oscillated with a frequency of 2 Hz over a period of one year to simulate the constant movement induced by wind in the Argentinian Pampa. Up now, signs of fatigue were never observed at one of the Small Black Spider antennas.

For transportation purposes the design of the Small Black Spider includes a folding mechanism. The joint of the lower dipole is displayed in panel (h). The folding mechanism allows to assemble the antenna completely in the lab and to make it operational within 15 minutes at the detector site. A picture of 30 Small Black Spider LPDAs folded and prepared for transport to AERA is visible in Fig. 7.5.

Figure 7.5: Preparation of the transport of 30 Small Black Spider antennas to AERA.

7.4   Series Production

In the course of the preparations for the first setup stage of AERA 35 Small Black Spider LPDAs have been produced. In the series production the material costs of a single antenna amount to 250 €. The 35 antennas produced have been distributed as follows:

- 2 antennas are used in Aachen for test measurements,

- 1 antenna is used for test measurements at the Nançay Radio Observatory,

- 1 antenna was used to study the radio background at the South Pole,

- 1 antenna is used for tests of the AERA electronics at the RU Nijmegen,

- 30 antennas have been shipped to the Auger site.

Of the 30 antennas that have been shipped to Auger, 24 SBSs are used to equip the regular stations of AERA stage one. One antenna is placed close to the central radio station as a reference antenna as visible in Fig. 5.7. Two SBSs are installed in the Maxima setup mentioned in Sec. 5.2.1. Three antennas remain as spares.

The reflection coefficients of the 25 SBSs installed at the AERA site are displayed in Fig. 7.6 (left). As each antenna consists of two separate polarization planes 50 measurements are overlapped in the plot. The similarity of the reflection characteristics of the antennas points at an excellent quality of the series production. When we neglect ohmic losses within the antenna structure the radiation efficiency ϵ of the SBS can be obtained as integral over the reflection curves:

$$\epsilon = \int_{\mathrm{bw}} (1 - R(f)) \, df \quad . \tag{7.10}$$
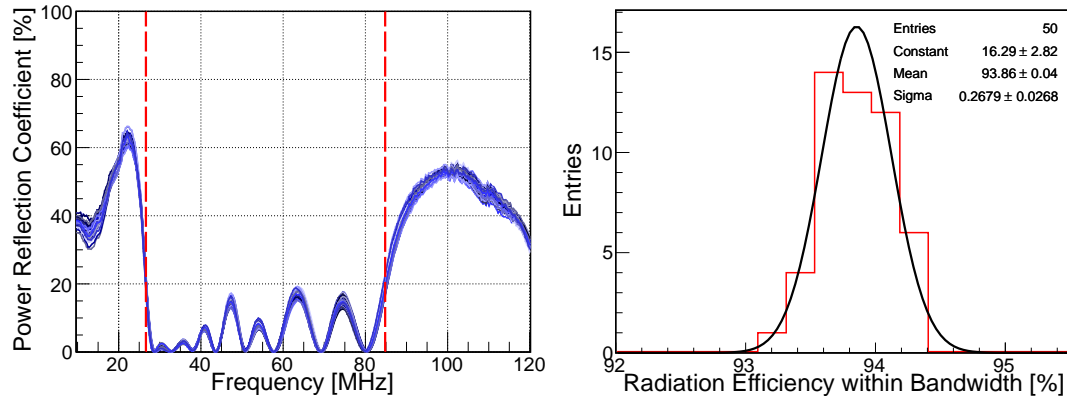
Figure 7.6: Series production quality of the SBS. Left: The reflection coefficients R of the 25 SBSs installed at the AERA site. Each antenna contributes with two independent antenna planes. Right: The radiation efficiency corresponding to the reflection coefficients in the left panel. From Refs. [152, 153].

We define the bandwidth of the SBS with the 20 % reflection points in Fig. 7.6 (left) from 27.2 to 86.1 MHz as indicated with the vertical lines. In Fig. 7.6 (right) the distribution of radiation efficiencies is displayed. The SBS features a radiation efficiency of 93.9 % with a spread of 0.3 % only within the series production.

7.5 Alignment of the Small Black Spider at AERA

The radio detector station of the first setup stage of AERA are located within an area of $\sim 600 \times 750$ m as depicted in Fig. 7.7. For convenience the antenna positions are chosen to be regular within the usual Auger coordinate system of UTM zone 19, southern hemisphere. In this coordinate system the positions are given in 'Easting' and 'Northing'. To deal with more handy numbers, the position of the SD tank 'Rodrigo' at (E = 448375.63 m, N = 6113924.83 m) [154, 123] is subtracted from the values of the positions of the AERA stations. As already stated in [155], lines of constant Easting are not necessarily parallel to the geographic North direction which corresponds to the circles of longitude. In the case of the AERA site the chosen UTM coordinate system deviates by 0.3° eastwards.

7.5.1 Measurement setup

7.5.1.1 Compass

As the magnetic field of the earth is relevant for the emission process of the radio signal we choose to orientate the antennas in the magnetic rather than the geographic North direction. The magnetic North direction is identified with help of the compass displayed in Fig. 7.8. Due to an optical system that is integrated into the body of the compass the device allows to pinpoint the direction of objects with a resolution of 1/3° [156].
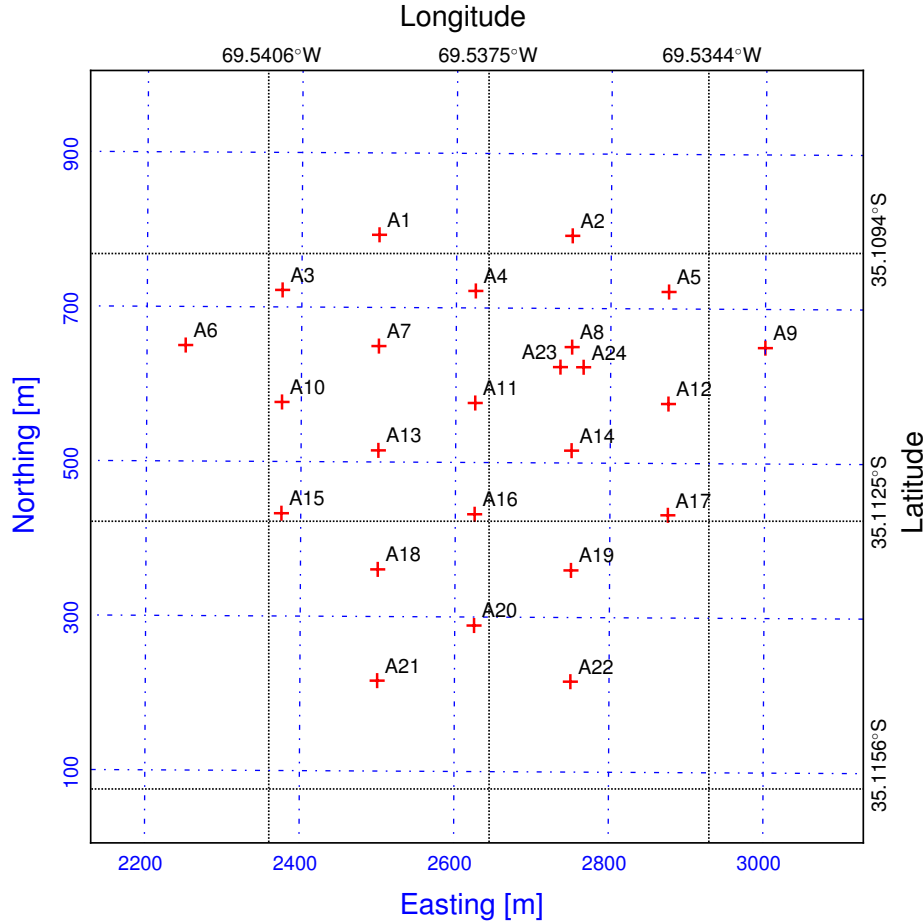
Figure 7.7: Overview of the site of the first phase of AERA. The positions of the detector stations are labeled as red crosses. In blue (-.) a UTM coordinate system with SD tank 'Rodrigo' as offset is indicated. In black (..) latitude and longitude circles are displayed.

7.5.1.2   Mounting Bracket

The direction of the compass has to be carried forward to the direction of the antenna. We define the antenna direction to be the pointing direction of the lower aluminum dipole that is labeled with 'N'. From an electrical point of view, the antenna structure hosts two identical antennas with their polarizations perpendicular to each other. In the following we will discuss only the direction of the antenna plane labeled with 'N'. The direction of the other antenna polarization is then obtained by adding 90° to the direction of the 'N' plane.

As visible in Fig. 7.9 the direction of the compass is carried forward to the direction of the antenna with a mounting bracket especially designed for this purpose. Due to its construction the bracket cannot be twisted in comparison to the dipole it is fixed to. The bracket is attached to the dipole labeled with 'N'. We observe that the metal pipeline tubes used as poles have themselves a magnetic field. To minimize disturbing deflections of this field during the alignment of the antenna to magnetic north, we attach the mounting bracket at the outer end of the lower dipole (Fig.
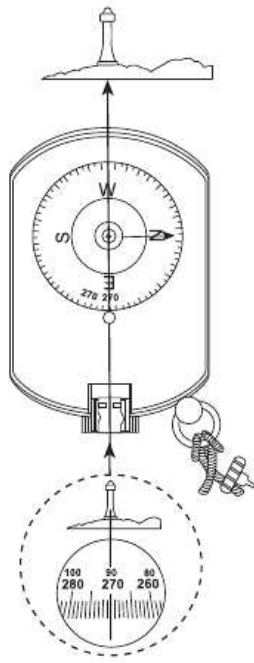
Figure 7.8: The Suunto compass used for the antenna alignment has built in optics which allow to sight direction with a precision of $1/3°$.

Figure 7.9: The compass is mounted on a bracket, especially designed to allow a torsion free fastening parallel to the lowest antenna dipole.

7.9). Furthermore, the position of the mounting bracket is chosen such that the pointing direction of the compass is in one line with the metal pole as shown in Fig. 7.10. If we assume that the horizontal component of the magnetic field of the pole spreads radially, the described mounting of the compass should minimize disturbances induced by the pole.

7.5.2 Antenna Alignment Measurement

With the setup described in Sec. 7.5 each antenna is turned during its installation procedure until the compass indicates the magnetic North direction. This can be done very precisely as the mounting brackets of the antenna itself allow a fine-tuning. The uncertainty of this turning procedure is negligible in comparison to the $1/3°$ mentioned in Sec. 7.5.1.1 as the scale of the compass does not have to be compared with an object in the landscape.

7.5.2.1 Angular Distance to Reference Mountain

After the rotation of the antenna the question remains if the compass is really indicating a direction that is not influenced by additional magnetic fields. To check this we measure for each station the direction towards a reference mountain with the compass being placed at the same position as during the antenna alignment. This azimuth angle is measured regarding the usual Auger conventions counting counterclockwise from East.

Figure 7.10: The compass mounting bracket is attached on the same side of the antenna as the metallic pole the antenna is attached to. In this way the influence of a possible magnetism of the pole is minimized as far as the pointing to the geo-magnetic North direction is concerned.
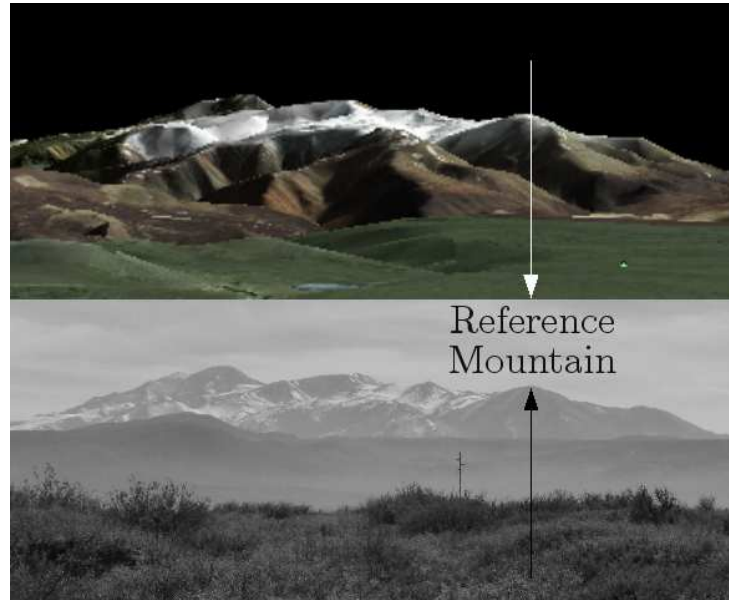

Figure 7.11: The mountain site observed from AERA towards the North direction in comparison to the mountain site visible with Google Earth in the same direction. As helpful reference point a mountain top of the Cerro Potrerillos is chosen.

Reference Mountain

As reference mountain we choose a mountain top which is easy to identify in the field and lies close to the magnetic North direction. A picture of the mountain site north of AERA is visible in the lower part of Fig. 7.11. The mountain that is chosen as reference mountain is part of the 'Cerro Potrerillos' and can also be identified with Google Earth as displayed in the upper part of Fig. 7.11. We find the position of the reference mountain to be at:

$$(\text{Lat,Lon})_{\text{RM}} = (34.54393^\circ S,\ 69.52005^\circ W)\,. \tag{7.11}$$
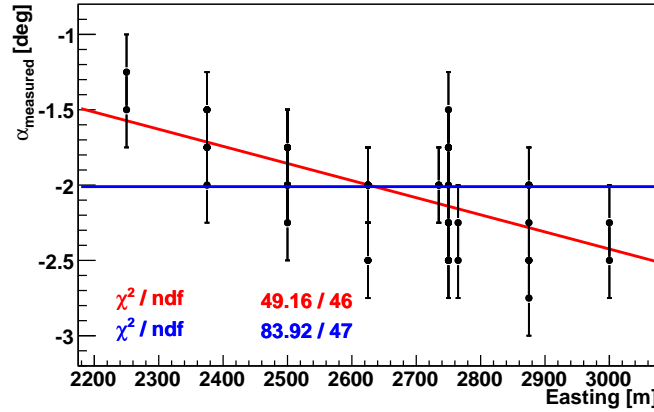
Figure 7.12: The measured angular distance to the reference mountain as a function of the easting of the detector stations. The reference mountain is located towards the North direction in a distance of ~ 60 km. Thus a movement in the East-West direction perpendicular to the line of sight to the mountain will change the angle towards the reference maximally. For comparison the χ^2-values of a constant and a linear fit indicate that we are able resolve the change in the angle towards the reference mountain within the extent of the first phase of AERA which is ~ 750 m in East-West.

This point lies in a distance of ~ 60 km from the AERA site.

Variation of Observed Position of the Reference Mountain within the AERA Array

To measure the direction of the reference mountain it is necessary to project the scale of the compass onto the measured object with help of the built-in optics of the compass. To minimize a possible bias of this measurement due to the operating person, the measurement is done by two persons independently. As 24 station are setup this results in 48 measurements of the direction towards the reference mountain.

As the extent of the 24 detector stations is ~ 750 m in East-West we expect the relative position of the reference mountain to change by $\arctan(0.75/60) \approx 0.7°$ between the two outermost AERA stations 6 and 9. Fig. 7.12 displays the measured angle between the direction identified as magnetic North by the compass and the reference mountain:

$$\alpha = \varphi_{north} - \varphi_{RM} \tag{7.12}$$

The values are given as a function of Easting of the radio detector stations. The uncertainty of the measured values is taken as $0.25°$ which corresponds to the precision with which we are able to read the scale projected to the mountain site. The uncertainty of the positions of the stations is governed by their positioning with a GPS device and is thus negligible for our measurements.

We find that we are able to observe the change in angle towards the reference mountain within the extent of the array.
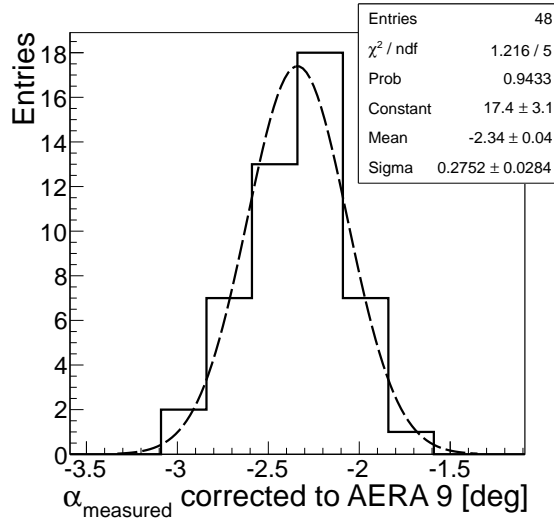
Figure 7.13: Angular distance between the antenna pointing direction and the reference mountain. The entries are corrected for the change in direction towards the reference mountain due to the different positions of the AERA stations that are visible in Fig. 7.12. For this purpose the position of AERA station 9 is used as reference.

Antenna Direction relative to the Reference Mountain

The variation of the angle towards the reference mountain from station to station is visible as slope in Fig. 7.12. This variation can be calculated independently from the choice of the coordinate system (as i.e. given in Fig. 7.7). Furthermore, the change in angle is robust against the precise position of the reference mountain, as the absolute values of the angles towards the reference mountain are effected in the same way when its position is changed. We can thus correct the measured angles throughout the array to refer to AERA station 9 (which is closest to the Central Radio Station). In Fig. 7.13 a histogram of the measured angles corrected to AERA 9 is displayed.

We find that at the time of alignment all antennas are pointing parallel within an accuracy of $\sigma_{point} = 0.28°$ in a direction that offsets by $2.34°$ to the East from the reference mountain seen from AERA 9. The task of the following chapters will be to find the absolute value of the antenna direction including systematic and further statistical uncertainties.

7.5.3   Uncertainties of the Alignment Measurement

In this section we identify possible major sources of uncertainties that effect the antenna alignment.

7.5.3.1   Mechanical Stability

To check if the antennas keep the direction they had at the time of alignment we repeat the measurement of their pointing direction at a subsample of 11 antennas. The measurement is performed 5 days after the setup of the last antenna in the field.
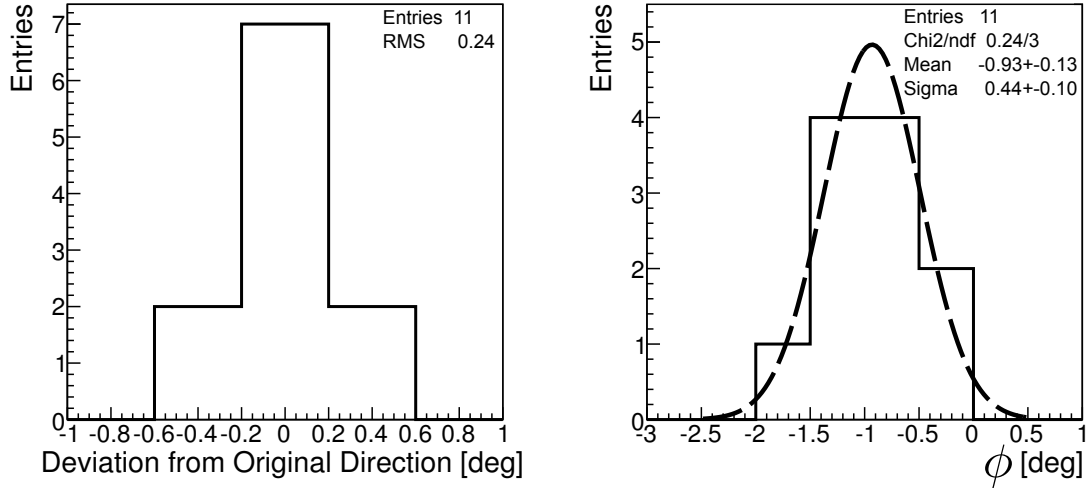
Figure 7.14: Left: Statistic uncertainty of the antenna alignment due to relaxation process of the antenna mechanics. Right: Histogram of multiple measurements of the direction of the same antenna with varying orientations and positions of the compass and its mounting bracket. The antenna investigated in this measurement had an offset of $\sim 1°$ from the final antenna direction which was adjusted afterwards. The width of the distribution yields the systematic uncertainty of the antenna alignment due to the choice of the mounting of the compass to the antenna.

This period includes times of bad weather with rain, snow and strong winds. The result of this repetition measurement is shown in Fig. 7.14.

If we assume that the antennas had relaxed into their final position at the time this measurement was conducted, the mechanical stability affects the alignment of the antennas with $\sigma_{mech} = 0.24°$ statistically.

7.5.3.2 Transfer of the Compass Direction to the Antenna

As described in Sec. 7.5.1.2 we have chosen a mounting procedure of the compass and its mounting bracket that should minimize magnetic influences of the pole on the antenna alignment. To estimate the impact of such choice on the alignment we perform multiple measurements of the direction of the same antenna while varying the position and orientation of the mounting bracket as well as of the compass. The result of this measurement is given in Fig. 7.14 (right). We find that we introduce a systematic uncertainty of $\sigma_{trans} = 0.44°$ due to the choice of mounting procedure.

7.5.3.3 Magnetism of the Setup

The magnetism of metallic objects might cause a systematic offset of the direction indicated as magnetic North by the compass and the true magnetic north. Metallic objects that are present at the same position in all measurements are i.e. the pole, a ladder used to climb to the compass, metal parts of the antennas or the mounting bracket itself. To detect such a deviation we repeat the measurement of the angular distance towards the reference mountain that is described in Sec. 7.5.2.1 but this
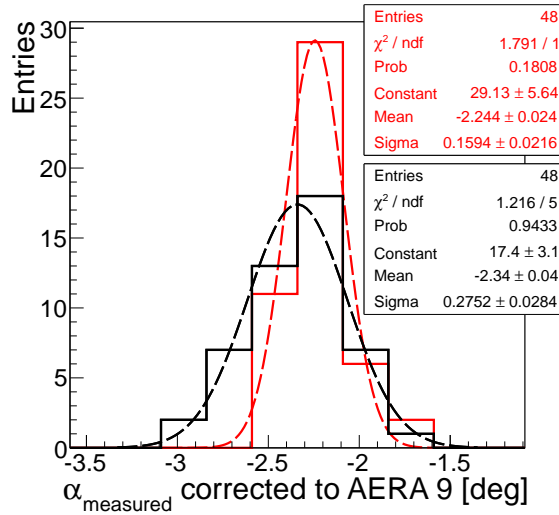
Figure 7.15: The result of the metal-free measurement (red) in comparison to the measurement carried out with the compass mounted to the antenna (black).

time taking special care to avoid any disturbing metal objects close by. The measurement is performed in a distance larger than 20 m north of each detector station. The measurement is performed by two persons independently.

In Fig. 7.15 the result of the metal free measurement is displayed in comparison to the result obtained during the antenna alignment (cf. Fig. 7.13). Again the measured angles are corrected to refer to AERA station 9. The width of the distribution in the case of the metal free measurement is sharper than in the first measurement. The reason for this might be that smaller disturbing magnetic effects have been reduced and that the metal free measurement is easier to perform as it does not have to be carried out on a ladder. We find that a systematic offset due to additional magnetism during the antenna alignment is small with $\sigma_{mag} = 0.1°$ only.

7.5.3.4 Direction of Reference Mountain

To transfer the measurement of the antenna direction from a relative to an absolute scale the absolute direction of the reference mountain has to be known. From severals test varying the position of the reference mountain we estimate that the direction towards the point given in Eqn. 7.11 aligns with the corresponding direction identified in field within $\sigma_{RM} = 0.2°$. Using the position of the reference mountain we calculate that the direction towards it deviates by $-1.14°$ from the geographic North direction as seen by AERA station 9.

7.5.4 Discussion of Antenna Alignment

Summarizing the result of the chapters 7.5.2 and 7.5.3, we calculate the absolute azimuth direction of the antennas:

$$\varphi_{antenna} = 86.52° \pm 0.37°(stat) \pm 0.49°(syst). \tag{7.13}$$
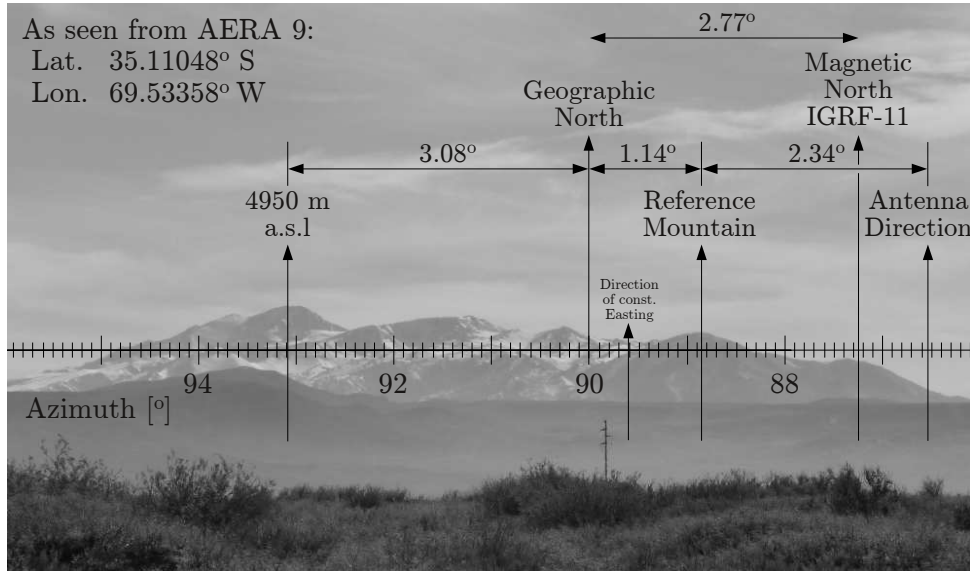
Figure 7.16: Overview of the mountain site relevant for the pointing of the antennas.

The statistical uncertainty indicates the parallelism of the antennas and applies to each antenna direction individually. The systematic uncertainty applies to the whole setup at once and refers to how the pointing direction of the antennas can be transfered to an absolute azimuth scale.

In Fig. 7.16 an overview of the most prominent directions to the North is given. The figure also displays a prediction for the direction of the magnetic field of the earth as calculated with the current International Geomagnetic Reference Field model (IGRF-11) [157]. The deviation between the direction of the earth's magnetic field and the geographic North direction is called declination δ. For May 2010 - when the antenna alignment was performed - the IGRF-11 model predicts an declination δ at the AERA site of:

$$\delta_{IGRF-11,\,May\,2010} = \varphi_{IGRF-11} - 90^\circ = -2.77^\circ\,, \tag{7.14}$$

changing by $0.13^\circ/year$ to the West. From Ref. [158] we estimate that the systematic uncertainty of this prediction due to i.e. the magnetism of the bed rock is about 0.4°.

Our best measurement of the declination at the AERA site results from the metal-free measurement described in Sec. 7.5.3.3. To this measurement only the width of the distribution displayed in Fig. 7.15 and the position of the reference mountain contribute as uncertainty:

$$\delta_{measured} = -3.38^\circ \pm 0.16^\circ(stat) \pm 0.2^\circ(syst)\,. \tag{7.15}$$

Independently from the alignment of the antennas we thus observe that our measurement of the declination is compatible within 2σ from model prediction of the magnetic field of the earth.

In both cases — $\delta_{measured}$ and $\delta_{IGRF-11,\,May\,2010}$ — the antenna directions align with the magnetic North direction within the discussed uncertainties.
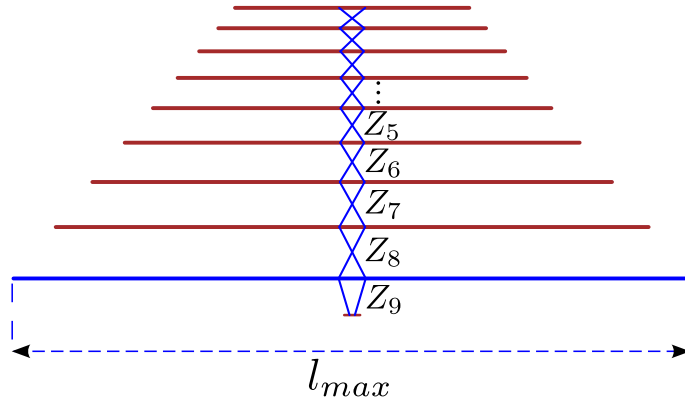
Figure 7.17: Simulation Model of the Small Black Spider LPDA. Input to the simulation are the start and the end points of the points of the dipoles, their diameters and the characteristic impedances of the pieces of wave guide between the dipoles. Depicted in blue are elements of the simulation model that will be used to fit the simulation to measured antenna characteristics. The parameters of the fit are the wave guide impedances $Z_1, \ldots, Z_9$ and the length of the longest dipole l_{max}.

7.6 Simulation Model for the Small Black Spider LPDA

In Sec. 6 we have motivated the vector effective length as central antenna characteristic needed for the reconstruction of radio data. To access the VEL on basis of antenna simulations with the NEC-2 program, a model of the SBS was created following the specifications of the real antenna as depicted in Fig. 7.17.

In Sec. 7.2 we have used the reflection coefficient $R(f)$ to control the quality of the series production of the SBSs. The reflection coefficient can as well be accessed in antenna simulations. We use the reflection coefficient to benchmark the quality of the antenna simulation model. In Fig. 7.18 a measured reflection curve and the reflection coefficients obtained from a simple and an adjusted antenna simulation model are depicted.

Input parameters to the simulation are the location, length and diameters of the dipoles. Moreover, the transmission line used to connect the dipoles is model piecewise from dipole to dipole in the simulation. Between each connection the characteristic impedance of the wave guide has to be chosen. Titled as 'simple' simulation is an antenna model that uses the nominal design parameters of the SBS to set up the simulation.

The simple simulation model exhibits a lack of sensitivity at lower frequency range. To improve the match between simulation and measurement we perform a fit of the simulation model to the measured data. As parameters of the fit we choose the length of the longest dipole and the impedances of the connecting waveguides.
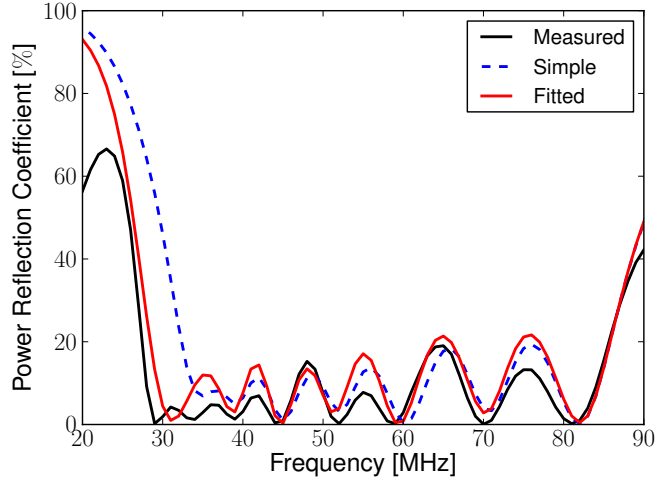
Figure 7.18: Measured and simulated reflection coefficients of the SBS.

The Lecher waveguide of the SBS consists of two wires with a diameter $d = 0.5$ mm in a distance D of 12.3 mm. The impedance of a such a two wire guide in air is [149]:

$$Z_l = 120\,\Omega \,\operatorname{arcosh}\left(\frac{D}{d}\right) \approx 467\,\Omega \quad . \tag{7.16}$$

The derivation of Eqn. 7.16 considers the capacity per unit length of the cylindrical shape of the wires. The dipoles connected to the central waveguide of the SBS impose an additional capacitive load that changes over the elongation of the line. An adjustment of the characteristics impedances used in the simulations hence seems promising.

As pictured in Fig. 7.2 an aluminum tube is used to realized the longest dipole of the antenna structure. The tube is connected with a regular dipole wire to the central waveguide. To model the impact of this design in the simulation we use the length of the lower dipole as a free parameter to the fit.

The adjustment of the simulation model is performed as least squares fit between the measured and the simulated reflection curve between 25 and 77 MHz. All integer frequency are accessed in the simulation which results in the comparison of 52 simulated data points to the measured characteristics for each evaluated antenna model. We observe that the higher frequency is range is relatively simple to match in the simulation. To stress the need for an adequate antenna description at the lower frequencies we adjust the objective function to the fit such that the frequencies ranges 25-28, 29-39, 40-77 MHz contribute with the same weight to the minimization.

The fit is performed by a simultaneous adjustment of the ten free model parameters using a particle swarm optimization [159]. Particle swarm optimization allows to search for the global minimum of an objective function. It minimizes the probability that the fit converges into a local minimum. We constrain the ranges of the free parameters to $(467 \pm 250)\,\Omega$ in the case of the impedances of the waveguide and to $l_{max} = (4.25 \pm 1)$ m for the length of the longest dipole. The result of the fit

Figure 7.19: The setup for calibration measurements of the Small Black Spider LPDA at the site of AERA. Left: Sketch of the measurement setup. A calibrated transmitter antenna is moved on a circle around the antenna under test to access different zenith angles. Middle: A picture of the realized setup. In the lower left the AERA station used for the calibration measurement is visible. At a distance of ∼30 m a balloon carries the calibrated transmitter antenna. The position of the transmitter is fixed by a three-legged rope system which provides the movement on the circle and a parallel orientation of the transmitter and receiver antenna. Right: Picture of the calibrated biconical antenna used as transmitter. The biconus has a length of 1.94 m. The antenna is carried by a balloon filled with 5 m^3 helium and fed by a coaxial cable running to the ground. The overall weight lifted by the balloon is ∼4.5 kg.

is displayed in Fig. 7.18 titled as 'fitted' reflection curve. The adjusted antenna model improves the match to the measured data in the lower frequency range. The fitted impedances range from 280 to 560 Ω. The length of the longest dipole is set to 4.82 m which is 0.57 m longer than in the mechanical layout. The complete simulation model is given in the appendix A.2. Deviations between simulations and measurement remain and will be quantified in terms of vector effective length in the calibration measurements of the SBS in the next section.

7.7 Measurement of the Characteristics of the Small Black Spider LPDA

In Sec. 6 we have motivated the vector effective length to be the central antenna characteristic needed to perform calibrated measurements of the electric field strength of incoming radio signals. The VEL can be calculated in simulations. However, it is desirable to perform the unfolding of the impact of the detector on the recorded signal on the basis of measured antenna properties.

In this section we present calibration measurements we have performed to access the VEL of the Small Black Spider LPDA installed at a regular position of the first stage of AERA. In our measurements we focus on the zenith dependence of the VEL as a function of frequency. In preceding measurements we have confirmed that azimuthal dependency of the VEL follows a simple sinusoidal function as expected for dipole-like antennas as the Small Black Spider LPDA [160].

7.7.1 Antenna Calibration Setup

So far directional properties of antennas for the detection of cosmic rays have been measured with down-scaled versions of the antenna under test (AUT) [161] or being constrained to a measurement of the scalar amplitude transfer without the vectorial phase information [162].

The experimental challenge in a calibration measurement with a full scale radio antenna is to realize a distance between transmitter and receiver antenna such that the wave emitted by the transmitter sufficiently approximates the plane wave condition at the AUT. It should be noted that the usual approximation at which distance this far field condition is fulfilled is given by $r_{\mathrm{ff}} > 2\,\delta^2/\lambda$, where δ the largest dimension of the transmitting antenna. This relation is valid only if δ is *larger* than the wavelength λ [130]. This is typically the case for dish antennas but not for the radio antennas discussed in this paper.

With respect to the longest wavelength of the AERA bandwidth of 10 m, in our calibration setup distances between transmitter and the AUT of 3λ are realized. Following the discussion in Ref. [163] we estimate that near-field components still present at a distance of 3λ will cause a variation of the power angular distribution of at most ± 0.5 dB when compared to a measurement performed at much larger distances.

In Fig. 7.19 an overview of the calibration setup is given. To access large distances at small zenith angles above the AUT a balloon is used to lift a calibrated transmitter antenna [164]. Ropes constrain the movement of the transmitter to a circle around the AUT and ensure a parallel orientation of the two antennas. In this way the $\vec{e}_\phi$-component $\mathcal{H}_\phi$ of the VEL can be accessed for various zenith angles.

The transmission measurement from the biconical antenna to the Small Black Spider is performed using a vector network analyzer [165]. The network analyzer simultaneously feeds the transmitter antenna and reads out the AUT. The signal delivered by the vector analyzer is adjusted to appear > 30 dB above the ambient radio background recorded by the AUT throughout the measurement bandwidth from 30 to 80 MHz. The impact of the coaxial cables needed for the connections are removed from the data by including them in the null calibration of the vector network analyzer prior to the measurement. The amplifier of the Small Black Spider is included in the transmission measurement. Hence, the setup allows us to measure $\mathcal{H}_{a,\phi}(\omega, \theta, \phi = 270°)$ as discussed in Eqn. 6.57 of Sec. 6.7.

7.7.2 Simulated Calibration Setup

To cross check the calibration measurement procedure we performed simulations of an equivalent setup using the numerical antenna simulation tool NEC-2 [138]. The simulated calibration setup includes a model of the Small Black Spider LPDA as well as a model of the biconical antenna. Both antenna models are placed in the simulation according to the geometries realized in the actual calibration setup. The sketch in Fig. 7.19 (left) is generated from an exemplary transmission measurement realized in NEC-2.
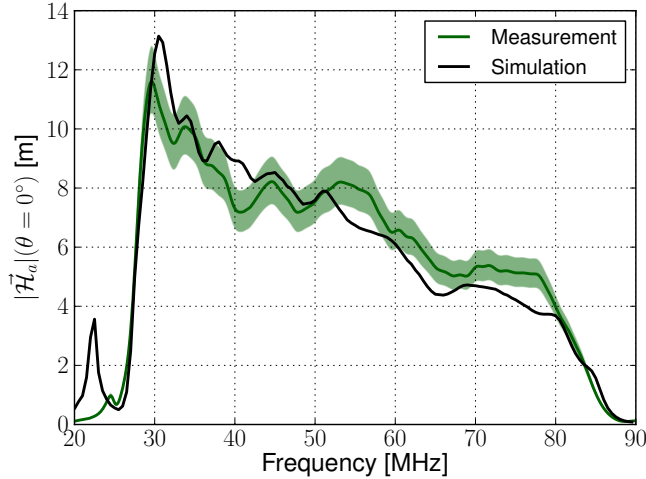
Figure 7.20: The amplified vector effective length $\vec{\mathcal{H}}_{a,\phi}$ of the Small Black Spider LPDA for the zenith direction as a function of frequency in measurement and simulation. The uncertainty of the measurement is dominated by the systematic uncertainties of the calibration of the transmitting antenna of 0.7 dB and by the precision of the transmission measurement, here 0.6 dB.

The simulation model of the transmitter antenna is excited by placing a voltage source at its footpoint. The NEC-2 simulation then calculates the power consumed by the transmitter and the consequent open terminal voltage $\mathcal{V}_{\mathrm{oc}}$ induced in the structure of the Small Black Spider. Following the discussion in Sec. 6.6 we process the terminal voltage to give the power delivered into a $50\,\Omega$ system which corresponds to the coaxial cables connected to the network analyzer.

In the field measurement not all power that is delivered by the signal source of the network analyzer is accepted by the transmitter. This has to be accounted for in the simulation by renormalizing the radiated power given by NEC-2 with the measured power acceptance of the transmitter antenna.

In the measurements at the AERA site signal reflections from the ground are included. We thus use the option of NEC-2 to model a ground plane in the simulation using the Fresnel reflection coefficients (cf. Sec. 6.8.3). The reflection coefficients depend on the relative permittivity ϵ_r and the conductivity σ of the soil. With $\sigma = 0.0014\,\Omega^{-1}\mathrm{m}^{-1}$ we assume a low conductivity which has been confirmed in initial test measurements at the AERA site. For low conductivities we find $\epsilon_r = 5.5$ to be a reasonable choice for the relative permittivity in typical ground scenarios [144]. The resulting ground exhibits a relatively low reflectivity.

As in real measurements we use the simulation to yield the ratio of signal received by the AUT and the signal used to operate the transmitter. Both data streams are then processed equally in further analysis.

7.7.3 Transmission Equation and Data Processing

For each zenith angle accessed in the setup we measure the S-Parameter S21 as a function of frequency. S21 is the complex ratio of the voltage amplitude $\mathcal{V}_a$ delivered by the AUT and the amplitude $\mathcal{V}_g$ delivered from the signal generator to the transmitter:

$$S21 = \frac{\mathcal{V}_a}{\mathcal{V}_g} \quad . \tag{7.17}$$

The voltage $\mathcal{V}_a$ is the response of the AUT to the electric field caused by the transmitter antenna $\mathcal{E}_\phi^t$:

$$\mathcal{V}_a = \mathcal{H}_{a,\phi}\,\mathcal{E}_\phi^t \quad . \tag{7.18}$$

Due to the configuration of the setup the electric field is contained in the $\vec{e}_\phi$-direction of the antenna-based coordinate system. Analog to Eqn. 6.64 the electric field of a transmitting antenna at a distance R is known in this case. For our calibration setup it is:

$$\mathcal{E}_\phi^t = -i\, Z_0\, \frac{1}{2\,\lambda\,R}\, \mathcal{I}_0^t\, \mathcal{H}_\phi^t\, e^{-i\omega R/c} \quad , \tag{7.19}$$

where H_ϕ^t is the VEL, $\mathcal{I}_0^t$ denotes the current in the transmitter antenna as depicted in Fig. 6.5, and c is the speed of light. When eqns. 7.18 and 7.19 are inserted in Eqn. 7.17 we receive a complex form of the Friis transmission equation:

$$S21 = -i\, Z_0\, \frac{1}{2\,\lambda\,R}\, \frac{\mathcal{I}_0^t}{\mathcal{V}_g}\, \mathcal{H}_\phi^t\, \mathcal{H}_{a,\phi}\, e^{-i\omega R/c} \quad . \tag{7.20}$$

To access the desired VEL of the AUT $\mathcal{H}_{a,\phi}$, the characteristics of the calibrated transmitting antenna $\mathcal{H}_\phi^t$ have to be applied. In our case these are given in terms of realized gain G_r. The realized gain refers to the transfer of signal power rather than signal amplitude and includes the reflections at the input of the transmitter antenna. In the appendix A.7 we derive that:

$$\frac{|\mathcal{I}_0^t|}{|\mathcal{V}_g|}\, |\mathcal{H}_\phi^t| = \sqrt{\frac{\lambda^2}{\pi\, Z_0\, Z_{tl}}\, G_{\text{cal}}^t} \quad . \tag{7.21}$$

The transmitter calibration $G_{\text{cal}}^t(\omega)$ is given by the manufacturer of the antenna as function of real numbers. Such simplification is acceptable if the transmitter antenna introduces a group delay which is constant over the measurement bandwidth only. This we have verified in preceding test measurements of the biconical antenna.

In summary we receive the measurement equation for the calibration setup by:

$$\mathcal{H}_{a,\phi} = i\, R\, S21\, \sqrt{\frac{Z_{tl}}{Z_0}}\, \sqrt{\frac{4\pi}{G_{\text{cal}}^t}}\, e^{i\omega R/c} \quad , \tag{7.22}$$

where we measure the distance R between the center of the transmitting antenna and the center of the lowest dipole of the Small Black Spider LPDA.
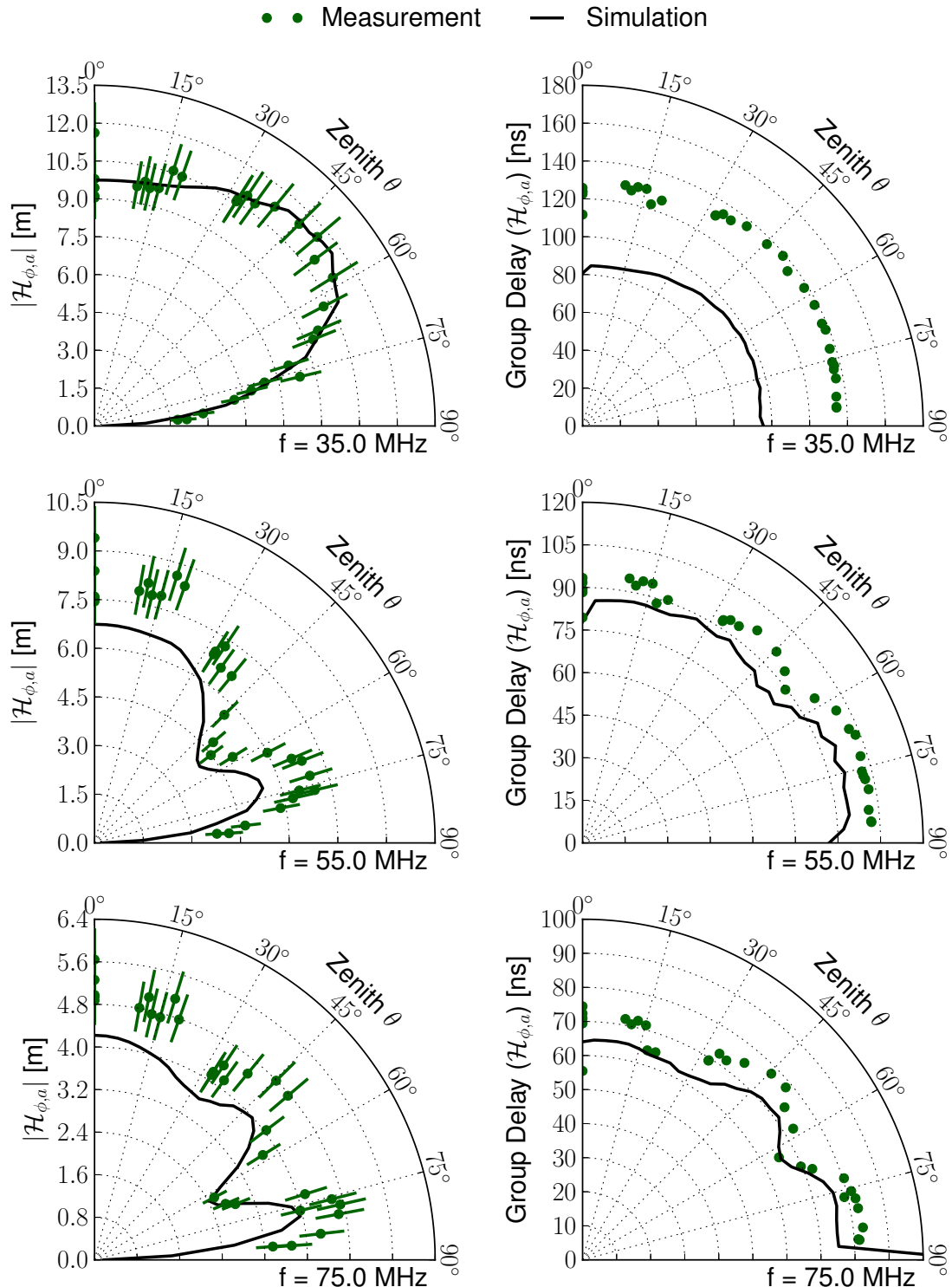
Figure 7.21: The VEL as a function of zenith angle for three different frequencies in measurement and simulation. Left column: The absolute values of the VEL. Right column: The phasing of the VEL expressed as group delay.
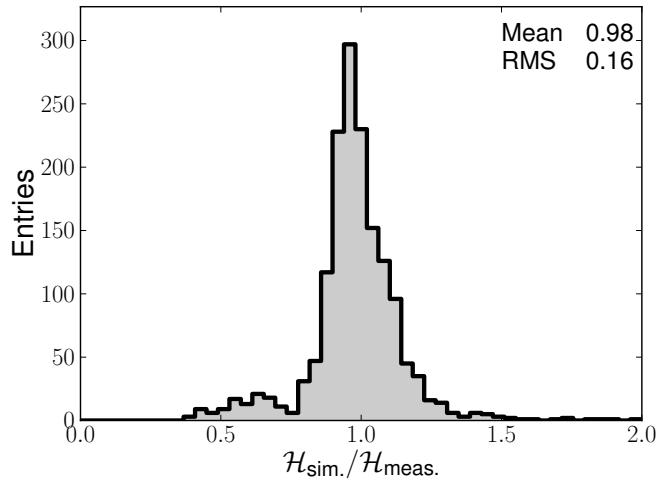
Figure 7.22: Histogram of the difference between the absolute values of the measured and the simulated VEL. Considered are frequencies which appear in both simulation and measurement.

7.7.4 Calibration Measurement Results

In Fig. 7.20 the absolute value of the amplified VEL of the Small Black Spider is displayed for the zenith direction $\theta = 0°$ as a function of frequency. For frequencies lower than 30 MHz and higher than 80 MHz the reception is strongly suppressed due to the presence of the filter elements in the amplifier (cf. Sec. 7). Within the bandwidth the VEL decreases with increasing frequency. With respect to Eqn. 6.35 this is the expected behavior for antennas which feature a gain that is constant as a function of frequency as LPDAs. The additional variations of the VEL within the frequency band occur due to the interplay of the LPDA's dipole elements which resonate at different frequencies.

For a set of three frequencies the dependence of the VEL on the zenith angle is shown in the left column of Fig. 7.21. For the low frequencies the antenna is most sensitive to zenith angles around 45°. At higher frequencies a side lobe pattern evolves with up to two lobes at the highest frequencies.

The primary cause for the side lobes is the constructive and destructive interference of the direct wave and the wave reflected from the ground at the position of the antenna with its lowest dipole at a height of 3 m. Note that a conclusion on the reception of transient signals can only be drawn if the wide band combination of these patterns including their respective phasing is regarded as we will do in Sec. 11.2.1.

With respect to the shape of the side lobe pattern we note a remarkably good agreement between measurement and simulation. For the combination of all zenith directions and all frequencies within the bandwidth we observe an agreement of the simulated and measured VEL of better than $\pm20\%$ which is displayed in Fig. 7.22.
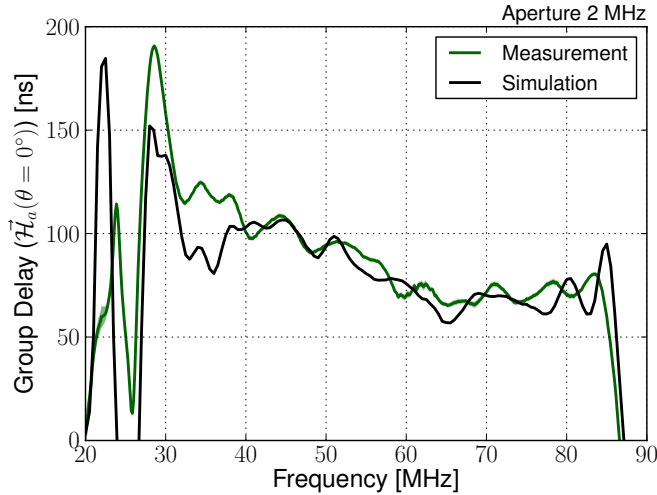
Figure 7.23: The group delay including the LNA for the zenith direction $\theta = 0°$ as a function of frequency for the Small Black Spider LPDA in simulation and measurement. The uncertainty of the group delay is < 1.3 ns and resulting from variations observed in multiple measurements.

The phasing of $H_{a,\phi}$ reveals the group delay induced by the Small Black Spider to the transmitted signal. The group delay τ is given by:

$$\tau(f) = -\frac{d}{d\omega} \arg(\mathcal{H}_{a,\phi}) \quad . \tag{7.23}$$

In Fig. 7.23 the group delay for the zenith direction is displayed. Within the measurement bandwidth from 30 to 80 MHz the group delay decreases by ~ 50 ns, where measurement and simulation agree on the functional dependence.

As will be discussed in detail in Sec. 11.2 a non-constant group delay induces the dispersion of the observed transient signal and thus reduces its peak amplitude. The group delay displayed in Fig. 7.23 results from a combination of the delay introduced by the logarithmic periodic structure of the Small Black Spider and the delay introduced by the filter elements of the amplifier. Although the amplifier has been designed to suppress the signal reception outside the bandwidth, it causes a non constant group delay also within the measurement bandwidth especially at lower frequencies. The most recent version of the AERA readout electronics is able to compensate digitally for the dispersion induced by non constant group delays of the read-out chain which we will report in a later paper.

In the right column of Fig. 7.21 the group delay for the Small Black Spider is shown as a function of zenith angle for three different frequencies. We find that also the group delay exhibits a side lobe pattern that is similar to the pattern observed in the case of the absolute values of the VEL. The shape of the group delay pattern is similar in the measurements and the simulations. The absolute values differ by up to 30 % depending on the considered frequency range as is also visible in Fig. 7.23.

Correction for a group delay that changes with incoming direction is important as single transient signal fronts will be observed at different detector stations.

In the presented measurement campaign we have accessed the $\vec{e}_\phi$-component of the VEL. The full VEL will be obtained in later calibration measurements.

8. Reconstruction of Radio Detector Data

In this chapter we present our methods for signal processing and reconstruction of data recorded with radio detector arrays. The chapter starts with the description of the RDAS software which is used as a common framework for the implementations. The second part of the chapter outlines the impact of the signal processing using the example of a measured air shower signal. Finally, we discuss the reconstruction of curved radio signal wave fronts.

8.1 RDAS: Software for the Reconstruction and Simulation of Radio Detector Arrays

The Radio Detector Array Simulation (RDAS) software [126, 166] is a dedicated program for the reconstruction and simulation of radio detector data. RDAS allows for full end-to-end simulations of complete radio detector arrays. The software includes the reconstruction and visualization of simulated and measured data. The development of RDAS started in 2007 according to object oriented programming standards in C++.

The RDAS software was developed continuously and served for the reconstruction of radio data from the BLS setup mentioned in Sec. 5.2.1 and the MAXIMA setup (cf. Sec. 5.2.1). RDAS was used for data analysis by various scientists in the Auger radio group [167, 168] and is up-to-date for the reconstruction of the first AERA data. RDAS served as a test bed for the implementation of radio detector functionality in the $\overline{\text{Off}}\underline{\text{line}}$ standard software framework of the Pierre Auger Observatory [132, 169]. Key functionalities of RDAS have been ported to the $\overline{\text{Off}}\underline{\text{line}}$ software which combines the radio reconstruction with reconstructions of the other air shower detectors of Auger.

8.1.1 Structure

RDAS has a threefold structure which provides a modular and flexible software setup. The software is divided into a detector part, a sequence of modules and an event interface. A sketch of the RDAS structure is visible in Fig. 8.1.

The detector part contains the information about the detector array setup. This is for instance the position and orientation of the antennas as well as their properties. The users chooses a series of modules which are then processed sequentially. The module use the detector information to manipulate the radio data which are stored in the event structure. Each module runs independently - the event structure is their common interface.

```
  Detector Description            Module Sequence              Event Interface

AntennaArray                 RawFileHandler               RDataEvent
   Pole/Station              ReadReas                        TraceProperties
      Antennas:              RDataEventFileHandler            Event
      SmallBlackSpider       Amplifier                       ReconstructedEvent
      BlackSpider            Cable                               Channels
      AluLPDA                DAQFilter                           EField
      Butterfly              Digitizer                       GeneratedEvent
      Lofar                  CalcResponses                       Channels
      Salla                  GalNoise                            EField
      ...                    SeizeRecData
                             WaveReconstruction
                             ReconstructEField
                             ...
```

Figure 8.1: The threefold structure of the RDAS software. The detector description is given by the `AntennaArray`. Modules manipulate the data which reside in the `RDataEvent` class acting as common interface. The arrows indicate in which way information can be exchanged. The two dashed lines in the module sequence indicate a functional separation of the modules into file I/O, signal processing and radio event reconstruction.

8.1.2   Module Description

Modules for Event I/O

<u>RawFileHandler</u>: Provides the read in of BLS, MAXIMA and AERA Stage 1 raw data files into the `RDataEvent` structure.

<u>ReadReas</u>: Provides the read in of simulated electric fields as generated by the REAS1, REAS2 and REAS3 air shower simulation softwares.

<u>RDataEventFileHandler</u>: The `RDataEvent` class provides the machinery for persistence. As the `RDataEvent` class is derived from a ROOT [170] `TObject` it inherits the possibility to be serialized in a `TFile` on hard disc. Adding `RDataEvents` as a branch in a `TTree` allows to display large data sets conveniently with the Event-Browser of RDAS which is described in Sec. 8.1.3. The `RDataEventFileHandler` provides convenient functionality for the necessary file I/O.

Modules for Data Processing

<u>Amplifier/Cable</u>: These modules handle the impact of cables and amplifiers to measured and simulated radio traces. Measurements of frequently used hardware parts are provided along with RDAS. These modules apply the characteristics including the respective phase information. In the case of measured data the modules allow to unfold the impact of the used electronics from the traces.

<u>DAQFilter</u>: This module is similar to the `Amplifier` and `Cable` modules. Additionally, the module provides digital filters with arbitrary bandwidths in the frequency domain. Tukey window functions [171] are available to be applied to traces in the time domain.

Digitizer: In the raw data files from the MAXIMA and AERA setup ADC counts from the digitizer are saved. The module converts the ADC counts into voltages at the input of the respective digitizer. For the AERA digitizer the frequency dependent parameterization proposed Ref. [172] is used.

CalcResponses: The module applies Eqn. 6.15 to calculate the antenna response to a given simulated electric field using the antenna characteristics provided by the **AntennaArray**. The handling of antenna characteristics within RDAS is explained in the appendix A.3. The antenna characteristics need to be accessed towards the incoming direction of the signal which is currently approximated with the air shower axis.

GalNoise: The parameterization of the Galactic noise by Cane [173] is used to add noise to simulated antenna responses. The module accesses the **AntennaArray** to receive the amplification characteristics of the used antenna. This is done without directional information as Cane's parameterization gives the average noise level induced by the Galaxy. Besides this average noise level the module optionally approximates the variation of the Galactic noise using a sinusoidal function.

UpSamplingChannels/HilbertEnvelope: Modules which provide an upsampling and the Hilbert envelope of sample traces. The effects of these modules will be explained by means of measured signals in Sec. 8.2.2.

Modules for Event Reconstruction

SeizeRecData: For the reconstruction of arrival directions the signal position in traces recorded in the different detector stations is needed. To find the radio signal within a given trace, a search for the maximum amplitude is performed. The module allows to reject faint signals on the basis of a signal to noise criterion. Hence also noise levels and signal amplitudes are evaluated in this module. Both voltage traces as well as electric field traces can be inspected.

Usually not the whole time span of the recorded trace is likely to contain the desired radio signal. **SeizeRecData** allows to search for the maximum amplitude in constrained time windows. The location of the time window can be proposed by a different module using the **RDataEvent** interface.

The **SeizeRecData** module can be applied to reconstructed electric field traces.

ArcReconstruction: The module is specialized for the reconstruction of radio events recorded with three radio detector stations. The two most prominent signals are selected. The two corresponding timing information constrain possible incoming directions of the wave to a circle. The circle defines a range of possible signal timings in the third detector station. Depending on the geometry this allows to shrink the time window which is used to search for the pulse in this station and results in a more reliable identification of fainter signals.

WaveReconstruction: Starting with the arrival times of a radio pulse in a set of detector stations, the module reconstructs the incoming direction of the wave. If the signal was detected by a sufficient amount of radio detector stations the distance

to the source of the signal can be reconstructed. A detailed description of this reconstruction is given in Sec. 8.3.

`ReconstructEField`: The module implements Eqn. 6.39 to reconstruct the electric field of an incoming pulse from the recorded voltage responses. The incoming direction of the pulse at the antenna is needed to access the proper antenna characteristics. This direction is approximated with the signal direction found in the foregoing reconstruction steps. The access to antenna characteristics within RDAS is explained in the appendix A.3.

8.1.3 Visualization of Radio Detector Data and Graphical User Interface

The RDAS software provides a graphical user interface to radio detector data that have been processed with RDAS. The RDAS EventBrowser is implemented in the Python programming language. It uses the Python interface of ROOT to access the graphical user interface functionality provided by ROOT. RDAS serializes its data format by means of ROOT `TTrees`. The RDAS EventBrowser allows to open these files and display the data. A EventBrowser window that displays a run of radio data measured with AERA is shown in Fig. 8.2.

The design of the EventBrowser implements two major points:

- The preparation of the graphical user interface but without the actual plotting routines. Plotting functionality is usually developed along with a specific analysis. The EventBrowser offers canvases to embed these plotting functionality that may reside outside the implementation of the EventBrowser. Here as well, the `RDataEvent` is used as common data interface.

- The EventBrowser excessively uses the functionality provided by `TTrees` to display variables stored in individual events for whole data sets at once. This applies both for plotting as well as for the application of cuts to the data. As selections in `TTrees` are performed on the basis of strings, the EventBrowser profits from the enhanced string manipulation capabilities of the Python programming language.

In our studies we found that the combination of different stages of data visualization in the EventBrowser is an effective tool especially for the characterization of early radio detector data.
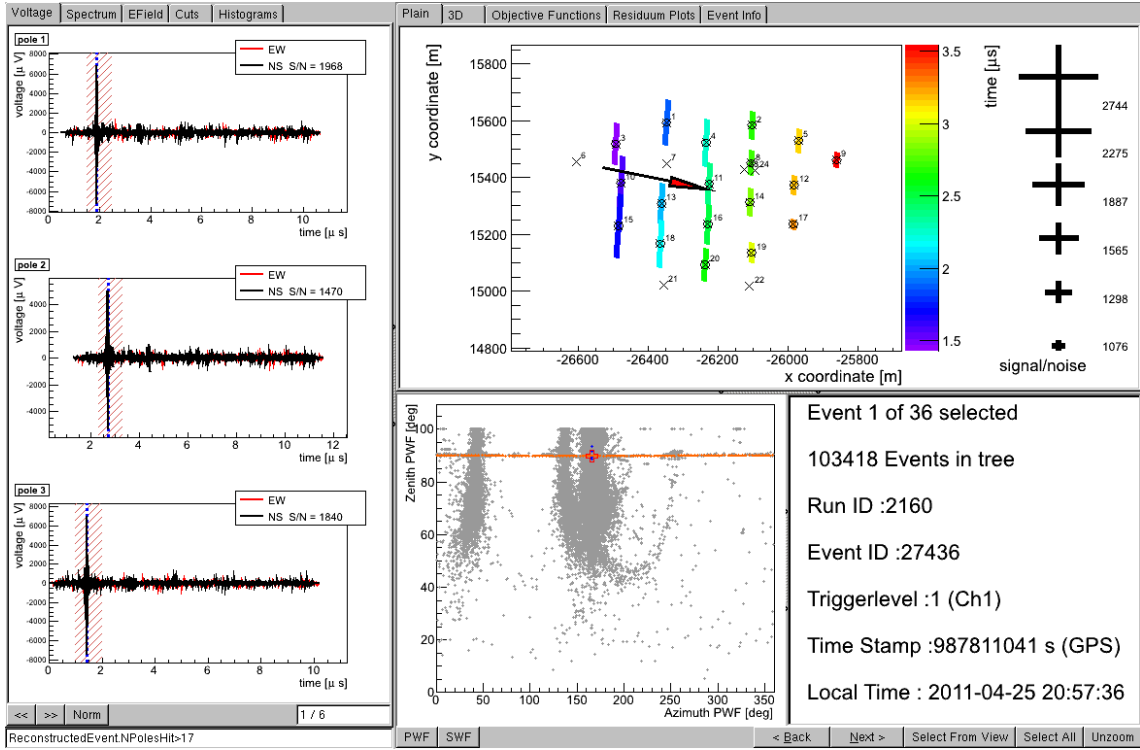
Figure 8.2: The RDAS EventBrowser is a graphical user interface to radio detector data. The EventBrowser offers a combined display of single radio events and sets of radio data. Traces recorded in single antennas can be seen in the left section of the window. An overview of the radio event as seen by the whole detector array is given in the upper right section. A sky view of the reconstructed arrival directions in the full data set and additional information of selected data is displayed in the lower right section. The tabulators indicate the various options of the EventBrowser such as the display of spectra or electric field reconstructions as well as details of the applied reconstruction modules. Moreover, the EventBrowser allows to apply arbitrary cuts to the data on the basis of cut strings as well as on-screen selections. The effects of cuts to the data can be controlled immediately as the EventBrowser provides direct access to histograms and scatter plots of all variables that are stored in the `RDataEvent` interface.

The displayed data is a transient noise signal that triggered 18 radio detector stations. The reconstruction yields an incoming direction close to the horizon.

8.2   Signal Processing

In this section we describe the data processing of radio detector traces. The different steps are implemented as modules in the RDAS software and are exercised here by means of an exemplary signal trace recorded with AERA. For the characterization of series of sampled data $\{x_1, \ldots, x_N\}$ we use the following definitions:

With 'peak amplitude' we denote the maximum absolute value within a series of samples:

$$A_{peak} = max(\{|x_i|, \ldots, |x_j|\})   , \tag{8.1}$$

where the search for the peak amplitude can be constrained to a excerpt of the sample series $\{x_i, \ldots, x_j\}$ with $1 \leqslant i \leqslant j \leqslant N$.

If the peak amplitude is found in the k-th sample, we use the timing position t_k associated to this sample as estimator for the peak position:

$$A_{peak} = |x_k| \quad \longrightarrow \quad t_{peak} = t_k   . \tag{8.2}$$

This implies that the timing information of signals are binned with the time difference Δt between neighboring samples:

$$\Delta t = t_j - t_{j-1}   . \tag{8.3}$$

The noise level σ_{noise} is calculated as root-means-square from a section of the trace which is chosen such that it does not contain a pulsed radio signal:

$$\sigma_{noise} = RMS(\{x_i, \ldots, x_j\})   . \tag{8.4}$$

We choose a linear definition of the signal-to-noise ratio with:

$$S/N = \frac{A_{peak}}{\sigma_{noise}}   . \tag{8.5}$$

8.2.1   Unfolding of Electronics and Digital Filtering

In Fig. 8.3 we show a single detector channel of AERA during the detection of an air shower in coincidence with the surrounding surface detector. The left panels of Fig. 8.3 display the signal in the time domain after each processing step. The right panels yield the corresponding power spectra of the traces. The signal is processed as follows with the numbering according to the panels of Fig. 8.3:

1. The raw files deliver ADC counts from a 12 bit digitizer. The baseline of the digitizer is set up be at 4096/2 counts to optimally use the dynamic range of the ADC for the detection of two-sided waveforms. The sudden pulse in the first part of the trace is the air shower signal. Three features are visible in the spectrum:

- Between 30 and 80 MHz there is a noise plateau which is governed by galactic noise.

- A radio transmitter disturbs the band at $\sim$ 67 MHz.
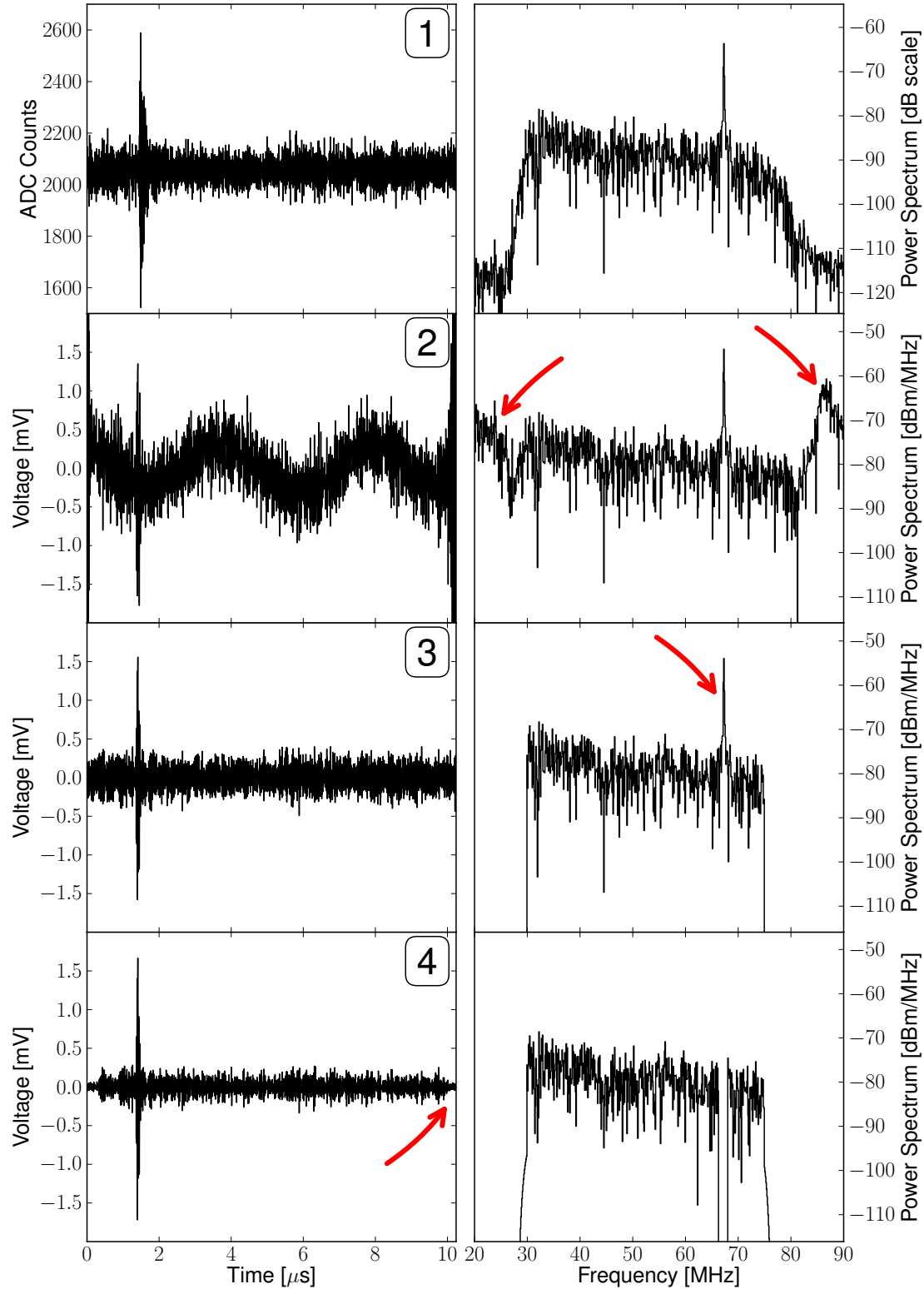
Figure 8.3: Processing of a signal trace recorded in an AERA detector station with an antenna pointing in East-West direction. Each column displays a step in the signal processing done with RDAS in an offline reconstruction. The left row shows the time domain signal. The corresponding spectra are given in the right row. The arrows mark topics which we refer to in the text.

- The filter setup of AERA strongly suppresses the signal reception below 30 and above 80 MHz. The noise still visible in this regions is induced from the readout electronics which add a small portion of internal noise to the signal.

2. The ADC counts are translated into voltages at the input of the ADC. Moreover, the impact of the analog parts of the signal chain are removed by an inverse application of Eqn. 6.56 using a S-parameter measurement of the hardware components. In the case of AERA these are cables and in particular the main amplifier.[1] The main amplifier includes filter elements. A portion of the noise is added to the signal after the filter elements. The removal of the filter characteristics from the spectrum hence leads to an overestimate of the signal level in frequency regions that were dominated by internal noise. Also in the time domain the signal is clearly distorted.

3. After the removal of the analog chain in the previous step a digital filter is needed to avoid the distorted regions of the spectrum. The bandwidth of the filter has to be adjusted such that regions are chosen which are dominated by external signals. Currently we use the -3 dB points of the filter setup which are imposed by the filter elements of the main amplifier in the case of the AERA chain. This yields an applicable bandwidth from 30 to 75 MHz which is selected with a rectangular filter. The trace now corresponds to the radio signal that can be measured directly at the output of the antenna using the same set of digital filters.[2]

4. In a final step the transmitter at 67 MHz is removed from the trace using a band stop filter. Due to the limited number of samples given to the Fourier transforms and the specific frequency of the transmitter, the transmitter power leaks into neighboring frequency bins. The width of the leakage is shrunk prior to the filtering by means of a Tukey window. The Tukey window fades the edges of sample series in the time domain with a cosine function. The width of fadeout is set to 0.9 μs such that it does not interfere with signal pulses which are located at later times. In comparison to panel 3 the signal-to-noise ratio has improved from 10 to 16.
The application of the window function requires that the width of the noise distribution is calculate after the signal pulse.

The described procedures are applied to all data that we will process from AERA in the next sections. In Sec. 9 we present an analysis based on data recorded with the BLS setup (cf. Sec. 5.2.1). The signal processing for the BLS setup is similar and has been adjusted to the actual filter setup. The transmitter at 67 MHz is not present in these measurements such that we can avoid the corresponding processing steps.

8.2.2 Upsampling and Hilbert Envelope

The two final steps of the signal processing is an upsampling of the signal trace and the creation of a trace envelope. The positive effects of these two methods have

---

[1] The low noise amplifier is treated as part of the antenna and hence removed when the antenna characteristics are applied to reconstruct the electric field.

[2] Note that the reconstruction of electric fields needs to be constrained to the common bandwidth as well.
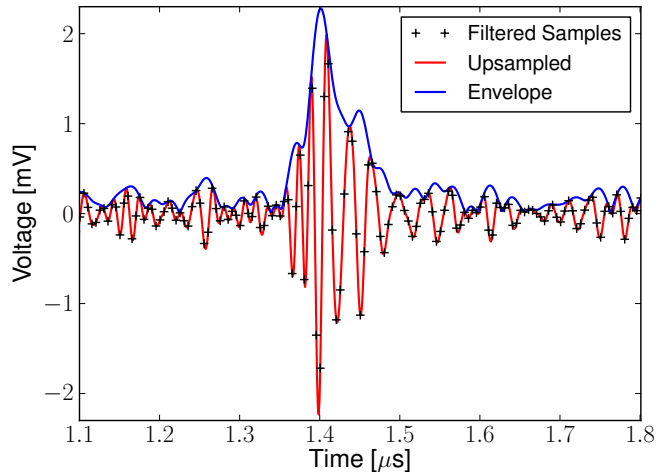
Figure 8.4: Upsampling and trace envelope: The filtered samples of trace containing an air shower signal are displayed as cross marker symbols. The red line shows the same data upsampled with a factor 5. In blue the envelope of the upsampled trace is given.

largely been explored for the LOPES radio detector [174, 175]. Guidelines for the technical implementation can be found in various textbooks, i.e. in Ref. [176] — we will here summarize their effects.

An excerpt of the filtered signal trace in the lower left panel of Fig. 8.3 around the pulse position is displayed in Fig. 8.4. The filtered signal samples are here given as cross marker symbols.

Upsampling

Radio signals from AERA are currently recorded with a sampling rate of 200 MHz. The highest frequency that can directly be accessed in the frequency domain is 100 MHz. A contribution of signal components above 100 MHz is suppressed by analog filters. The Nyquist-Shannon sampling theorem [177] states that in this case all information of the recorded waveform is determined by the series of sampled points. Hence also the signal progression between the recorded samples is known. Upsampling is the method to access additional points from the full curve progression. The result of an upsampling by a factor of $N = 5$ from a sample distance of $\Delta t = 5$ ns to 1 ns is visible in Fig. 8.4.

The position of the peak amplitude t_{peak} is used to determine the arrival time of a signal in an individual radio detector station. Upsampling allows to remove a possible limitation of the timing resolution imposed by progression of the sample series with discrete time intervals Δt.

For AERA a timing resolution of 1 ns is envisaged. Using an upsampling factor of 5 to achieve a sample distance of $\Delta t = 1$ ns reduces the statistical uncertainty of the peak position t_{peak} to $\Delta t / \sqrt{12} \approx 0.3$ ns. This is sufficiently small to avoid a limitation of the timing resolution of our method due to a discrete trace sampling.
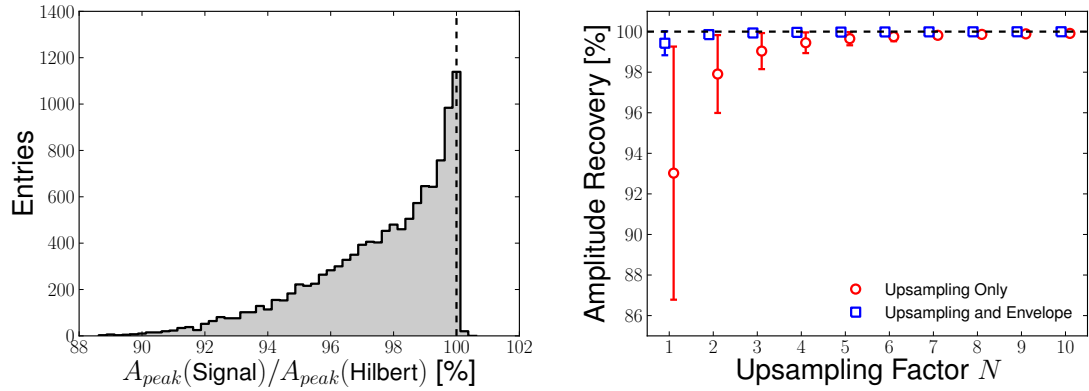
Figure 8.5: Left: The peak amplitudes found in radio traces recorded with AERA are compared to the maximum values derived from the corresponding trace envelopes. Often both estimators of the signal amplitude yield similar values where the envelope is a tight upper bound to the trace samples. Right: The percentage of peak amplitude that is recovered from radio traces as a function upsampling factor.

Signal Envelope

The final processing step indicated in Fig. 8.4 is the creation of the signal envelope. The envelope of a trace is useful for the discussion of bandpass filtered signals. Looking at Fig. 8.4 the signal can be decomposed into two parts: One component exhibits a fast time variation governed by a frequency ω_0, where ω_0 can be thought of the mid-frequency of the passband. In addition, signal components are present which vary slowly with respect to $1/\omega_0$. A representation of the signal is given with:

$$V(t) = A(t) \cdot e^{-i(\omega_0\, t + \varphi(t))} = A(t) \cdot e^{i\Phi(t)} \quad , \tag{8.6}$$

where $A(t)$ is the amplitude envelope and $\Phi(t)$ the instantaneous phase of the signal. When the instantaneous phase is essentially a real-valued function, the intensity I of the signal is directly indicated by the envelope $I \propto |A(t)|^2$ [178]. In either case the maximum value of the envelope marks the point in time of the highest energy concentration of the signal [179].

Several methods exist to estimate the signal envelope. In our studies we use the so-called Hilbert envelope which was found in Ref. [174] to be an adequate choice for radio detector signals. The use of the envelope diminishes the impact of the bandwidth limitation of the detector to the recorded signal. Even when the signal is upsampled, the maximum value $max(A(t))$ might not be realized in the sample series due to the exact distribution of zero crossings within the signal duration.

In the left panel of Fig. 8.5 we study the maximum values obtained from Hilbert envelopes $A_{peak}(\text{Hilbert})$ in comparison to the corresponding peak amplitudes $A_{peak}(\text{Signal})$ obtained from the signals directly. To avoid possible discrepancies induced by the sampling, all signals have been upsampled with a factor of 1000 prior to the comparison. A set of 10000 pulses recorded with AERA is used.

The maximum values are always smaller than their envelope counterparts besides a few outliers:

$$A_{peak}(\text{Signal}) \leqslant A_{peak}(\text{Hilbert}) \quad . \tag{8.7}$$

On average they realize 97.6 % of the Hilbert envelope in the given data set. As the distribution of $A_{peak}(\text{Signal})$ closely approaches the maximum values defined by the Hilbert envelopes we conclude that the Hilbert envelope reduces a bias induced by the bandwidth limitation of the detector. The use of $A_{peak}(\text{Signal})$ resembles a consistent estimator to the value that can be obtained with $A_{peak}(\text{Hilbert})$ directly.

In the right panel of Fig. 8.5 we use the signals from the left panel to investigate the impact of the chosen upsampling factor on the maximum values. Displayed are the distributions of peak amplitude A_N for a given upsampling factor N divided by the corresponding maximum peak amplitudes obtained using $N = 1000$. The average and spread of the distributions is shown for the direct use of the trace and for the values obtained from the envelopes.
With an increasing upsampling factor both methods saturate towards a maximum value. Especially in the case of using $A_{peak}(\text{Signal})$ upsampling is important to avoid variations induced by the sample distance. Using the envelope yields a more stable estimator of the peak amplitude in the trace. In combination with an upsampling to 1 ns we receive an estimator of A_{peak} contained in the sample series that is stable at a level of $\pm 0.02\%$ when compared to higher upsampling factors.

We will use the upsampling to 1 ns in combination with the envelope to determine the peak amplitude A_{peak} as well as its position t_{peak} in all further data processing:

$$A_{peak} \equiv A_{peak}(\text{Hilbert}) \quad . \tag{8.8}$$

8.3 Directional Reconstruction

The `WaveReconstruction` module mentioned in Sec. 8.1.2 fits the progression of a radio wave front over the detector array using the relative timing of the signal seen in different detector stations.
Using a planar wave front as model for the observation yields the incoming direction of the signal as it was detected in at least three detector stations.
When at least four detector stations are participating in an event also a spherical wave front can be fitted to the data. The fit of a spherical wave reconstructs not only the direction (θ, ϕ) where the signal has come from, but also the distance R where the source of the signal was located. A principal sketch of the reconstruction can be seen in Fig. 8.6.

The details of this reconstruction scheme and its performance we have discussed in Ref. [180]. We will here outline the aspects which have direct impact to our data analysis in the next sections.

8.3.1 Reconstruction of Horizontal Signal Directions

For the reconstruction of the source point $\vec{R}$ of a wave an assumption for the speed of signal propagation is needed. A fix choice for this speed — for instance by the
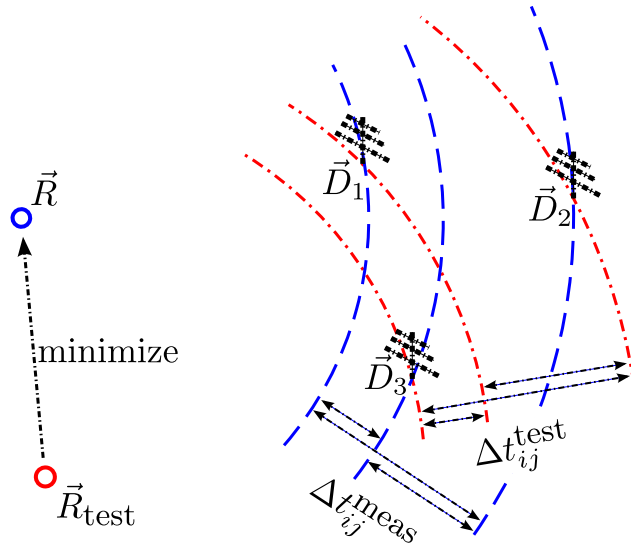
Figure 8.6: Sketch of the reconstruction of a source point $\vec{R}$ of a signal. From the signal position in the individual detector stations the relative timings $\Delta t_{ij}^{\mathrm{meas}}$ are determined and compared to the time differences $\Delta t_{ij}^{\mathrm{test}}$ arising from a hypothetical source point $\vec{R}_{\mathrm{test}}$. The algorithm defines a corresponding χ^2-function which is minimized to find the source point that matches the measured data best. Note that for a reconstruction of a source point in three dimensions, the signal needs to be detected in at least four detector stations.
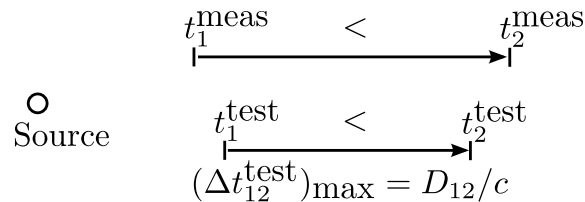
Figure 8.7: Sketch of the best fit (bottom) to a timing difference, that apparently requires a speed of signal propagation slower than the speed of light (top). The fit will propose a source point such that the maximum possible timing difference $(t_{12}^{\mathrm{test}})_{\mathrm{max}}$ is realized. Comparing the residuals $(t_1^{\mathrm{test}} - t_1^{\mathrm{meas}})$ and $(t_2^{\mathrm{test}} - t_2^{\mathrm{meas}})$ the best fit is realized in this scenario when the timing offset is distributed equally between the two residuals. This results in an early-late effect along the propagation direction of the signal.

speed of light — imposes a sudden limitation of accessible timing differences Δt_i in reconstruction procedure. For a given distance D_i between two detector stations the maximal timing difference that the reconstruction can use to compose a signal hypothesis is:

$$(\Delta t_{ij}^{\mathrm{test}})_{\mathrm{max}} = D_{ij}/c \quad . \tag{8.9}$$

Measured timing differences can exceed this maximum due to the limited resolution of the detector. This effect is especially frequent for signals which originate from source points that lie within the relatively flat plane defined by the positions of the detector stations. A sketch showing the consequences for the timing residuals $t_i^{\mathrm{test}} - t_i^{\mathrm{meas}}$ that will be observed in the reconstruction is displayed in Fig. 8.7.
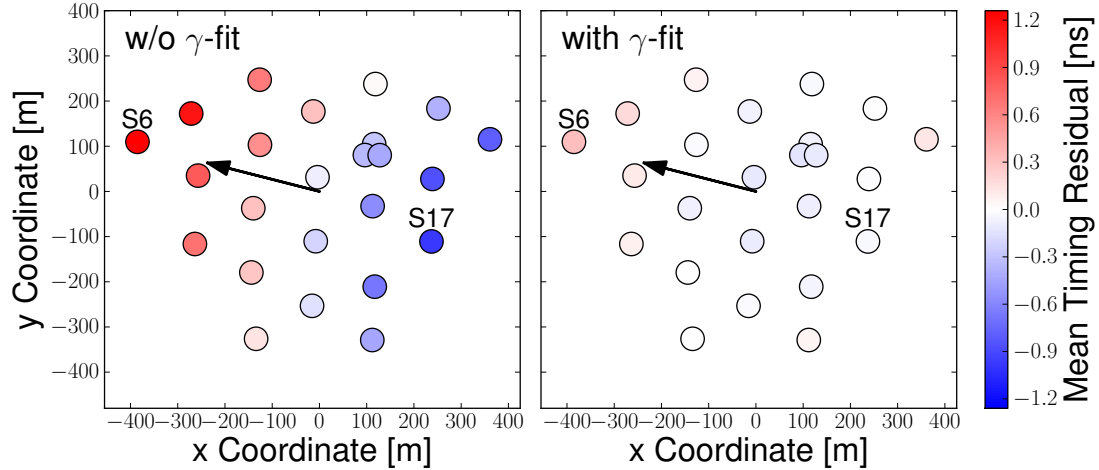
Figure 8.8: Map of timing residuals. The circles mark the positions of AERA detector stations that participate in the reconstruction of a single point that is source to 10^5 simulated radio signals. The source point is located in 2150 m distance along the direction indicated by the arrow. The color scale maps the average timing residuals of the detector positions realized in the reconstruction. Left: Using a simple source fit results in systematic timing bias along the axis towards the source location. The bias is induced by the statistical timing uncertainties of the measurement in the detector stations. Right: A reconstruction that adapts the speed of signal propagation yields unbiased residual distributions.

The detector stations that are closer to a source point will tend to detect signals earlier than proposed by the reconstruction resulting in positive timing residuals. For the distant detector stations the situation is inversed.

In Fig. 8.8 (left) we simulate the reconstruction of a single source point with the AERA array. The circles mark the positions of the AERA detector stations. The source point is located in a distance of ~ 2.2 km within the plane defined by the detector stations in the direction indicated by the arrow. The arrival times from 10^5 signals originating from this source point at the different antennas were calculated including a statistical uncertainty of 5 ns. The number of detector stations participating in individual events is chosen realistically from the corresponding distribution observed in AERA (cf. Fig. 10.2). The color code indicates the average timing residual observed in the reconstruction of the source point at each detector position.

As expected, we observe a systematic bias in the reconstruction that evolves over the detector array along the propagation direction of the signals. The filled histograms in Fig. 8.9 denote the underlying residual distributions of the two detector station 6 and 17 which show the largest bias in this geometric configuration. The distributions deviate from a centered arrangement by a few nano-seconds.
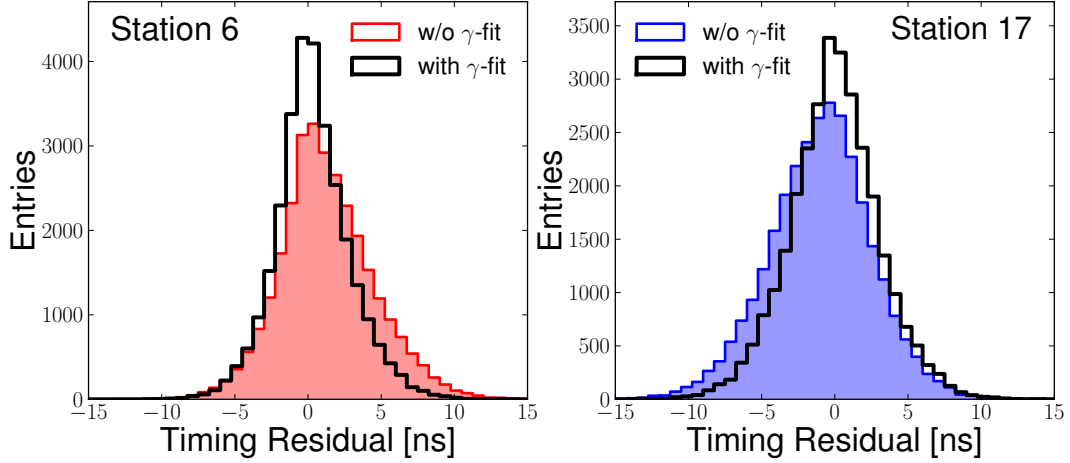
Figure 8.9: The distributions of the timing residuals for the two most extreme detector station seen in Fig. 8.8.

To avoid these systematic offsets we add an additional fit parameter γ in the reconstruction. The γ-parameter allows to change the speed of signal propagation. A timing hypothesis t_i^{test} for a signal arriving at an detector station location $\vec{D}_i$ is then calculated with:

$$t_i^{\text{test}} = |\vec{R} - \vec{D}_i|/(\gamma \cdot c) \quad , \tag{8.10}$$

where $\vec{R}$ is the location of the source point. The γ-factor is a free parameter to our fit to find the source location. The fit is implemented as χ^2-minimization. The γ-parameter is here taken into account by adding the following term to the χ^2-sum:

$$\frac{(1 - \gamma^2)}{(\sigma_\gamma)^2} \quad . \tag{8.11}$$

The amount of contribution of this term to the signal hypothesis is determined by value of σ_γ. To adjust this parameter, we interpret the signal detection as a measurement of the speed of light c. The value of σ_γ is then the relative uncertainty of the measured speed and can be estimated from the distance between the detector stations and the timing uncertainty to be:

$$\sigma_\gamma = \frac{c}{\Delta D} \cdot \sqrt{2}\sigma_t \quad . \tag{8.12}$$

We currently use $\Delta D = 150$ m which is a typical distance between detector station in the first stage AERA and $\sigma_t = 1$ ns as envisaged timing resolution.

In Fig. 8.8 (right) the average timing residuals found in the reconstruction including the γ-factor are displayed. The systematic offsets observed in the left part of the diagram are now avoided. In the given data set we find an average factor of $<\gamma> = 0.997 \pm 0.004$ (RMS) which corresponds to a slight reduction of the signal speed on average. The distributions of the residuals for station 6 and 17 are displayed in Fig.
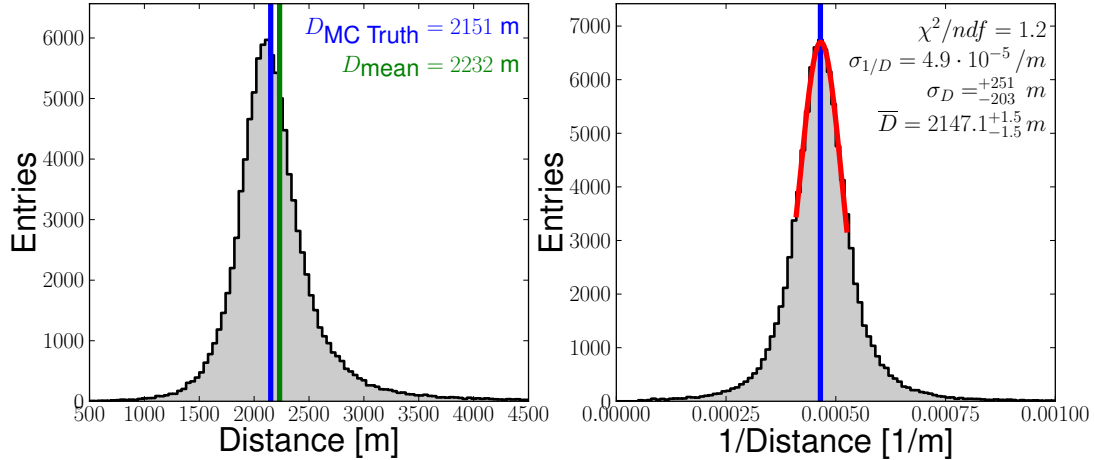
Figure 8.10: The distribution of reconstructed distances of multiple transients from a single source. Left: The direct distance distribution does not realize an unbiased or consistent estimator for the distance to the source. The average of the distribution is too large and the most probable value is too small. Right: The use of the inverse distance distribution yields the desired estimator for the source distance.

8.9 as black histograms. The fit of the γ-factor strongly reduces the bias induced by statistical timing uncertainties to the source point reconstruction.

As the bias is specific for incoming direction towards the horizon, we apply the additional γ-fit only to zenith directions $\theta > 80°$ in the usual reconstruction scheme. An unbiased reconstruction towards the horizon will be important for a timing calibration of AERA performed in Sec. 10.2.

8.3.2 Estimator for the Source Distance

From the Monte-Carlo data set used in the previous section we investigate the reconstructed distance towards the source point of the signals. We measure the distance with respect to a fix point within the detector array which we identify the barycenter of the detector stations. [3].

The distribution of reconstructed distances is displayed in Fig. 8.10 (left). The reconstructed distances are closely related to the true distance which have used to initiate the Monte-Carlo. However, the mean value of the distribution is larger than the initial distance whereas the most probable value is too small.

Looking at the right panel of Fig. 8.10 we find that an unbiased and consistent estimator to the source distance is given by the inverted distance distribution. Fitting a Gaussian to the inverted distribution we reconstruct the following values in the example:

$$\overline{D} = 2147 \pm 2\,\mathrm{m} \tag{8.13}$$

---

[3]The barycenter corresponds to the origin of the arrows given in Fig. 8.8.

with

$$\sigma_{68\%} = \pm \begin{pmatrix} 250 \\ 200 \end{pmatrix} \mathrm{m} \quad \hat{=} \quad \pm \begin{pmatrix} 12 \\ 9 \end{pmatrix} \% \quad , \tag{8.14}$$

which indicates a precise reconstruction of the source point from multiple detections of its signals. The 68%-quantiles roughly indicate distance resolutions that can be achieved in the reconstruction of single radio signals with this method.

9. Measurement of the Lateral Distribution Function

9.1 Measurement Setup and Reconstruction of Radio Data

The data used in the chapter was recorded with the measurement setup described in Sec. 5.2.1. The setup consisted of three radio detector stations. Two stations were continuously equipped with logarithmic-periodic dipole antennas (LPDAs). At the third station first a prototype wire antenna was installed which was replaced by a LOFAR antenna during data taking.

A voltage trace for a clear radio signal measured at all three stations of the setup is visible in Fig. 9.1. The voltage traces have a total length of 10 μs where $\sim$ 2 μs before and 8 μs after a trigger has occurred are recorded. At each station a North-South (NS, black curve) and a East-West (EW, red curve) polarized antenna is mounted.

As a first step of reconstruction, the signal at the foot-point of the antenna is identified. The effects of the readout setup such as cables, filters and amplifiers are removed from the raw data except for the antenna and the low noise amplifier (LNA) which are treated as conjoint hardware part.

To identify pulses in the voltage trace a signal-to-noise ratio threshold is used, where we define the signal-to-noise of a signal as:

$$S/N = \frac{A_{peak}}{\sigma_{noise}} \quad , \tag{9.1}$$

where A_{peak} is considered amplitude in the envelope of the traces as described in Sec. 8.2. The noise rms of the respective measurement is determined from the first 2 μs of the voltage trace.

With the knowledge of cable lengths, distances between the antennas and timing offsets the position of radio signals is confined to lie in a time window from 2.41 to 3.07 μs within the 10 μs of recorded data. Within this search window the overall highest peak of the three stations is identified and accepted if its S/N ratio is greater than a certain parameter.

With the knowledge of the position of this radio pulse, the search window for the other two stations can be reduced further. Here, the reduced size of the search window is used to relax the minimum signal-to-noise requirement to the pulse.
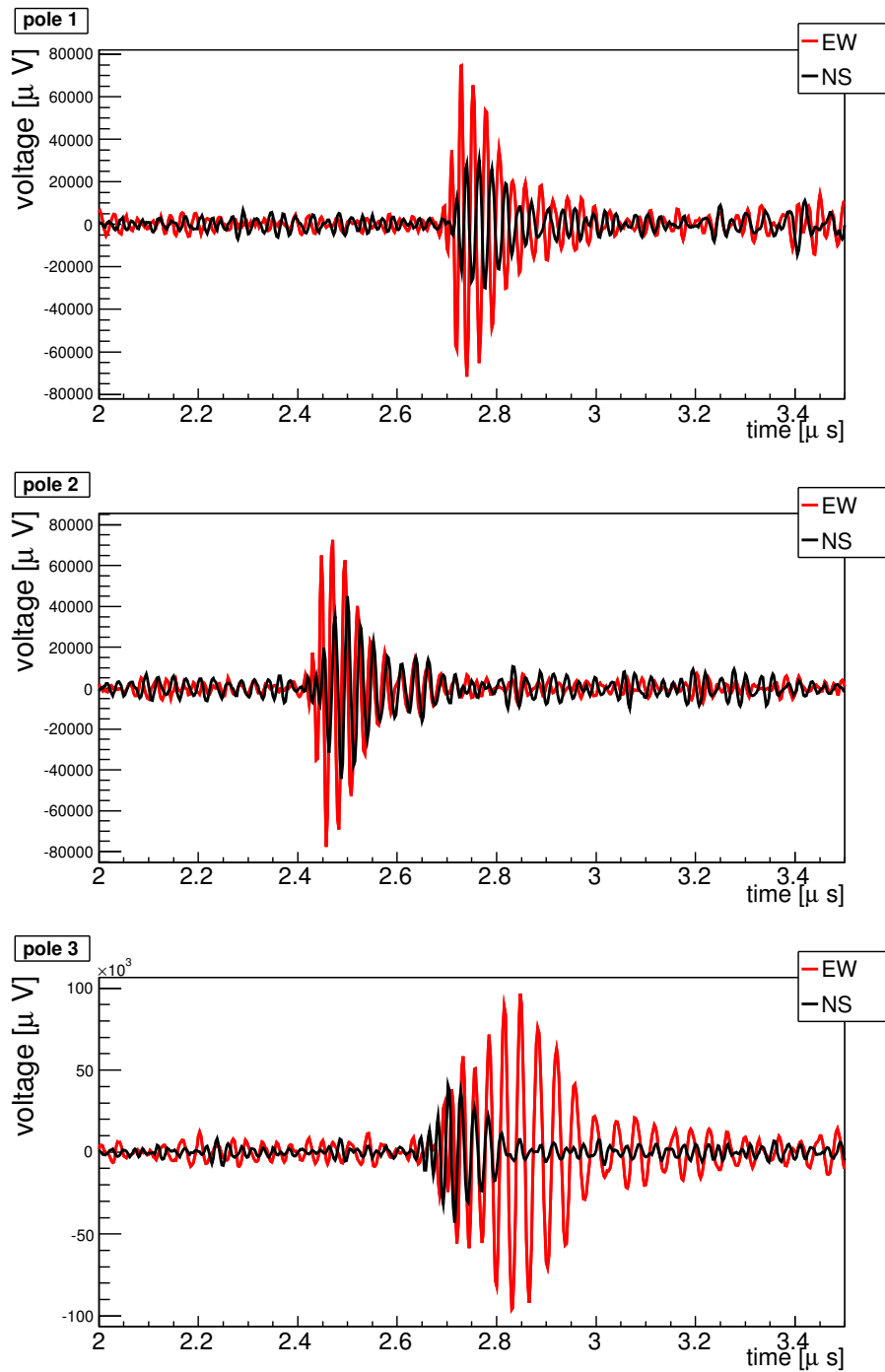
Figure 9.1: Excerpt of a voltage trace of a radio pulse detected at all three stations of the radio detector. Each station is mounted with a East-West and North-South polarized antenna (red and black curve).

With the obtained timing information of the radio signal and the position of the antennas, the direction of arrival of the radio signal is reconstructed. Here, the three different measurement locations of the detector setup allow for a reconstruction of a plane wave.

To obtain a physical quantity that is independent of the detector setup, the electric field at each station is reconstructed using the method described in Sec. 6.5 using the reconstructed incoming direction of the signal. An electric field resulting from this reconstruction can be seen in Fig. 9.2.

To minimize the shift of the position of the pulses within the recorded trace the almost dispersion-less group delay of the 160 m coaxial cable is not unfolded from the data.

The induced group delay of the effective height of the antenna $\vec{\mathcal{H}}$ depends on the incoming direction of the radio signal. Hence the positions of the radio pulses in the electric field traces should be more precise when the proper incoming direction is used to remove the impact of the antenna from the data. Therefore, the cycle of fitting the incoming direction to the pulse positions and reconstructing the electric field is iterated a few times.

9.2 Data Set and Cuts

The data used in this note was taken from April 2007 till May 2008. In this period 494 events were triggered by the scintillator panels in coincidence with the SD detector. Thus major shower properties are known from the SD reconstruction which we can use to confirm the radio reconstruction.

In Fig. 9.3 an overview of the azimuth, zenith and energy distribution of recorded air showers is shown. The azimuth distribution is flat and the zenith distribution is roughly proportional to $\cos(\theta)\sin(\theta)$ which is the expected behavior for a flat detector geometry. We note that for higher zenith angles no events are recorded. The energies range from about $10^{16.5}$ eV to 10^{19} eV.

From these 494 events 62 events can be reconstructed identifying a pulse with a reasonable S/N-level at all three detector stations. To check whether the reconstruction is successful, the direction of the shower reconstructed by the radio detector is compared to the information of the SD detector. Figure 9.4 shows a histogram of the angular distance between the direction of the shower from the radio and the SD reconstruction. A few events have a huge angular distance of up to 120° and are thus unlikely to be related to the air shower event seen in the SD or reconstructed incorrectly. Thus, only events with an angular distance less than 20° are accepted as successfully reconstructed. 44 events pass this criterion.

For angular distances less than 20°, a Rayleigh function fits the data well. Hence, the angular resolution can be determined to $\sigma_{68\%} = 8.5° \pm 0.7°$.
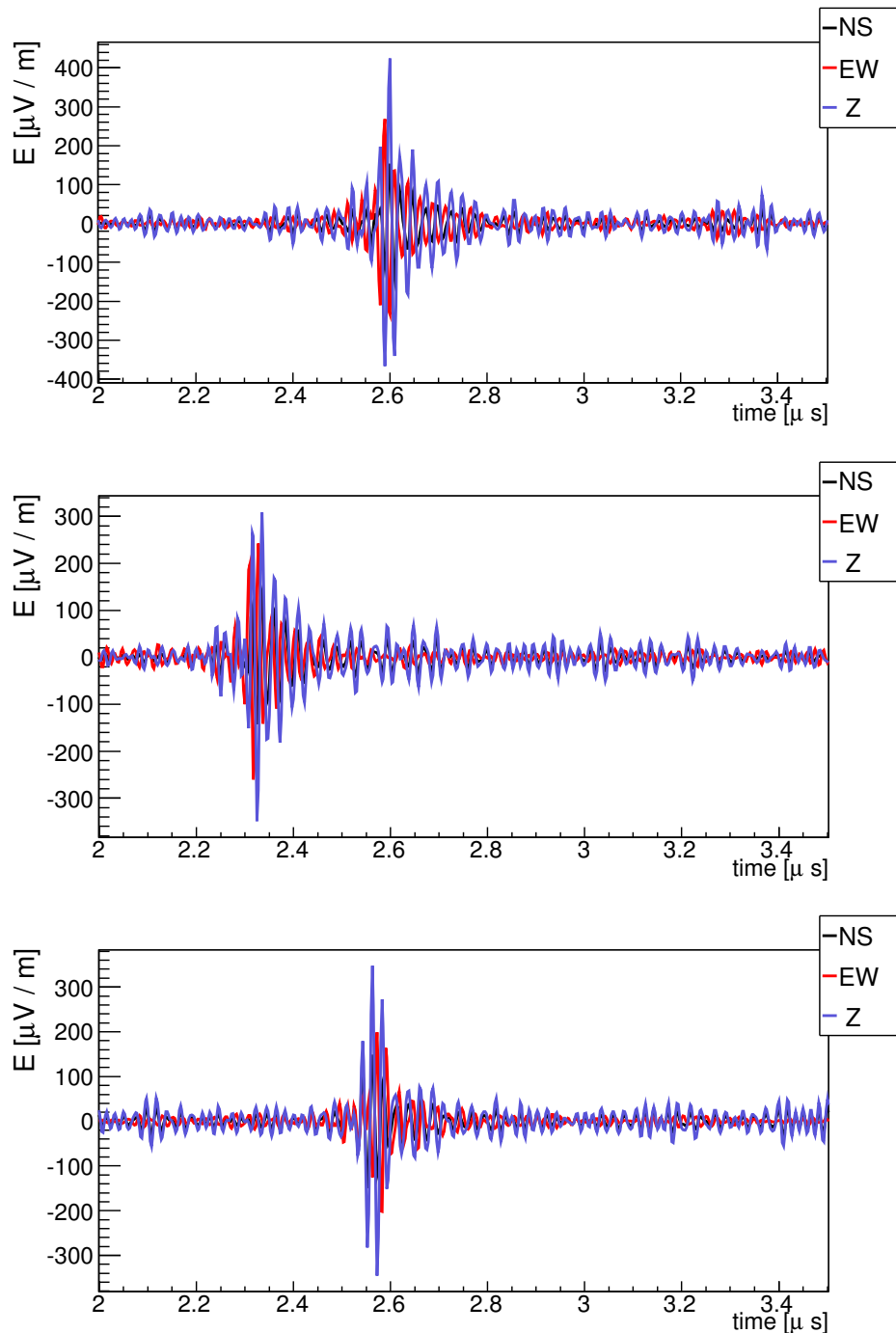
**Figure 9.2:** Reconstructed electric field traces of the radio signal displayed in Fig. 9.1.
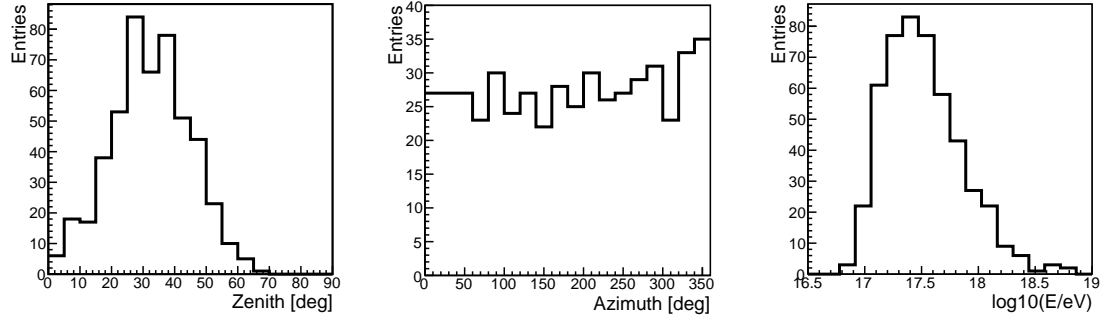
Figure 9.3: Zenith, azimuth and energy distribution of all radio events triggered in coincidence with SD. Angles and energies are taken from the SD reconstruction.
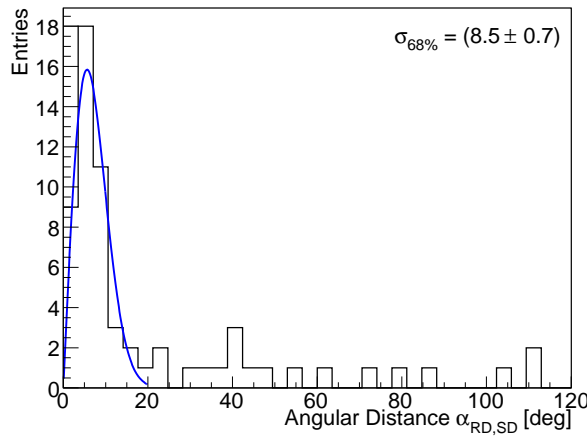

Figure 9.4: Angular difference between the direction of the shower from the radio and the SD reconstruction.

In Fig. 9.5 the signal-to-noise ratios of the events remaining in the selection are displayed. We find that all pulses exceed a signal-to-noise ratio of 3.6.

The zenith, azimuth and energy distribution of the successfully reconstructed events are shown in figure 9.6. The distributions have no significant change compared to all 494 triggered events. We note that successful reconstructions are not restricted to the events with the highest energies.

Figure 9.7 displays the positions of the three stations, the positions of the shower cores of all triggered events and the positions of the shower cores of the successfully reconstructed events. The shower cores of the reconstructed showers still distribute widely around the stations, but the number of events decreases at larger distances.
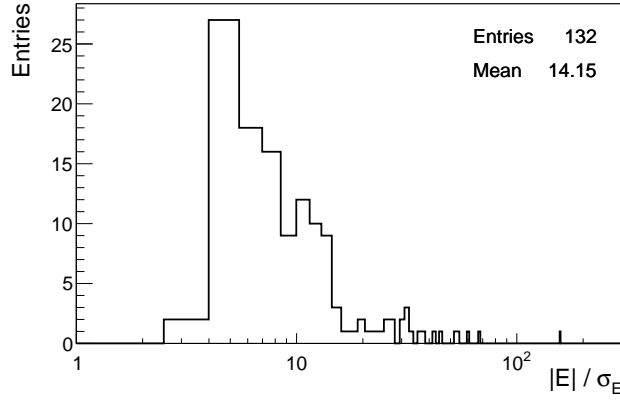
Figure 9.5: The signal-to-noise ratios of all events for which a pulse could be identified in all three antennas.
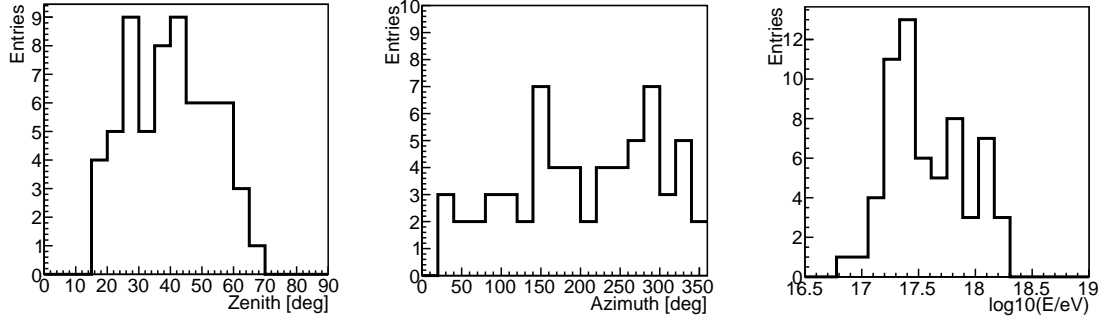
Figure 9.6: Zenith, azimuth and energy distribution of the events successfully reconstructed with the Radio detector. The angle and energy information is taken from the SD reconstruction.

In tab. A.4 the Auger Ids of the radio events yet remaining in the selection are listed. Seven events are identified which were recorded during thunderstorms or where no thunderstorm information is available [181]. As the presence of additional electric fields during thunderstorms can influence the generation of the radio pulse [182, 183] we reject these events from our analysis.

As mentioned in Sec. 9.1 only the antennas mounted at station 1 and 2 have the same specification. Hence, for the analysis the next sections only the signals measured at station 1 and 2 will be used.

During the measurement period filter setups with different bandwidths ($BW_1 \approx 31$ MHz, $BW_2 \approx 18$ MHz) were employed. Usually the same filter setup was used for all antennas, however, in the case of two events the antennas at station 1 and 2 were operated with different filter setups. As we do not know if the air shower signal is distributed over the whole frequency range equally we exclude these two events from our analysis (cf. tab. A.4).

Using these selection criteria 35 events remain in our data set.
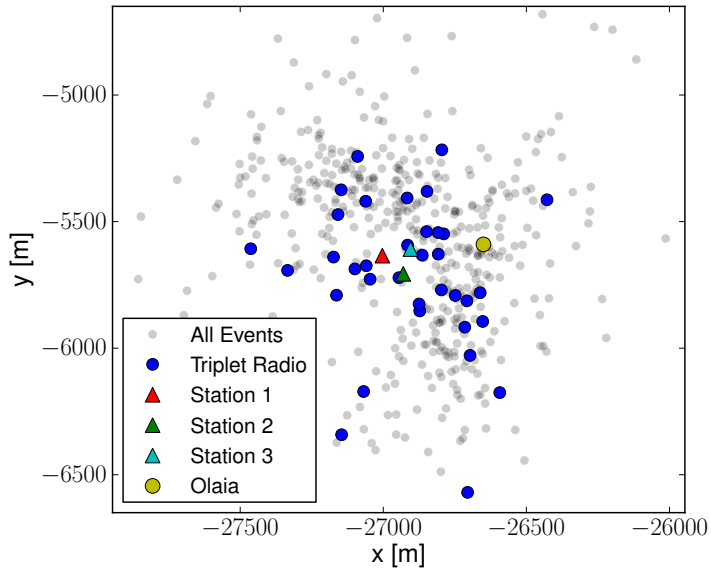
Figure 9.7: Positions of the three stations of the radio detector, the nearest SD tank Olaia and the shower cores of the 494 detected UHECRs in coincidence with the SD detector (gray circles). The successfully reconstructed events are marked in solid blue.

9.3 Lateral Signal Distribution

To investigate the dependency of the intensity of the radio signal on the lateral distance to the shower axis, we assume that the signal of single air shower events measured at the two independent antenna positions is governed by two sets of parameters.

The first parameter set influences the signal in the individual antennas in the same way. Such parameters are i.e. the energy of the primary particle or the angle of the shower axis towards the magnetic field of the earth.

The second set of parameters applies to the radio intensity measured at each antenna position individually. In the case of a simple LDF model the only such parameter will be the distance D between the shower axis and the measurement position. Following the suggestion of Allan [64] for single air shower events a purely exponential LDF is used to describe the measurements done in various experiments [65, 184]. However, simulations of the air shower signal suggest that also the angle of the observing position in the shower plane influences the signal strength [77].

In the following we are going to test the hypothesis of a LDF that is primarily governed by the lateral distance D between shower axis and observing position. In this case the intensity at each antenna can be factorized into its dependency on D and its dependency on other shower parameters:

$$S(E, \alpha_B, D, ...) = S(E, \alpha_B, ...) \cdot S(D) \qquad . \qquad (9.2)$$

Here E - the energy of the primary particle - and α_B - the angle to the earth's magnetic field - are representatives for further properties of the air shower which are the same at all observing positions.

Using this separation ansatz, we investigate the difference in signal strength ΔS measured in two antennas from the same air shower event:

$$\frac{\Delta S}{\Sigma S} = \frac{S_1 - S_2}{S_1 + S_2} \tag{9.3}$$

$$= \frac{S(E, \alpha_B, ...) \cdot S(D_1) - S(E, \alpha_B, ...) \cdot S(D_2)}{S(E, \alpha_B, ...) \cdot S(D_1) + S(E, \alpha_B, ...) \cdot S(D_2)}$$

$$= \frac{S(D_1) - S(D_2)}{S(D_1) + S(D_2)} \quad , \tag{9.4}$$

where D_1 and D_2 are the perpendicular distances between the respective station and the shower axis. Thus, we have defined a quantity that depends on the distances to the shower axis only. [1]

In figure 9.8, a sketch of the geometrical situation is shown. Depending on the direction of the shower, station 1 and 2 measure the signal at two different distances D_1 and D_2. The difference in the distance ΔD ranges from 0 m, if the shower axis is parallel to the connecting line of station 1 and 2, up to ~ 103 m which is the distance between station 1 and 2.

In the following section, we will analyze the behavior of the relative difference of intensity $\frac{\Delta S}{\Sigma S}$ in combination with the distances D_1 and D_2. Note that for all calculations the core position and the shower direction from the SD reconstruction will be used.

9.3.1 Characterization of the Test Values

9.3.1.1 Relative Difference of Intensity

The reconstruction described in section 9.1 delivers the radio signal in terms of a field strength vector as a function of time. As we are interested in absolute signal strength, we calculate the signal intensity as follows:

$$S_{BW} = \frac{1}{Z_0 \cdot BW} \cdot (E_{NS}^2 + E_{EW}^2 + E_Z^2) \quad , \tag{9.5}$$

where $Z_0 \approx 120\pi$ is the impedance of free space and $E_{NS,EW,Z}$ are the peak values of the individual field components read from their respective envelopes.

During the measurement period two different filter setups with different bandwidths ($BW_1 = 31$ MHz, $BW_2 = 18$ MHz) were used. To account for this the signal intensity is normalized to the corresponding bandwidth.

As can be seen in Fig. 9.9 (left) the measured intensities range over a few orders of magnitude.

---

[1]Allan [64] already suggested that the scaling parameter R_0 of an exponential LDF might depend itself i.e. on the zenith angle θ. Following the observations done in [65] we could assume for instance $R_0 = R_0' \cdot (1 - \sin\theta)$. Such interdependency is not canceled in the quantity $\Delta S/\Sigma S$ and will lead to an additional scatter of the data points.
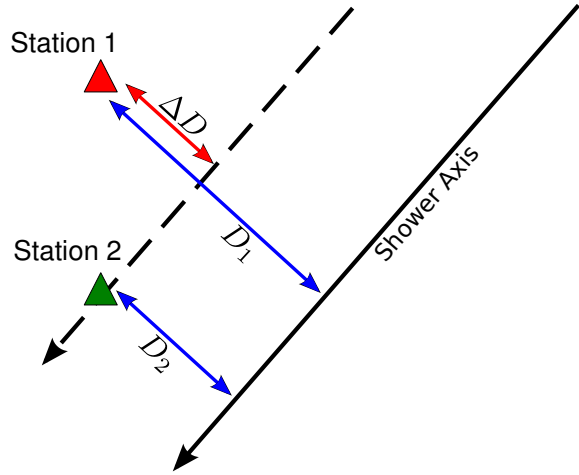
**Figure 9.8:** Geometry of the radio detector setup. D_1 and D_2 are the perpendicular distances between the respective station and the shower axis. Depending on the direction of arrival of the air shower the difference of D_1 and D_2 (ΔD) can vary from 0 m to the distance between station 1 and 2 of ~ 103 m.
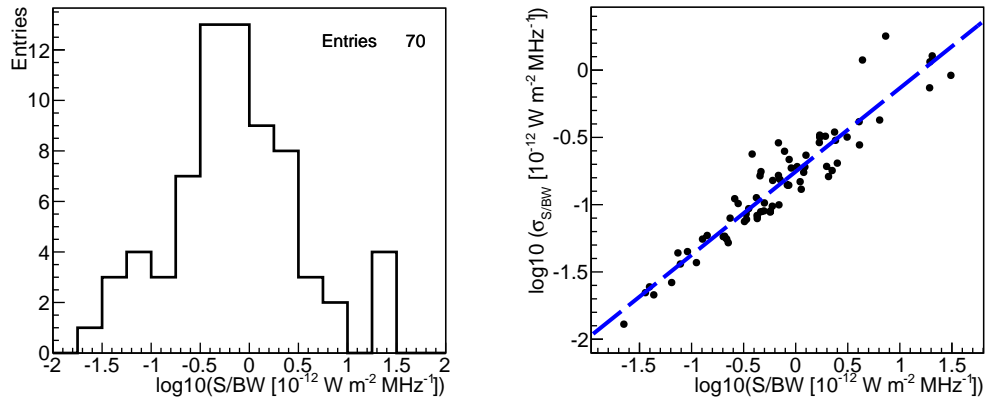

Figure 9.9: Left: Intensity distribution of radio events. To compare the intensity measured with different bandpass filters, the intensity is normalized to the bandwidth. Right: The dependency of $\sigma_{S_{BW}}$ on S_{BW}. The dashed line is a fit to the data which yields $\sigma_{S_{BW}} \propto S_{BW}^{0.62\pm0.03}$ - the uncertainty of S_{BW} thus increases with about the square root of S_{BW}.

Uncertainty Calculation

The noise of the measurement is dominated by the galactic noise background [185]. We use the width of the noise distribution as uncertainty on the measured field
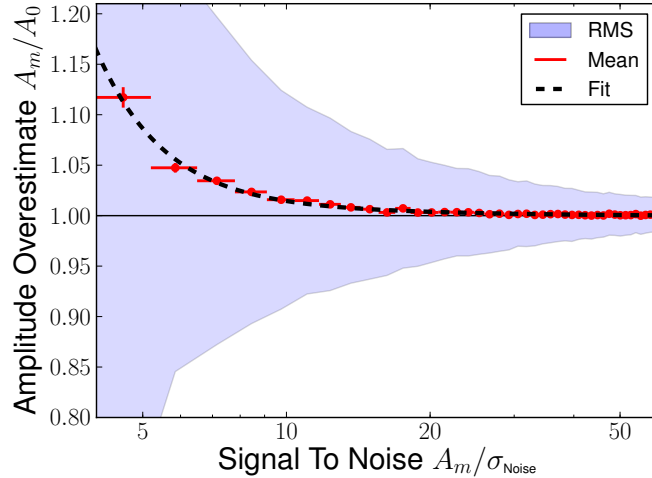
Figure 9.10: The systematic shift in the reconstruction of the signal amplitude in the Envelope of the trace due to noise. Towards low signal-to-noise ratios the reconstruction tends to overestimate the measured amplitude. The ratio of the reconstructed to the true amplitude as determined from simulations is given as the red symbols. The development of the systematic shift as function of frequency is matched with a function $f(x) = 1 + a\,e^{-b\,x} + c\,x^{-3}$. The statistical uncertainty of the amplitude due to noise is indicated as blue band and covered by the discussion in Fig. 9.9.

strength. If we assume that the noise of station 1 and 2 is uncorrelated, the uncertainty of $\frac{\Delta S}{\Sigma S}$ can be calculated analytically:

$$\sigma_S = \frac{2E}{Z_0} \cdot \sigma_E \tag{9.6}$$

$$\sigma^2_{\frac{\Delta S}{\Sigma S}} = \left(\frac{1}{S_1 + S_2} - \frac{S_1 - S_2}{(S_1 + S_2)^2} \right)^2 \sigma^2_{S_1} + \left(\frac{-1}{S_1 + S_2} - \frac{S_1 - S_2}{(S_1 + S_2)^2} \right)^2 \sigma^2_{S_2}$$

$$= 4 \cdot \frac{S_2^2 \sigma^2_{S_1} + S_1^2 \sigma^2_{S_2}}{(S_1 + S_2)^4} \quad . \tag{9.7}$$

In figure 9.9 (right) σ_S is plotted as a function of S. We find that σ_S increases approximately with the square root of S which is equivalent to a constant uncertainty induced by the electric field:

$$S = \frac{1}{Z_0} \cdot \vec{E}^2 \quad \Rightarrow \quad \sigma_S = \frac{2E}{Z_0} \cdot \sigma_E \quad \text{and} \quad \sigma_E \approx const.$$

$$\Rightarrow \sigma_S \propto E \propto \sqrt{S} \quad . \tag{9.8}$$

Systematics in Amplitude Reconstruction

As discussed we use the envelopes of the sampled traces to determine the respective peak amplitudes. Following the discussion in Ref. [186] the read-out amplitude will be overestimated due to presence of additional noise in the trace.

To evaluate this systematic shift we simulate noise traces which are generate according to the galactic noise intensity using the RDAS software. As signal a delta

functions with varying amplitudes are added to the traces. The traces are then limited to the common bandwidth of the detector.

In Fig. 9.9 the peak values read out from the trace envelopes at the signal position are compared to the readings obtained from pure signal traces without additional noise. The initial amplitude is varied such that different signal-to-noise ratio are accessed. Regarding the ratios of readings with and without noise, the reconstruction overestimates the peak amplitude especially at low signal to noise ratios. We use a function:

$$f(x) = 1 + a\,e^{-b\,x} + c\,x^{-3} \quad \text{with} \quad a = 7.5 \cdot 10^{-3},\, b = 5.4 \cdot 10^{-2},\, c = 10 \qquad (9.9)$$

to match the observed dependency. This function is used to correct the measured peak values in the following.

In Fig. 9.9 also the statical variation of the peak amplitude due to the presence of noise is indicated as blue band. The impact of the statistical uncertainty is already covered in our analysis with Eqn. 9.6. It should be noted that the statistical uncertainty dominates the uncertainty of the signal. We find that the correction of the peak amplitude derived in this section influence the results obtained the later sections of this analysis within the respective uncertainties only.

9.3.1.2   Distance to Shower Axis

The perpendicular distance from the station to the shower axis can be calculated with

$$D = \frac{|(\vec{X}_{Pole} - \vec{X}_{ShowerCore}) \times (\vec{X}_{Pole} - \vec{X}_{ShowerAxis})|}{|\vec{X}_{ShowerAxis} - \vec{X}_{ShowerCore}|} \quad , \qquad (9.10)$$

where $\vec{X}_{Pole}$ is the position of the station, $\vec{X}_{ShowerCore}$ is the position of the shower core and $\vec{X}_{ShowerAxis}$ is an additional point on the shower axis which can be computed from the position of the shower core and the direction of the shower defined by the zenith (θ) and azimuth (ϕ) angle. The difference in the distance to the shower axis of station 1 and 2 (ΔD) then is:

$$\Delta D = D(\vec{X}_{Pole1}) - D(\vec{X}_{Pole2}) \qquad . \qquad (9.11)$$

Uncertainty Calculation

The uncertainties of the distance to the shower axis from station 1 (D_1) and station 2 (D_2) are correlated. If the direction of the shower is parallel to the connecting line of station 1 and 2, the position of the shower core will not have any effect on ΔD. But if the shower direction is perpendicular to the connecting line of station 1 and 2, the position of the shower core will have a huge influence on ΔD.

To determine the uncertainty on ΔD the position of the shower core and the zenith and azimuth angles are varied 1000 times within their uncertainties for each event. We use the root mean square of the resulting distribution as uncertainty of ΔD.
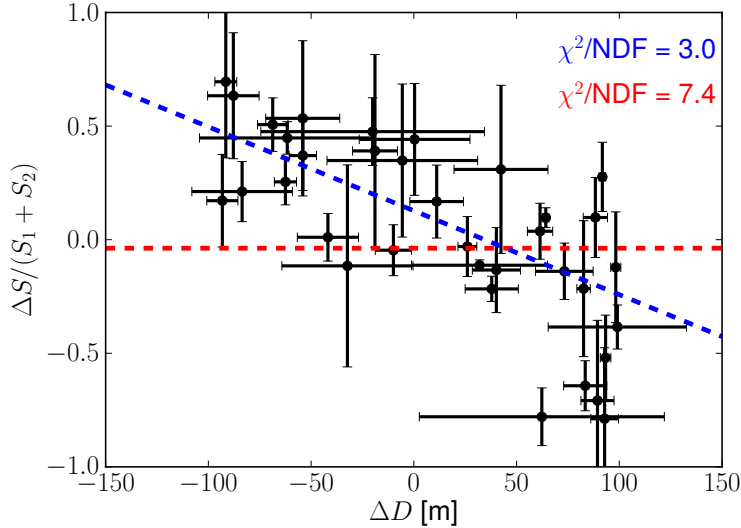
Figure 9.11: Relative difference of the intensity of station 1 and 2 as a function of the difference of the distance to shower axis $\Delta D = D_1 - D_2$. A slope (dashed blue) and a constant (dashed red) is fitted to the data and the respective χ^2/ndfs are displayed.

9.3.1.3   Relative Difference of the Intensity depending on Different Distances

As we have now calculated the uncertainties on the test quantities we can analyze the dependency of $\frac{\Delta S}{\Sigma S}$ on ΔD. In Figure 9.11, $\frac{\Delta S}{\Sigma S}$ is plotted as a function of ΔD. We observe a linear decrease that can be quantified by fitting a slope and a constant to the data. The χ^2/ndfs show that the slope describes the data better than a constant.

The data matches the expected behavior. If ΔD is negative, the shower passes station 1 more closely than station 2. Therefore, station 1 should measure a larger intensity than station 2 which results in a positive value for $\frac{\Delta S}{\Sigma S}$.

The fit of the slope to the data yields:

$$\Delta S/\Sigma S = (0.13 \pm 0.03) + (-0.0057 \pm 0.0004)/\text{m} \cdot \Delta D \quad . \tag{9.12}$$

We observe an axis offset which not consistent with zero. This is surprising as the symmetry of the observables with respect to the measurement setup suggest the axis offset to vanish. A possible cause for the positive axis offset is that signals recorded at station 1 are systematically larger than those from station 2. In the next section we thus investigate the noise recorded along with the air shower signals to receive an independent calibration of the measurement setup.

9.3.1.4   Calibration of Measured Radio Intensity

From the first 2 μs of each recorded trace the noise RMS is calculated (cf. Sec. 9.1). In Fig. 9.12 (left) these σ_{Noise} values are displayed as a function of sidereal time. As
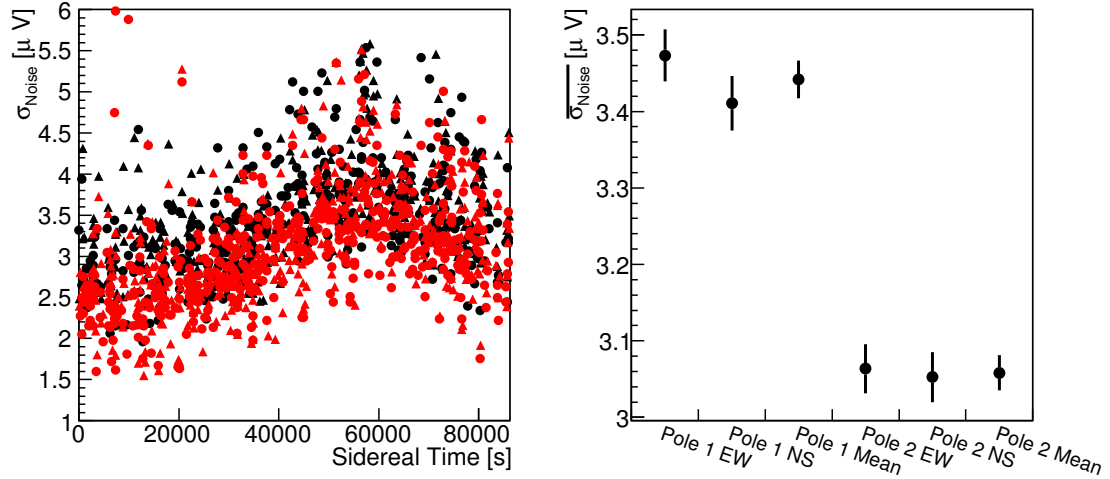
Figure 9.12: Noise observed in the complete dataset. On the left-hand side the individual noise measurements are plotted as a function of sidereal day time and separated into measurements from station 1 EW (black triangles), station 1 NS (black circles), station 2 EW (red triangles) and station 2 NS (red circles). On the right-hand side the data is merged into the mean behavior of the four channels and finally into the mean behavior of the two stations. The noise observed at station 1 is enhanced by a factor of 1.13 ± 0.01 in comparison to station 2.

the observation of noise is not necessarily constrained to the presence of air shower signals in the trace, data from station 1 and 2 is taken into account using all 494 events. Only data which suffers extraordinary high noise levels or broken channels is rejected. The variation of the noise with the galaxy points at the low noise levels obtained in these measurements [185].

If the mean noise levels at station 1 and 2 are investigated as done in Fig. 9.12 (right) we find that the noise recorded at station 1 is stronger than the noise observed at station 2 by a factor of 1.13 ± 0.01. If we assume that the noise at both stations is dominated by the galactic noise we conclude that recorded amplitudes suffer a systematic shift between the two stations which we will correct for in the following data analysis.

In Fig. 9.13 the plot from Fig. 9.11 is redone but this time the traces from station 2 have been enhanced by the factor 1.13 before evaluating them for the analysis. The fit of a slope now yields:

$$\Delta S / \Sigma S = (0.02 \pm 0.03) + (-0.0036 \pm 0.0004)/\text{m} \cdot \Delta D \quad . \tag{9.13}$$

We observe that the axis offset is now well compatible with zero which fits the expectation regarding our test quantities (cf. Sec. 9.3.1.3). As the data displayed in Fig. 9.13 does not depend systematically on the noise observed in the measurements we receive an independent confirmation that the relative calibration is successful.
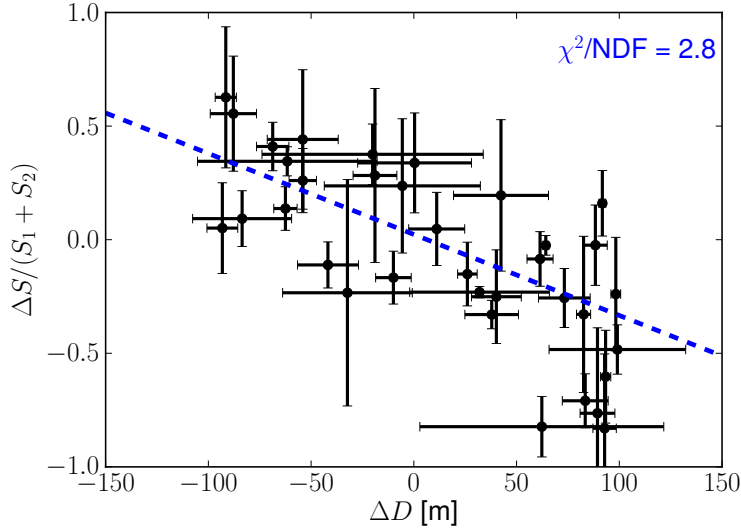
Figure 9.13: Relative difference of the intensity of station 1 and 2 as a function of the difference of the distance to shower axis $\Delta D = D_1 - D_2$. The same data as in Fig. 9.11 is displayed but this time a relative calibration of station 1 and 2 is applied. The fit of a straight line now yields an axis offset that is well compatible with zero (see Eqn. 9.13).

In the following analysis functional dependencies will be fitted to the data. This will be done with an axis offset fixed to zero. Note that the two combinations of:

1. Fixing the axis offset to zero and applying the relative calibration

2. Releasing the axis offset and leaving the data uncalibrated

will vary the results within their uncertainties only.

9.3.2   Analysis of Radio Data

Fig. 9.14 shows a histogram of the mean absolute distance $\bar{D} = (D_1 + D_2)/2$ of the two antennas to the shower axis for the detected events. The detected events distribute between distances from 50 m up to 750 m to the shower axis.

In Fig. 9.15 the events are grouped into events which have distances $\bar{D} < 150$ m, 150 m $< \bar{D} < 300$ m and $\bar{D} > 300$ m.

For each of these groups, $\Delta S / \Sigma S$ is plotted as a function of ΔD and a straight line is fitted. In the lower right display of Fig. 9.15 the slope of the corresponding fits is depicted as a function of mean distance in the three distance bins. We observe that the fitted slope is different for each group. The slope decreases with increasing distances to the shower axis.

9.3.2.1   Impact of Different LDF Models on $\Delta S / \Sigma S$ vs. ΔD vs. $\bar{D}$

To establish a connection between our test variables ($\frac{\Delta S}{\Sigma S}$, ΔD and $\bar{D}$) and the lateral distribution function (LDF), the impact of LDFs exhibiting an exponential falloff and LDFs following a power law is investigated. The LDF test models are:
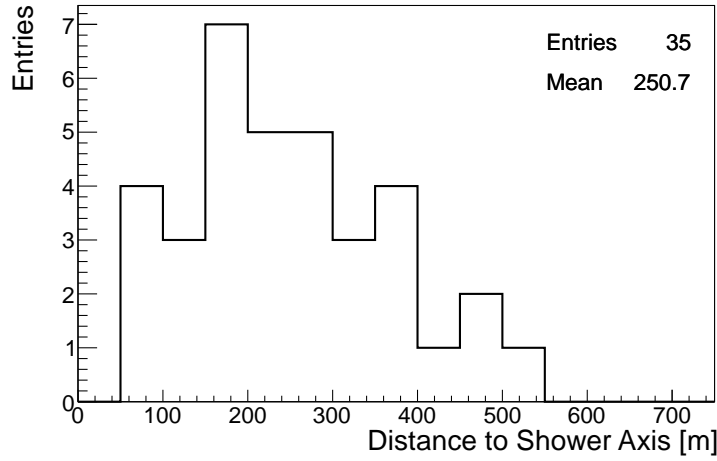
Figure 9.14: Distribution of the mean antenna distance perpendicular to the shower axis: $\bar{D} = (D_1 + D_2)/2$.
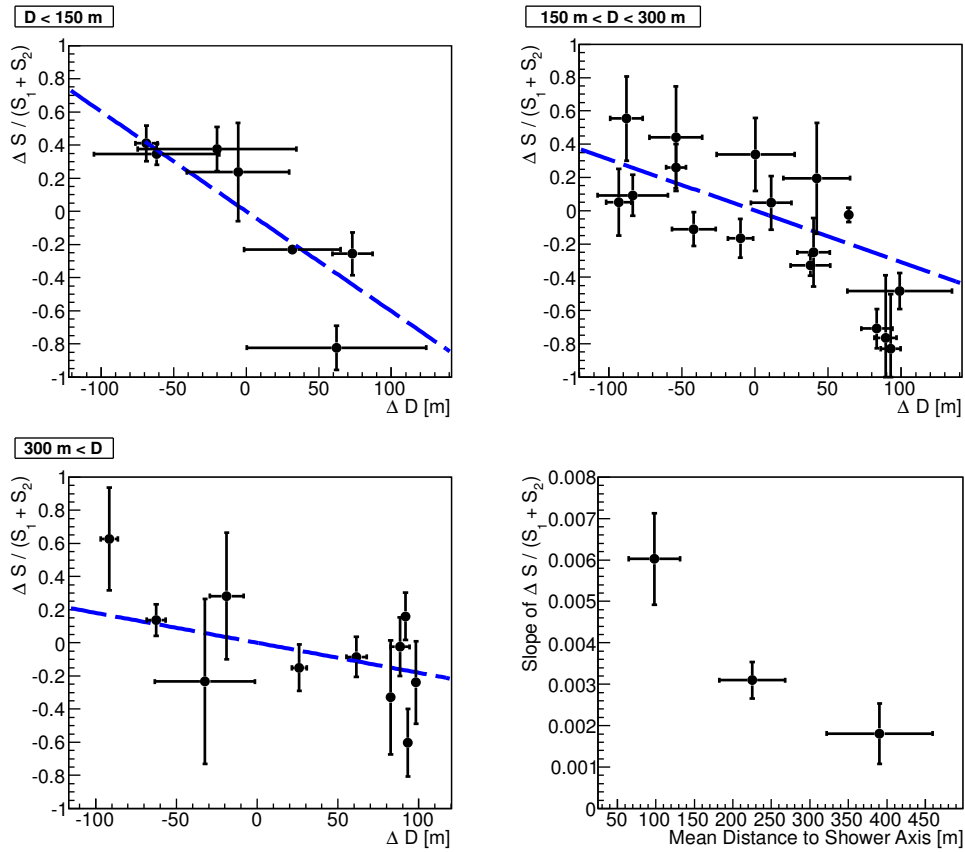
Figure 9.15: The radio events are split into three groups according to their distance $\bar{D}$ towards the shower axis. A straight line is fitted to the data. In the lower right display the (negative) slope of the fits is plotted as a function of mean distance in the respective distance bin. The bars in the x-direction indicate the RMS of the distance distribution in the corresponding bin.

- $S(D) \propto D^{-x}$, with x the power law index

- $S(D) \propto e^{-D/R_0}$, with R_0 the scaling parameter. [2]

To evaluate the test values we make use of the following relations:

$$D_1 = \bar{D} + \frac{\Delta D}{2} \quad \text{and} \quad D_2 = \bar{D} - \frac{\Delta D}{2} \quad , \tag{9.15}$$

where D_1 and D_2 are the distances to the respective station positions (cf. Fig. 9.8).

LDF Model $S(D) \propto D^{-x}$

For $S \propto D^{-x}$ we find that the variables have to following interdependency:

$$\frac{\Delta S}{\Sigma S} = \frac{D_1^{-x} - D_2^{-x}}{D_1^{-x} + D_2^{-x}} = \quad \dots \overset{\bar{D} \gg \Delta D/2}{\approx} \dots \quad = -\frac{x \Delta D}{2 \bar{D}} \quad . \tag{9.16}$$

For the details of the calculation see the appendix A.5. Consequently, fitting a straight line to the data:

$$\frac{\Delta S}{\Sigma S} = m \cdot \Delta D \tag{9.17}$$

as done i.e. in Fig. 9.15 will result in a slope m that changes with distance $\bar{D}$ to the shower axis from where the data was obtained:

$$-\frac{x \Delta D}{2 \bar{D}} \overset{!}{=} m \cdot \Delta D \quad \Rightarrow \quad m = \frac{x}{2 \bar{D}} \quad . \tag{9.18}$$

LDF Model $S(D) \propto e^{-D/R_0}$

In the case of an exponential LDF $S(D) \propto e^{-D/R_0}$ we find that $\frac{\Delta S}{\Sigma S}$ is independent of the absolute distance to the shower axis $\bar{D}$:

$$\frac{\Delta S}{\Sigma S} = \frac{e^{-\frac{D_1}{R_0}} - e^{-\frac{D_2}{R_0}}}{e^{-\frac{D_1}{R_0}} + e^{-\frac{D_2}{R_0}}} = \frac{e^{-\frac{D_1}{R_0}}\left(1 - e^{\frac{D_1 - D_2}{R_0}}\right)}{e^{-\frac{D_1}{R_0}}\left(1 + e^{\frac{D_1 - D_2}{R_0}}\right)} = \frac{1 - e^{\frac{\Delta D}{R_0}}}{1 + e^{\frac{\Delta D}{R_0}}} \tag{9.19}$$

$$\overset{R_0 \gg \Delta D}{\approx} \frac{-\frac{\Delta D}{R_0}}{2 + \frac{\Delta D}{R_0}} \overset{R_0 \gg \Delta D}{\approx} -\frac{\Delta D}{2 R_0} \quad . \tag{9.20}$$

Therefore, the fit of a straight line to the data should result in a slope m that does not change with distance $\bar{D}$ and that is directly related to the scaling parameter R_0:

$$\frac{\Delta S}{\Sigma S} = m \cdot \Delta D \overset{!}{=} -\frac{\Delta D}{2 R_0} \quad \Rightarrow \quad m = -\frac{1}{2 R_0} \quad . \tag{9.21}$$

---

[2]Note that this definition of the scaling parameter R_0 refers to the signal *power* rather than the signal *amplitude* falloff. This induces a factor 2 between $R_{0,\text{ power}}$ used here and $R_{0,\text{ amplitude}}$ used in other analysis:

$$R_{0,\text{ power}} = \frac{R_{0,\text{ amplitude}}}{2} \quad . \tag{9.14}$$
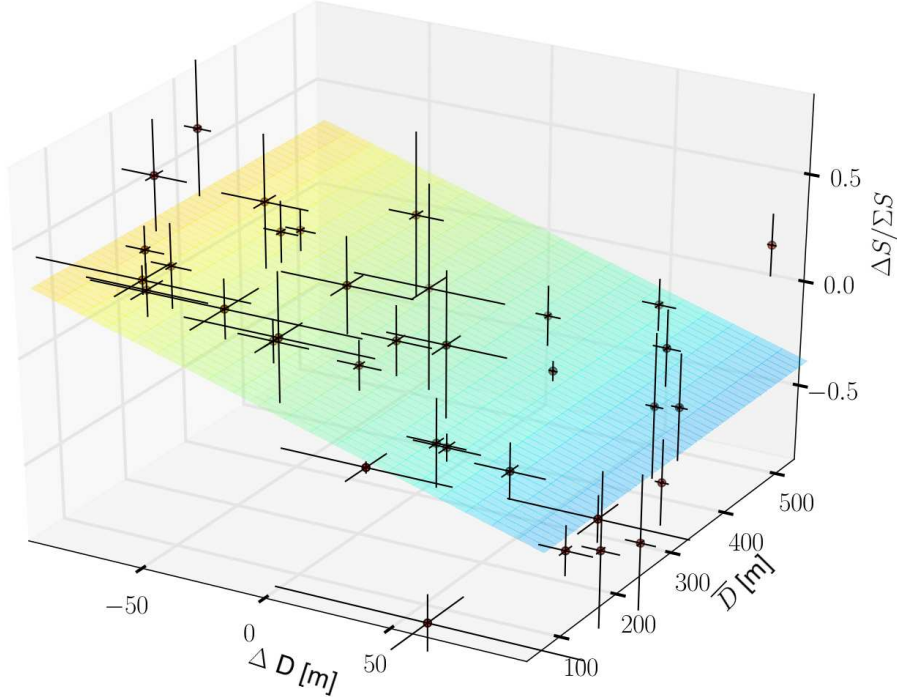
Figure 9.16: The measured data points. The positions ($\frac{\Delta S}{\Sigma S}$, ΔD and $\bar{D}$) are displayed by the circles. The bars yield the corresponding uncertainties. The plane is the fit of an exponential LDF model to the data.

Discussion

The calculations presented above show that our set of observables ($\frac{\Delta S}{\Sigma S}$, ΔD and $\bar{D}$) is in principle able to discriminate different LDF models and to reconstruct the underlying model parameters.

As a first step we will interpret the data in terms of the exponential and the power law model and reconstruct the corresponding parameters.

As a second step we will use Monte Carlo data following different LDF models to check the reliability of the reconstruction as well as to recover systematic effects.

9.3.2.2 Direct Reconstruction of Model Parameters

In Fig. 9.16 and 9.17 the observables $\frac{\Delta S}{\Sigma S}$, ΔD and $\bar{D}$ are plotted in three dimensions. This allows us to directly fit the LDF models to the data without introducing a binning to one of the parameters as it was done for illustration in Fig. 9.15.

In Fig. 9.16 the exponential LDF model has been fitted to the data. In this case the fit of a flat plane which does not change with the distance $\bar{D}$ recovers the scaling parameter R_0 as discussed in Eqn. 9.21. We find:

$$R_{0,\text{direct}} = (146 \pm 13)\,\text{m} \qquad \chi^2/\text{ndf} = 2.7 \qquad . \qquad (9.22)$$
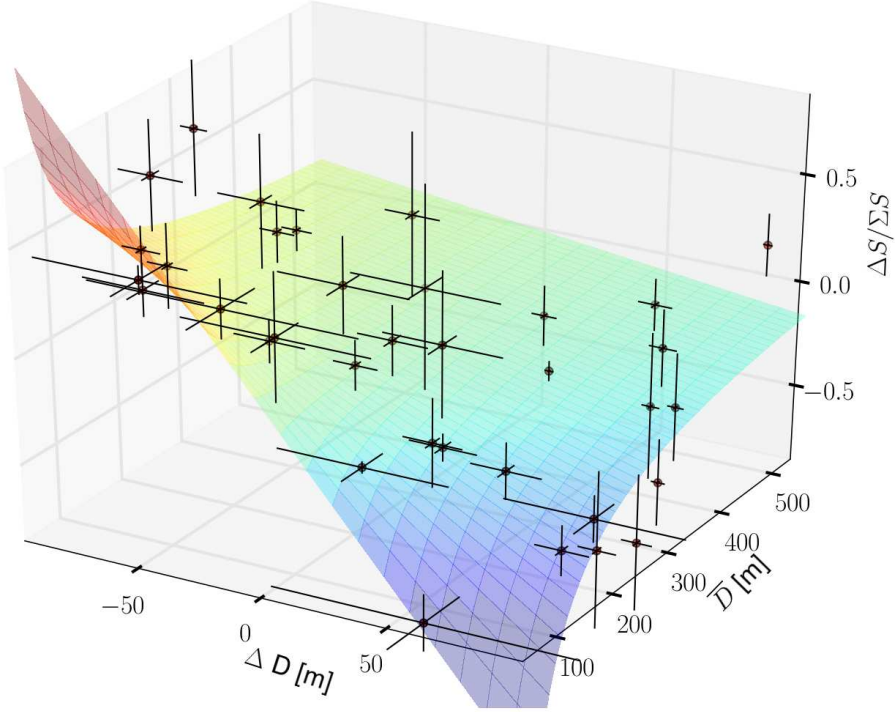
Figure 9.17: The measured data points. The positions ($\frac{\Delta S}{\Sigma S}$, ΔD and $\bar{D}$) are displayed by the circles. The bars yield the corresponding uncertainties. The plane is the fit of an LDF model following a power law to the data.

As the uncertainties of $\bar{D}$ are parallel to the fitted plain, they do not contribute to calculation of the χ^2. Consequently, the 3-dimensional fit in the case of the exponential LDF model is equivalent to the fit performed in Fig. 9.13. Note that now the axis offset is fixed to zero as discussed in Sec. 9.3.1.4.

In Fig. 9.17 the power law LDF model has been fitted to the data. This is achieved by evaluating the functional dependency of the parameters given in Eqn. 9.16. We find:

$$x_{\mathrm{direct}} = 1.48 \pm 0.17 \qquad \chi^2/\mathrm{ndf} = 1.9 \qquad . \tag{9.23}$$

In the next section we will use Monte Carlo data to check if the direct fit of the models to the data yields the true model parameters. This is especially necessary as the approximations made in Sec. 9.3.2.1 do not strictly need to be fulfilled throughout the whole data set. If systematic effects occur, the Monte Carlo will allow us to reconstruct the most probable model parameters. Moreover, we will be able to interpret the χ^2/ndfs in terms of a probability that the prediction of the respective model matches the data.
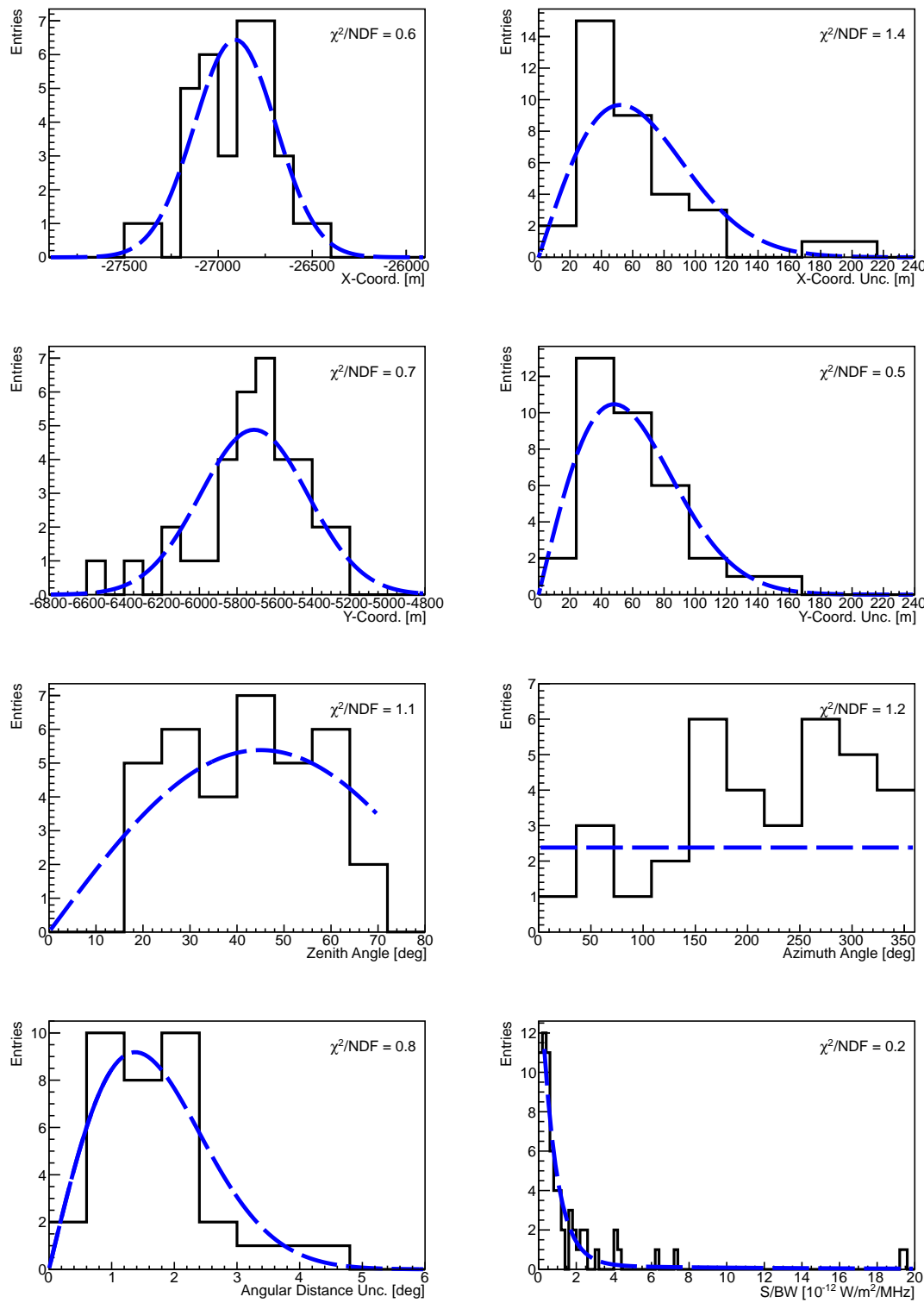
Figure 9.18: The distributions of the measured quantities needed to calculate the variables $\frac{\Delta S}{\Sigma S}$, ΔD and $\bar{D}$. The dashed line are the fits to the data used to initiate the generation of Monte Carlo data.

9.3.2.3   Generation of Monte Carlo Data

To receive a realistic set of Monte Carlo data we parameterize the distributions of the measured quantities which are needed to derive our observables of interest. The relevant distributions and their fit functions are displayed in Fig. 9.18 and shortly described here:

- The x- and y-coordinates of the shower core positions are fitted with a Gaussian. For the choice of random shower core positions the slight banana-shape of the measured core positions visible in Fig. 9.7 is approximated by using the correlation coefficient between the x- and y-coordinates.

- The uncertainties of the x- and y-position can be matched with a Rayleigh distribution.

- We choose the zenith angle distribution to follow $\cos(\theta)\sin(\theta)$ up to zenith angles of 70°.

- The azimuth angle will be distributed uniformly from 0° to 360°.

- The point spread function associated with the uncertainty of the incoming direction is matched with a Rayleigh distribution.

- The initial Poynting vector intensity of the radio pulse fitted with a exponential. As the measured distribution exhibits a steep rise towards lower amplitudes and a tail with single amplitudes towards high intensities, we choose to fit a double exponential function to match the overall shape.

- The uncertainty of the signal intensity is taken from the parameterization given in Fig. 9.9.

Following the statistics of the measured data set, we generate Monte Carlo data sets starting with 35 initial variables chosen randomly from the fits to the distributions shown in Fig. 9.18.

Here the initial signal amplitude which was chosen from Fig. 9.18 (lower right) is treated as signal $S(\bar{D})$ at the mean distance $\bar{D}$ from the antennas to the shower axis. Then the exact signal at the antenna distance D (D_1 and D_2) can be calculated in the case of the exponential LDF via:

$$S(D) = S(\bar{D}) \cdot e^{\frac{\bar{D}-D}{R_0}} \quad , \tag{9.24}$$

and in the case of a LDF following a power law with:

$$S(D) = S(\bar{D}) \cdot \left(\frac{\bar{D}}{D}\right)^x \quad . \tag{9.25}$$

Having obtained all initial quantities, each variable is varied randomly according to its uncertainties. Finally, the observables $\frac{\Delta S}{\Sigma S}$, ΔD and $\bar{D}$ are calculate following the same procedure as for the measured data (cf. Sec. 9.3.1).
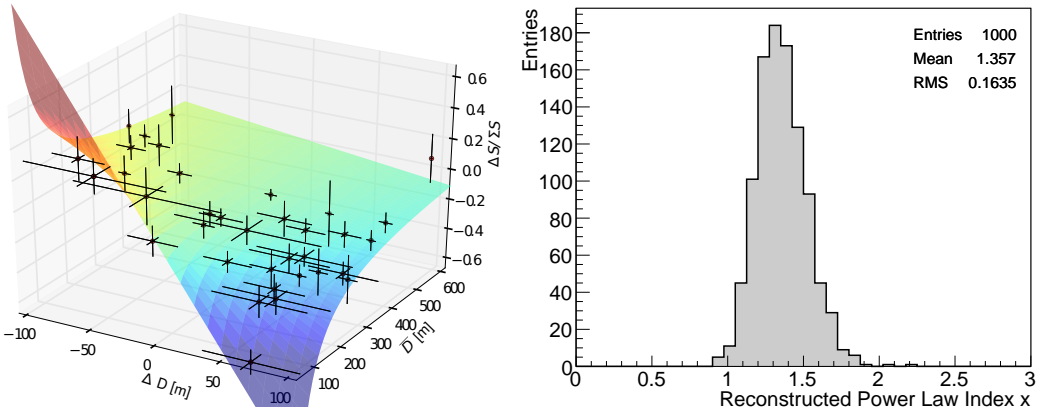
Figure 9.19: Left: An example data set generated with the Monte Carlo using a power law LDF with an index $x = 1.25$. The data set consists of 35 radio events which matches the number of events in the measured data set. The surface is the fit to this data set which is used to recover the power law index. Right: 1000 MC data sets such as in the left panel have been realized all exhibiting a power law index of $x = 1.25$. Displayed is the distribution of reconstructed power law indices which were received using fits to the data. See text for details.

9.3.2.4 Systematics of LDF Reconstruction

In Fig. 9.19 (left) an example MC data set is displayed that was generated using a power law LDF with an index of $x = 1.25$. The surface is the corresponding fit to this data set. For the right panel of Fig. 9.19 1000 MC data sets were realized all following an index of $x = 1.25$. Displayed is the distribution of the power law indices that were reconstructed using fits to the data.

The width of the distribution indicates the impact of the statistical uncertainties of the test variables onto the reconstruction of the LDF parameters. We note that the RMS of the distribution agrees with the uncertainties directly obtained by the fits to the data such as given i.e. in Eqn. 9.23.

We observe an offset between the initial and the mean reconstructed LDF parameter. To investigate this systematic offset in more detail we generate MC data sets such as in Fig. 9.19 (right) with varying initial LDF parameters. In Fig. 9.20 the mean and the RMS of the consequential distributions of the reconstructed LDF parameters is displayed as a function of the respective initial parameter. The left panel of Fig. 9.20 shows the behavior in the case of an exponential LDF and the right panel in the case of a power law LDF.

The reconstructions for the LDF models tend to overestimate the initial LDF parameters. This is due to the validity of the approximations made in Sec. 9.3.2.1 which were used to derive a reconstruction strategy. In the next section we will use the MC data generated for Fig. 9.20 to recover the most probable LDF model parameters for the measured data with a maximum likelihood method.
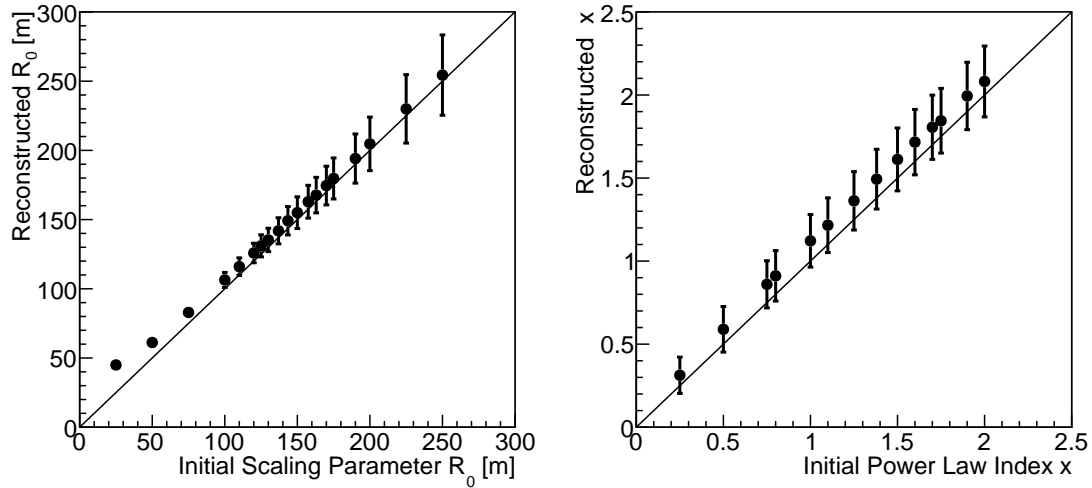
Figure 9.20: Reconstructed LDF model parameters as a function of the initial values used to generate the respective Monte Carlo data. For each LDF model parameter 1000 Monte Carlo sets with 35 data points each were realized. The bars in y-direction denote the RMS of the corresponding distribution of reconstructed parameters. The lines give x=y. Left: An exponential LDF was used to generate the MC data. Right: The LDF is represented by a power law.

9.3.2.5   Maximum Likelihood Reconstruction of Measured Data

The upper panel of Fig. 9.21 shows the distributions of the reconstructed exponential LDF model parameters which were also used for Fig. 9.20 (left). The displayed initial scaling parameters vary from $R_0 = 75$ m to 250 m. The red cross denotes the fit result and uncertainty obtained from the measured data set (cf. Eqn. 9.22). From each of the normalized histograms we read the height of the bin which would contain the measured data point. This height represents the likelihood that the reconstruction of the respective MC data set yields a similar parameter as in the case of the measured data.

In the lower panel of Fig. 9.21 the negative log-likelihoods for the different initial parameters are plotted. A parabola is fitted to the central values. In this way we receive the estimator for the best exponential LDF parameter in the case of the maximum likelihood method:

$$R_0 = (140 \pm 9)\,\text{m} \quad . \tag{9.26}$$

This result is close to the value obtained using the direct fit to the data (cf. Eqn. 9.22).

In Fig. 9.22 the same procedure is done in the case of the LDF model exhibiting a power law with indices ranging from $x = 0.5$ to 2. We receive:

$$x = 1.38 \pm 0.17 \quad . \tag{9.27}$$

Here, the power law index x is smaller than the index reconstructed with the direct fit (Eqn. 9.23). Thus the maximum likelihood method allows us to reconstruct the
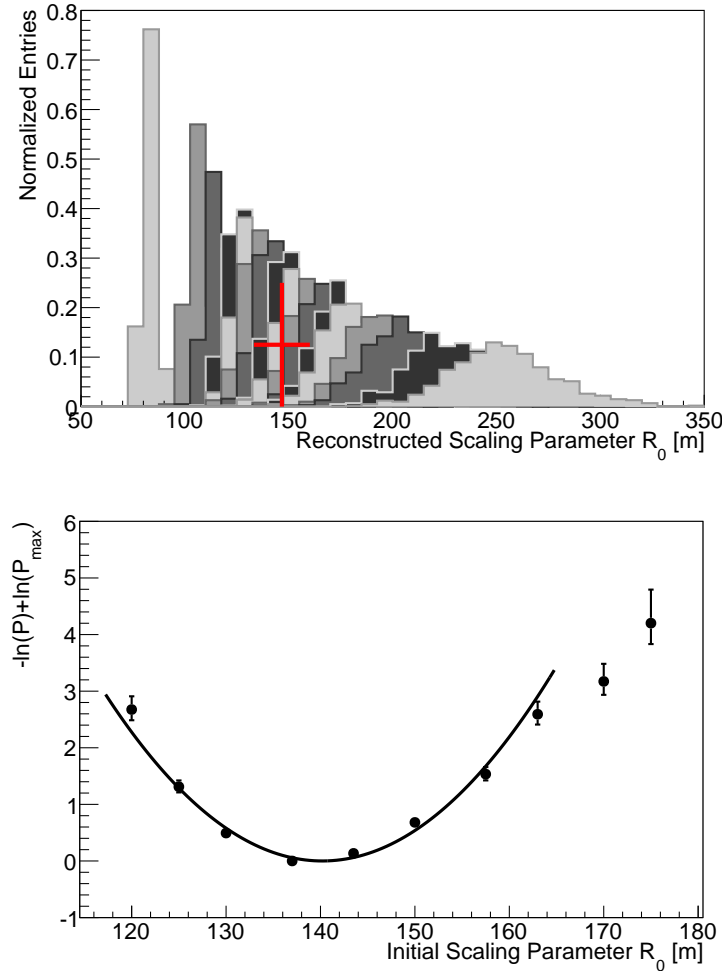
**Figure 9.21:** The maximum likelihood method applied to the measured data in the case of the exponential LDF model. See text for details.

most probable power law index without the impact of the systematic shift which we discussed in Sec. 9.3.2.4.

9.3.2.6   LDF Model Falsification using χ^2/ndf Probability

In Eqn. 9.22 and 9.23 the direct fit of LDF models to the measured data results in χ^2/ndfs which we would like to interpret in terms of a probability that the respective LDF model produces a data set that is at least as extreme as the measured data. However, the fits used to reconstruct the LDF model parameters do not fully reflect the LDF models' predictions for the data due to the approximations done in Sec. 9.3.2.1. Consequently we are not allowed to read the desired P-values from the cumulative distribution function of the χ^2/ndf usually provided in the theory of statistical analysis. Thus we use our Monte Carlo to generate the desired χ^2/ndf distributions.

For both LDF models under test we have reconstructed the model parameter matching the measured data best (cf. Sec. 9.3.2.5). We use these best model parameters
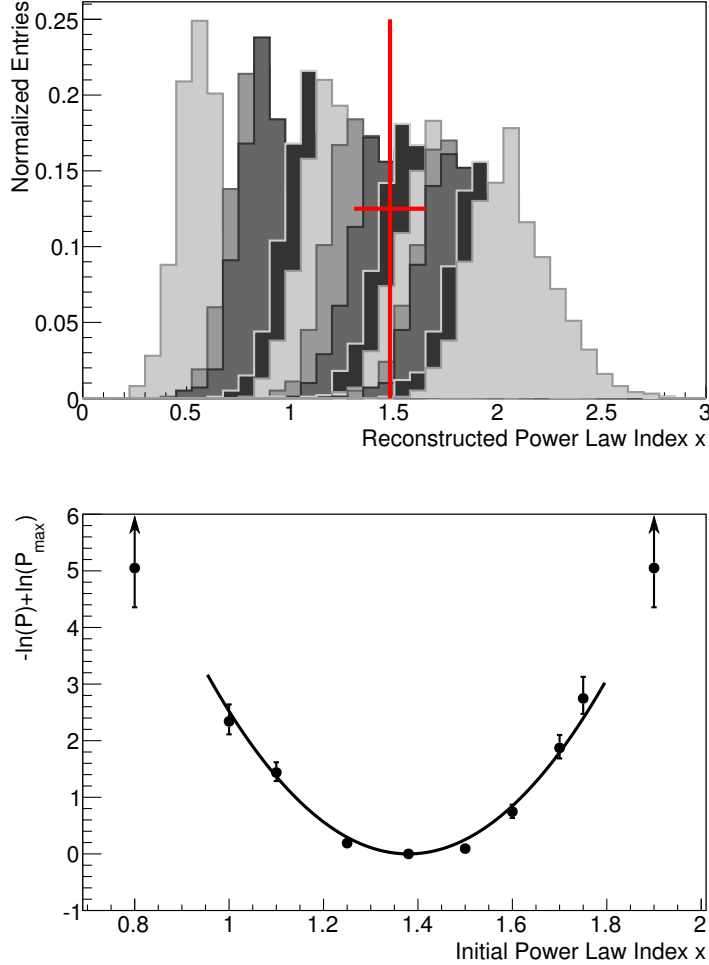
Figure 9.22: The maximum likelihood method applied to the measured data in the case of the power law LDF model. See text for details.

including their respective uncertainties to generate 10000 MC data sets for each LDF model. These MC data sets are reconstructed to receive the χ^2/ndf distributions that are displayed in Fig. 9.23.

In the case of the exponential LDF model with the scaling parameter $R_0 = (140 \pm 9)\,\mathrm{m}$ only two out of the 10000 MC data sets results in a χ^2/ndf larger than the $\chi^2/\mathrm{ndf} = 2.7$ resulting from the fit to the measured data (red line in Fig. 9.23 (left)). Thus we receive for the exponential LDF model:

$$R_0 = (140 \pm 9)\,\mathrm{m} \quad \text{with} \quad P = 0.0002 \quad \hat{=} \quad 3.72\,\sigma \tag{9.28}$$

where $3.72\,\sigma$ is the difference between measured data and model prediction in terms of standard deviations.
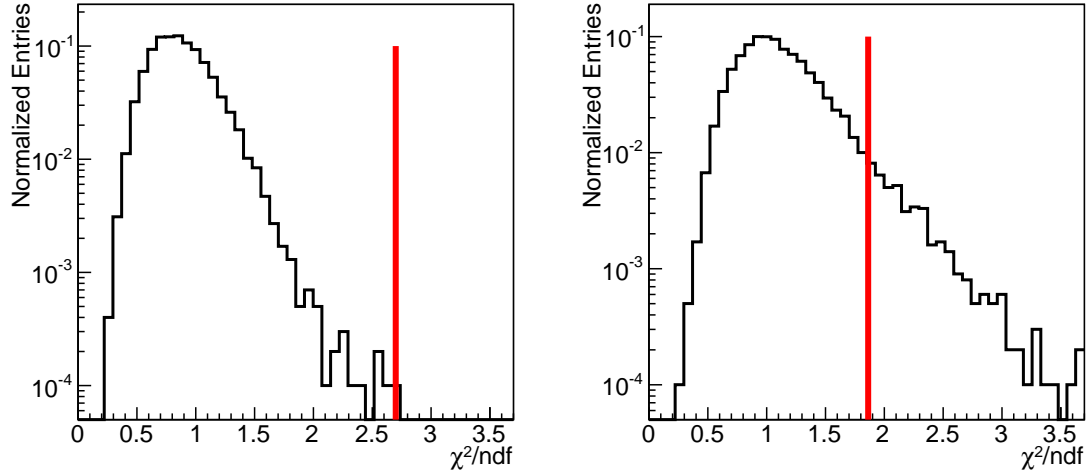
Figure 9.23: The χ^2/ndf distribution from the fits to 10000 MC data sets generated with an exponential LDF (right) and a power law LDF (right). Both LDF models are initiated with the most probable model parameters found in Sec. 9.3.2.5 including the respective uncertainties. The red lines show the χ^2/ndfs resulting from the model fits to the measured data.

The right panel of Fig. 9.23 gives the χ^2/ndf distribution for the power law LDF model with a parameter $x = 1.38 \pm 0.17$. Integrating the distribution starting from the measured $\chi^2/\mathrm{ndf} = 2.0$ results in:

$$ x = 1.38 \pm 0.17 \quad \text{with} \quad P = 0.046 \quad \hat{=} \quad 1.99\,\sigma \quad . \tag{9.29} $$

9.3.3   Discussion

We conclude that a purely exponential LDF $S(D) \propto e^{-D/R_0}$ is excluded by the data with $\sim 3.7\,\sigma$. In this model the signal strength in single air shower events is the same at all observing positions at a fixed distance D to the shower axis and the parameter R_0 does not depend on further variables. Within this LDF model we recover $R_0 = (140 \pm 9)$ m as most probable scaling parameter.

Previous LDF analysis [167] performed on a subset of the data discussed in this note resulted in scaling parameters R_0 ranging from 40 to 75 m which is a factor of two smaller than the result we have obtained here.[3]

From the LOPES data in Fig. 3.5 a scaling parameter R_0 of ~ 80 m was obtained as mean of scaling parameters from single air shower events [65]. [3] The corresponding distribution is relatively wide with a tail towards much larger scaling parameters beyond 750 m. In the case of CODALEMA data [8] we read $R_0 \approx 125$ m. [3] A conclusion if the results are contradictory or not cannot be drawn here.

---

[3]These values have been translated into a scaling parameter referring to the signal intensity as discussed in Eqn. 9.14.

In the case of the hypothesis of a LDF exhibiting a power law shape $S(D) \propto D^{-x}$ we find $x = 1.38 \pm 0.17$ as most probable power law index. From our MC study we learn that the measured data deviates $\sim 2.0\,\sigma$ from the model prediction which does not falsify this model as explanation for the observed behavior. The theoretical calculations done in [77] favor more complex LDF shapes than a purely exponential or a purely power law. However, the exemplary LDFs given in [77] might be matched with a power law more accurately than with an exponential function.

In [65] also a power law is used to fit the LDF of single air shower events measured with LOPES. The mean power law index observed there is $x = 1.90 \pm 0.08$.[4] In the case of LOPES data the power law LDF was found to match the data worse than an exponential LDF.

---

[4]The LOPES result for the power law index has been multiplied by a factor of two to convert to a description of the signal power which is used in this note.

10. Analysis with Self-Triggered Data from AERA

In this chapter we present our studies on self-triggered radio data that was recorded during the start up phase of AERA. In the first section we focus on a characterization of the full data set. In the second section we investigate the timing resolution of the radio detector stations. Finally we study algorithms for a removal of noise events in comparison to air showers detected in coincident with the Auger surface detector.

10.1 The AERA Event Data Set

The data considered in this analysis comprises the full AERA data set from the start of data taking in September 2010 until the end of May 2011. At the time being this is the full data that has been transfered from the detector site to Europe. In Fig. 10.1 we show the accumulated number of radio events as a function of time.

Currently the central DAQ of AERA is set up to record radio signals that are detected in multiple detector stations. A rough guideline to the trigger setting is
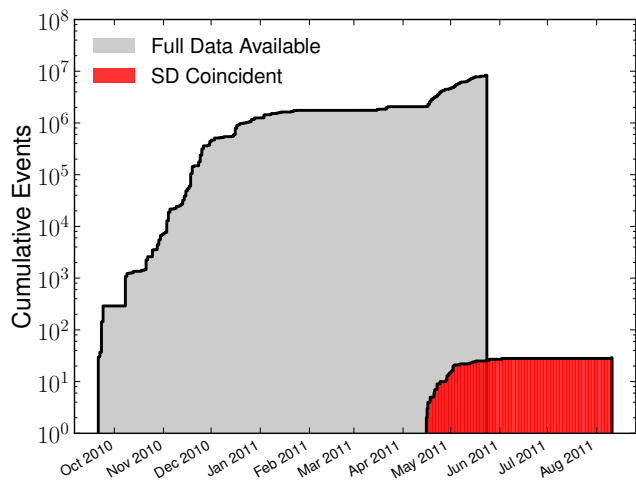
Figure 10.1: Cumulative Events Recorded with AERA. In the full data set available in Europe by Sep. 2011 are $\sim 8.4 \cdot 10^6$ self triggered radio events. Considered are events where a directional reconstruction is possible. This requires at least 3 RDSs participating an the event. Radio events that are associated with an air shower recorded with the SD are transfered dedicatedly to Europe. The coincident events are counted including those which were recorded in only two RDSs. (All data up to run 2175 for the full data set, up to run 2323 for the SD coincident events.)
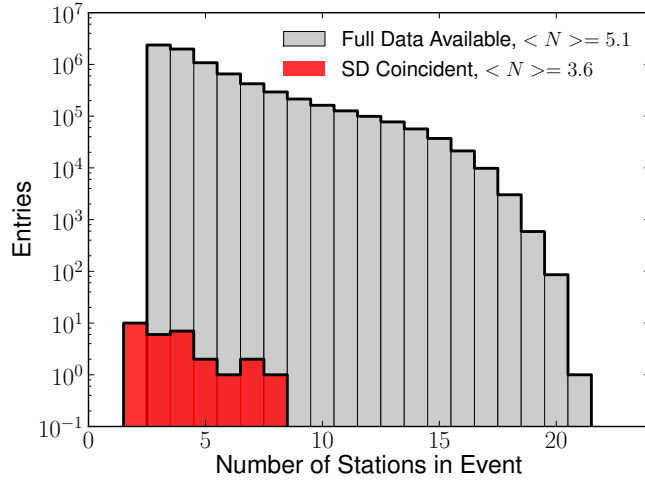
Figure 10.2: The number of RDSs participating in radio events. A single self-triggered event was observed with 21 radio detector stations.

that at least two neighboring detector stations have triggered within $5\,\mu$s. However, the precise settings have changed during the data taking. Recently, the trigger has been adjusted to increasingly suppress signal directions towards the horizon using additional criteria [187]. Moreover, every 10 s a signal trace is requested from all detector stations creating a set of minimum bias data. Overall $25.3 \cdot 10^6$ events were recorded in the given time span. These including $\sim 10^6$ minimum bias events.

We are interested in the following in the directional reconstruction of self-triggered radio pulses. This requires that at least three RDSs participate in an event. All figures are constrained to this type of self-triggered data which amounts to $8.3 \cdot 10^6$ events in Fig. 10.1.

Indicated in Fig. 10.1 are as well radio events that are detected in coincident with the surrounding Auger surface detector. The search for coincident events is performed using a time window $\pm 20\,\mu$s for the air shower to be detected in both detectors. All air shower events are considered which fulfill on of the following criteria [187]:

- at least one of the 10 closest SD stations surrounding the core of AERA participated,

- the air shower core is reconstructed by the SD within a distance of 2.5 km from the SD station 'Kathy Turner' which is located within the AERA array.

Coincident radio detector events are extracted from the usual data stream and transfered for analysis dedicatedly. With this method 37 radio events were initially identified as coincident events where 8 signals are found unlikely to be associated with an air shower event in an offline analysis. True air shower signals turn out to be delayed on average by $\sim 8.25\,\mu$s in comparison to the surface detector reconstruction. False events are rejected from the set of 'coincident' events considered in the figures.
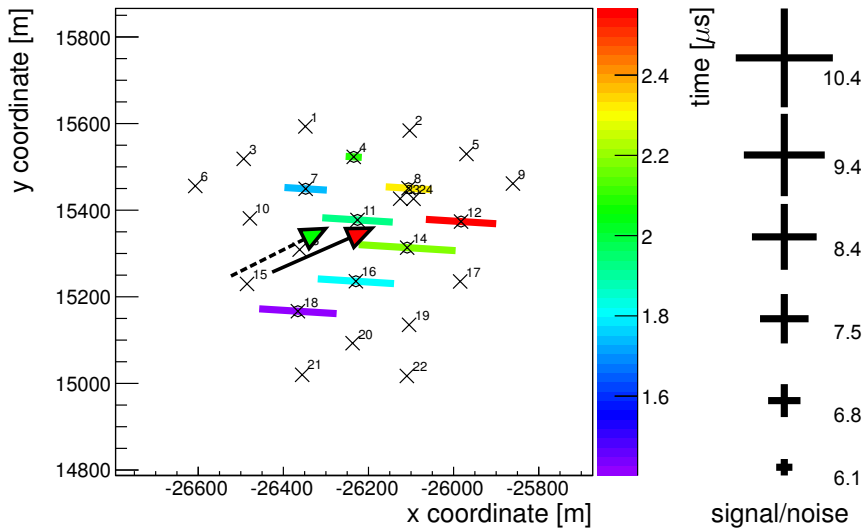
Figure 10.3: An air shower that was recorded with AERA in coincidences with the SD. For the triggered RDSs the signal to noise ration of the air shower signal is indicated by the bar symbols. The color scales show the relative timing of the radio signal in the stations. The solid red arrow indicated the core position and direction of the air shower axis as reconstructed from the radio data. The dashed green arrow maps the corresponding SD reconstruction. The air shower had an energy of $E_{SD} \approx 5 \cdot 10^{17}$ eV.

The expected number of coincident events is roughly one to two per day in the current configuration of AERA. In April 2010 where most of the coincident events were recorded a rate of 0.3 to 0.9 coincidences per day was realized [188]. Note that the coincident events are still part of the full data set.

In Fig. 10.2 we show the number of RDSs participating in radio events. For the coincident data also two-station events are displayed. The high multiplicities of RDSs participating events of the full data set indicates that strong transient noise signals are being recorded in the detector array. A display of a noise signal was given in Fig. 8.2. An air shower recorded in coincidences with the SD can be seen in Fig. 10.3.

10.1.1 Directional Distribution of Radio Signals

We use the methods described in Sec. 8 to run a reconstruction of the full AERA data set. In Fig. 10.4 the distribution of incoming directions of the recorded signals is displayed.

Events that were detected with three RDSs are reconstructed with a plane wave fit. For higher station multiplicities a spherical wave front is used to reconstruct the direction. As discussed in Sec. 8.3 the spherical wave reconstruction yields the distance to the source in addition to the direction. The reconstructed distances will be studied in the later sections of this analysis.

The majority of events in the data set can be attributed to man made sources that are located close to the horizon. The horizon is indicated in Fig. 10.4 as the outer dashed line. Along the horizon the distribution of events is strongly peaked towards
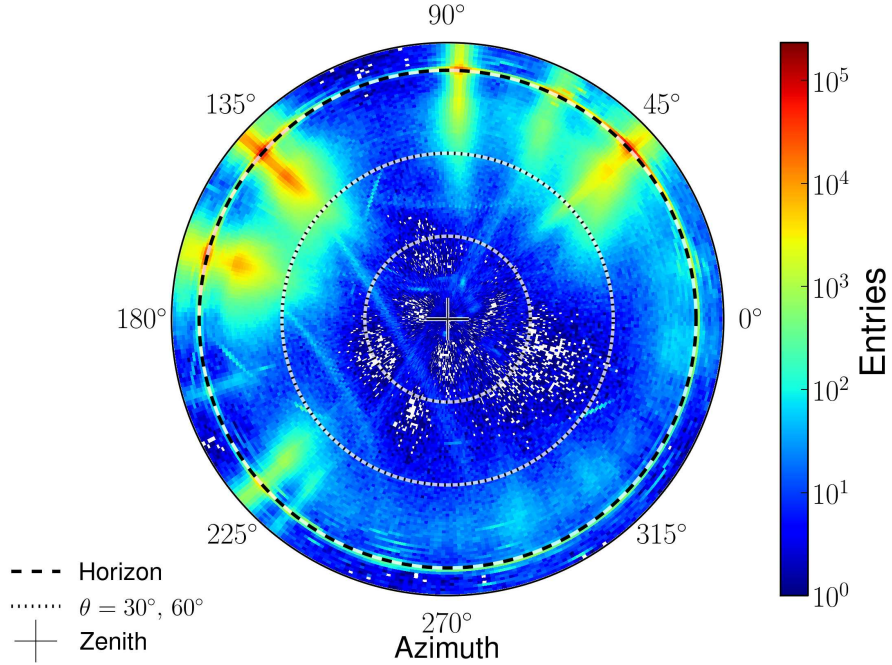
Figure 10.4: Distribution of the reconstructed directions from the full AERA data set in local polar coordinates. Distinct directions are visible which contribute the majority of recorded events. Note the logarithmic scale of the color axis.

distinct directions. We will discuss some of these 'hot spots' in more detail in Sec. 10.2.2.

We observe a scatter of the events around the hot spots. Here the logarithmic scale of the figure should be noted. The scatter introduces a smearing of the zenith angles towards smaller readings such that a fraction of the events originating from the horizon is reconstructed towards elevated directions.

We notice bow-like structures at different positions in the angular distribution. In Sec. 10.3.1 these structures will be attributed to specific geometric configurations of RDSs that participated in radio events.

The corresponding angular distribution of coincident air shower events is given in Fig. 10.5. Here as well, the air shower directions reconstructed from the radio data are displayed. From 29 identified air showers signals 10 events were only recorded in two RDSs. This amounts to 19 displayed entries. A more efficient detection of air showers with incoming directions perpendicular to the geo-magnetic field vector as discussed in Sec. 3.1.3 is also apparent for the coincident data of AERA. The air shower direction reconstructed by the SD (not given in the plot) matches the radio reconstruction on average with $\sim 4°$.

10.1.2   Observation of Detector Plane

The three-dimensional position of the RDSs were measured in a dedicated differential GPS survey to a precision of a few centimeters [118]. For the reconstruction these
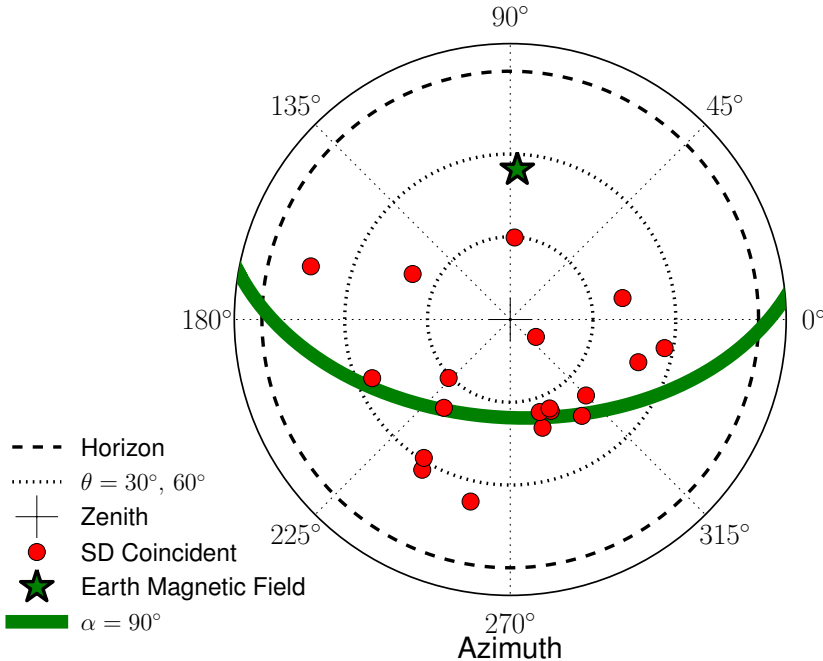
Figure 10.5: The reconstructed arrival directions of air showers that were recorded with AERA in coincidence with the SD. The circle markers denote the direction derived from the radio data reconstruction. The distribution indicates that arrival directions perpendicular to the Earth's magnetic field ($\alpha = 90°$) are detected more frequently.

positions are evaluated in the Cartesian coordinate system 'Pampa Amarilla' which is the Auger standard local coordinate system.[1] In Fig. 10.6 (left) the measured positions of the RDSs are displayed. For convenience we have subtracted here the average position of the array. Note the difference in scale used for the xy-coordinates and the z-coordinate.

Within the lateral extend of AERA of ~ 750 m the z-coordinates of the RDSs rise from East to West by ~ 5 m. The RDSs are located on a tilted plane which is inclined by $0.32°$ with respect to the 'Pampa Amarilla' coordinate system. Deviations of the positions from this plane are small. Regarding the location of AERA at the western perimeter of the Auger site (cf. Fig. 4.1) a rising terrain towards the direction of the Andes seems reasonable.

The local terrain has direct impact on the reconstruction of sources of transient signals that are located in horizontal directions. An excerpt of the angular distribution in Fig. 10.4 for directions close to the horizon ($\theta = 90°$) can be seen in Fig. 10.6 (right). Also the projection of the detector plane to the polar coordinate system is indicated. The reconstructed incoming direction of transient radio signals tend to align with the plane of the detector array. We see two reasons which cause this behavior:

---

[1]We implement the same transformation as the Auger $\overline{\text{Off}}\underline{\text{line}}$ software.
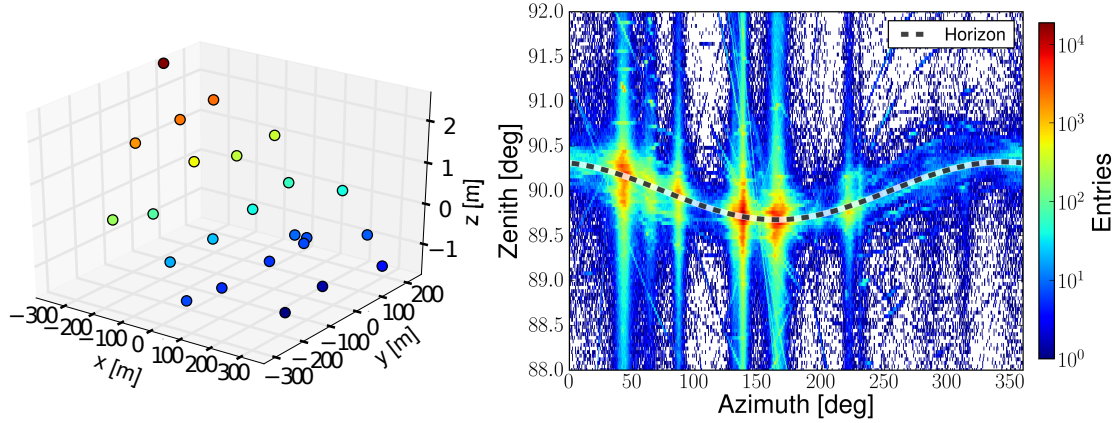
Figure 10.6: Left: The 3-dimensional placement of the antennas in the Auger coordinate system. The positions were measured using a differential GPS. This allows for a precision of the position of better than 10 cm in each dimension. For the reconstruction the survey positions have been transformed to the Auger coordinate system 'Pampa Amarilla'. In the given coordinate system AERA is located on a tilted plane with its normal vector pointing towards $\phi = 344.36°, \theta = 0.32°$. Right: The tilt of the detector plane is visible when transient signals coming from horizontal directions are observed. The angular distribution follows the plane of the detector, which is indicated as black dashed line.

- The flat plane indicated by the locations of the RDSs might continue well beyond the extend of the detector array. Sources of transient signals can be located in the continued plane of the detector. In the next sections we will see that the typical distances towards the sources are a few km.

- Incoming directions that are parallel to the detector plane yield the maximum possible relative signal timing differences between RDSs. As discussed in Sec. 8.3.1 the measured timing differences can exceed this maximum since the detector resolution is limited and systematic timing offsets might be present. In these cases the fit of a wave front to match the data will tend to choose an incoming direction in the detector plane. This minimizes the timing residuals in the reconstruction.

With respect to the large number of detected events towards the horizon a mixture of both effects seems likely.

10.1.3 Trigger Time and Timing from Pulse Position

The RDSs record time series with a length of 10.24 μs. The time of the trigger decision is given by a timestamp which progresses with a step size of one ns. The pretrigger time defines the amount of samples that are saved before the position of the actual trigger decision. Our reconstruction scheme uses the pretrigger time and the timestamp to define the starting time of the sample series. Using the methods described in Sec. 8.2 the sample series is prepared for a novel search for the pulse position including an upsampling and the creation of an Hilbert envelope.
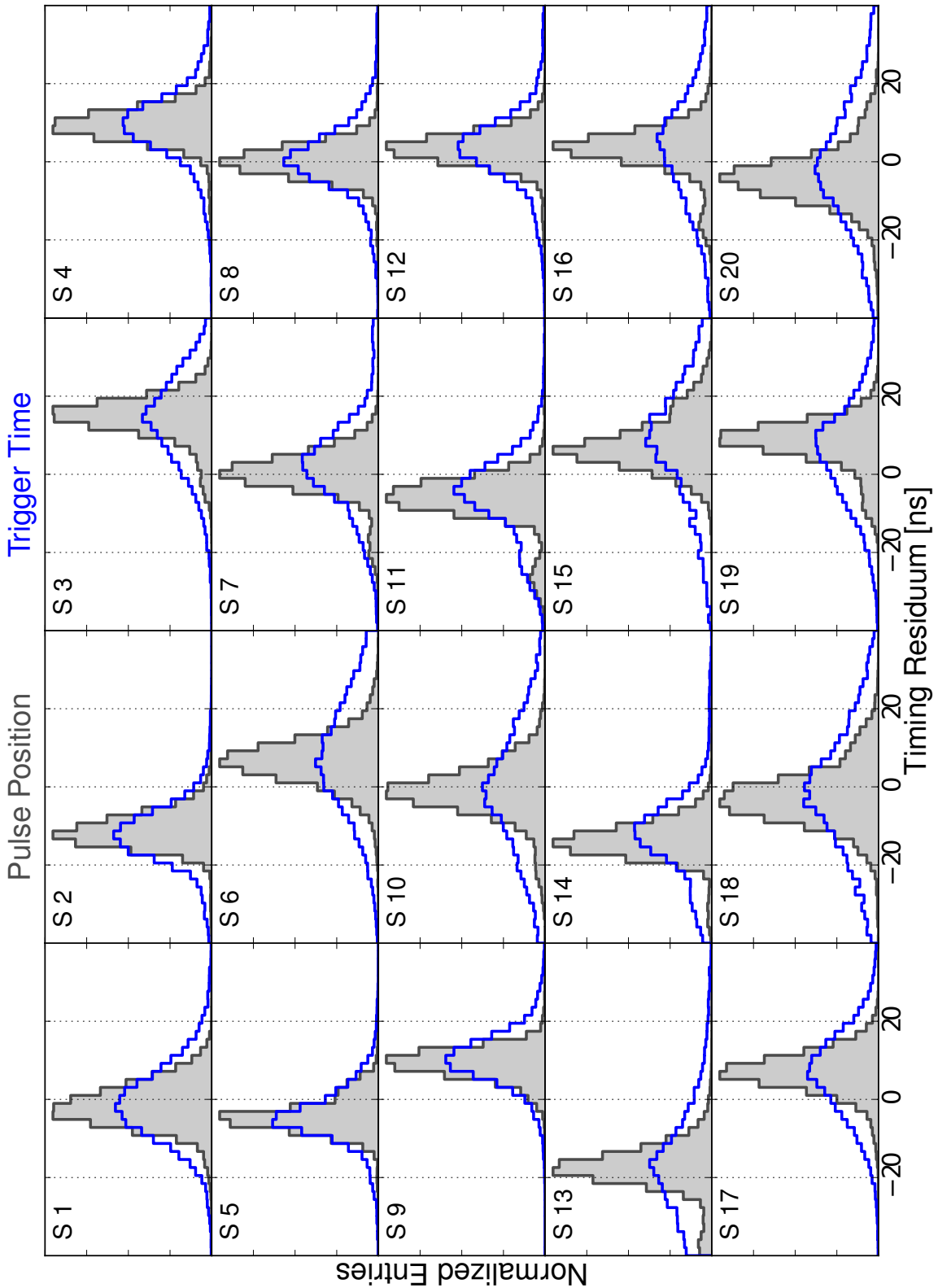
Figure 10.7: Timing residuals observed in the reconstruction of a spherical wave at the individual detector stations. Two options are tested: First, the trigger time is used to reconstruct the wave front. This yields the hollow distributions. Second, the trigger time is used to identify the starting time of the sampled data trace. The timing position of the signal is then searched for using upsampling and an Hilbert envelope resulting in the filled histograms. We observe that the explicit search for the pulse position improves the timing resolution. We find systematic offsets in the timing of the individual detector stations.

As a cross check to this procedure we repeat the directional reconstruction shown in Fig. 10.4 using the trigger time given by the RDSs directly. For the comparison we choose $2 \cdot 10^5$ events with $N > 10$ participating RDSs. The large number of stations should allow for a stable reconstruction even if the timing of single stations is scattered. In Fig. 10.7 the consequential timing residuals $t_i^{\mathrm{res}} = t_i^{\mathrm{fit}} - t_i^{\mathrm{meas}}$ with respect to the reconstruction of a spherical wave are displayed.

The distribution of timing residuals is investigated for each RDS individually. The search for the pulse position results in more narrow distributions than in the case of the direct use of the trigger time. The average RMS of the 'trigger time' distributions is ~ 14 ns whereas we find ~ 6 ns using the pulse position. The explicit search for the pulse position hence significantly improves the timing resolution realized in the measurements.

Moreover, we observe that the individual RDSs exhibit systematic timing offsets of up to 20 ns. These we will correct for in the next section.

10.2 Initial Timing Calibration of the AERA Data

In the following we assume that each RDSs has a static timing offset with respect to the other detector stations. Our goal is to find these offsets and use them as calibration constants in our reconstruction. Looking at Fig. 10.7 a first estimate of the timing offset is given by the averages of the displayed distributions. For a calibrated data set we require that the residual distributions are centered around zero for all detector stations. We propose the following iterative procedure to find the calibration constants:

1. The average timing offsets of the individual RDSs are used as calibration constants in a repeated reconstruction of the data.

2. The repeated reconstruction yields new timing offsets. Presumably these are smaller than the previous constants. The new offsets are added to the forgoing constants.

3. The residual distributions of some of the RDSs possess a double peak structure (e.g. Station 11 in Fig. 10.7). We currently treat the minor peaks as secondary effects and avoid their impact on the average of the residual distribution. This is realized by performing an outliers rejection during the reconstruction of individual events.

4. The foregoing steps are repeated until the systematic offsets in the residual distributions vanish.

To receive an unbiased estimate of the timing offset of an individual RDSs from the reconstruction of an event, the timing residuals are calculated with respect to a reconstruction that is performed without the inspected detector station. Here, also the outliers rejection is applied. Stations which have a timing residual $|t_i^{\mathrm{res}}| > t^{\mathrm{cut}}$
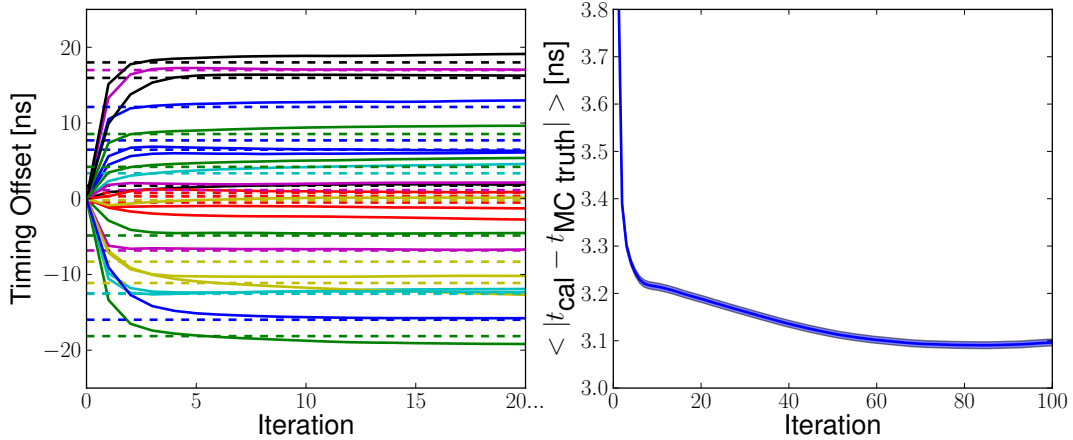
Figure 10.8: Iterative Timing Algorithm applied to Monte Carlo data. Left: A single realization of the timing calibration. The dashed vertical lines indicate the 'true' timing offset used to initiate the MC. Each solid line shows the reconstructed offset of an RDSs as proposed by the calibration after each iteration. Right: The average remaining timing offset observed in 150 MC realizations. The band indicates the uncertainty of the average value. The largest timing offsets are removed in the first few iterations. Then a slow improvement of the timing is observed until iteration 80. In the Monte Carlo study we observe an average precision of the calibration of ~ 3 ns.

are neither taken into account for the residual distributions nor used to determine the residuals of the other stations participating in the event. The maximum time difference t^{cut} allowed to take part in the analysis is tightened in each iteration n of the calibration. We choose a slow progression with the number of iterations as follows:

$$t^{\text{cut}}(n) = t^{\text{cut}}_{\min} \cdot \underbrace{1600^{0.75^n}}_{\approx 1.5 \text{ for } n=10} \quad , \tag{10.1}$$

which efficiently starts rejecting outliers beyond $n = 10$ iterations. The minimal time is set to $t^{\text{cut}}_{\min} = 2$ ns which ranges at the envisaged timing resolution for AERA of 1 ns.

10.2.1 Application to Monte Carlo Data

To test our calibration procedure we use sets of Monte Carlo data. The simulated timings of RDSs are generated using three discrete source points of wave fronts located towards the horizon according to the three dominant hot spots at $\phi = 45°, 135°$ and $170°$ in Fig. 10.4. Each simulated event is detected by a minimum of $N > 10$ RDSs where the exact number of stations is chosen from the measured multiplicity distribution shown in Fig. 10.2. Within a set of Monte Carlo data a systematic timing offset is applied to each RDS. The offsets are distributed uniformly between -20 and 20 ns. Moreover, a statistical uncertainty of 2 ns is added to each generated timing information.

In Fig. 10.8 (left) the iterative calibration procedure is applied to a set of MC data consisting of 2700 events. The timing constants proposed by the calibration
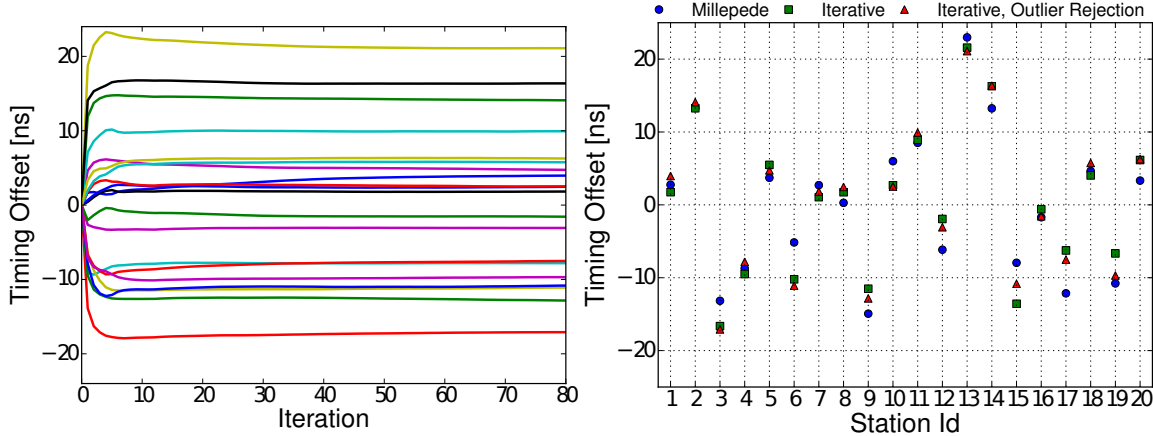
Figure 10.9: Left: Iterative timing algorithm applied to the measured data set. Each line represents the timing offset of one RDS proposed by the calibration as a function of iterations. As expected from Fig. 10.8 the largest variations are observed in the first iterations. Beyond iteration 50 only minimal changes occur. Right: Comparison of timing calibration results. To cross check the result of the timing calibration, we applied a simplified version of the algorithm and the MillePede II minimizer to the data. We find that the methods yield similar predictions for the timing offsets of the individual detector stations. Note that in principal 21 RDSs have contributed to the data set. However, only small statistics were recorded with station 21 in the given data set.

are displayed as a function of iterations. The vertical dashed lines indicate the systematic offsets used to initiate the simulation. The calibration yields the largest variation of the proposed timing offsets in the first few iterations. With an increasing number of iterations a slower variation remains. For most RDSs the largest part of the systematic offset is recovered after a few iterations.

To study the precision of the calibration in more detail we investigate the average offset between the initial timing offsets and the constants proposed by the algorithm. In the right part of Fig. 10.8 the average difference observed in 150 MC data sets is shown. In the average distribution as well the largest timing offsets are removed in the first iterations. Above iteration $n \approx 10$ the outliers rejection sets in and results in a slow improvement of the timing up iteration 80. For the application to data we stop the algorithm after 80 iterations. Note that a stable result is only obtained when the fit of the γ-factor is included in the reconstruction to avoid systematic offsets induced by the statistical timing uncertainty as discussed in Sec. 8.3.1. Using the combination of systematic offsets in the vicinity of 20 ns and statistical uncertainties of 2 ns we can recover the calibration constants at a level of 3 ns.

10.2.2 Timing Calibration Results

For the application of the iterative timing calibration we choose a set of high quality events from the AERA data. We currently use data recorded before March 2011 to avoid possible implications arising from a switch from UTC to GPS timestamps in the hardware performed at that time. The corresponding runs comprise $1.75 \cdot 10^6$ events. The following requirements are applied for the selection:

- The number of triggered RDSs is $N > 10$.

- The reconstructed γ-factor ranges between 0.98 and 1.02 and the χ^2/ndf of the spherical wave reconstruction is less than 100. These criteria avoid clearly unphysical timing configurations of the RDSs. Such configurations can for instance be caused by a false identification of the signal position in the trace. In rare cases, the fit of the speed of signal propagation with the γ-factor is used by the reconstruction to match unphysical situations.

- The distance to the source point of the spherical wave is less than 20 km. This cut is intended to select point-like sources of radio signals near AERA.

With these criteria 35300 signals are selected from the data set. The events distribute over a period of three months. A major contribution of half of the events is given by a specific run of data taking over two days at the end of November 2010 (run 1417). In Fig. 10.9 (left) we show the application of the calibration procedure to this data set.

The calibration of the measured data exhibits a similar progression with the number of iterations as observed in the MC. In the case of the measured data the outliers rejection has a more prominent impact visible around the 10th iteration. Here the minor second peaks visible in Fig. 10.7 are rejected from the calibration. In the further iterations only slight variations are observed.

In Fig. 10.9 (right) the timing constants after $n = 80$ iterations are depicted for each RDS. The offsets range at a level of ± 20 ns. As a cross check we have performed a calibration of the same data using two additional methods. The first method realizes the same procedure as described above but without the outliers rejection. The second method implements a least squares minimization using the MillePede II program [189].

All methods propose similar calibration constants for the detector stations. The proposed timing offsets are compatible with the resolution of 3 ns claimed in Fig. 10.8 (right).

In Fig. 10.10 the residual distributions resulting from the data set used for the calibration are displayed. The application of the proposed timing constants strongly improves the shape of the distributions. We observe that slight offsets of the maximum values of the distribution remain due to asymmetric timing contributions at some stations. These will be the subject of further studies. Comparing the three calibration algorithms we observe slight advantages of the iterative algorithm including the outliers rejection. For most RDSs this algorithm provides that the most probable value of the residual distributions are centered at zero.

In Fig. 10.11 we inspect the impact of the calibration to the full data set up to March 2011. Displayed are the residual distributions of all RDSs in a common histogram both for the calibrated and uncalibrated data. All events with $N > 5$ stations are taken into account. Events with lower station multiplicity are not considered for the
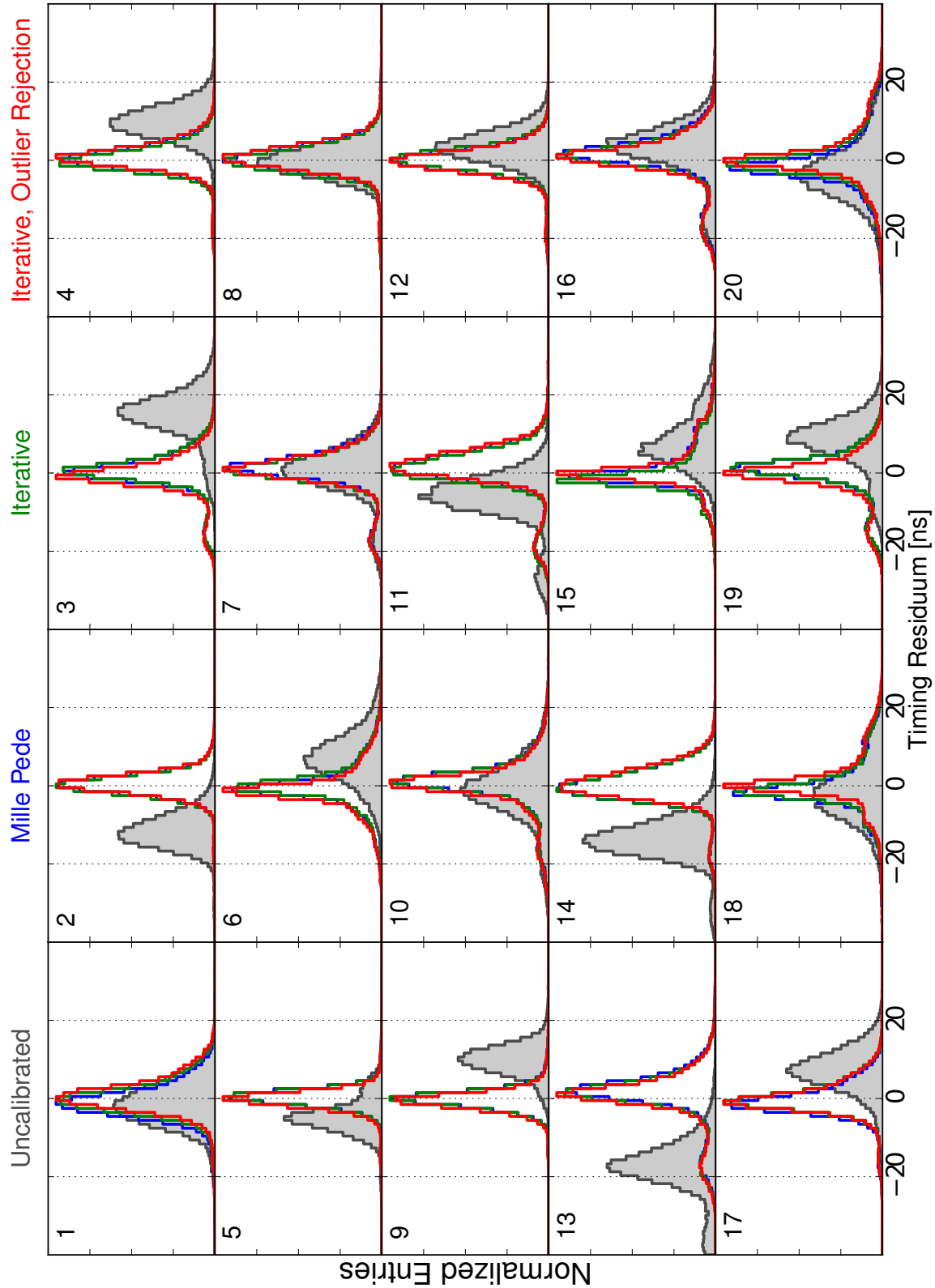
Figure 10.10: The timing residuals observed in the data set used for calibration with the three calibration methods. All methods improve the timing in comparisons to the uncalibrated data which is shown in the filled histograms. We observe that slight offsets of the maximum values of the distribution remain due to asymmetric contributions at some stations. We notice slight advantages of the iterative algorithm including outliers rejection. For future calibrations the use of the MillePede algorithm seems promising when additional constraints to the timing constants of the RDSs can be applied.
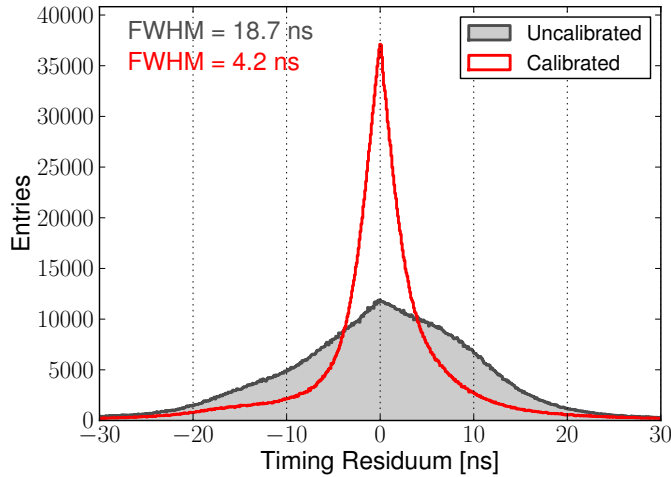
Figure 10.11: Timing residuals in the calibrated and uncalibrated data set. All data with more than N>5 stations is considered. Also after the calibration the residual distribution exhibits tails to larger residuals. As estimator to the distribution with use the full width at half maximum. The calibration improves the timing by more than a factor four. The distribution indicates that in most of the recorded data a resolution of ~ 2 ns is realized.

display. For these events the degrees of freedom degenerate in the spherical wave fit including the γ-factor which leads to an overestimate of the timing resolution.

In the combined calibrated data the timing residuals distribute symmetrically around zero. The asymmetry of the uncalibrated distribution indicates the initial timing offsets. The width of the calibrated distribution is significantly narrowed in comparison to the uncalibrated data. To estimate the improvement of the timing resolution we use the full width at half maximum (FWHM) to characterize the distributions. For the uncalibrated data we find a FWHM of ~ 19 ns which improves to ~ 4 ns when the calibration is applied. For a Gaussian distribution the FWHM roughly indicates twice the standard deviation (FWHM $\approx 2.35\,\sigma$). In our case the calibrated distribution is still clearly non-Gaussian including tails towards larger residuals. However, for the majority of events we conclude that a timing resolution of ~ 2 ns is realized.

The observation of systematic timing offsets between the RDSs was not expected prior to the data taking as identical GPS timing systems are used in AERA. However, in more recent investigations comparing identical GPS systems in laboratory [190] as well as first results of the Beacon timing system installed at AERA [191] indicate that the GPS timing systems are subject to individual drifts of 5 to 20 ns on time scales of several hours. As we have performed the calibration on a data set that was accumulated over larger periods of time the reconstructed calibration constants indicate average offsets of the timing systems. Here should be noted that the installed Beacon system can monitor timing drifts to a sub-nanosecond precision [192], however, constant offset cannot be recovered with the current installation. A combined application of different calibration methods seems promising for further timing calibrations.
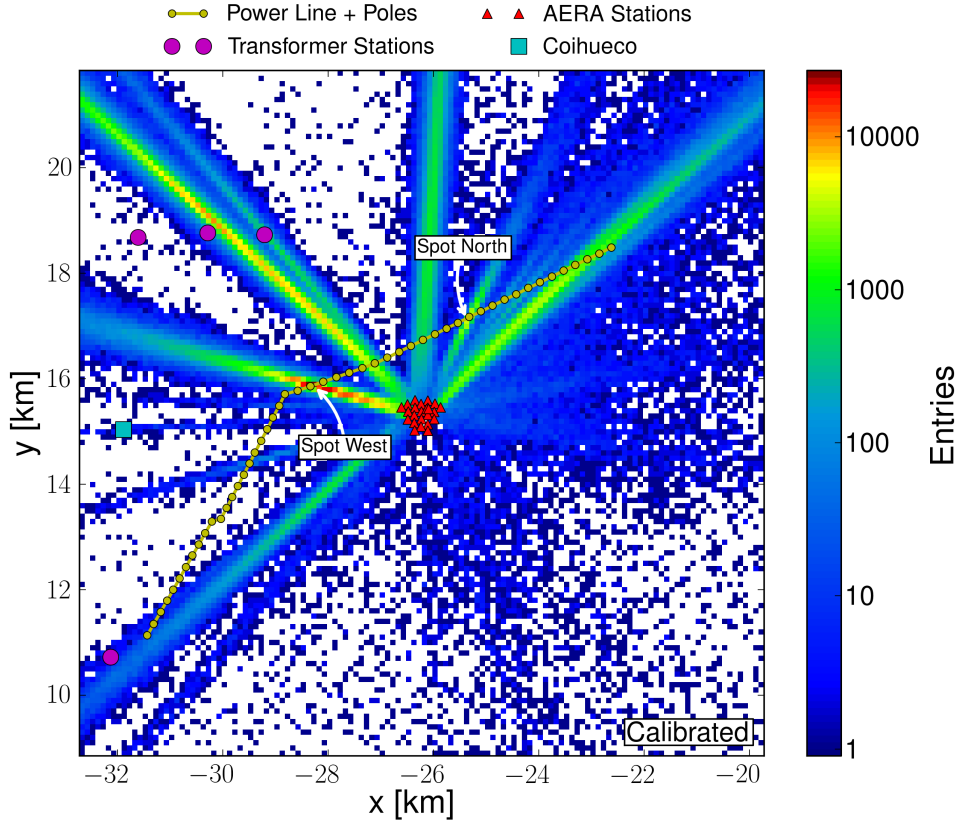
Figure 10.12: Maps of the x and y position of the source point reconstructed from the full data set. The map is generated from calibrated data with a binning resolution of 100×100 m^2. At the 'Spot West' a single bin is filled with 27000 entries. Note the logarithmic color scale.

In the following we apply the calibration constants to the full data set and investigate the impact on the directional and distance reconstructions of the measured radio events.

10.2.3 Calibrated Source Point Reconstruction

We study the spatial distribution of source locations of radio signals that were recorded with $N > 5$ RDSs. We consider the full data set of AERA up to end of May 2011.

The fit of a spherical wave front to the recorded signals yields the direction and the distance towards the source of the transient. With respect to the local coordinate system of AERA we receive a three-dimensional distribution of the source locations. From the angular distribution which we have investigated in Fig. 10.4 we know that most of the recorded signals originate from horizontal directions. In Fig. 10.12 we hence constrain the display of the source locations to a two dimensional map of the AERA terrain. The map presents a section with a width of 13×13 km^2 centered on the position of AERA. The source locations are given as a two-dimensional histogram with a bin width of 100×100 m^2. The colors show the number of reconstructions
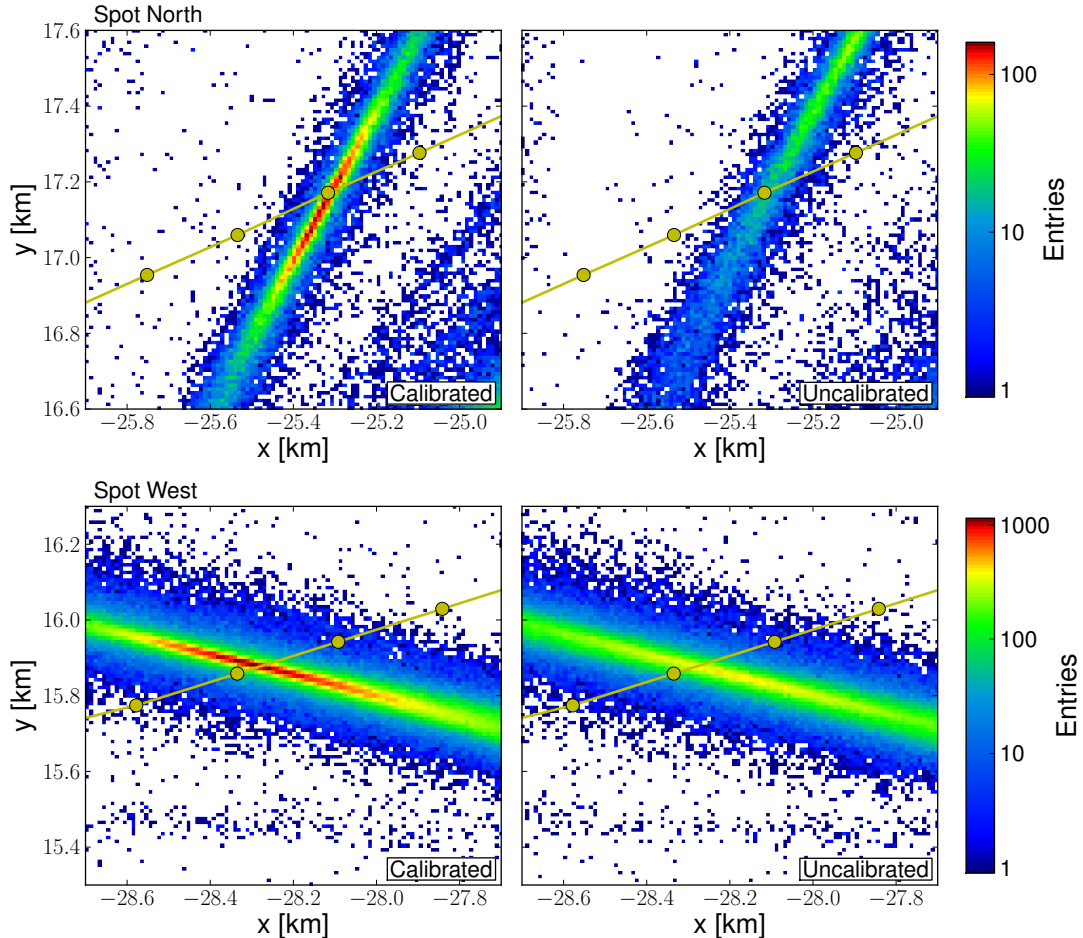
Figure 10.13: A zoom into the two most prominent spots of Fig. 10.12: Spot North in the top panel, Spot West in the lower panel. The symbols denote the power line.

falling into each bin in a logarithmic scale to stress the detailed features of the distribution.

In addition to the source locations the positions of suspected transmitters of transient signals are charted on the map. These include the course of the closest power line, the related power line poles and the site of the Auger fluorescence telescope 'Coihueco'. The mapped transformer stations have already been identified to be sources of transients in a mobile search for transmitters [193].

The same prominent directions which we have observed in the angular distribution of Fig. 10.4 appear in Fig. 10.12 as elongated bands centered towards the detector array. Obviously, the distance from the array to a source point cannot be reconstructed as precisely as the direction towards it. Note that the logarithmic color scale is here somewhat misleading and exaggerates the width of the radial distributions.

We find that most of the reconstructed source locations are associated with the power line and its poles. Most prominent are here the spots labeled as 'Spot North' and 'Spot West'. In the proximity of the Spot West we count 27000 entries in a single bin of the histogram. In total $1.9 \cdot 10^6$ source locations are registered in the

map section. As well the more eastern parts of the power line seem to contribute with several source locations.

The group of three transformer stations indicates the location of the village 'El Sosneado'. El Sosneado extends from the transformers further North and West. From the three transformers only the eastern one is directly indicated by the data.

Towards the South-East direction in the map only few source locations in the proximity of AERA are observed. These directions point into the plain of the Pampa where the major part of the surface detector array is located.

For the display of the source locations we have chosen the data set where the timing calibration of the previous section has been applied. Due to the wide range of the map in Fig. 10.12 the differences caused by the timing calibration can hardly be discriminated in comparison to the uncalibrated distribution. The number of entries in the most significant bin, however, is reduced from 27000 to 15000 in the case of the uncalibrated data. In Fig. 10.13 detailed maps of the two hot spots are visible for both the calibrated and the uncalibrated data.

The close-up of Spot North is shown in top row of Fig. 10.13. Again the power line is indicated in the plot. If we assume that the transients emerge from the closest power line pole then the reconstruction of the uncalibrated data overestimates the distance from AERA towards the source point. However, in the case of the calibrated data the distribution centers both in distance and direction on the pole of the power line. Here should be noted that the applied timing calibration does not make any assumption on the position of the sources of the transients that are used to derive to the calibration constants.

The details of the Spot West can be seen in lower row of Fig. 10.13. Most remarkable is here that the number of events that are reconstructed on top of the power line strongly increases when the calibration is applied. The position of the power line pole is missed by only a few 10 meters.

Currently it is unclear what causes the emission of transient signals from the power line. Transients from transformer stations are likely to be associated with arcing which appears at typical time scales associated to the AC frequency of the civil power supply [194].

We study the angular resolution towards the two hot spots in the left row of Fig. 10.14. The upper histogram corresponds to the Spot North and the lower histogram to Spot West. In both cases the spread of the angular reconstruction is reduced by the calibration. A fit to the inner part of the distributions yields a resolution of 0.3°. In the case of the Spot North in the upper histogram, we also notice a slight shift of the distribution.

In the right row of Fig. 10.14 we show the inverse distance distributions of the two spots. As discussed in Sec. 8.3.2 the inverse distances distribution yields a proper estimator for the location of sources of multiple signals. Especially in the case of the Spot North in the upper right panel the distribution is strongly shifted by the calibration. The shift results in the spatial distribution of this spot centered on the pole of the power line in Fig. 10.13 (upper left). In both cases the distributions are more distinct when the calibration is applied.
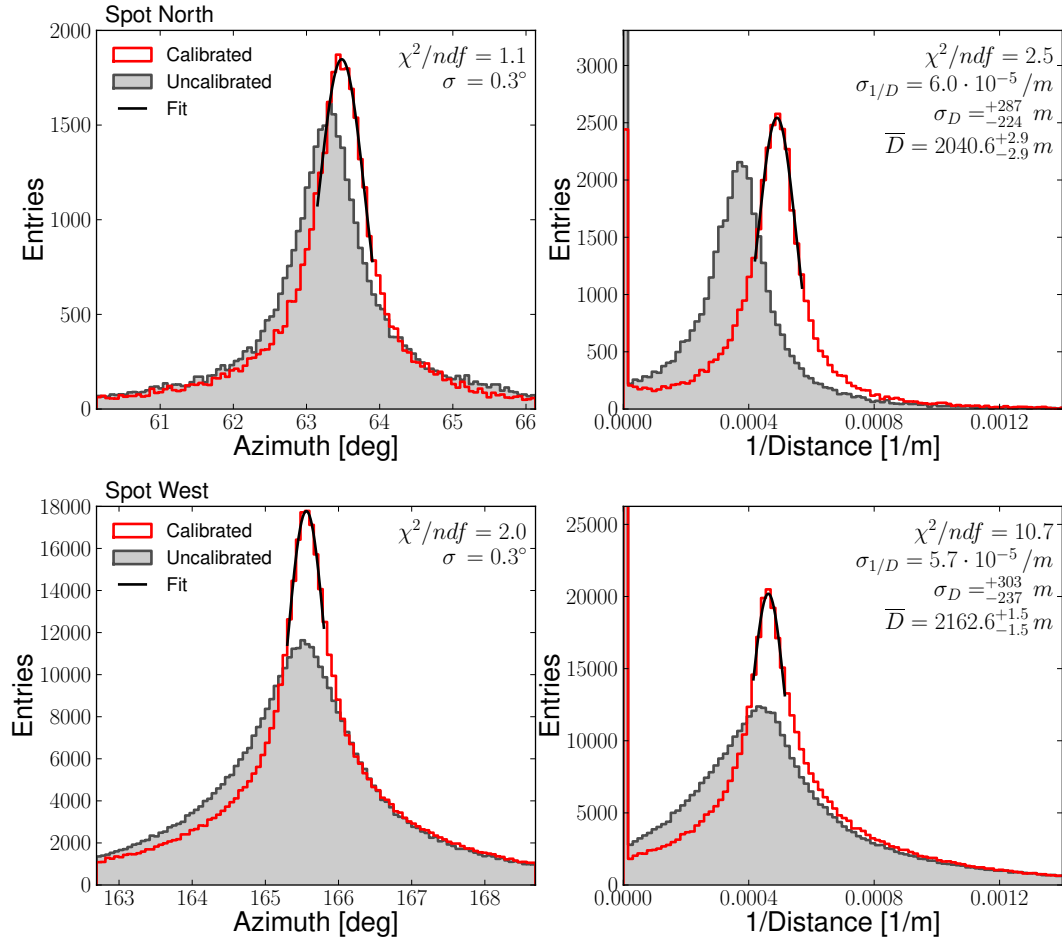
Figure 10.14: Improvement of Spatial Resolution as an example of Spot North (top row) and Spot West (bottom row). Left column: The azimuth distribution in the corresponding direction. Right column: The distance distribution. Note that the estimator for the distance of a single source causing multiple events is obtained from the 1/distance distribution.

Both spots are located in a distance slightly larger than 2 km from AERA. The uncertainties indicated by the σ-quantiles are the precision obtained in the reconstruction of single signals emerging from this distance. The distance resolution ranges at a level of 10 - 14 %. In Sec. 8.3.2 we have studied the distance resolution of a similar source point configuration realized in a set of MC data. In the simulated data the timing resolution of the individual RDSs was limited to 5 ns. The distance resolution observed in the MC data is similar to the precision we find now in the measured data. This indicates that in the full data set a timing resolution of $\sim$ 5 ns is realized including the calibration. Although the distance and angular distributions are strongly peaked we observe non-Gaussian tails which point at the presence of systematic timing effects beyond constants offsets.

Overall, the spatial distributions indicate that the correction for constant timing offsets significantly improves the resolution of AERA. Several efforts are on their way to investigate the timing of the RDSs in further detail.
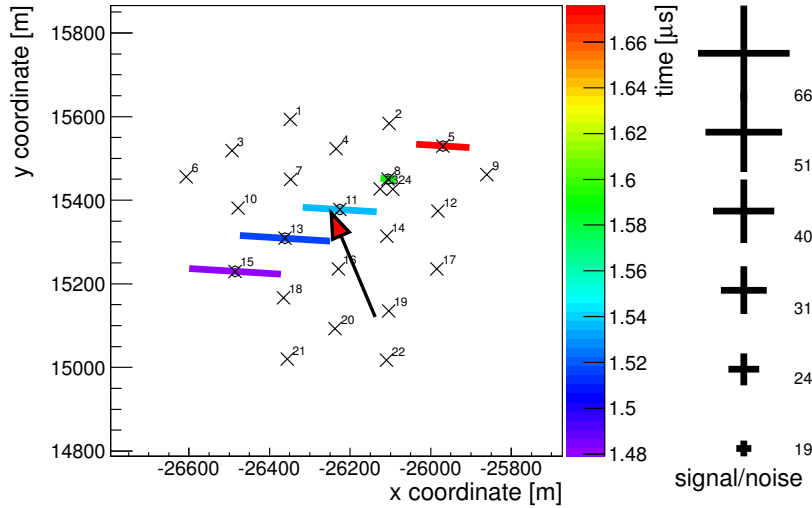
Figure 10.15: Exemplary event with aligned triggered RDSs. This class of event causes the circular structures visible in Fig. 10.4 towards small zenith angles.

10.3 Search for Air Shower Signals in the AERA Data Set

In this section we present methods to create a data set which is enriched with radio signals from cosmic rays. In the previous section we have seen that most of the recorded signals originate from source points located in the horizontal plane which is a first criterion for the rejection of background signals. Looking at the angular distribution in Fig. 10.4 there is, however, a serious amount of scatter from the horizontal directions such that also the angular regions towards the zenith are dominated by horizontal sources.

10.3.1 Geometry Discriminator

A major reason for the contamination of elevated zenith angles by horizontal sources we identify by looking at the configuration of RDSs in events that are reconstructed towards the circular structures in Fig. 10.4. An exemplary event is given in Fig. 10.15.

The triggered RDSs in the displayed event align on one of the symmetry axis of the detector array. The reconstructed incoming direction is indicated with the arrow. However, each incoming direction which can be accessed by a rotation of the arrow around the axis defined by the aligned RDSs will cause the same timing pattern in triggered stations. For such station geometries the reconstruction will hence tend to choose an arbitrary direction on the circle. As a large number of events is detected from few distinct directions circular structures appear in the angular distribution.

To avoid these event geometries we use the positions of the first two triggered stations in an event to define an axis through the detector array. As geometry discriminator we sum the distance towards this axis for the remaining stations in the event. In
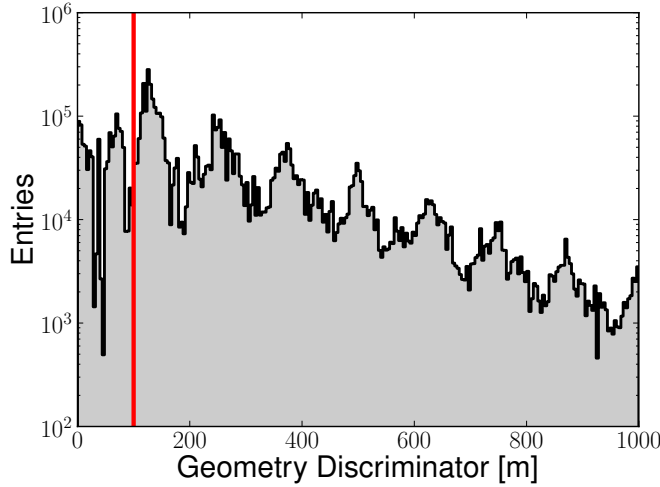
Figure 10.16: The geometry discriminator is an estimator for station geometries that do not allow for a proper angular reconstruction such as depicted in Fig. 10.15. The distribution is here constraint to the smallest values that appear in the data set. Small values of the source discriminator indicated an undefined geometry for the reconstruction. The red vertical line represents a cut that removes large parts of the circular structures in the angular distribution.

Fig. 10.16 the geometry discriminators for a large number of recorded events are displayed. The distribution peaks at positions that represent distinct configurations of RDSs participating in events.

The typical distance between two neighboring detector stations in AERA stage one is 150 m. With respect to events that are recorded with three neighboring RDSs located in a triangle typical geometry discriminators of 130 m are realized. As a cut we require a geometry discriminator > 100 m which safely rejects stretched configuration of triggering radio detector stations in AERA stage one. In Fig. 10.17 (top) the angular distribution of the events that are rejected with this criterion is displayed. As can be seen all circular structures are selected. Moreover, we find that most of the substructures that are present at directions towards the horizon are also caused by particular RDS configurations.

In the lower diagram of Fig. 10.17 the angular distribution with applied cut on the geometry discriminator is visible. In comparison to the uncut distribution in Fig. 10.4 the directions towards small zenith angles are much more sparsely populated. Still, the major source directions and some substructures remain.
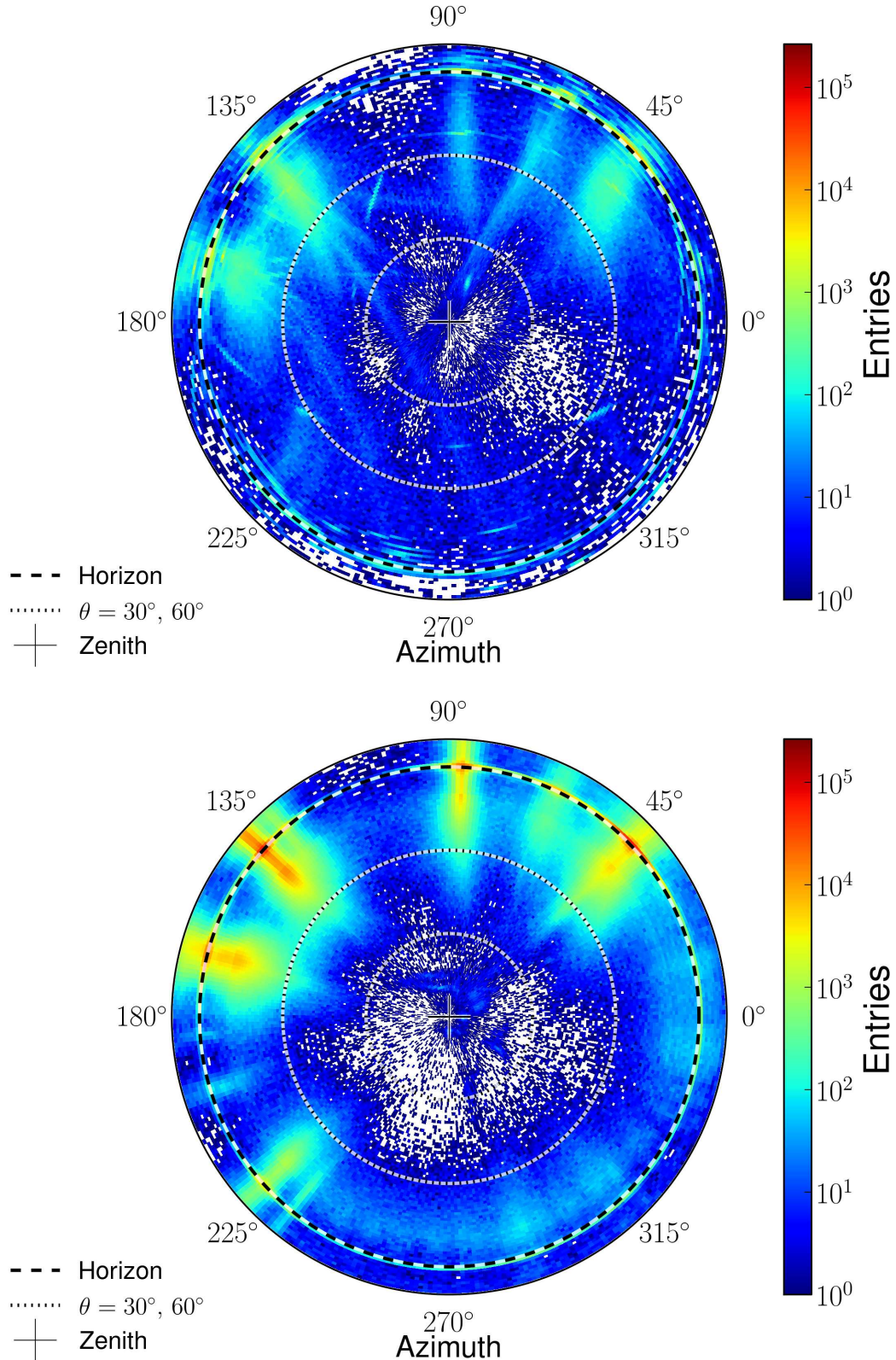
Figure 10.17: The geometry veto applied to data. Top: The directions of the events that are rejected by the cut on the geometry discriminator > 100 m. The cut applies to ∼ 13% of the data set. Bottom: The sky map of event directions with applied geometry discriminator cut. For both plots the data set with applied timing calibration is used.
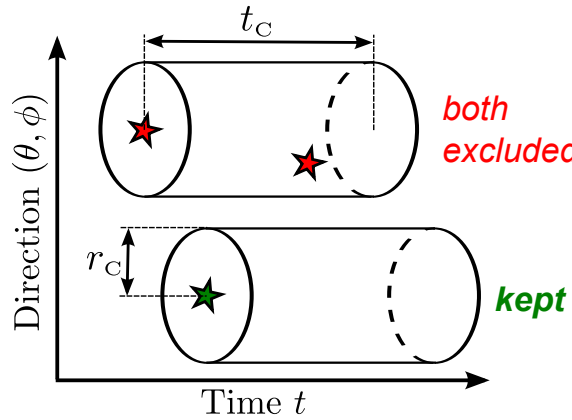
Figure 10.18: Sketch of the cone cut algorithm. Each event (star symbol) defines an angular region with a radius r_C and a length in time t_C counted from the time the signal was detected. If a second event falls into this space, both events are rejected. Only events that are separated in time and space are treated as candidates for air showers and kept for further analysis.

10.3.2   Cone Cut Algorithm for the Removal of Transient Noise Sources

In first approximation extensive air showers are distributed uniformly in time and direction when detected with AERA. In contrast to this isotropic distribution, sources of transient noise yield a background that is strongly directed and often culminated over distinct periods of time.

We have discussed noise sources that are located on the ground in the last section. During noisy periods these induce trigger rates in AERA that well exceed 1 Hz. Two examples of transient noise sources that are not located statically on the ground but moving are displayed in Fig. 10.19.

Thunderstorms and airplanes are examples for sources of transient noise that appear sporadically but then induce a large number of events from a changing direction. An ansatz for the removal of sources of multiple signals from the data set is sketched in Fig. 10.18.

An event defines an angular region with a radius r_C and a length in time t_C. With respect to a sphere with the detector in its center this resembles a conical geometry. All events that fall into the cone defined by the first event are rejected including the initial event. Even if an event is already rejected it is used to define a further cone which can reject more distant events.

The cone cut algorithm has two parameters: the angular radius r_C and the length of the cone t_C. To study the impact of these two parameters on the removal of background and the selection of air showers we make use of the data set in which air showers were identified in coincidence with the SD. With respect to Fig. 10.1 this is the data in the overlap region from the mid of May until the end of June 2011 (all runs with ID $\geqslant 2150$ and ID $\leqslant 2174$).
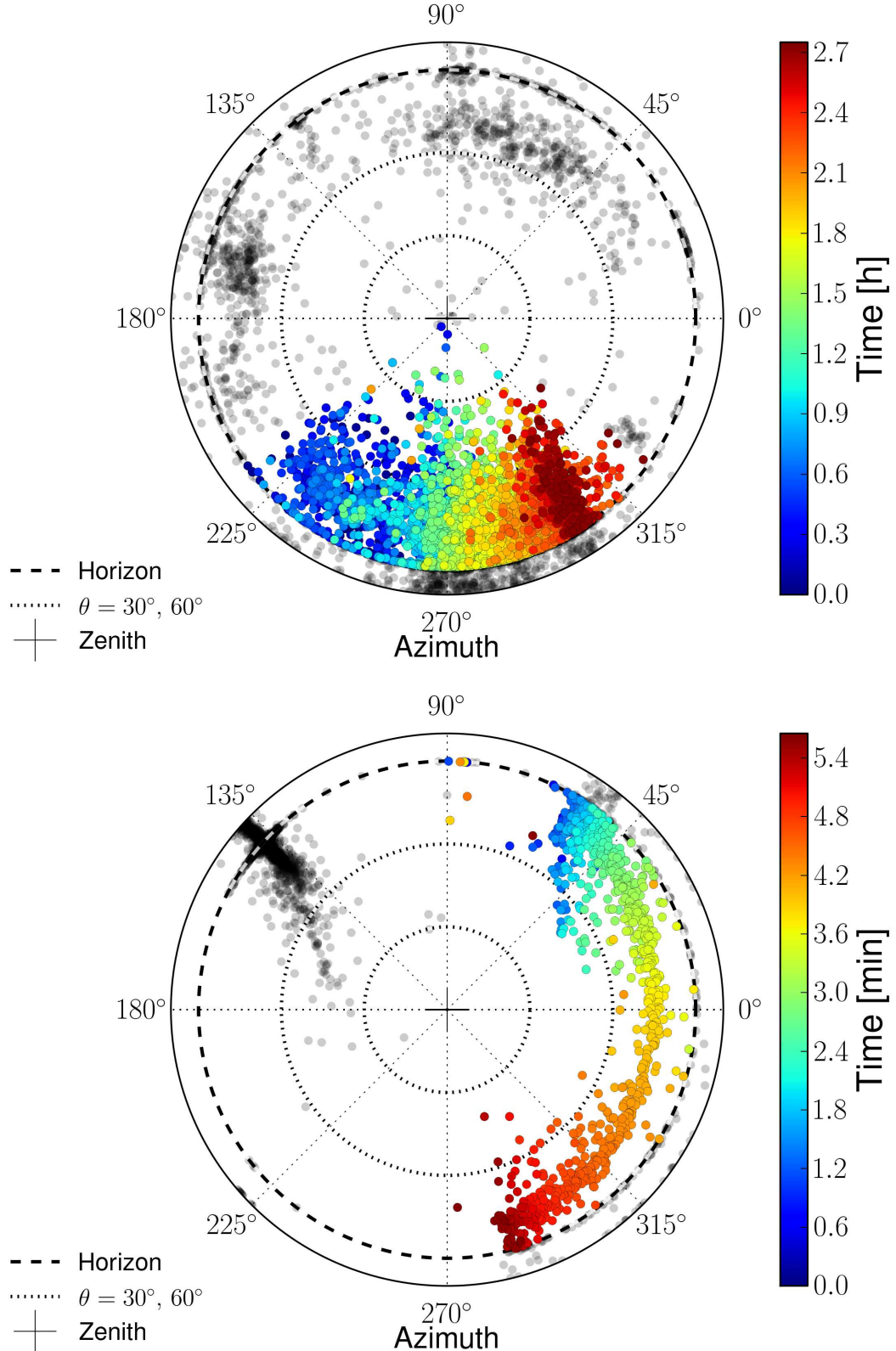
Figure 10.19: Sporadic Source of Transient Signals. Note the difference in the time scales between the two plots indicated by the color scale. Top: A thunderstorm detected in AERA (run 1588). A wide source region of transients is observed over ∼ 3 hours passing AERA in southern directions from the Andes in the West towards to Pampa in the East. Bottom: The first airplane observed with AERA (run 2161 starting at GPS timestamp 988229880). The plane is detected within a time span of ∼ 5 minutes passing AERA in the East and flying towards the South. Airplanes were up to now only reported from one of the pioneering radio setups [108]. In both plots transient signals of other sources during the same time spans are indicated in gray.
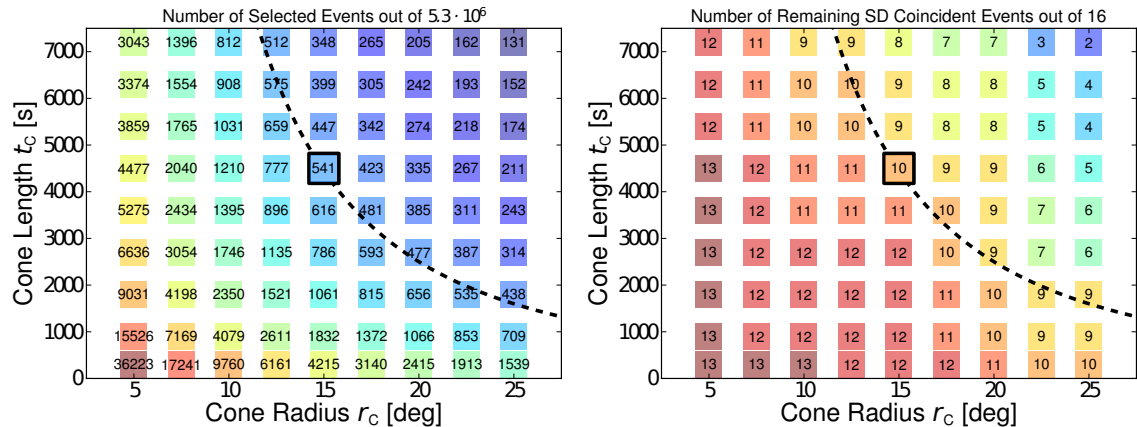
Figure 10.20: Event selection with cone cut. Left: Number of events remaining in the selection after the application of the cone cut with the indicated parameters. Right: Number of coincident air shower events that are still present in the selections on the left-hand side with the respective settings.

We apply the cone cut to the full data of these runs with which comprises $5.3 \cdot 10^6$ events after the geometry cut described in the previous section. Within these data there are at 16 air shower signals with $N \geqslant 3$ RDSs which were identified due to their coincidence with the SD. Since we expect AERA to have a lower energy threshold than the SD, the number of recorded air shower signals in the data set should be larger than 16.

In Fig. 10.20 (left) the number of remaining events is studied as a function of the two cone cut parameters. We vary the radius between $5°$ and $25°$ and the time from 5 to 105 minutes. As expected an increasing cone radius as well as increasing cone length lowers the number of events that remain in the data set. Typical reduction factors in comparison to the full data set range at 10^{-4}. We observe that some reconstructions fall into the cones of several 10^5 events.

Within the remaining events we count the number of coincident air showers that are still present. As can be seen in the right panel of Fig. 10.20, the number of air shower events is much less impacted by the cone cut than the full data set.

Both parameters, cone radius r_{C} and cone length t_{C}, have a significant influence on the number of selections. If we think of events that are isotropically distributed in time and direction then the cone volume $V_{\mathrm{C}} = r_{\mathrm{C}}^2 \cdot t_{\mathrm{C}}$ defines a decay constant to the number of events remaining in the data set when the algorithm is applied. In Fig. 10.21 we study the number of remaining events as a function of cone volume.

We first consider the number of remaining coincident events. Here the picture of an isotropic distribution that decays with increasing volume of the cone is matched. We fit an exponential function to the progression.

Looking at the full data set we find a suppression that is initially enhanced in comparison to the exponential decay. The cone cut strongly suppresses anisotropic portions in the full event distribution. At some point the further reduction of events resembles the progression observed in the case of the coincident events. This indi-
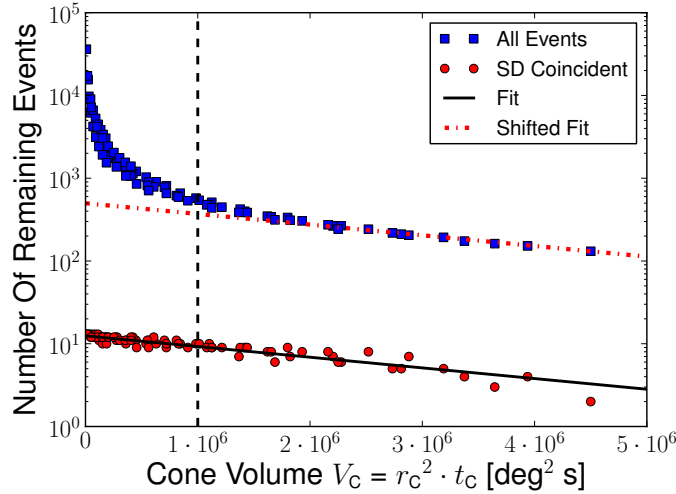
Figure 10.21: Choice of parameters for the dynamic cone cut. The number of remaining events in the full data set is observed as a function of cone volume. For each cut the number of coincident events still remaining in the data set is counted. The two observables develop differently with increasing volume of the cone.

cates that for even larger cone volumes only portions of a distribution are cut to which also the coincident events can be counted.

To select events originating from this more isotropic distribution we compare the shapes of the progressions with increasing cone volume as indicated in Fig. 10.21. We roughly identify a cone volume $V_{\rm C}^{\rm cut} = 10^6$ deg^2 s where the transition in the event rejection takes place. With respect to the parameter space displayed in Fig. 10.20 this cone volume corresponds to the dashed lines. With $r_{\rm C} = 15°$ and $t_{\rm C} = 4500$ s we perform a moderate choice of parameters for the cone cut algorithm.

Looking at the number of coincident events we conclude that cone cut algorithm realizes an efficiency of

$$\varepsilon = \frac{10}{16} \approx 60\% \tag{10.2}$$

in this pre-selection of recorded data. The 541 remaining events have recently been subject to further detailed analysis using the reconstruction of the three-dimensional electric field as a follow up to our studies in Sec. 9. Inspecting the polarization vector of the selected signals, 27 events are identified that are very likely to be cosmic ray induced air showers [195]. Within this set of 27 events 9 of the coincidences with the SD remain. Hence a purity of at least:

$$\rho \geqslant \frac{9}{27} = 30\% \tag{10.3}$$

is realized in the combination of the two selection methods. We conclude that the cone cut algorithm is an efficient tool for the selection of cosmic rays from a large number of background events. Together with the mentioned polarization vector analysis it enables AERA to identify air showers only by means of the radio detection technique.

11. Antenna Evaluation for the Next Stage of AERA

11.1 Antennas for the Detection of Radio Signals from Cosmic Ray Induced Air Showers

In this chapter we present three antennas that have been evaluated for the next setup stage of AERA. The three antenna models investigated are highly diverse and address the task of radio detection of air showers with different concepts. All antennas presented are the result of several stages of development taking into account the experience gained in smaller radio detection setups both in Europe and at the site of the Pierre Auger Observatory.

This is necessary as the environmental conditions of the Argentinian Pampa impose special demands on the antenna structure for instance through wind loads of up to 160 km/h. Hence, the durability and consequent costs for maintenance directly impact on the success of an antenna model especially with respect to a detector design with a large number of detector stations.

With respect to the electrical properties of the radio sensors it is useful consider the antenna as integral combination of the metallic structure capturing the signal and the first low noise amplifier (LNA). Whereas the structure determines the directional properties of the antenna, the ultra-wideband reception of the antenna is ruled by the combination of both elements.

Requirements on the directional properties of the antenna are imposed by the laminar layout of the radio detector array. At each detector station the full sky needs to be observed such that omni-directional antennas are used. To reduce a bias due to the polarization characteristics of the antenna the construction requires a placement of at least two perpendicular sensors at each detector station.

Currently, the properties of the radio pulse and its generation mechanism are subject to research beyond its utilization to measure the underlying cosmic ray. Hence the antennas are sensitive in a broad frequency range to allow for a maximum detail of the observation. At AERA limitations are given by the presence of AM band transmitters below 30 MHz and FM band transmitters mainly above 80 MHz.

11.1.1 The Small Black Spider Antenna

In the current first setup stage of AERA the Small Black Spider antenna is used (cf. Sec. 5.3). Within more than one year of placement in the field the antenna has

Figure 11.1: The Salla antenna during test measurements at the Nançay Radio Observatory. The Salla realizes a Beverage antenna as a dipole loop of 120 cm diameter. The antenna is readout at the top with an LNA. The amplified signal is guided through the antenna structure to the bottom.

proven to be both — robust against the environmental conditions of the Argentinian Pampa and sensitive to radio signals from cosmic ray induced air showers. The Small Black Spider antenna is hence a natural candidate for the next deployment stage of AERA. The details of the antenna and its logarithmic periodic design we have discussed in Sec. 7.

11.1.2   The Salla Antenna

The short aperiodic loaded loop antenna 'Salla' realizes a Beverage antenna as dipole loop of 120 cm diameter. The Salla antenna has been developed with the focus to provide a minimal design that fulfills the need for both, ultra-wideband sensitivity and minimized costs for production and maintenance of the antenna in a large scale radio detector. The compact structure of the Salla makes the antenna robust and easy to manufacture. A picture of a cross polarized Salla is displayed in Fig. 11.1.

The Beverage antenna design includes a terminal resistance within the antenna structure to give a specific shape to the directivity. In the case of the Salla a resistance of $500\,\Omega$ connects the ends of the dipole arms at the bottom of the antenna. The antenna is read out at the top which is also the position of the LNA. While signals coming from the top direction will induce a current directly at the input of the amplifier, the reception from bottom directions is strongly suppressed as the captured power is primarily consumed within the ohmic resistor rather than amplified by the LNA. The resulting strong suppression of directions towards the ground reduces the dependence of the antenna on environmental conditions which might vary as a function of time and are thus a source of systematic uncertainty. With the inclusion of
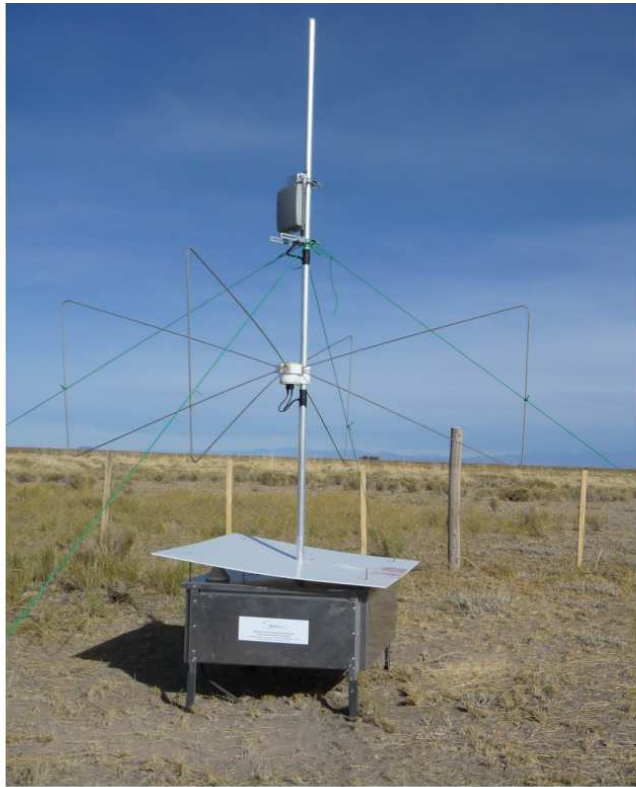
Figure 11.2: The Butterfly antenna installed at the site of the Pierre Auger Observatory. The antenna is installed in a height of 1.5 m above ground. The antenna construction aims at a close integration with a box containing the read out electronics and a center pole which is also used to carry an antenna for wifi communication.

an ohmic resistor the Salla especially challenges its amplifier as only $\sim 10\%$ of the captured signal intensity are available at the input of the LNA. Proper matching between the antenna structure and the LNA is realized with a 3:1 TLT. The structure of the Salla creates a sensitivity which is flat as a function of frequency.

Salla antennas are used at the Tunka-133 radio detector [196] and have been tested in a radio detection setup at the Auger site and within the LOPES experiment. A detailed description of the Salla antenna is given in [197].

11.1.3 The Butterfly Antenna

The 'Butterfly' is a bowtie antenna and the successor of the antennas used for the CODALEMA [198] radio detector. The Butterfly has a dimension of $2 \times 2 \times 1$ m^3 and is constructed with electrically short dipoles. The dipole signals are fed directly into the input of the LNA at the center of the antenna. The dipoles are realized in a self-supporting frame structure which reduces the sensitivity to heavy wind loads and simplifies the construction. The Butterfly antenna is presented in Fig. 11.2.

The Butterfly explicitly uses the presence of the ground to enhance its signal. The center of the antenna is installed at a height of 1.5 m. Here, the direct wave and the wave reflected on the ground add constructively in the antenna throughout the

full bandwidth and most incoming directions. In the case of the Butterfly antenna ultra-wideband sensitivity is obtained by designing the input impedance of the LNA depending on the impedance of the fat dipole structure as a function of frequency. In this way, the sensitivity of the dipole has been optimized to allow for an efficient detection also of wavelengths that are much longer than the dimension of the antenna structure. The LNA itself is a dedicated ASIC and does not require a TLT transformer since its input is differential [199].

In the current extension of the CODALEMA experiment [68] 33 Butterfly antennas are deployed. The antenna was used successfully to observe cosmic rays in one of the pioneering setups at Auger [63]. In Ref. [200] the details of the Butterfly antenna are presented.

11.2   Comparison of Transient Antenna Responses

From the comparison of the measured and the simulated antenna characteristics in Sec. 7.7 we conclude that overall the simulations give a realistic description of the Small Black Spider antenna characteristics. In this section we use simulations to compare the three antennas presented in Sec. 11.1 with respect to their response to transient signals.

11.2.1   Simulation of the Vector Effective Length

To investigate the transient response characteristics of the antennas we simulate the respective VELs with the NEC-2 program. In the case of the Small Black Spider the simulated antenna model is identical to the one presented in Sec. 7.7. Simulation models for the Butterfly and the Salla antennas have been created following the corresponding structure specifications. The Butterfly antenna is explicitly designed to be used at a height of 1.5 m above ground which we have realized in the simulation. The other two antennas are simulated with the lowest sensitive element at the current installation height of the AERA antennas of 3 m.

For the simulated calibration measurements in Sec. 11.1 we have explicitly introduced a transmitting antenna as the source of the electric field. For the comparison between the different antennas we access the VEL from direct simulations of the receiving antenna without an additional transmitter. The simulated antenna characteristics presented in this section thus avoid possible deficiencies of the transmitter simulation and correspond to calibration measurements performed at very large distances. The desired VELs are accessed from the simulation as described in Sec. 6.8.2.

11.2.2   Characteristics of the Ultra-Wideband Vector Effective Length

In Fig. 11.3 the absolute values of the VELs and in Fig. 11.4 the corresponding group delays are displayed as a function of frequency for the three tested antennas. In the case of the Small Black Spider the depicted characteristics correspond to the
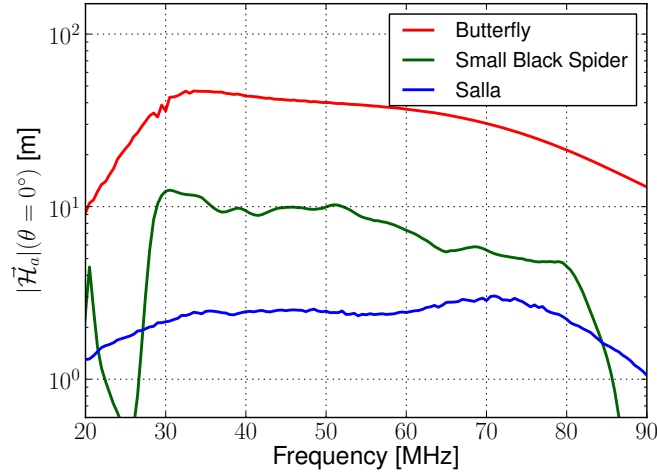
Figure 11.3: The vector effective length as a function of frequency for the zenith direction for the three tested antennas. Note the logarithmic scale on the y-axis.

displays in Figs. 7.20 and 7.23 with slight changes due to the adapted simulation setup.

The absolute values of the VEL are rather different for the three antennas. The amplifier of the Butterfly antenna exhibits the strongest gain resulting in large values for the VEL. The amplifiers of the Salla and the Small Black Spider feature similar amplifications, however, the VEL of the Salla is reduced as the antenna is loaded with an ohmic resistor.

Note that these average levels of the VELs do not reflect the signal-to-noise ratio obtained in measurements.

Regarding the dependence of the VEL as a function of frequency, both the Butterfly and the Small Black Spider focus on the performance at lower frequencies. The two antennas have been optimized with respect to the frequency content of the radio pulse which is predicted to be governed by longer wavelengths especially when observing air showers at large distances from the shower axis [86, 84].

In addition the Small Black Spider acts as a sharp bandpass to the AERA band. Also the Butterfly slightly attenuates signals below 30 MHz to avoid short band transmitters.

The drop-off in sensitivity visible for the Butterfly antenna at the highest frequencies results from the specific observation direction of $\theta = 0°$ chosen for the display. Here, the constructive interference of the direct and the wave reflected from the ground is diminished at the height of the Butterfly of 1.5 m above ground for frequencies above 70 MHz.

The Salla antenna has been designed for highest sensitivity at 70 MHz by approaching a situation of conjugate matching between the impedance of the antenna structure and the input impedance of the LNA (cf. Sec. 6.4). As will be discussed in Sec. 11.3 the intensity of the radio background noise decreases with frequency. In
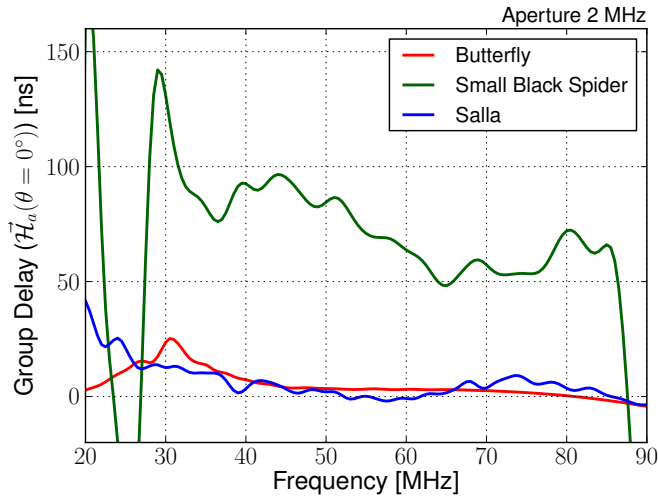
Figure 11.4: The group delay induced by the antennas for signals coming from the zenith direction $\theta = 0°$. A deviation from a non-constant group delay induces dispersion of the measured transient signal.

combination with an increasing antenna sensitivity the Salla is intended to create noise spectra that are flat as a function of frequency.

In Fig. 11.4 the group delays of the antennas are pictured. In comparison to the Small Black Spider, the Butterfly antenna and the Salla feature an almost constant group delay within the considered bandwidth from 30 to 80 MHz.

11.2.3   Transient Antenna Characteristics

Up to now we have discussed the Fourier transform of the VEL $\vec{\mathcal{H}}_a$. Antenna characteristics inspected at discrete frequencies correspond to the properties of the antenna that will be observed under the reception of mono-frequent signals which implies an infinite signal duration. The transient response is encoded in the development of the antenna characteristics as a function of frequency.

To evaluate the distortion introduced to transients by variations of the VEL we apply the inverse Fourier transform and inspect the VEL in the time domain:

$$\vec{H}_a(t) = \mathcal{F}^{-1}(\vec{\mathcal{H}}_a(\omega)) \quad [\text{m Hz}] \quad . \tag{11.1}$$

The examination of the VEL in the time domain combines the full frequency range and takes into account the respective phase relations. Since the bandwidth is limited by the antenna characteristics the treatment of the VEL in the time domain results in a useful estimator.

The result of the transformation in Eqn. 11.1 is displayed in Fig. 11.5 restricted to a common bandwidth of 30 to 80 MHz. In the time domain the antennas characteristics can be interpreted in terms of a transient wave form. The response to an incoming signal is calculated as convolution of the respective displayed VEL and the incoming wave.
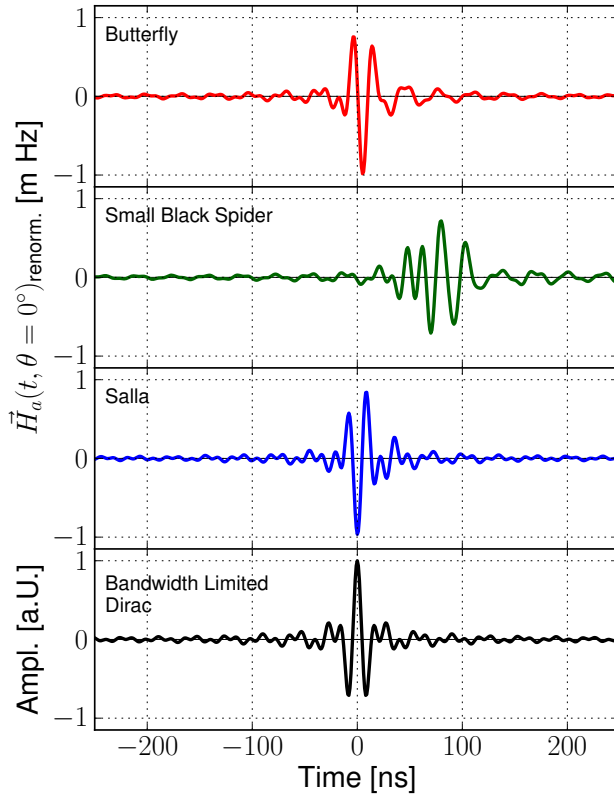
Figure 11.5: The VEL in the time domain for the zenith direction $\theta = 0°$. The VELs have been limited to a common bandwidth of 30 to 80 MHz. The functions are renormalized to their respective maximum peak value which would be realized without dispersion in the antenna. The bandwidth limited Dirac pulse corresponds to an ideal antenna which introduces a bandwidth limitation to incoming signals only.

For comparison also a bandwidth limited Dirac pulse is shown. The shape of the Dirac pulse corresponds to a flat transfer function without dispersion. Hence, the Dirac pulse represents the VEL of an antenna that fully reproduces the shape of incoming signals within the bandwidth.

The Salla and the Butterfly antenna almost realize an unbiased reproduction of incoming signals. The relatively large average group delay of the Small Black Spider already indicated in Fig. 11.4 is visible in Fig. 11.5 as a time delay of $\vec{H}_a(t)$. In comparison to the other antennas the Small Black Spider introduces the largest signal distortion. The pulse is broadened which corresponds to the dispersion induced by the variations of the group delay within the bandwidth.

As normalization to the characteristics displayed in Fig. 11.5 we choose the peak value of the respective $\vec{H}_a(t)$ that would be realized if the VEL was not distorted owing variations of its group delay. We find that the Salla and the Butterfly antenna keep $> 95\%$ of their peak amplitudes whereas the maximum VEL of the Small Black Spider is reduced to $\sim 70\ \%$ of the undispersed waveform.
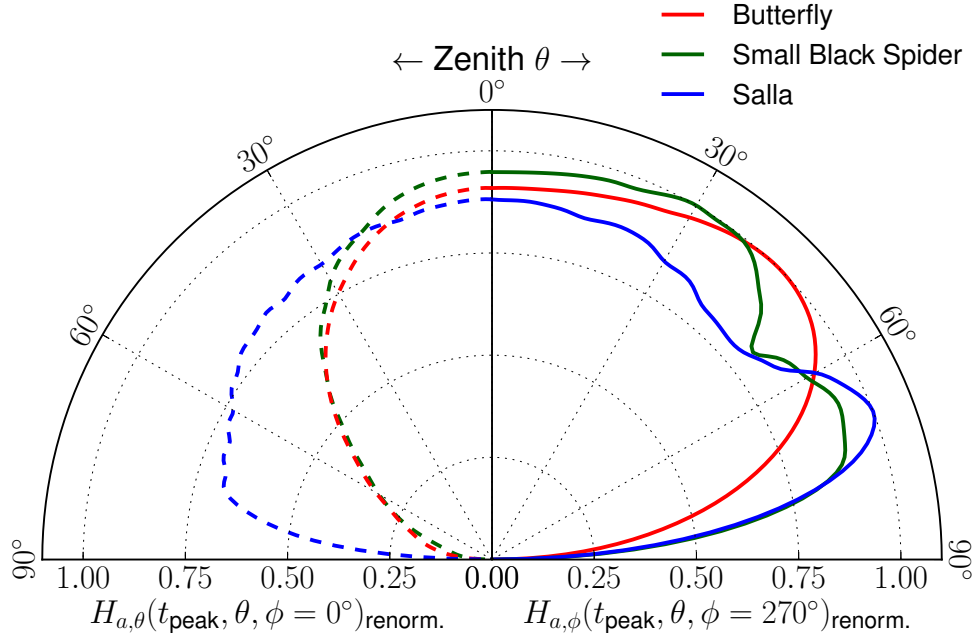
Figure 11.6: Peak directional diagram: Displayed is development of the peak amplitude of the VEL in the time domain as visible in Fig. 11.5 as a function of zenith angle. The two components of the VEL are treated separately. The zenith angle dependence of the $\vec{e}_\theta$-component of the VEL is shown in the left part of the diagram. In the right part the $\vec{e}_\phi$-component is depicted. Two azimuthal directions have been chosen to maximize the readings of the respective VEL component (see Fig. 6.3). The readings are normalized to the maximum peak value obtained in the zenith angle range. For the zenith direction $\theta = 0°$ both components represent the same antenna characteristic which results in a connecting condition for the left and the right part of the diagram.

In the calibration measurements with the Small Black Spider we have seen that the directional properties of an antenna depend on the considered frequency (cf. Fig. 7.21). Extending the idea in Ref. [201], we investigate the peak value of the VEL in the time domain as a function of incoming direction in Fig. 11.6. The plot is subdivided for the two components of the VEL $H_{a,\theta}$ and $H_{a,\phi}$. In the case of the Small Black Spider the function $H_{a,\phi}(t_{\text{peak}}, \theta, \phi = 270°)$ in the right part of the diagram is hence a wideband representation of the directional characteristics displayed in Fig. 7.21.

For the Small Black Spider antenna we find that the side lobe structure is less distinct in the case of the transient characteristic when compared to the side lobes at single frequencies (Fig. 7.21). The peak response of the Salla antenna is reduced for zenith angles towards $\theta \sim 50°$ when the $\vec{e}_\phi$-component is considered. In this polarization direction the Butterfly antenna features the least complex coverage of the zenith angle range up to 70°. The suppression of zenith angles towards the horizon depends on the heights of the antenna above the ground.

In the discussion of Fig. 6.1 we motivated that dipole-like antennas become insensitive when the incoming direction of the signal aligns with the dipole axis of the

antenna. In Fig. 11.6 the development of the $\vec{e}_\theta$-component of the peak response is dominated by this geometric effect in the case of the Small Black Spider and the Butterfly antenna. Here, the circular construction of the Salla antenna leads to a rather constant peak response up to high zenith angles. This results in an enhanced reception of vertically polarized signals from directions close to the horizon.

11.3   Observation of Galactic Noise Intensity

The response voltage to an incoming transient signal needs to be discriminated from a continuous noise floor that overlaps the desired waveform. The sensitivity of an antenna can therefore be expressed in terms of signal-to-noise ratio as obtained from measurements. The contribution of the signal to this ratio we have investigated in the previous sections. To characterize the noise that is recorded with the antennas we have performed dedicated test measurements which we will present in this section.

Beyond human-made noise the dominant source of continuous radio signal in the bandwidth from 30 to 80 MHz is the galactic radio background. This diffuse galactic background emission is mainly caused be charged particle gyrating in the magnetic fields of our galaxy [202].

The spectral irradiance $I_\nu(\nu)$ of galactic background depends on the considered frequency and the observed direction in the sky. The frequency dependence can be described by a power law:

$$I_\nu(\nu) \propto \nu^{-\beta} \quad , \qquad [I] = \text{Wm}^{-2}\text{Hz}^{-1} \quad . \tag{11.2}$$

The spectral index β ranges from 2.4 to 2.9 and depends on the frequency range and on the observation direction [203].

The dominant contributions to the galactic radio background come from directions towards the galactic plane. The tested antennas are set up to simultaneously observe a half-sphere of the sky. Consequently, variations of the recorded noise level will occur due to the rise and fall of the galactic plane in the field of view of the antennas.

The galactic noise background represents an irreducible background contribution to the observation of air shower signals. However, the variations of the galactic radio signal can be considered as a measure of the antenna sensitivity. These measurements we have performed at the Nançay Radio Observatory.

11.3.1   Observation of the Galactic Radio Background

The antenna test bench at the site of the Nançay Radio Observatory is dedicated to the comparison and improvement of antennas used in radio astronomy. Owing its radio quietness the Nançay site features similar observing conditions as the site of the Pierre Auger Observatory.

The three considered antenna (cf. Sec. 11.1) were installed in the test bench for simultaneous observation of the radio background intensity with their read out dipole
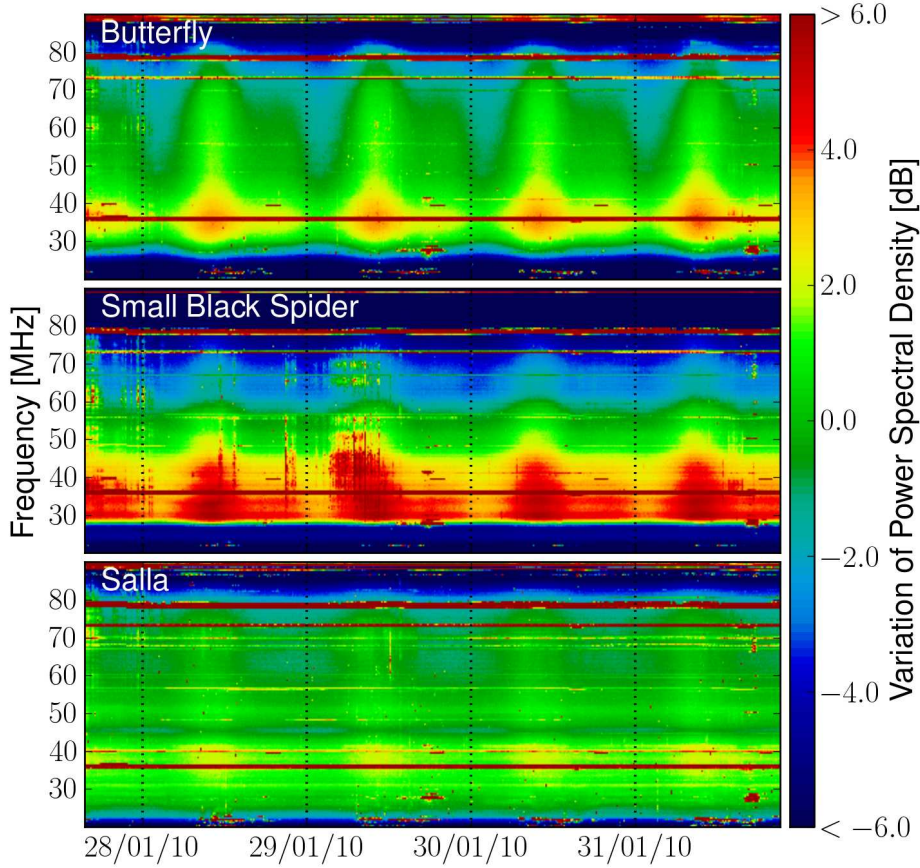
Figure 11.7: Continuous spectra recorded simultaneously with the three tested antenna at the test bench of Nançay Radio Observatory over a period 4 days. An offset value is subtracted from the data of each antenna to allow for a common scale of the power axis. From top to bottom: Butterfly Offset = -50.1 dBm/MHz, Small Black Spider Offset = -62.9 dBm/MHz, Salla Offset = -67.5 dBm/MHz. See text for details.

axes pointing in East-West direction. Besides different coaxial cables, all antennas were read out with the same chain of analog electronics which we have set up to access frequencies between 22 and 82 MHz. Spectra from the different antennas were recorded in consecutive sweeps with the same spectrum analyzer. In our measurements we receive one spectrum every ~ 4 seconds per antenna. Within the measured bandwidth the continuous noise floor of the readout chain is more than 10 dB lower than the average signal power delivered by the Salla antenna which provides the lowest signal power of the three antennas.

In Fig. 11.7 the dynamic spectra derived from 10^5 spectrum sweeps for each antenna are displayed. The readings of the spectrum analyzer are normalized to the resolution bandwidth of the device to yield the recorded power spectral density.

In the dynamic spectra FM band transmitters appear as horizontal lines at the highest frequencies. At the lowest frequencies short wave transmitters are visible with varying amplitude due to the changing conditions of the ionosphere. In the relevant frequency range from 30 to 80 MHz only few weak transmitters are present,
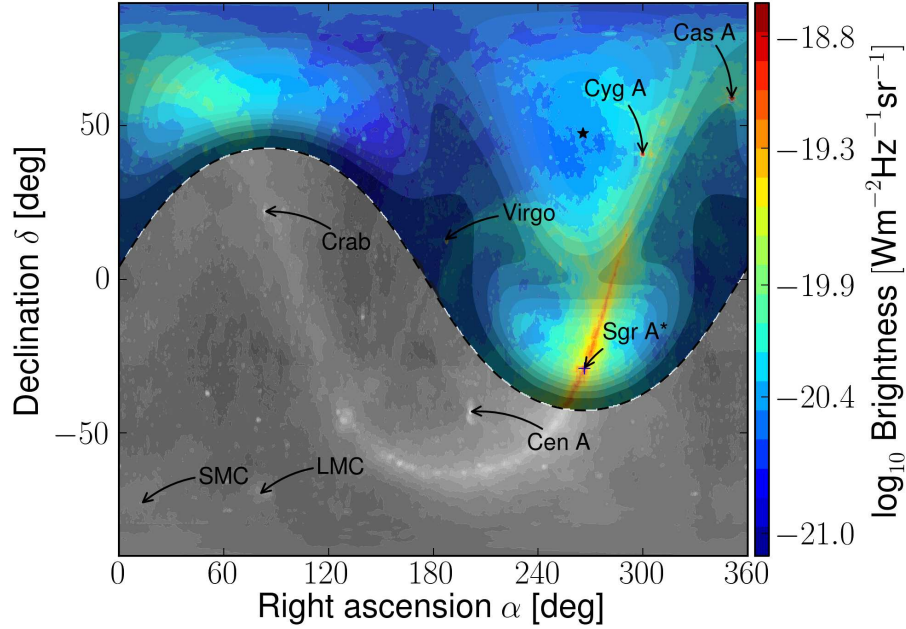
Figure 11.8: Map of galactic noise intensity generated with LFmap at 55 MHz. Temperatures have been translated to intensities following the Rayleigh-Jeans law. The colored data show noise intensities in the field of view of the Nançay Radio Observatory at a specific time. The horizon is displayed as dashed line. The shade over the colored data indicates the relative antenna sensitivity of the Small Black Spider LPDA at the corresponding frequency oriented in east-west direction at Nançay. The measured side lobe in Fig. 7.21 (middle of left column) is here pointing in the direction of the galactic center (Sgr A*). Please refer to a colored version of this plot.

some of them only appearing for short periods of time. Vertical glitches are indicators for an overdrive of the antenna over short periods of time.

For all three tested antennas a variation over a wide frequency range with a day-like periodicity is visible. This variation results from the changing position of the galactic disc in the field of view of the antennas and follows the sidereal day time. The sidereal day is ~ 4 minutes shorter than the Julian day which is not resolved in the displayed measurement period of 4 days. We have verified the observation of the sidereal period with repeated measurements in the test bench several months apart [152]. For the site of the Pierre Auger Observatory long term background observations are described in Ref. [113].

We observe that the variation of the visible galactic radio sky is mapped differently by the antennas onto the recorded power spectral density. Especially in the case of the Salla the amplitude of the variation appears to be less distinct than in the case of the other antennas.

11.3.2   Simulation of Galactic Radio Background Reception

For proper judgment of the measured variations in Fig. 11.7, the directional sensitivities of the antennas need to be taken into account. For this we calculate a
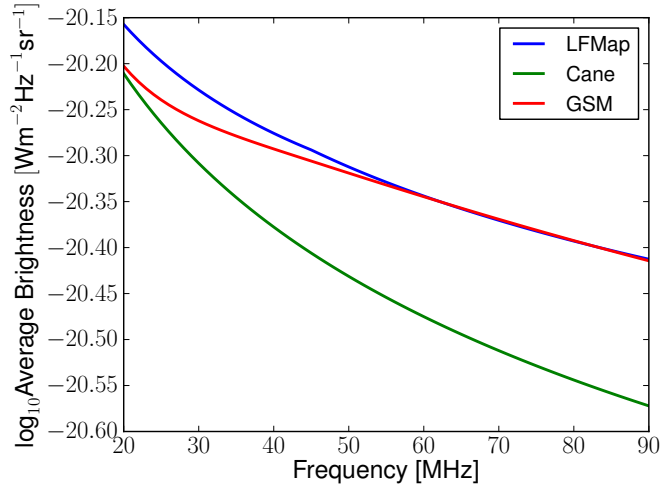
Figure 11.9: Comparison of integrated irradiance for three radio descriptions of the galactic radio background.

prediction of the progression of the power received due to the galactic radio emission using the LFmap program [204]. LFmap combines radio background maps measured at different wavelength and allows for an interpolation to arbitrary frequencies using appropriate power law indices (cf. Eqn. 11.2). We obtain the background brightness B as maps of brightness temperature T_B in equatorial coordinates. The brightness is the spectral irradiance per unit solid angle and given by the Rayleigh-Jeans law:

$$B(\nu, \alpha, \delta) = \frac{2k}{c^2} \nu^2 T_B \quad [B] = \mathrm{Wm}^{-2}\mathrm{sr}^{-1}\mathrm{Hz}^{-1}, \tag{11.3}$$

where k is the Boltzmann constant. In comparison to alternative descriptions of the galactic radio background given by Cane [173] and the global sky model GSM [205] we find an agreement of the three models at a level of ~ 1 dB by considering the spectral irradiance integrated over the full sky which is displayed in Fig. 11.9.

An exemplary map of the galactic radio background generated at 55 MHz is displayed in Fig. 11.8. Besides the brightness the dashed curve indicates the field of view that contributes to the recorded noise power at the location of the Nançay Radio Observatory at the given time. The relative directionality of the Small Black Spider antenna for the corresponding frequency is represented by the gray shade.

The noise that is recorded in the measurement is the convolution of the currently visible radio background and the projection of the antenna characteristics onto the sky. The received power spectral density is given by:

$$P_\nu(\nu) = \int_\Omega B(\nu, \alpha, \delta)\, A_e(\nu, \theta, \phi)\, d\Omega \quad, \tag{11.4}$$

where A_e is the effective aperture of the antenna including mismatch effects and losses (cf. 6.29). The antenna based coordinates (θ, ϕ) are accessed according to the
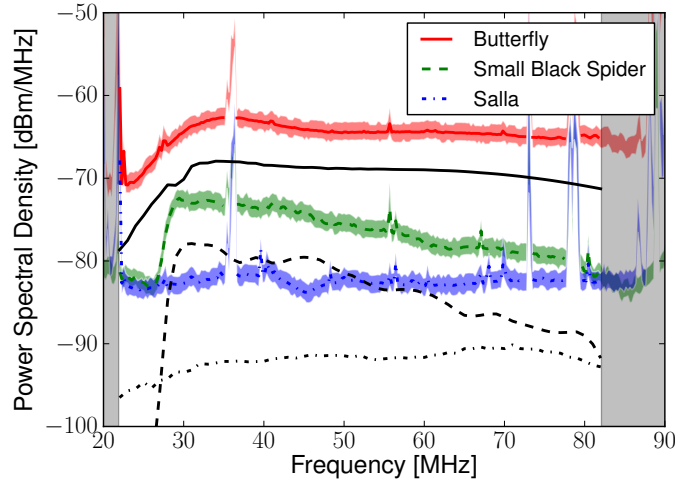
Figure 11.10: The average spectra at the Nançay Radio Observatory with the tested antennas during periods of maximum galactic noise. The colored lines indicate the mean of the measured data and its spread. The data have been corrected for the characteristics of the signal chain to yield the power spectral density after the LNA of the respective antenna. The black curves display the corresponding simulations. The gray shaded areas lie outside the -3dB points of the filter setup used in the test bench.

equatorial coordinates (α, δ), the local sidereal time and the location of the Nançay Radio Observatory.

In the case of an unpolarized radio brightness a factor $1/2$ is introduced explicitly in Eqn. 11.4 to account for polarization mismatch [206]. However, if we replace the effective antenna aperture with the VEL using the result from A.8, the polarization loss is included naturally in the time averaged measurement of the spectrum analyzer:

$$P_\nu(\nu) = \frac{1}{2} \frac{Z_0}{Z_L} \int_\Omega B(\nu, \alpha, \delta) \, |\vec{\mathcal{H}}_a(\nu, \theta, \phi)|^2 \, d\Omega \quad . \tag{11.5}$$

In Fig. 11.10 the average spectra measured in periods of maximum galactic noise level is displayed in comparison to the corresponding simulations based on Eqn. 11.5. The simulated VELs are the same as for the transient response discussion in Sec. 11.2. To give the noise power delivered after the amplifier of the antenna, the measured data are corrected for the characteristics of the subsequent readout electronics. While the shape of the simulations reproduce the measurements, we observe that the simulations predict a noise level which systematically ~ 4 dB below the measured data for all three antennas. For the Small Black Spider we have cross checked the simulation results with spectrum observations at the site of AERA. Here, we do not observe differences of the absolute scale of measurements and simulations. In the following discussion we focus on relative variations of the background noise as a function of time.
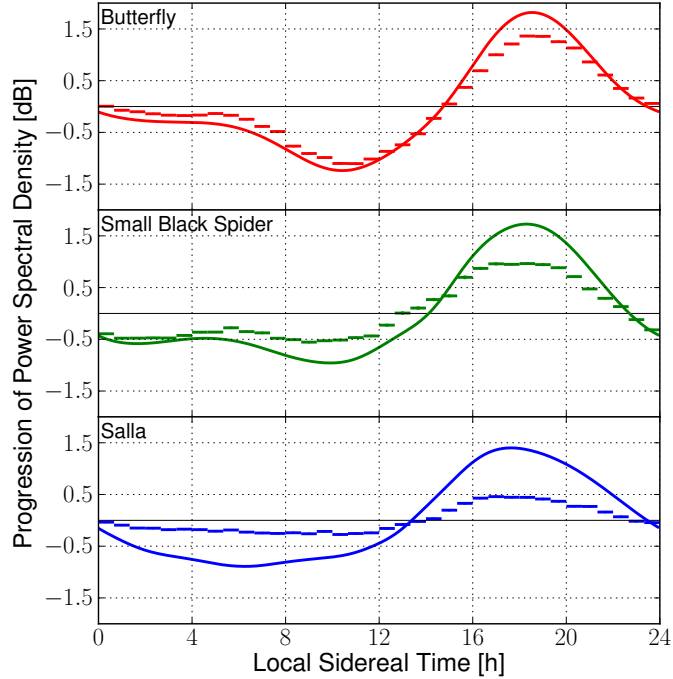
Figure 11.11: Galactic Variation at the Nançay Radio Observatory at 55 MHz depicted for the Butterfly (top), Small Black Spider (middle) and Salla (bottom). The symbols display the measured data, the solid lines show the corresponding simulations.

11.4   Comparison of Radio Background Variation

In Fig. 11.11 the progression of the power spectral density as a function of the sidereal time is shown for the measurements and the simulations.

The measured progression corresponds to a cut in the dynamic spectra of Fig. 11.7 at 55 MHz where the data have been condensed in the given time binning. For comparison, the measured and the simulated curves are shifted to a common mean value.

Due to the individual projections of the antenna sensitivities to the sky, the progression of the noise power differs between the antennas. Notably, the point in time when the maximal and the minimal galactic noise is observed depends on the antenna. An example comparing different antenna orientations is given in the A.9.

The simulation overestimates the progression of the noise level without any additional noise sources but the galactic noise. The measured progression of the Butterfly antenna almost follows this ideal curve. If we assume that the simulated variation yields a valid prediction of the noise progression, we conclude that additional external noise sources are negligible for our measurement. At 55 MHz the Butterfly realizes a variation of ~ 2.5 dB between galactic maximum and minimum where the simulation predicts a maximum variation of ~ 3.1 dB. For the other two antennas the variation is less distinct.
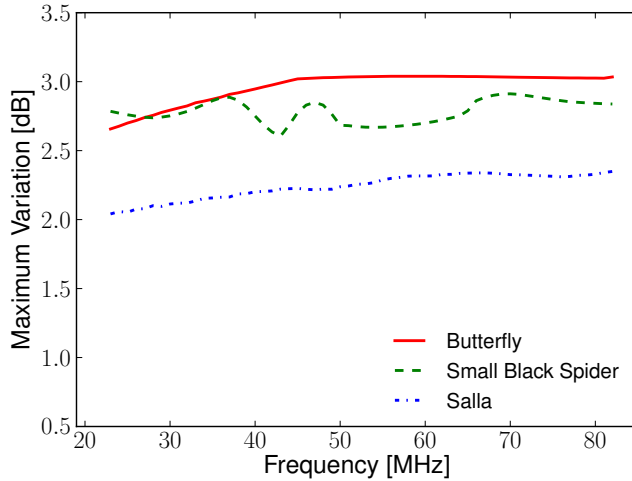
Figure 11.12: The variation of the galactic noise level obtained from simulations for the three antennas. The Butterfly is predicted to observe the largest difference in received power between galactic maximum and minimum. The variation of the Small Black Spider depends most strongly on the frequency. The galactic noise measured with the Salla is predicted to be least dependent on the time of observation.

To evaluate the measured variations with respect to noise that is added in the antenna internally we have to take into account that the predicted maximal variation depends on the antenna individually. Displayed in Fig. 11.12 is the maximum variation for the full considered frequency range.

The projection of the directional properties of the Butterfly antenna yields a larger maximal variation than in the case of the other two antennas. The deviations throughout the bandwidth in the case of the Small Black Spider indicate the lobe structure of the antenna evolving with frequency.

The displayed maximum variation V_{max} is the ratio of maximal to minimal received galactic noise:

$$V_{\mathrm{max}}(\nu) = \frac{P_{\mathrm{max}}(\nu)}{P_{\mathrm{min}}(\nu)} \quad . \tag{11.6}$$

For simplicity we assume that the antenna is adding internally an additional noise floor P_{int} that is constant with frequency. The realized variation is then:

$$V_{\mathrm{r}}(\nu) = \frac{P_{\mathrm{max}}(\nu) + P_{\mathrm{int}}}{P_{\mathrm{min}}(\nu) + P_{\mathrm{int}}} \quad . \tag{11.7}$$

We are interested in the fraction f of internal relative to the galactic noise. In Eqn. 11.7 we count the fraction f relative to the maximum noise that is predicted throughout the whole bandwidth:

$$V_{\mathrm{r}}(\nu) = \frac{P_{\mathrm{max}}(\nu) + f \cdot P_{\mathrm{max}}(\nu_{\mathrm{max}})}{P_{\mathrm{min}}(\nu) + f \cdot P_{\mathrm{max}}(\nu_{\mathrm{max}})} \quad . \tag{11.8}$$

In Fig. 11.13 the measured variation is displayed as a function of frequency for the three antennas. The simulated variations from Fig. 11.12 have been adjusted with noise fractions f to match the realized variations.
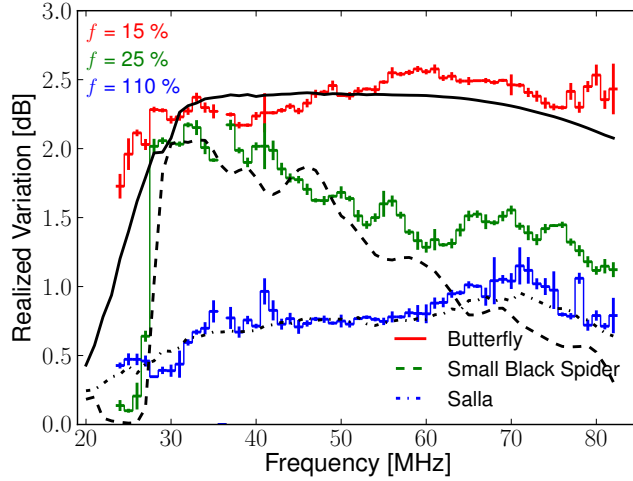
Figure 11.13: The measured galactic variation for the three antennas as a function of frequency. Also given is the expected variation from simulations as in Fig. 11.12 but with a noise power added that is constant in frequency. The given percentages denote the strength of the added noise floor relative to the maximum signal expected from the galactic background.

The realized variation of the Salla antenna ranges below 1 dB. With respect to the predicted variation we find that more than half of the power spectral density delivered by the Salla is produced in the antenna internally even during the galactic maximum.

The Small Black Spider realizes almost the full variation at the lowest frequencies indicating a fraction of internal noise of $\sim 25\%$. However, at the higher frequencies the fraction of galactic noise is being reduced.

The Butterfly antenna provides a power spectral density which is strongly dominated by the galactic noise background over the full frequency range which constitutes the best observing conditions to transient signals in terms of continuous background noise.

12. Summary

Radio detection of air showers originating from ultra-high energy cosmic rays is considered world wide as a candidate technique for the next generation of Earth bound observatories. In the research and development of this technique major challenges concern the antenna sensor, signal processing, self triggering and data interpretation. In this thesis we have performed hardware and software developments, central simulations studies, theoretical calculations, calibrations and data analysis for the overall development of two engineering radio arrays at the Pierre Auger Observatory with special emphasis on the antenna sensor.

With AERA — the Auger Engineering Radio Array — the Pierre Auger Collaboration addresses both technological and scientific questions to the radio detection of air showers. AERA will check the feasibility of the radio-detection technique on large instrumented areas and is thus intended to serve as a blueprint for the next generation of ground-based cosmic-ray detectors. The installation of the first stage of AERA is the startup for the construction of a 20 km^2 radio detector consisting of 160 autonomous self-triggered detector stations sensitive to frequencies from 30 to 80 MHz. The first stage is taking data since the last quarter of 2010 and is successfully recording signals from cosmic rays.

The Small Black Spider is a successful implementation the logarithmic-periodic antenna design for the detection of cosmic rays. As a result of our constant R&D the Small Black Spider has proven to be both — resistants against the environmental conditions of the Argentinian Pampa and sensitive to air shower signals. Our logarithmic periodic antennas are the backbone of the measurements in the first stage of AERA and also at one pioneering radio detector installation at the Auger site.

The transient nature of the air shower signal requires a detailed description of the antenna sensor to allow for a calibrated measurement of the incident signal. We identify the vector effective length as suitable quantity to perform the calculation of the antenna response to transient signals including multiple reflections, interference and polarization effects. We find that our discussion is beyond the scope of current literature for the desired frequency range.

Having identified the relevant antenna characteristics we reported the calibration of the Small Black Spider antenna used at AERA. For the first time, the zenith angular dependency of the sensitivity of a full scale radio detector antenna was measured including the vectorial phase information. This allowed us to calculate the vector effective length of the antenna on an absolute scale which includes effects of the pulse dispersion.

With RDAS — the Radio Detector Array Simulation — we have developed a dedicated software for the signal processing and reconstruction of radio detector array

data. Applying the vector effective length we demonstrated the three dimensional reconstruction of the incident electric field from the voltage traces and the information on the shower direction. The RDAS software has been designed according to object oriented programming standards and modular packaging.

We studied the lateral fall-off of the radio signal with air shower data from the pioneering radio detector installation. In our analysis we were able to demonstrate that an exponential lateral signal fall-off which is the usual shape in phenomenological parameterizations of the radio pulse is disfavored in comparison to a dependence of a falling power law.

We furthermore analyzed the first AERA data that were recorded during the start-up phase. Using the reconstruction of a spherical wave front we characterized major sources of transient signals in the vicinity of AERA both in direction and distance. Inspecting the residuals of our reconstruction we reported systematic timing offset of the AERA detector stations. In an initial timing calibration we significantly improved the resolution in the reconstruction of radio signals of AERA realizing a timing resolution of 5 ns.

We introduced a new method for the dynamic removal of transient noise signals from the AERA data. Our method realizes a background rejection of 10^{-4} while keeping air showers with an efficiency of 60 %. The performed pre-selection enables a purity of at least 30 % in the identification of cosmic rays in the purely self-triggered radio detector data set of AERA.

In view of the challenge of the next setup stage of AERA we have evaluated in detail three candidate antennas each pursuing a different strategy to allow for an optimal reception of air shower signals. Considered were the logarithmic-periodic dipole antenna, a loaded dipole loop antenna and an active bowtie antenna.
On the basis of the vector effective length we studied the transient response characteristics of each antenna in the time domain. We find that the logarithmic-periodic dipole antenna induces dispersion to the received transient waveform. In the case of the bowtie and the loop antenna almost the full peak amplitude of the signal is preserved.

At the Nançay Radio Observatory we have performed simultaneous measurements of the galactic radio background with the three antennas. Observing the variation of the measured noise power as a function of sidereal time we tested the antennas for an optimal continuous noise performance. We find that the active bowtie antenna is superior in both the noise performance and the transient response. For the next setup stage of AERA we choose the bowtie as sensor to the coherent radio emission from cosmic ray induced air showers.

In recent years the potential of the measurement of radio pulses as new technique for astro-particle physics has been rediscovered. The Auger Engineering Radio Array will allow to gain new insights into the nature of cosmic rays. Our methods for background removal, signal characterization and detector optimization are important contributions to the further success of the radio detection technique.

A. Appendix

A.1 Response to a Moving Source of Coherent Radiation

In Eqn. 6.6 the response of an antenna to an incoming signal is calculated in the time domain as convolution of the electric field and the VEL:

$$V(t) = \vec{H}(t) * \vec{E}(t) \quad . \tag{A.1}$$

The convolution operation is commutative. Hence we can use

$$V(t) = \vec{E}(t) * \vec{H}(t) \tag{A.2}$$

to write the corresponding convolution integral as follows:

$$V(t) = \int\limits_{-\infty}^{\infty} \vec{E}(\tau) \cdot \vec{H}(t - \tau)\, d\tau \quad . \tag{A.3}$$

The function $\vec{H}(t - \tau)$ is a translation of the function $\vec{H}(t)$ to the position τ. Translations can be expressed using a convolution with a Dirac delta function:

$$\vec{H}(t - \tau) = \vec{H}(t) * \delta(t - \tau) \quad . \tag{A.4}$$

Plugging Eqn. A.4 into Eqn. A.3 yields:

$$V(t) = \int\limits_{-\infty}^{\infty} \vec{E}(\tau) \cdot (\vec{H}(t) * \delta(t - \tau))\, d\tau \quad . \tag{A.5}$$

The electric field in Eqn. A.5 acts to the convolution of the VEL and the delta function as scalar. We use the associativity of the convolution operation with scalar multiplications to write:

$$V(t) = \int\limits_{-\infty}^{\infty} \vec{H}(t) \, * \, \vec{E}(\tau)\, \delta(t - \tau)\, d\tau \quad . \tag{A.6}$$

Using the identity $\delta(-x) = \delta(x)$ yields the result claimed in Eqn. 6.27:

$$V(t) = \int\limits_{-\infty}^{\infty} \vec{H}(t, \theta, \phi) \, * \, \vec{E}(\tau)\, \delta(\tau - t)\, d\tau \quad . \tag{A.7}$$
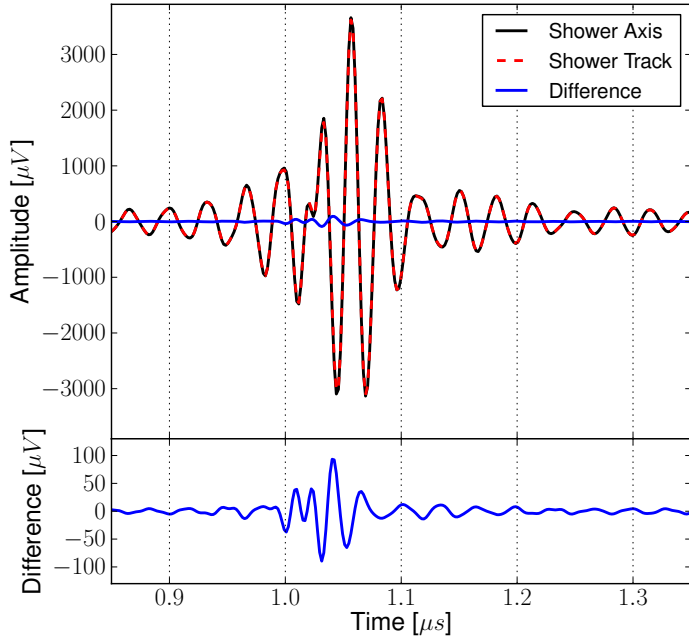
Figure A.1: Vector Effective Length for source of radiation that moves as shown in Fig. 3.17 and for the approximation of a fix incoming direction identified with the air shower axis. The lower panel shows the difference induced by the approximation. The largest differences occur before the maximum of the response

Eqn. A.7 allows to change the incoming direction of the pulse throughout the pulse development using $(\theta(t),\ \phi(t))$. With respect to a calculation performed on sampled data Eqn. A.7 implies that the electric field is decomposed into series of functions where each function holds the electric field value of a certain sample and zeros otherwise. The response voltage is then given as the superposition of the responses to each of the functions in the series. Here, the direction used to access the VEL in response calculation can be chosen according to the time development of the incoming direction.

In Fig. A.1 the response of a Small Black Spider LPDA to the simulated electric field in Fig. 3.16 is calculated. The response calculation is once performed using the fix direction of the air shower axis and once using the development of the incoming direction which is given in Fig. 3.17.

The lower panel of Fig. A.1 allows a closer look at the difference between the two calculations. In the example a difference of 100 μV in maximum is not exceeded. A typical noise level obtained with the Small Black Spider LPDA at the AERA site is $\sim 140\,\mu$V (RMS) during radio quite observing conditions. The width of the noise background adds to each recorded signal sample as statistical uncertainty.

A.2 NEC-2 Simulation Model for the Small Black Spider LPDA

An exemplary simulation model for the Small Black Spider LPDA is given below. The 'GW', 'LD' and 'TL' keys define the structure of the antenna. 'FR', 'EX' and 'RP' label a specific task for the simulation to be calculate with the structure defined above.

CM	Small Black Spider									
CE										
GW	1	25	-2.411	0	0.0	2.411	0	0.0	0.015	
GW	2	23	-1.860	0	0.323	1.860	0	0.323	0.0015	
GW	3	21	-1.630	0	0.606	1.630	0	0.606	0.0015	
GW	4	19	-1.427	0	0.853	1.427	0	0.853	0.0015	
GW	5	17	-1.250	0	1.07	1.250	0	1.07	0.0015	
GW	6	15	-1.095	0	1.26	1.095	0	1.26	0.0015	
GW	7	13	-0.960	0	1.427	0.960	0	1.427	0.0015	
GW	8	11	-0.840	0	1.572	0.840	0	1.572	0.0015	
GW	9	9	-0.735	0	1.7	0.735	0	1.7	0.0015	
GW	100	3	-0.05	0	-0.23	0.050	0	-0.23	0.0015	
GE	0									
LD	5	1	0	0	37700000					
LD	5	2	0	0	58000000					
LD	5	3	0	0	58000000					
LD	5	4	0	0	58000000					
LD	5	5	0	0	58000000					
LD	5	6	0	0	58000000					
LD	5	7	0	0	58000000					
LD	5	8	0	0	58000000					
LD	5	9	0	0	58000000					
EK										
TL	1	13	2	12	-280.146	0	0	0	0	0
TL	2	12	3	11	-347.885	0	0	0	0	0
TL	3	11	4	10	-352.997	0	0	0	0	0
TL	4	10	5	9	-450.686	0	0	0	0	0
TL	5	9	6	8	-503.641	0	0	0	0	0
TL	6	8	7	7	-556.997	0	0	0	0	0
TL	7	7	8	6	-514.716	0	0	0	0	0
TL	8	6	9	5	-459.545	0	0	0	0	0
TL	100	2	1	13	501.819	0	0	0	0	0
FR	0	99	0	0	2	1	0	0	0	
PT	-1									
EX	0	9	5	0	1.	0				
RP	0	6	8	1000	0	0	4.50E+01	4.50E+01		
EN										

A.3   Continuous Interpolation of Antenna Characteristics

To calculate the antenna response to an incoming electric field as well as for the reconstruction of the electric field (cf. Eqns. 6.15 and 6.38) the vector effective length $\vec{\mathcal{H}}$ of the antenna has to be applied. In Eqn. 6.17 we have investigated the components of the complex vector of the VEL:

$$\vec{\mathcal{H}} \;=\; \vec{e}_\theta \, \mathcal{H}_\theta + \vec{e}_\phi \, \mathcal{H}_\phi \tag{A.8}$$

$$\;=\; \vec{e}_\theta \, |\mathcal{H}_\theta| \, e^{i\varphi_{\mathcal{H}_\theta}} + \vec{e}_\phi \, |\mathcal{H}_\phi| \, e^{i\varphi_{\mathcal{H}_\phi}} \quad . \tag{A.9}$$

The VEL can hence be split into four components: two absolute values $|\mathcal{H}_\theta|$, $|\mathcal{H}_\phi|$ and two phases $\varphi_{\mathcal{H}_\phi}$, $\varphi_{\mathcal{H}_\phi}$. All four are themselves functions of the incoming direction of the signal (θ, ϕ) and of the frequency, i.e. $|\mathcal{H}_\theta| = |\mathcal{H}_\theta|(\theta, \phi, \omega)$. In the simulation of the antenna with NEC-2 the four components can be accessed at discrete points $(\theta_i, \phi_i, \omega_i)$. To apply the simulation in the response calculations, the antenna characteristics need to be prepared for a continuous interpolation in the three dimensions. In Fig. A.2 the surfaces of the four components is displayed for a single frequency of 55 MHz. The closed surfaces indicate that arbitrary directions (θ, ϕ) can be accessed which is realized within RDAS using Delaunay triangles interpolation provided by the `TGraph2D` class of the ROOT program. The directional characteristics are interpolated at each frequency that has been simulated. The access to arbitrary frequencies is realized in a second linear interpolation step. The antenna descriptions available for RDAS are also included in the $\overline{\text{Off}}\underline{\text{line}}$ software. Here, functionality is currently being implemented to realize a 3 dimensional spline interpolation [207].

The usual spherical coordinate system for the description of antenna characteristics is mapped in Fig. A.2 to a rectangular coordinate system as this is convenient for the interpolation. The surfaces of the absolute values we have discussed in a spherical coordinate systems for instance in the Figs. 6.3 and 6.12. In the rectangular coordinate system given here the similarity of the SBS to a dipole antenna is evident as the azimuth dependency of the absolute values are given by:

$$|H_\phi| \propto \sqrt{\sin^2(\phi + \phi_1)} \quad \text{and} \quad |H_\theta| \propto \sqrt{\sin^2(\phi + \phi_2)} \tag{A.10}$$

with a phase offset $\Delta\phi = \phi_2 - \phi_1 = 90°$ between the two components. The usual $\sin^2\phi$ dependency of dipole radiation refers to the signal power rather then the signal amplitude treated here. The positions where the absolute values vanish correspond to the situations where the respective polarization is perpendicular to the rods of antenna. When progressing over such a direction the phase flips by exactly 180°. Besides the flip the phases do not change for different azimuth angles on lines of constant zenith angles. As long as a simple symmetry of the antenna is given, the interpolation of the azimuth angle could be avoided as this dependency can be calculated analytically for all four surfaces.
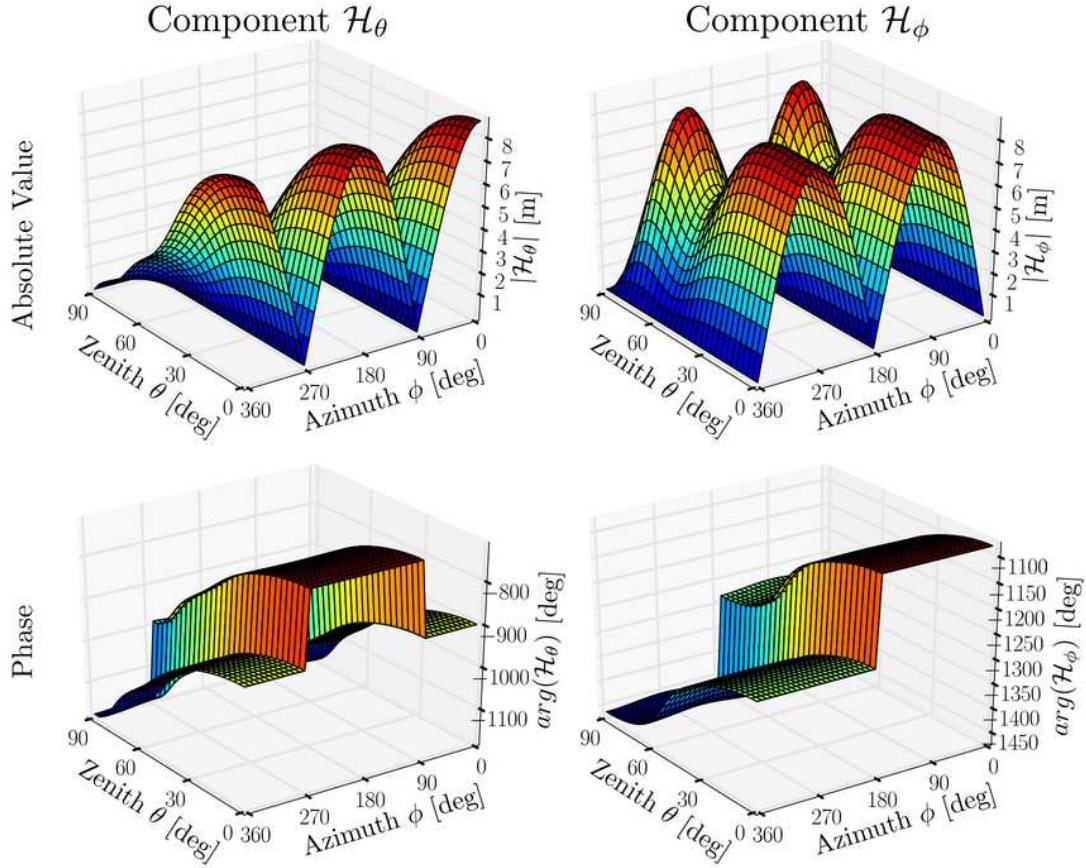
Figure A.2: Simulated components of the VEL prepared for continuous interpolation here at a frequency of 55 MHz. Simulated is a SBS antenna including ground.

A.4 List of Events in LDF Study

List of events that are reconstructed within 20° angular distance from the corresponding SD reconstruction in the BLS setup. Events which were recorded during thunderstorms are marked as well as events for which no thunderstorm data is available [181]. The last column indicates events where the filter setup used for radio detector station 1 differs from the setup of station 2.

	Auger Event Id	Thunderstorm	No Electric Field Data	BW Station 1 $\neq$ Station 2
1	3388259			
2	3388350			
3	3398213			
4	3400512			
5	3404052	?	x	
6	3404386	?	x	
7	3404697	?	x	
8	3425295			

9	3454027			
10	3497935			
11	3526626			
12	3529758			
13	3531785			
14	3824872			
15	3834831			
16	3913232			
17	3913273			
18	3984177			
19	4226086			
20	4235335			
21	4237272			
22	4238035			
23	4243652			
24	4294748			
25	4346034			
26	4349437		x	
27	4352818			
28	4584157			
29	4602085		x	
30	4626060			
31	4633032		x	
32	4654714			
33	4691610			
34	4698935			
35	4700239			
36	4701978			
37	4706727			
38	4718144			
39	4721607			
40	4740076			
41	4743906			
42	4790902		x	x
43	4791122			x
44	4803364			x

A.5 Detailed calculation for LDF Model $S(D) \propto D^{-x}$

For S $\propto D^{-x}$ we find that the variables have to following interdependency:

$$\frac{\Delta S}{\Sigma S} = \frac{D_1^{-x} - D_2^{-x}}{D_1^{-x} + D_2^{-x}} \tag{A.11}$$

$$= \frac{(\bar{D} + \frac{\Delta D}{2})^{-x} - (\bar{D} - \frac{\Delta D}{2})^{-x}}{(\bar{D} + \frac{\Delta D}{2})^{-x} + (\bar{D} - \frac{\Delta D}{2})^{-x}} \tag{A.12}$$

$$= \frac{(\bar{D} - \frac{\Delta D}{2})^{x} - (\bar{D} + \frac{\Delta D}{2})^{x}}{(\bar{D} - \frac{\Delta D}{2})^{x} + (\bar{D} + \frac{\Delta D}{2})^{x}} \quad . \tag{A.13}$$

Now using the series expansions [208]:

$$\left(\bar{D} - \frac{\Delta D}{2}\right)^{x} \overset{|\frac{\Delta D}{2}|<|\bar{D}|}{=} \frac{1}{\bar{D}^{-x}} + \frac{-x\frac{\Delta D}{2}}{\bar{D}^{-x+1}} - \dots \tag{A.14}$$

and

$$\left(\bar{D} + \frac{\Delta D}{2}\right)^{x} \overset{|\frac{\Delta D}{2}|<|\bar{D}|}{=} \frac{1}{\bar{D}^{-x}} - \frac{-x\frac{\Delta D}{2}}{\bar{D}^{-x+1}} + \dots \tag{A.15}$$

we can approximate the numerator of Eqn. A.13:

$$(\bar{D} - \frac{\Delta D}{2})^{x} - (\bar{D} + \frac{\Delta D}{2})^{x} \approx -x\Delta D\bar{D}^{x-1} \tag{A.16}$$

and the denominator as well:

$$(\bar{D} - \frac{\Delta D}{2})^{x} + (\bar{D} + \frac{\Delta D}{2})^{x} \approx 2\bar{D}^{x} \quad . \tag{A.17}$$

Thus we receive overall:

$$\frac{\Delta S}{\Sigma S} \approx \frac{-x\Delta D\bar{D}^{x-1}}{2\bar{D}^{x}} = -\frac{x\Delta D}{2\bar{D}} \tag{A.18}$$

which is the result claimed in Eqn. 9.16.

A.6 Renormalization of S-Parameter S21

When characterizing an amplifier with scattering parameters, the S-Parameter S21 yields the amplified voltage amplitude normalized to the incoming voltage amplitude $\mathcal{V}_+$ delivered by the signal generator:

$$S21 = \frac{\mathcal{V}_a}{\mathcal{V}_+} \quad . \tag{A.19}$$

The realized VEL discussed in section 6.6 relates the incoming electric field to the voltage over the input impedance of the amplifier $\mathcal{V}_L$. From the S-parameter measurement the voltage at the amplifier input is calculated analog to Eqn. 6.47 using the voltage reflection coefficient Γ_L:

$$\mathcal{V}_L = \mathcal{V}_+ (1 + \Gamma_L) = \mathcal{V}_+ (1 + S11) \tag{A.20}$$

where the reflection coefficient corresponds to the scattering parameter $S11$. Hence, the amplification of the response of the antenna to an electric calculated with the VEL is given as:

$$\frac{\mathcal{V}_a}{\mathcal{V}_L} = \frac{\mathcal{V}_a}{\mathcal{V}_+(1 + S11)} = \frac{S21}{1 + S11} \equiv S21' \quad . \tag{A.21}$$

A.7 Vector Effective Height and Realized Gain

The active component of the power that is consumed by an antenna used as transmitter is given by:

$$P^t = |\mathcal{I}_0^t|^2 \cdot Re(Z_a^t) \quad . \tag{A.22}$$

$\mathcal{I}_0^t$ is the current within the antenna structure analog to the receiving case depicted in Fig. 6.5. Z_a^t is the impedance of the transmitter. The power that is delivered through the coaxial cable to the transmitter is:

$$P_g = \frac{|\mathcal{V}_g|^2}{Z_{tl}} \quad , \tag{A.23}$$

where the voltage amplitude $\mathcal{V}_g$ is the denominator of the S-parameter S21. Due to the impedance mismatch between the transmitter antenna and the coaxial cable only a fraction of the power P_g is available to be consumed by the antenna:

$$|\mathcal{I}_0^t|^2 \cdot Re(Z_a^t) = \frac{|\mathcal{V}_g|^2}{Z_{tl}}(1 - |\Gamma^t|^2) \quad , \tag{A.24}$$

with Γ^t the voltage reflection coefficient of the transmitting antenna to the coaxial cable. We resort Eqn. A.24 and multiply with the squared VEL of the transmitter:

$$\frac{|\mathcal{I}_0^t|^2}{|\mathcal{V}_g|^2}|\mathcal{H}_\phi^t|^2 = \frac{1}{Re(Z_a^t)Z_{tl}}(1 - |\Gamma^t|^2)|\mathcal{H}_\phi^t|^2 \quad . \tag{A.25}$$

In Eqn. 6.35 we have derived the relationship between VEL and gain. Introducing this interrelation on the right hand side of Eqn. A.25 yields:

$$\frac{|\mathcal{I}_0^t|^2}{|\mathcal{V}_g|^2}|\mathcal{H}_\phi^t|^2 = \frac{\lambda^2}{\pi Z_0 Z_{tl}} \underbrace{(1 - |\Gamma^t|^2)G^t}_{G_{\text{cal}}^t} \quad , \tag{A.26}$$

which is the result claimed in Eqn. 7.21. The calibration of the transmitter antenna G_{cal}^t is given by the manufacturer including the reflection at the input of the antenna.

A.8 Effective Aperture and Vector Effective Length

In Eqn. 6.29 the power available to the load due to an incident wave is given in terms of the maximum effective aperture of the antenna. The maximum effective aperture is realized under conjugate matching and without losses in the antenna. If

losses and mismatching effects are included we refer to the effective aperture A_e as:

$$P_L = A_e\, S \quad .$$ (A.27)

The available power is also accessible via the realized vector effective length:

$$P_L = \frac{1}{Z_L}\frac{|\mathcal{V}_L|^2}{2} = \frac{1}{Z_L}\frac{|\vec{\mathcal{H}}_r\, \vec{\mathcal{E}}|^2}{2}$$ (A.28)

The vector product in Eqn. A.28 is the projection of the electric field vector onto the vector of the VEL. To disentangle the vectorial from the power calculation a polarization factor p is introduced [127]:

$$p = \frac{|\vec{\mathcal{H}}_r\, \vec{\mathcal{E}}|^2}{|\vec{\mathcal{H}}_r|^2|\vec{\mathcal{E}}|^2} \quad ,$$ (A.29)

such that:

$$P_L = p \cdot \frac{1}{Z_L}\frac{|\vec{\mathcal{H}}_r|^2\, |\vec{\mathcal{E}}|^2}{2} \quad .$$ (A.30)

Using Eqn. 6.28 we introduce the intensity of the wave from which is also used in Eqn. A.27:

$$P_L = p \cdot \frac{Z_0}{Z_L}|\vec{\mathcal{H}}_r|^2\, S \quad .$$ (A.31)

Hence we receive the relation between realized VEL and the effective aperture:

$$A_e = p\frac{Z_0}{Z_L}|\vec{\mathcal{H}}_r|^2 \,.$$ (A.32)

For an unpolarized signal the electric field vector and the vector of the effective length will align randomly in time. In time averaged measurements the expectation value of the polarization factor is hence:

$$< p >= 1/2 \quad .$$ (A.33)

A.9 Galactic Noise Variation at the AERA site

In Fig. A.3 a map of galactic noise intensity generated with LFmap at 45 MHz at the AERA site is displayed. The colored data shows the noise intensities in the field of view of the AERA site. The horizon is displayed as dashed line. The shade over the colored data indicates the relative antenna sensitivity of the Small Black Spider LPDA at the corresponding frequency oriented in North-South direction. At the displayed time the galactic center is visible in the side lobe of the antenna which causes the hump at 23 h LST in the top panel of Fig. A.4. In comparison to Fig. 11.8 the scale of the brightness is changed owing the different frequency.

In Fig. A.4 we show the progression of the Galactic Noise intensity measured with the Small Black Spider reference antenna close to the Central Radio Station of AERA. The plot summarizes two continuous spectrum observations that have both
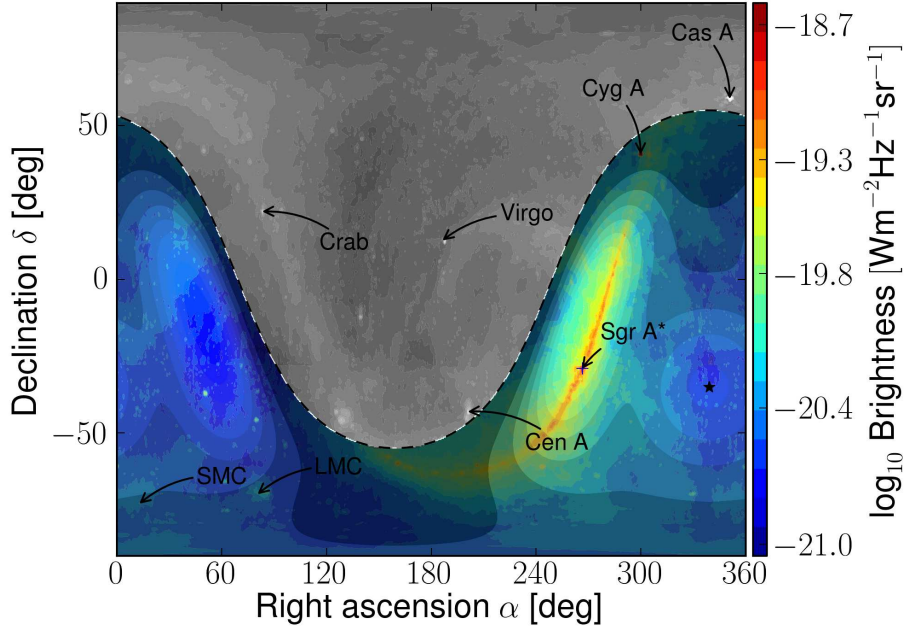
Figure A.3: Map of Galactic radio background at the AERA site. Please see text in A.9 for details.

been performed over several days. One measurement is done with the antenna polarization pointing in East-West direction, one in North-South. A cut in the continuous spectra at 45.3 MHz is chosen to show the variation of the noise. The change in the noise progression predicted by the simulation is found also in the measured data. In the North-South polarization a more complex progression is observed due to the appearance of the Galactic center in a side lobe of the antenna.

The average spectra during galactic maximum (here taken as 17.5 to 18.5 h LST) and the spectra during galactic minimum (here taken as 1.5 to 2.5 h LST) are displayed in Fig. A.5. A variation between the galactic maximum and minimum of 2 to 3 dB is visible in the measured data. As in the case of the measurement at the Nançay site the antenna cannot completely realize the low noise level during the Galactic minimum. The overall scale of the noise intensity is matched by the simulations.
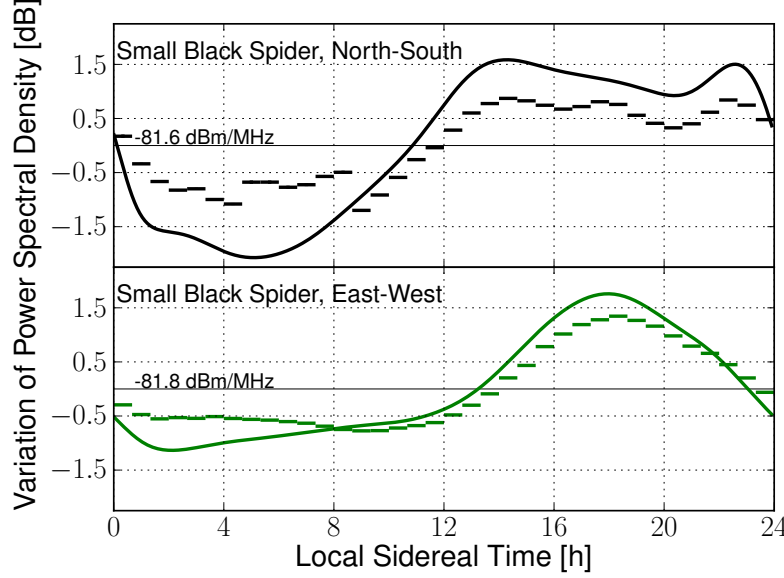
Figure A.4: The progression of the noise level due to the galactic radio background recorded at the AERA site at 45.3 MHz. In the top panel the Small Black Spider LPDA is aligned in the North-South and in the bottom panel in the East-West direction. The measured data is displayed as profile. Uncertainties of the mean values are given but small. The solid lines show the simulated progression. RFI disturbs the measurement in the North-South direction around 6 h LST. Nevertheless, distinct differences between the two alignments of the antenna are visible. The two bumps in the North-South polarization around 14 and 23 h LST correspond to the consecutive appearance of the galactic disc in the two main lobes of the antenna.
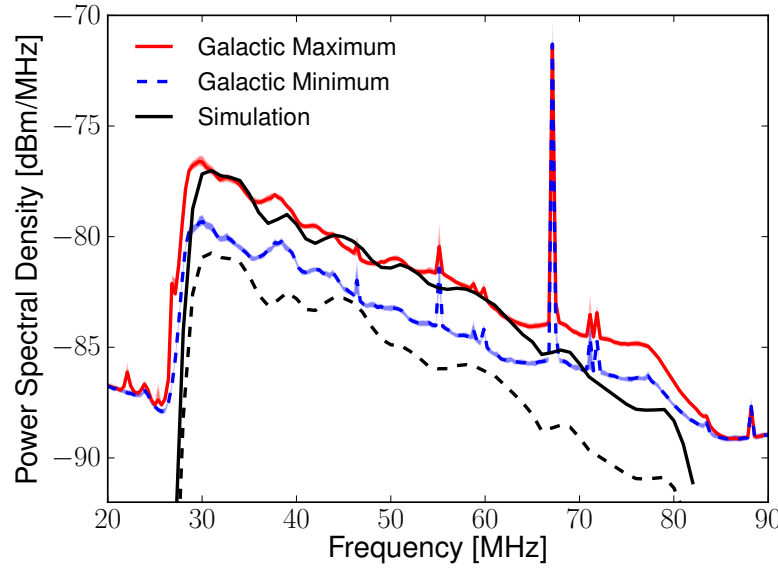
Figure A.5: Galactic Minimum and Maximum at the AERA site measured with reference antenna in the East-West polarization. As black lines the corresponding simulations are displayed.

B. List of Acronyms

AERA	Auger Engineering Radio Array
ADC	Analog-to-Digital Converter
AGN	Active Galactic Nuclei
AM	Amplitude Modulation
AMBER	Air-shower Microwave Bremsstrahlung Experimental Radiometer
AMIGA	Auger Muon and Infill for the Ground Array
AUT	Antenna Under Test
BLS	Balloon Launching Station
CODALEMA	COsmic ray Detection Array with Logarithmic ElectroMagnetic Antennas
CORSIKA	COsmic Ray SImulations for KAscade
CRS	Central Radio Station
DAQ	Data AQuisition
EASIER	Extensive Air Shower Identification using Electron Radiometer
EFIE	Electric Field Integral Equation
FADC	Flash Analog-to-Digital Converter
FD	Fluorescence Detector
FM	Frequency Modulation
FWHM	Full Width at Half Maximum
GPS	Global Positioning System
HEAT	High-Elevation Auger Telecopes
KASCADE	KArlsruhe Shower Core and Array DEtector
LDF	Lateral Distribution Function
LMC	Large Magellanic Cloud

LNA	Low Noise Amplifier
LOFAR	LOw Frequency ARray
LOPES	LOfar PrototypE Station
LPDA	Logarithmic-Periodic Dipole Antenna
LST	Local Sidereal Time
MAXIMA	Multi Antenna eXperiment in Malargüe Argentina
MC	Monte Carlo
MGMR	Macroscopic GeoMagnetic Radiation model
MIDAS	MIcrowave Detection of Air Showers
MOM	Method Of Moments
NEC	Numerical Electromagnetics Code
PAO	Pierre Auger Observatory
PMT	Photomultiplier Tube
REAS	Radio Emmission from Air Showers
RDAS	Radio Detector Array Simulation
RDS	Radio Detector Stations
RFI	Radio Frequency Interference
SALLA	Short Aperiodic Loaded Loop Antenna
SBS	Small Black Spider antenna
SD	Surface Detector
SMC	Small Magellanic Cloud
TLT	Transmission Line Transformer
UHECR	Ultra-High Energy Cosmic Ray
UTC	Universal Time Coordinated
VEL	Vector Effective Length

List of Figures

References

[1] V. Hess. *Über Beobachtungen der durchdringenden Strahlung bei sieben Freiballonfahrten.* Z. Phys., 13: p. 1084 (1912).

[2] J. Abraham, M. Aglietta, I. C. Aguirre et al. *Properties and performance of the prototype instrument for the Pierre Auger Observatory.* Nucl. Instrum. Methods Phys. Res., Sect. A, 523: pp. 50–95 (2004). doi:10.1016/j.nima.2003. 12.012.

[3] J. Abraham, P. Abreu, M. Aglietta et al. *The fluorescence detector of the Pierre Auger Observatory.* Nucl. Instrum. Methods Phys. Res., Sect. A, 620(2-3): pp. 227 – 251 (2010). doi:10.1016/j.nima.2010.04.023.

[4] F. Salamida for the Pierre Auger Collaboration. *Update on the measurement of the CR energy spectrum above 10^{18} eV made using the Pierre Auger Observatory.* Proceedings of 32nd International Cosmic Ray Conference (2011).

[5] J. V. Jelley, J. H. Fruin, N. A. Porter et al. *Radio Pulses from Extensive Cosmic-Ray Air Showers.* Nature, 205: pp. 327–328 (1965).

[6] H. R. Allan, R. W. Clay and J. K. Jones. *Frequency Spectrum of Air Shower Radio Pulses.* Nature, 225: pp. 253 – 254 (1970). doi:10.1038/225253a0.

[7] D. J. Fegan and P. P. O'Neill. *Lateral Distribution of u.h.f. Radio Emission associated with Cosmic Ray Showers.* Nature Physical Science, 241: pp. 126–128 (1973). doi:10.1038/physci241126b0.

[8] D. Ardouin, A. Bellétoile, D. Charrier et al. *Radio-detection signature of high-energy cosmic rays by the CODALEMA experiment.* Nucl. Instrum. Methods Phys. Res., Sect. A, 555: pp. 148–163 (2005).

[9] W. Apel, T. Asch and A. Badea. *Progress in Air Shower Radio Measurements: Detection of Distant Events.* Astropart. Phys., 26: pp. 332–340 (2006). doi: 10.1016/j.astropartphys.2006.07.003.

[10] S. Fliescher for the Pierre Auger Collaboration. *Radio detection of cosmic ray induced air showers at the Pierre Auger Observatory.* Nucl. Instrum. Methods Phys. Res., Sect. A (2010). doi:10.1016/j.nima.2010.11.045.

[11] P. Auger, P. Ehrenfest, R. Maze, J. Daudin and R. A. Fréon. *Extensive Cosmic-Ray Showers.* The American Physical Society, 11: pp. 288–291 (1939). doi: 10.1103/RevModPhys.11.288.

[12] W. Kolhörster, I. Matthes and E. Weber. *Gekoppelte Höhenstrahlen.* Die Naturwissenschaften, 26: p. 576 (1938). doi:10.1007/BF01773491.

[13] E. S. Seo, J. F. Ormes, R. E. Streitmatter et al. *Measurement of cosmic-ray proton and helium spectra during the 1987 solar minimum.* Astrophysical Journal, 378: pp. 763–772 (1991). doi:10.1086/170477.

[14] N. Grigorov, V. Nesterov, I. Rapoport and I. Savenko. *Study of energy spectra of primary cosmic rays at very high energies on the Proton series of satellites.* Space Research XII, Academic Verlag, Berlin, p. 1617 (1972).

[15] M. Nagano, M. Teshima, Y. Matsubara et al. *Energy spectrum of primary cosmic rays above $10^{17.0}$ eV determined from extensive air shower experiments at Akeno.* J. Phys. G. Nucl. Part. Phys., 18: pp. 423–442 (1992).

[16] A. Haungs, T. Antoni, W. Apel and A. Badea. *KASCADE: Astrophysical results and tests of hadronic interaction models.* Nuclear Physics B - Proceedings Supplements, 151: pp. 167–174 (2006).

[17] A. Haungs, W. D. Apel, J. C. Arteaga and F. Badea. *The Cosmic Ray Energy Spectrum Measured with KASCADE-Grande.* Proceedings of the 31st International Cosmic Ray Conference (2009).

[18] B. N. Afanasiev et al. Proceedings Int. Symposium of Extremely High Energy Cosmic Rays, 32 (1996).

[19] M. Lawrence, R. Reid and A. Watson. *The cosmic ray energy spectrum above $4 \cdot 10^{17}$ eV as measured by the Haverah Park array.* J. Phys G.: Nuc. Part. Phys., 17: pp. 733–757 (1991).

[20] D. Bird, S. Corbato, H. Dai and B. Dawson. *The Cosmic-Ray Energy Spectrum Observed by the Fly's Eye.* The Astrophysical Journal, 424: pp. 491–502 (1994).

[21] R. Abbas, T. Abu-Zayyad and M. Allen. *First Observation of the Greisen-Zatsepin-Kuzmin Suppression.* Phys.Rev.Lett., 100 (2008).

[22] A. Kounine. *Status of the AMS Experiment.* XVI International Symposium on Very High Energy Cosmic Ray Interactions ISVHECRI (2010).

[23] J. R. Hörandel, W. D. Apel, F. Badea et al. *Results from the KASCADE, KASCADE-Grande, and LOPES experiments.* Journal of Physics: Conference Series, 39: p. 463 (2006). doi:10.1088/1742-6596/39/1/122.

[24] J. Blümer, R. Engel and J. R. Hörandel. *Cosmic rays from the knee to the highest energies.* Progress in Particle and Nuclear Physics, 63: pp. 293 – 338 (2009).

[25] K. Nakamura et al. (Particle Data Group). *2010 Review of Particle Physics.* J. Phys. G: Nucl. Part. Phys., 37: p. 075021 (2010). doi:10.1088/0954-3899/37/7A/075021.

[26] W. R. Webber, G. A. Simpson and H. V. Cane. *Radio emission, cosmic ray electrons, and the production of gamma-rays in the Galaxy.* Astrophysical Journal, Part 1, 236: pp. 448–459 (1980). doi:10.1086/157761.

[27] A. Haungs, W. D. Apel, F. Badea et al. *Investigating the 2nd knee: The KASCADE-Grande experiment.* Journal of Physics: Conference Series, 47: p. 238 (2006). doi:10.1088/1742-6596/47/1/029.

[28] J. Abraham, P. Abreu, M. Aglietta et al. *Measurement of the Depth of Maximum of Extensive Air Showers above 10^{18} eV.* Phys. Rev. Lett., 104(9): p. 091101 (2010). doi:10.1103/PhysRevLett.104.091101.

[29] J. Matthews. *A Heitler model of extensive air showers.* Astroparticle Physics, 22(5-6): pp. 387–397 (2005).

[30] R. U. Abbasi, T. Abu-Zayyad, M. Al-Seady et al. *Indications of Proton-Dominated Cosmic-Ray Composition above 1.6 EeV.* Phys. Rev. Lett., 104: p. 161101 (2010). doi:10.1103/PhysRevLett.104.161101.

[31] P. Abreu, M. Aglietta, E. Ahn et al. *The Pierre Auger Observatory V: Enhancements.* arXiv:1107.4807v1 (2011).

[32] K. Martens for the Telescope Array Collaboration. *The Telescope Array and its Low Energy Extension.* Nuclear Physics B - Proceedings Supplements, 165: pp. 33 – 36 (2007). doi:10.1016/j.nuclphysbps.2006.11.006.

[33] T. Abu-Zayyad, K. Belov, D. J. Bird et al. *Evidence for Changing of Cosmic Ray Composition between 10^{17} and 10^{18} eV from Multicomponent Measurements.* Phys. Rev. Lett., pp. 4276–4279 (2000). doi:10.1103/PhysRevLett.84.4276.

[34] E. Waxman and J. Miralda-Escudé. *Images of Bursting Sources of High-Energy Cosmic Rays: Effects of Magnetic Fields.* The Astrophysical Journal Letters, 472: p. 89 (1996).

[35] R. Beck. *Galactic and Extragalactic Magnetic Fields.* Space Science Reviews, 99: pp. 243–260 (2001). doi:10.1023/A:1013805401252.

[36] J. Candia, E. Roulet and L. N. Epele. *Turbulent diffusion and drift in galactic magnetic fields and the explanation of the knee in the cosmic ray spectrum.* Journal of High Energy Physics, 12: p. 033 (2002). doi:10.1088/1126-6708/2002/12/033.

[37] J. D. Barrow, P. G. Ferreira and J. Silk. *Constraints on a Primordial Magnetic Field.* Phys. Rev. Lett., 78: pp. 3610–3613 (1997). doi:10.1103/PhysRevLett.78.3610.

[38] K. Dolag, D. Grasso, V. Springel and I. Tkachev. *Constrained simulations of the magnetic field in the local Universe and the propagation of ultrahigh energy cosmic rays.* J. Cosmol. Astropart. Phys., 01 (2005). doi:10.1088/1475-7516/2005/01/009.

[39] V. Berezinsky, A. Gazizov and S. Grigorieva. *On astrophysical solution to ultra high energy cosmic rays.* Phys. Rev. D. (2006). doi:10.1103/PhysRevD. 74.043005.

[40] K. Greisen. *End to the Cosmic-Ray Spectrum?* Phys. Rev. Lett., 16: pp. 748–750 (1966). doi:10.1103/PhysRevLett.16.748.

[41] G. Zatsepin and V. Kuzmin. *Upper Limit of the Spectrum of Cosmic Rays.* JETP Lett. (USSR), 4: pp. 78–80 (1966).

[42] D. Allard, M. Ave, N. Busca et al. *Cosmogenic neutrinos from the propagation of ultrahigh energy nuclei.* Journal of Cosmology and Astroparticle Physics, 09: p. 005 (2006). doi:10.1088/1475-7516/2006/09/005.

[43] J. W. Cronin. *Cosmic rays: the most energetic particles in the universe.* Reviews of Modern Physics, 71: pp. 165–172 (1999).

[44] R. Aloisio, V. Berezinsky, P. Blasi et al. *A dip in the UHECR spectrum and the transition from galactic to extragalactic cosmic rays.* Astroparticle Physics, 27: pp. 76 – 91 (2007). doi:10.1016/j.astropartphys.2006.09.004.

[45] J. Linsley. *Evidence for a Primary Cosmic-Ray Particle with Energy 10^{20} eV.* Phys. Rev. Lett., 10: pp. 146–148 (1963).

[46] R. E. Williams, B. Blacker, M. Dickinson et al. *The Hubble Deep Field: Observations, Data Reduction, and Galaxy Photometry.* Astronomical Journal, 112: pp. 1335–1384 (1996).

[47] J. Abraham, M. Aglietta, C. Aguirre et al. *An upper limit to the photon fraction in cosmic rays above 10^{19} eV from the Pierre Auger Observatory.* Astroparticle Physics, 27: pp. 155–168 (2007). doi:10.1016/j.astropartphys. 2006.10.004.

[48] E. Fermi. *On the Origin of the Cosmic Radiation.* Phys. Rev., 75: pp. 1169 – 1174 (1949).

[49] A. M. Hillas. *The origin of ultra-high-energy cosmic rays.* Ann. Rev. Astron. Astrophys., 22: pp. 425–444 (1984).

[50] A. R. Bell. *The acceleration of cosmic rays in shock fronts. II.* Royal Astronomical Society, Monthly Notices, 182: pp. 443–455 (1978).

[51] J. Abraham, P. Abreu, M. Aglietta et al. *Correlation of the highest-energy cosmic rays with the positions of nearby active galactic nuclei.* Astroparticle Physics, 29: pp. 188–204 (2008). doi:10.1016/j.astropartphys.2008.01.002.

[52] P. Abreu, M. Aglietta, E. Ahn et al. *Update on the correlation of the highest energy cosmic rays with nearby extragalactic matter.* Astroparticle Physics, 34(5): pp. 314 – 326 (2010). doi:10.1016/j.astropartphys.2010.08.010.

[53] R. U. Abbasi, T. Abu-Zayyad, M. Allen et al. *Search for Correlations between HiRes Stereo Events and Active Galactic Nuclei*. Astropart. Phys., 30: pp. 175–179 (2008).

[54] M. P. Veron-Cetty. *A catalogue of quasars and active nuclei: 12th edition.* Astronomy and astrophysics: A European journal, 455: pp. 773–777 (2006).

[55] O. C. Alkhofer. *Introduction to Cosmic Radiation.* Verlag Carl Thiemig (1975).

[56] B. Keilhauer. *Investigation of Atmospheric Effects on the Development of Extensive Air Showers and their Detection with the Pierre Auger Observatory.* Ph.D. thesis, Universität Karlsruhe (2003).

[57] F. Arciprete, M. Bohacova, J. Bluemer et al. *AIRFLY: Measurement of the Air Fluorescence Radiation Induced by Electrons.* Nuclear Physics B - Proceedings Supplements, 150: pp. 186 – 189 (2006). doi:10.1016/j.nuclphysbps.2004.06.007.

[58] T. Gaisser and A. Hillas. *Reliability of the Method of Constant Intensity Cuts for Reconstructing the Average Development of Vertical Showers.* Proceedings of the 15th International Cosmic Ray Conference, 8: p. 353 (1977).

[59] M. Unger. *Shower Profile Reconstruction from Fluorescence and Cherenkov light.* GAP-2006-010 (2006). Internal note of the Pierre Auger Observatory.

[60] M. Nagano and A. A. Watson. *Observation and implications of the ultrahigh-energy cosmic rays.* Reviews of Modern Physics, 72: pp. 689–732 (2000).

[61] A. Haungs, H. Rebel and M. Roth. *Energy spectrum and mass composition of high-energy cosmic rays.* Reports on Progress in Physics, 66 (2003). doi:10.1088/0034-4885/66/7/202.

[62] D. Ardouin, A. Belletoile, C. Berat et al. *Geomagnetic origin of the radio emission from cosmic ray induced air showers observed by CODALEMA.* Astroparticle Physics, 31: pp. 192 – 200 (2009).

[63] B. Revenu. *Radio detection of cosmic ray air showers by the RAuger experiment, a fully autonomous and self-triggered system installed at the Pierre Auger Observatory.* Nucl. Instrum. Methods Phys. Res., Sect. A (2010). doi:10.1016/j.nima.2010.11.087.

[64] H. Allan, R. Clay and J. Jones. *Radio Pulses from Extensive Air Showers.* Nature, 227: pp. 1116–1118 (1970).

[65] W. D. Apel, J. C. Arteaga, T. Asch et al. *Lateral Distribution of the Radio Signal in Extensive Air Showers Measured with LOPES.* Astroparticle Physics, 32: p. 294 (2009).

[66] H. R. Allan, R. W. Clay, J. K. Jones, A. T. Abrisomov and K. P. Neat. *Radio Pulse Production in Extensive Air Showers.* Nature, 222: pp. 635 – 637 (1969). doi:doi:10.1038/222635a0.

[67] F. D. Kahn and I. Lerche. *Radiation from Cosmic Ray Air Showers.* Proceedings of the Royal Society of London, 289: pp. 206–213 (1966).

[68] O. Ravel for the CODALEMA Collaboration. *The CODALEMA experiment.* Nucl. Instrum. Methods Phys. Res., Sect. A (2010). doi:10.1016/j.nima.2010.12.057.

[69] E. Fraenkel, K. de Vries, W. Docters, O. Scholten and A. van den Berg. *Observation of the charge-excess effect in cosmic-ray-induced radio pulses.* GAP-2011-097 (2011). Internal note of the Pierre Auger Observatory.

[70] A. Horneffer and the LOPES Collaboration. *Primary Particle Energy Calibration of the EAS Radio Pulse Height.* Proceedings of the 30th International Cosmic Ray Conference (2007).

[71] W. Heitler. *The quantum theory of radiation.* Oxford University Press, 3 ed. (1954).

[72] J. Hörandel. *Cosmic Rays from the Knee to the second Knee:* 10^{14} *to* 10^{18} *eV.* Modern Physics Letters A (2007).

[73] D. Heck, J. Knapp, J. Capdevielle, G. Schatz and T. Thouw. *CORSIKA: A Monte Carlo Code to Simulate Extensive Air Showers.* Report FZKA 6019, Karlsruhe (1998).

[74] F. Schmidt. *CORSIKA Shower Images.* http://www.ast.leeds.ac.uk/~fs/showerimages.html.

[75] G. Askaryan. Soviet Phys. JETP Lett. (USSR), 14: p. 441 (1962).

[76] D. Saltzberg, P. Gorham, D. Walz et al. *Observation of the Askaryan Effect: Coherent Microwave Cherenkov Emission from Charge Asymmetry in High-Energy Particle Cascades.* Phys. Rev. Lett., 86: pp. 2802–2805 (2001). doi: 10.1103/PhysRevLett.86.2802.

[77] K. D. de Vries, A. M. van den Berg, O. Scholten and K. Werner. *The lateral distribution function of coherent radio emission from extensive air showers: Determining the chemical composition of cosmic rays.* Astroparticle Physics, 34: pp. 267–273 (2010).

[78] H. Falcke and P. Gorham. *Detecting Radio Emission from Cosmic Ray Air Showers and Neutrinos with a Digital Radio Telescope.* Astroparticle Physics, 19: p. 477 (2003).

[79] J. Jackson. *Classical Electrodynamics*, vol. 2. John Wiley & Sons, Inc. (1975).

[80] A. M. van den Berg. *Radio detection of high-energy cosmic rays at the Pierre Auger Observatory.* Proceedings of the 30th International Cosmic Ray Conference, 5: pp. 885–888 (2008).

[81] World Data Center for Geomagnetism. http://wdc.kugi.kyoto-u.ac.jp/igrf/index.html.

[82] International Association of Geomagnetism and Aeronomy, Working Group V-MOD. *International Geomagnetic Reference Field: the eleventh generation.* Geophys. J. Int., 183: pp. 1216–1230 (2010). doi:10.1111/j.1365-246X.2010. 04804.x.

[83] K. Werner and O. Scholten. *Macroscopic Treatment of Radio Emission from Cosmic Ray Air Showers based on Shower Simulations.* Astropart.Phys., 29: pp. 393–411 (2008).

[84] O. Scholten, K. Werner and F. Rusydi. *A Macroscopic Description of Coherent Geo-Magnetic Radiation from Cosmic Ray Air Showers.* Astropart. Phys., 29: pp. 94–103 (2008).

[85] O. Scholten, K. D. de Vries and K. Werner. *Coherent radiation from extensive air showers.* Nuclear Instruments and Methods in Physics Research Section A: Accelerators, Spectrometers, Detectors and Associated Equipment (2010). doi:10.1016/j.nima.2010.11.125.

[86] M. Ludwig and T. Huege. *REAS3: Monte Carlo simulations of radio emission from cosmic ray air showers using an "end-point" formalism.* Astropart. Phys., 34: pp. 438 – 446 (2011). doi:10.1016/j.astropartphys.2010.10.012.

[87] C. W. James, H. Falcke, T. Huege and M. Ludwig. *An 'endpoint' formulation for the calculation of electromagnetic radiation.* submitted to Phys. Rev. E, arXiv:1007.4146v2 (2011).

[88] T. Huege, M. Ludwig, O. Scholten and K. de Vries. *The convergence of EAS radio emission models and a detailed comparison of REAS3 and MGMR simulations.* Nucl. Instrum. Methods Phys. Res., Sect. A (2010).

[89] T. Huege, R. Engel, A. Haungs et al. *The REAS2 code for the simulation of radio emission from extensive air showers.* GAP-2008-088 (2008). Internal note of the Pierre Auger Observatory.

[90] S. Lafebre, H. Falcke, J. Hörandel, T. Huege and J. Kuijpers. *Prospects for determining air shower characteristics through geosynchrotron emission arrival times* (2010).

[91] T. Huege, R. Ulrich and R. Engel. *Monte Carlo simulations of geosynchrotron radio emission from CORSIKA-simulated air showers.* Astroparticle Physics, 27: pp. 392–405 (2007).

[92] M. Ludwig. *Modelling of radio emission from cosmic ray air showers.* Ph.D. thesis, Karlsruhe Institut für Technologie (KIT) (2011).

[93] P. W. Gorham, N. G. Lehtinen, G. S. Varner et al. *Observations of microwave continuum emission from air shower plasmas.* Phys. Rev. D, 78: p. 032007 (2008). doi:10.1103/PhysRevD.78.032007.

[94] M. Monasor, M. Bohacova, C. Bonifazi et al. *The Microwave Air Yield Beam Experiment (MAYBE): measurement of GHz radiation for Ultra-High Energy Cosmic Rays detection.* Proceedings of 32nd International Cosmic Ray Conference (2011).

[95] R. Smida, H. Blümer, R. Engel et al. *First results of the CROME experiment.* Proceedings of 32nd International Cosmic Ray Conference (2011).

[96] P. Allison for the Pierre Auger Collaboration. *Microwave detection of cosmic ray showers at the Pierre Auger Observatory.* Proceedings of the 32nd International Cosmic Ray Conference (2011).

[97] J. Blümer and the Pierre Auger Collaboration. *The northern site of the Pierre Auger Observatory.* New Journal of Physics, 12 (2010). doi:10.1088/1367-2630/12/3/035001.

[98] H. Dembinski. *Measurement of the flux of ultra high energy cosmic rays using data from very inclined air showers at the Pierre Auger Observatory.* Ph.D. thesis, RWTH Aachen University (2009).

[99] C. Bonifazi for the Pierre Auger Collboration. *The angular resolution of the Pierre Auger Observatory.* Nuclear Physics B - Proceedings Supplements, 190: pp. 20–25 (2009). doi:10.1016/j.nuclphysbps.2009.03.063.

[100] X. Bertou, P. Allison, C. Bonifazi et al. *Calibration of the surface array of the Pierre Auger Observatory.* Nucl. Instrum. Methods Phys. Res., Sect. A, 568: pp. 839 – 846 (2006). doi:10.1016/j.nima.2006.07.066.

[101] J. Abraham, P. Abreu, M. Aglietta et al. *Trigger and aperture of the surface detector array of the Pierre Auger Observatory.* Nucl. Instrum. Methods Phys. Res., Sect. A, 613: pp. 29 – 39 (2010). doi:10.1016/j.nima.2009.11.018.

[102] R. Pesce for the Pierre Auger Collaboration. *Energy calibration of data recorded with the surface detectors of the Pierre Auger Observatory: an update.* Proceedings of 32nd International Cosmic Ray Conference (2011).

[103] H. J. Mathes for the Pierre Auger Collaboration. *The HEAT Telescopes of the Pierre Auger Observatory Status and First Data.* Proceedings of the 32nd International Cosmic Ray Conference (2011).

[104] F. Sánchez for the Pierre Auger Collaboration. *The AMIGA detector of the Pierre Auger Observatory: an overview.* Proceedings of the 32nd International Cosmic Ray Conference (2011).

[105] I. C. Maris for the Pierre Auger Collaboration. *The AMIGA infill detector of the Pierre Auger Observatory: performance and first data.* Proceedings of 32nd International Cosmic Ray Conference (2011).

[106] The EASIER group. *Evidence for a GHz emission from air-showers.* GAP-2011-082 (2011). Internal note of the Pierre Auger Observatory.

[107] The EASIER group. *A First Look At The EASIER MHz Data.* GAP-2011-081 (2011). Internal note of the Pierre Auger Observatory.

[108] B. Revenu for the Pierre Auger Collaboration. *Autonomous detection and analysis of radio emission from air showers at the Pierre Auger Observatory.* Proceedings of 32nd International Cosmic Ray Conference (2011).

[109] H. Rottgering, R. Braun, P. D. Barthel et al. *LOFAR - Opening up a new window on the Universe.* Cosmology, galaxy formation and astroparticle physics on the pathway to the SKA (2006).

[110] A. M. van den Berg, J. Coppens, S. Harmsma et al. *First detection of radio signals from cosmic rays at the Pierre Auger Observatory.* GAP-2007-065 (2007). Internal note of the Pierre Auger Observatory.

[111] C. Timmermans for the HiSPARC Collaboration. *Setup and first results of the HiSPARC experiment.* Proceedings of the 29th International Cosmic Ray Conference (2005).

[112] C. Timmermans. Private Communication (2007).

[113] J. Coppens. *Observation of radio signals from air showers at the Pierre Auger Observatory.* Nuclear Instruments and Methods in Physics Research Section A: Accelerators, Spectrometers, Detectors and Associated Equipment, 604: pp. 41 – 43 (2009). doi:10.1016/j.nima.2009.03.119.

[114] H. Schoorlemmer. Private Communication (2011).

[115] A. M. van den Berg (corresponding author). *Observation of Askaryan effect in air showers (in preparation)* (2011).

[116] S. Acounis, A. Belletoile, D. Charrier et al. *First detection of radio signals from cosmic ray air showers with a self triggered, fully autonomous system.* GAP-2007-130 (2007). Internal note of the Pierre Auger Observatory.

[117] F. Schröder, T. Asch, L. Bähren et al. *New method for the time calibration of an interferometric radio antenna array.* Nucl. Instrum. Methods Phys. Res., Sect. A, 615: pp. 277 – 284 (2010).

[118] K. Weidenhaupt and G. Zarza. *Differential GPS Survey AERA Phase I.* Private Communication (2010).

[119] A. Aminaei, P. Dolron, J. Hörandel and J. Kelley. *AERA EMC Tests at ASTRON.* Private Communication (2010).

[120] C. Ruehle. *Advanced digital self-triggering of radio emission of cosmic rays.* Nucl. Instrum. Methods Phys. Res., Sect. A (2010). doi:10.1016/j.nima.2010.11.017.

[121] N. Mandolesi, G. Morigi and G. G. C. Palumbo. *Radio pulses from extensive air showers during thunderstorms — the atmospheric electric field as a possible cause.* Journal of Atmospheric and Terrestrial Physics, 36: pp. 1431–1435 (1974).

[122] M. Ender for the LOPES Collaboration. *Radio emission of extensive air showers during thunderstorms.* Proceedings of the 31st International Cosmic Ray Conference (2009).

[123] J. Hörandel. *Configurations for a Radio Antenna Array at the Pierre Auger Observatory.* GAP-2009-034 (2009). Internal note of the Pierre Auger Observatory.

[124] P. Lautridou. *Results of the radio-detection experiment CODALEMA.* Nuclear Instruments and Methods in Physics Research Section A: Accelerators, Spectrometers, Detectors and Associated Equipment, 604: pp. S13 – S19 (2009).

[125] C. Riviére. Private Communication.

[126] S. Fliescher for the Pierre Auger Collaboration. *Radio Detector Array Simulation: A Full Simulation Chain for an Array of Antenna Detectors.* Nucl. Instrum. Methods Phys. Res., Sect. A, 604: pp. 225 – 229 (2009). The author contributed the analysis on the comparison of measured air showers and air showers simulated with REAS2. The reconstruction is realized in the RDAS software. The analysis is not part of this thesis.

[127] C. R. Anderson. *An Introduction to Ultra Wideband Communication Systems.* Prentice Hall Communications Engineering and Emerging Technologies Series (2005).

[128] M. Thumm, W. Wiesbeck and S. Kern. *Hochfrequenzmesstechnik : Verfahren und Messsysteme.* Teubner (1997).

[129] R. C. Jones. *A New Calculus for the Treatment of Optical Systems.* J. Opt. Soc. Am, 31: pp. 488–493 (1941). doi:10.1364/JOSA.31.000488.

[130] C. A. Balanis. *Antenna Theory: Analysis and Design.* John Wiley & Sons, Inc. (2005).

[131] *IEEE Standard Definitions of Terms for Antennas.* IEEE Std 145-1993 (1993). doi:10.1109/IEEESTD.1993.119664.

[132] P. Abreu, M. Aglietta, E. Ahn et al. *Advanced functionality for radio analysis in the Offline software framework of the Pierre Auger Observatory.* Nucl. Instrum. Methods Phys. Res., Sect. A, 635: pp. 92 – 102 (2011). doi:10.1016/j.nima.2011.01.049. The contribution by the author to this article is Fig. 3 including caption (introduction of a spherical coordinate system). The figure and the radio extension of the 'Offline' software are not part of this thesis.

[133] J. P. Hamaker, J. D. Bregman and R. J. Sault. *Understanding radio polarimetry. I. Mathematical foundations.* Astron. Astrophys. Suppl. Ser., 117: pp. 137–147 (1996). doi:10.1051/aas:1996146.

[134] W. Sörgel and W. Wiesbeck. *Influence of the Antennas on the Ultra-Wideband Transmission.* EURASIP Journal on Applied Signal Processing, 3: pp. 296–305 (2005). doi:10.1155/ASP.2005.296.

[135] W. A. Davis and K. Agarwal. *Radio Frequency Circuit Design.* Wiley Series in Microwave and Optical Engineering (2001).

[136] M. E. Brinson and S. Jahn. *Qucs: A GPL software package for circuit simulation, compact device modelling and circuit macromodelling from DC to RF and beyond.* International Journal of Numerical Modelling: Electronic Networks, Devices and Fields, 22: pp. 297–319 (2009). doi:10.1002/jnm.702.

[137] H. Carlin. *The Scattering Matrix in Network Theory.* IRE Transactions on Circuit Theory, 3: pp. 88 – 97 (1956).

[138] G. Burke and A. Poggio. *Numerical Electromagnetics Code (NEC) method of moments, parts I, II, III.* Tech. rep., Lawrence Livermore National Laboratory (NEC-l (1977), NEC-2 (1981), NEC-3 (1983)).

[139] NEC2. *Version nec-2-14.1.* http://patch-tracker.debian.org/package/nec/2-14.1.

[140] P. W. Gorham, F. E. Baginski, P. Allison et al. *The ExaVolt Antenna: A Large-Aperture, Balloon-embedded Antenna for Ultra-high Energy Particle Detection* (2011).

[141] K. Stewart, B. Hicks, P. Ray et al. *LOFAR antenna development and initial observations of solar bursts.* Planetary and Space Science, 52: pp. 1351 – 1355 (2004).

[142] W. C. Gibson. *The Method of Moments in Electrodynamics.* Champman & Hall/CRC (2008).

[143] *4Nec2.* http://home.ict.nl/˜arivoors/.

[144] ITU Recommendation. *ITU-R P.527-3 Electrical Characteristics of the Surface of the Earth.* ITU-R Recommendations & Reports (1992).

[145] A. M. van den Berg, G. Zarza and K. Weidenhaupt. *Measurement of the Low Frequency Resistivity of Soil at the Auger Engineering Radio Array.* GAP-2011-036 (2011). Internal note of the Pierre Auger Observatory.

[146] H. Gemmeke. *Advanced Detection Methods of Radio Signals from Cosmic Rays for KASCADE Grande and Auger.* International Journal of Modern Physics A, 21: pp. 242–246 (2006).

[147] D. E. Isbell. *Log Periodic Dipole Arrays.* IRE Transactions on Antennas and Propagations, 8: pp. 260–267 (1960).

[148] T. Winchen. *Measurements of the Continuos Radio Background and Comparison with Simulated Radio Signals from Cosmic Ray Air Showers at the Pierre Auger Observatory.* Diploma Thesis (2007).

[149] K. Rothammel and A. Krischke. *Rothammels Antennenbuch*, vol. 12. DARC Verlag Baunatal (2001).

[150] M. Stephan for the Pierre Auger Collaboration. *Antennas, Filters and Preamplifiers designed for the Radio Detection of Ultra-High-Energy Cosmic Rays.* Proceedings of Asia-Pacific-Microwave Conference 2010, pp. 1455–1458 (2010).

[151] M. Stephan. *Design and Test of a Low Noise Amplifier for Radio Antennas Measuring Atmospheric Showers.* GAP-2010-045 (2010). Internal note of the Pierre Auger Observatory.

[152] O. Seeger for the Pierre Auger Collaboration. *Logarithmic periodic dipole antennas for the Auger Engineering Radio Array.* Nucl. Instrum. Methods Phys. Res., Sect. A (2010). doi:10.1016/j.nima.2010.10.140.

[153] K. Weidenhaupt. Private Communication (2010).

[154] Offline. *Auger SD Station List* (2010).

[155] B. Revenu and P.Billoir. *Notions of geodesy and the UTM coordinate system. Proposition of a local cartesian coordinate system for the southern Auger site.* GAP-2001-28 (2001). Internal note of the Pierre Auger Observatory.

[156] Suunto. *Suunto KB-series User's guide.* http://www.suunto.com/en/ Products/Precision_instruments/SUUNTO-KB-14.

[157] R. Showstack. *In Brief: Updated International Geomagnetic Reference Field.* EOS, Transactions American Geophyscal Union, 91: p. 142 (2010).

[158] F. Lowes. *The International Geomagnetic Reference Field: A "Health" Warning.* http://www.ngdc.noaa.gov/IAGA/vmod/igrfhw.html (2010).

[159] J. Kennedy and R. Eberhart. *Particle swarm optimization.* Proceedings of IEEE International Conference on Neural Networks, 4: pp. 1942 – 1948 (1995).

[160] O. Seeger. *Absolute Calibration of the Small Black Soider Antenna for the Pierre Auger Observatory.* Diploma Thesis, RWTH Aachen University (2010).

[161] O. Krömer. *Empfangssystem zur Radioobservation hochenergetischer kosmischer Schauer und sein Verhalten bei Selbsttriggerung.* Ph.D. thesis, University Karlsruhe (2008).

[162] S. Nehls, A. Hakenjos, M. Arts et al. *Amplitude calibration of a digital radio antenna array for measuring cosmic ray air showers.* Nucl. Instrum. Methods Phys. Res., Sect. A, 589: pp. 350 – 361 (2008). doi:10.1016/j.nima.2008.02.092.

[163] J. D. Kraus and R. J. Marhefka. *Antennas.* McGraw-Hill (2003).

[164] Schwarzbeck Mess-Elektronik. *BBAL 9136 Biconical Antenna with VHHBB 9124 Balun.*

[165] Rohde & Schwarz. *FSH4 (model 24) Handheld Spectrum Analyzer 100 kHz to 3.6 GHz with preamplifier, tracking generator and internal VSWR bridge.*

[166] T. Asch, M. Erdmann, S. Fliescher et al. *Simulation of an Array of Antenna Detectors.* GAP-2008-177 (2008). Internal note of the Pierre Auger Observatory. The author contributed the software description and the analysis on the comparison of measured and simulated air showers.

[167] J. Coppens and C. Timmermans. *Lateral Distribution of Radio Signals from Extensive Air Showers.* GAP-2009-126 (2009). Internal note of the Pierre Auger Observatory.

[168] N. Palmieri, S. Fliescher and T. Huege. *Polarization Analysis for BLS 2007 Radio Auger Data.* GAP-2009-105 (2009). Internal note of the Pierre Auger Observatory. The author reviewed and corrected the manuscript.

[169] S. Fliescher, D. Fraenkel, B. Fuchs et al. *The radio extension of Auger Offline.* GAP-2010-056 (2010). Internal note of the Pierre Auger Observatory in preparation for the published article Ref. 132 including 15 authors. Contributions by the author to the note are Para. 3.6.5, Fig. 8 including caption and the Appendix A.1.21 (introduction of a spherical coordinate system and software interface description).

[170] R. Brun and F. Rademakers. *ROOT — An Object Oriented Data Analysis Framework.* Nucl. Instrum. Methods Phys. Res., Sect. A, 389: pp. 81 – 86 (1997). doi:10.1016/S0168-9002(97)00048-X.

[171] F. Harris. *On the use of windows for harmonic analysis with the discrete Fourier transform.* Proceedings of the IEEE, 66: pp. 51 – 83 (1978). doi: 10.1109/PROC.1978.10837.

[172] J. Kelley and C. Timmermans. *Calibration of the AERA Phase 1 Digitizer.* GAP-2011-028 (2011). Internal note of the Pierre Auger Observatory.

[173] H. V. Cane. *Spectra of the non-thermal radio radiation from the galactic polar regions.* Royal Astronomical Society, Monthly Notices, vol. 189: pp. 465–478 (1979).

[174] T. Asch. *Self-triggering of Radio Signals from Cosmic Ray Air Showers.* Ph.D. thesis, Forschungszentrum Karlsruhe (2009).

[175] F. Schröder. *Instruments and Methods for the Radio Detection of High Energy Cosmic Rays.* Ph.D. thesis, Karlsruher Institut für Technologie (KIT) (2011).

[176] A. V. Oppenheimer, R. W. Schafer and J. R. Buck. *Discrete-Time Signal Processing.* Prentice Hall (1999).

[177] C. E. Shannon. *Communication in the Presence of Noise.* Proceedings of the IRE, 37: pp. 10–21 (1949). doi:10.1109/JRPROC.1949.232969.

[178] J. Shamir. *Optical systems and processes.* SPIE — The International Society for Optical Engeneering (1999).

[179] B. Boashash. *Estimating and Interpreting the Instantaneous Frequency of a Signal-Part 1: Fundamentals.* Proceedings of the IEEE, 80: pp. 519–538 (1992). doi:10.1109/5.135376.

[180] M. Erdmann, S. Fliescher and L. Mohrmann. *Reconstruction of the Wave Front of Radio Signals at AERA.* GAP-2011-092 (2011). Internal note of the Pierre Auger Observatory. The author reviewed and corrected the manuscript.

[181] H. Schoorlemmer. Private Communication (2010).

[182] W. N. Charman. *Atmospheric Electric Field as a Possible Cause of Radio Pulses from Extensive Air Showers.* NATURE, 215: pp. 497–498 (1967).

[183] M. Melissas, T. Huege and A. Haungs. *Measurements of high amplitude radio events during thunderstorms.* GAP-2010-065 (2010). Internal note of the Pierre Auger Observatory.

[184] D. Ardouin, A. Bellétoile, D. Charrier et al. *Characteristics of radioelectric fields from air showers induced by UHECR measured with CODALEMA.* 20th European Cosmic Ray Symposium (2006).

[185] J. Coppens, A. M. van den Berg, S. Harmsma et al. *Analysis of Galactic Radio Background Noise.* GAP-2007-123 (2007). Internal note of the Pierre Auger Observatory.

[186] K. Holland, S. Grebe, H. Schoorlemmer and C. Timmermans. *The effect of noise on reconstructable parameters in radio detection.* GAP-2011-021 (2011). Internal note of the Pierre Auger Observatory.

[187] S. Grebe, J. Kelley and C. Timmermans. Private Communication (2011).

[188] J. Kelley for the Pierre Auger Collaboration. *AERA: the Auger Engineering Radio Array.* Proceedings of the 32nd International Cosmic Ray Conference (2011).

[189] V. Blobel and C. Kleinwort. *A New Method for the High-Precision Alignment of Track Detectors* (2007).

[190] C. Ruehle. *Private Communication* (2011).

[191] F. Schröder and R. Rink. *First Results of the AERA Beacon.* Private Communication (2011).

[192] F. Schröder, H. Bozdog and O. Krömer. *Test Measurements for the Time Calibration of AERA with a Beacon.* GAP-2009-085 (2009). Internal note of the Pierre Auger Observatory.

[193] A. M. van den Berg, W. Docters, E. D. Fraenkel, K. de Vries and K. Weidenhaupt. *Locating transient noise sources at Radio Detection sites.* GAP-2011-083 (2011). Internal note of the Pierre Auger Observatory.

[194] A. Nelles, K. Weidenhaupt, J. Kelley et al. *A Survey of Narrowband and Broadband Radio-frequency Interference at AERA .* GAP-2011-062 (2011). Internal note of the Pierre Auger Observatory. The author contributed the analyis on the reconstruction of background signals.

[195] M. Erdmann, S. Fliescher, L. Mohrmann and K. Weidenhaupt. *A Novel Method of Selecting Cosmic Ray Candidates.* GAP-2011-108 (2011). Internal note of the Pierre Auger Observatory. The author contributed the analyis on the background rejection.

[196] B. Antokhonov, S. Berezhnev, D. Besson et al. *TUNKA-133: A new array for the study of ultra-high energy cosmic rays.* Bulletin of the Russian Academy of Sciences: Physics, 75: pp. 367–370 (2011). doi:10.3103/S1062873811030075.

[197] H. Gemmeke, O. Krömer, W. Apel et al. *New Antenna for Radio Detection of UHECR.* Proceedings of the 31st International Cosmic Ray Conference (2009).

[198] B. Revenu for the CODALEMA collaboration. *Design and performances of a fully autonomous antenna for radio detection of extensive air showers.* Proceedings of the 30th International Cosmic Ray Conference (2007).

[199] D. Charrier for the CODALEMA Collaboration. *Design of a low noise, wide band, active dipole antenna for a cosmic ray radiodetection experiment.* IEEE Antennas and Propagation Society International Symposium, pp. 4485–4488 (2007). doi:10.1109/APS.2007.4396539.

[200] D. Charrier. *Antenna development for astroparticle and radioastronomy experiments.* Nucl. Instrum. Methods Phys. Res., Sect. A (2010). doi: 10.1016/j.nima.2010.10.141.

[201] S. Licul. *Ultra-Wideband Antenna Characterization and Modeling.* Ph.D. thesis, Virginia Tech (2004).

[202] A. H. Bridle. *The spectrum of the radio background between 13 and 404 MHz.* Mon. Not. R. astr. Soc., 136: p. 219 (1967).

[203] K. Lawson, C. Mayer, J. Osborne and M. Parkinson. *Variations in the Spectral Index of the Galactic Radio Continuum Emission in the Northern Hemisphere.* Monthly Notices of the Royal Astronomical Society, 225: pp. 307–328 (1987).

[204] E. Polisensky. *LFmap: A Low Frequency Sky Map Generating Program.* Long
        Wavelength Array (LWA) Memo Series, 111 (2007).

[205] A. D. Oliveira-Costa, M. Tegmark, B. M. Gaensler et al. *A model of diffuse
        Galactic radio emission from 10 MHz to 100 GHz.* Monthly Notices of the
        Royal Astronomical Society, 388: pp. 247–260 (2008). doi:10.1111/j.1365-2966.
        2008.13376.x.

[206] J. D. Kraus. *Radio Astronomy.* McGraw-Hill Bock Company (1966).

[207] B. Fuchs. Private Communication (2011).

[208] I. N. Bronstein, K. A. Semendjajew, G. Grosche et al. *Taschenbuch der Ma-
        thematik.* Teubner (1996).

Acknowledgements

Stefan Fliescher

Dipl.-Phys.

Persönliche Daten

Geburtsdatum	09.11.1981
Geburtsort	Mönchengladbach
Staats-angehörigkeit	deutsch

Qualifikation

Jun. 2001	**Abitur**, *Gymnasium Rheindahlen*, Mönchengladbach.
Okt. 2002 - Jun. 2008	**Studium der Physik**, *RWTH Aachen University*, Aachen, Abschluss: Diplom-Physiker.
ab Aug. 2008	**Promotion in Physik**, *RWTH Aachen University*, Aachen.